Growth and remodelling of the left ventricle post myocardial infarction

August 2018

Declaration of Authorship

I, XIN ZHUAN, declare that this thesis titled, 'Growth and Remodelling of the Left Ventricle Post Myocardial Infarction' and the work presented in it are my own. I confirm that:

- This work was done wholly or mainly while in candidature for a research degree at this University.
- Where any part of this thesis has previously been submitted for a degree or any other qualification at this University or any other institution, this has been clearly stated.
- Where I have consulted the published work of others, this is always clearly attributed.
- Where I have quoted from the work of others, the source is always given. With the exception of such quotations, this thesis is entirely my own work.
- I have acknowledged all main sources of help.
- Where the thesis is based on work done by myself jointly with others, I have made clear exactly what was done by others and what I have contributed myself.

Signed: _____

Date: _____

"If living in a world using Maths as language, I want to be a rock star."

Abstract

Living organs in human bodies continuously interact with the *in vivo* bio-environment, while reshaping and rearranging their constituents, responding to external or internal stimuli through life cycles. For instance, living tissues adjust the growth (or turnover) rates of their constituents to develop (volumetric and mass) changes as the tissues adapt to the pathological or physiological changes in bio-environment. From the perspective of biomechanics, changes in the bio-environment will induce the growth and remodelling (G&R) process and reset the mechanical environment. Consequently, the mechanical cues will feed back to G&R processes. In the long run, the interaction between G&R and the mechanical response of living organs plays an important role in regulating the organ formulation or pathological growth.

To understand the interaction between the mechanical response and the G&R process, an important ingredient in evaluating the involved mechanics is knowledge of the solid mechanical properties of the soft tissues. Residual stress, resulting from G&R of soft tissues, is important in modelling the mechanics of soft tissues, which still presents a modelling challenge for including residual stress in cardiovascular applications. For G&R of living organs, changes of tissue structure and volume are also important determinants for organ development. This raises academic challenges for the understanding of the evolution of material properties and mechanical response of living tissues within a dynamic environment.

To investigate the stress states (residual strain or residual stress) of living organs, the experimental results showed that the arterial slices would spring open after cutting along the radial directions, which indicates the residual strain in organs estimated by the opening angle [23]. The residual strain, which is the elastic strain between zero-stress and no-load states, indicates the existence of residual stress after removal of the external loads. The residual stress is considered to modulate the growth and remodelling process in living organs. The evolution of residual stress could relieve the information about the history of growth, which could help to better the understanding of the formation of organs and the development of diseases.

Besides the residual stress, G&R processes are regulated by other factors, while the principles governing those mechanism are still not fully understood. Obviously, improving knowledge in this particular field will give huge potential for the design and optimization of clinical treatments to efficiently save more lives.

From a general mechanics perspective to investigate the G&R process in living tissues, the questions are: How does the residual stress influence the fibre remodelling and the material properties of entire organs? How to determine the combined effects of growth (in the stressed configuration) and remodelling on the fibre structure? How to develop a framework for investigating G&R processes occurring in the stressed configuration?

For arteries, multiple layer models are developed to analytically study residual stress in living organs. For the heart, due to its complex structure and geometry, most previous studies used the unloaded configuration or one-cut configuration as the stress-free configuration to estimate the stress state. However, both experimental and theoretical studies have suggested that: 1) residual stress will significantly influence the stress distribution in the heart. 2) a simple (or single) cut does not release all the residual stress in the heart. We build a multi-cut model and show that multiple cuts are required to release the residual stresses in the left ventricle. Our results show that with the 2-cut and 4-cut models (one radial cut followed by circumferential cuts), agreement with the measured opening angles and radii can be greatly improved. This suggests that a multi-cut model should be used to predict the residual stresses in the left ventricle, at least in the middle wall region. We further show that tissue heterogeneity plays a significant role in the model results, and that an inhomogeneous model with combined radial and circumferential cuts should be used to estimate the correct order of magnitude of the residual stress in the heart.

Understanding the healing and remodelling processes induced by myocardial infarction (MI) of the heart is important and the mechanical properties of the myocardium post-MI can be indicative for effective treatments aimed at avoiding eventual heart failure. MI remodelling is a multiscale feedback process between the mechanical loading and cellular adaptation. In this thesis, we use an agent-based model to describe collagen remodelling by fibroblasts regulated by chemical and mechanical cues after acute MI, and upscale into a finite element (FE) 3D left ventricular model. This enables us to study the scar healing (collagen deposition, degradation and reorientation) of a rat heart post-MI. Our results, in terms of collagen accumulation and alignment, compare well to published experimental data. In addition, we show that different shapes of the MI region can affect the collagen remodelling, and in particular, the mechanical cue plays an important role in the healing process.

For volumetric growth, recently, when the idea of growth is applied to study the evolution of organ formations, it's usually assumed that growth always occurs in the natural (reference) configuration. In some researches, it is assumed that the growth could release all the residual stress, and that further growth will start from the updated but stress-free configuration. However, living organs are actually exposed to external loading all the time, while the growth should occur from the residually-stressed current configuration. In this thesis, A theoretical framework is developed to calculate the mechanical behaviour of soft tissue after introducing inhomogeneous growth in a residually-stressed current configuration, which avoids assuming that the growth occurs in a 'virtual' reference configuration. Moreover, the theoretical framework is introduced to couple the growth and fibre remodelling process to describe the mechanical behaviour of living tissues.

Acknowledgements

It's my great honor to express my sincere gratitude to all the people and organizations who offer helps and supports during my PhD period.

I would like to thank my supervisors Prof. Raymond Ogden and Prof. Xiaoyu Luo. They both shared their solid academic fundamentals and wide views on researching with my during my research. Prof. Ogden is one of the greatest scientists I ever met. During period to develop my own research interests, his effects are the sources of enthusiasm and inspirations to go through the hardness. Considerately, He gives me keys to open the doors to the hidden academic world. Prof. Luo shares her great experience during my research program, which I deeply appreciated. She can always sense my mistakes by simply checking my calculation results, rather than going through all details. She is considered as a 'research magic' charming me. I somehow self-centered during my research, especially when I tried to develop the methodology or theoretical frameworks. They both are inspiriting and patient to guide me to the proper directions, making me continuously improve myself to explore the academic world.

The School of *Mathematical and Statistic* provided a joyful environment to conduct my research. I met the fantastic researchers here, and also had opportunities to experience the greatest education system in the world. Many thanks for University of Glasgow shelling my during my second longest student period, which is taken as my home ever of my life. I appropriated everyone sharing his/her knowledge and experience with me here, especially my colleges from research group.

My families offer their unconditional loves and effects to support and heal me from all emotional or physical hardnesses. Without them, I can't be no where. It's my best lucky to have them as my parents, well-being wife, grandpa and all other relatives.

I would like to thank my country and people. I'm proud to be one of Chinese people, whose home country has a long history but going through so many misfortunes. We are the witnesses for a upcoming great historic era of China which applies its energetic motivations to contribute to the rest of world. It's my fortune to live in this time.

It's my great pleasure to feedback my knowledge and creativities to the social and academic communities in my rest life.

Contents

List of Figures

List of Tables

Abbreviations

EDF	**E**nergy **D**ensity **F**unction
FE	**F**inite **E**lement
G&R	**G**rowth and **R**emodelling
LV	**L**eft **V**entricle
MI	**M**yocardial **I**nfarction
P-K	**P**iola- **K**irchhoff
SEF	**S**train **E**nergy **F**unction

Symbols

$\mathbf{c}$	distance vector
d	normalized distance parameter
$\mathbf{e}_i$ (or $\mathbf{E}_i$)	ith orthogonal basis
$\mathbf{f}$	fibre vector
$\mathbf{g}_j$ (or $\mathbf{G}_j$)	ith reciprocal basis
$\mathbf{g}^i$ (or $\mathbf{G}^i$)	ith natural basis
k	measurement of opening angle
m	mass of body
$\mathbf{n}$ (or $\mathbf{N}$)	direction vector in current (reference) configuration
r (or R)	radii of body
p	Lagrange multiplier
q (or Q)	survival rate of the living tissue
o (or o^*)	observer
$\mathbf{v}$	velocity of material point
$\mathbf{v}_i$	ith external cues for fibroblast migration
$\mathbf{x}$ (or $\mathbf{x}^*$)	vector of material point in specific configuration
$\mathscr{B}$ (or $\mathscr{V}$)	specified configuration of body
$\mathbf{C}$ ($\mathbf{b}$)	right (left) Cauchy-Green tensors
$C(\bullet)$	chemokine concentration
D_{ij}	growth–rate coefficient
D_c	diffusion coefficient
d$\mathbf{S}$ (or d$\mathbf{s}$)	the area vector in a specified configuration
$\mathbf{E}$ ($\mathbf{e}$)	Green (Lagrange) strain tensor
$\mathbf{F}$ (or $\mathbf{A}$)	deformation tensor

$\mathbf{F}_e$	elastic deformation tensor
$\mathbf{F}_g$ (or $\mathbf{G}$)	growth tensor
$H(\bullet)$	Heaviside function
$\mathbf{I}$	unit tensor
I_i	ith invariance
I_0	Bessel function of the first kind of order zero
$\mathbf{M}$ ($\mathbf{m}$)	line element vector in reference (current) configuration
M_i	weight factors for ith external cue
$N(\bullet)$	the number of collagen fibres
$\mathbf{K}$	First P–K stress
J	determine of deformation tensor (volumetric ratio)
P_i	ith rate parameter of fibroblast activation
$\mathbf{R}$ (or $\mathbf{Q}$)	rotation tensor
$\mathbf{S}$	nominal stress (tensor)
S_{cell}	value of the fibroblast migration speed
$\mathbf{T}$ ($\boldsymbol{\sigma}$ or $\sigma*$)	Cauchy stress
$\mathbf{U}$ & $\mathbf{V}$	positive definite symmetric (deformation) tensors
V (or v)	volume of body
$\mathbf{X}$ (or $\mathbf{X}^*$)	vector of material point in reference configuration
$W(\bullet)$	SEF
W_i	scaling factors for ith external cue
$\boldsymbol{\Gamma}^i_{jk}$	Christoffel symbol
$\boldsymbol{\Gamma}$	velocity gradient (tensor)
δ_{ij}	Kronecker delta symbol
θ (or Θ)	fibre angle
$\varphi(\bullet)$	fibre density function
Φ	volumetric fraction
λ	stretch
ρ	density of body
$\boldsymbol{\rho}$	fibroblast resultant cue
σ^2	variance
$\boldsymbol{\tau}$	residual stress

Ω	boundary of region

To persons caring or cared for me.

Chapter 1

Introduction

Living organs in human bodies continuously interact with *in vivo* bio-environment, while reshaping and rearranging their constituents under chemical, mechanical or genetic stimuli through their life cycles. During mature periods, these processes remain in a stable and homeostatic state. However, changes of internal or external bio-environments will disrupt the balance, and tissues will grow and remodel in response to an insult. For example, heart diseases will stimulate the local healing process for myocardium remodelling. Besides, physiologically, exercise may induce healthy and reversible growth and remodelling. After adjusting the growth (or turnover) rates of constituents for living organs, they will develop volumetric and mass tissue changes to adapt to the pathological or physiological changes in their bio-environment. From the perspective of biomechanics, changes in the bio-environment will induce the growth and remodelling (G&R) process, which change the material properties of living organ by changing tissue structure. Then, the mechanical environment will be reset. Consequently, the mechanical cues will feed back to the G&R processes. In the long run, the interaction between G&R and mechanical response of living organs plays an important role in regulating the organ formulation or pathological growth.

Therefore, to understand the interaction between the mechanical response and the G&R process, an important ingredient in evaluating the involved mechanics is knowledge of the solid mechanical properties of the soft tissues. Residual stress, resulting from G&R of soft tissues, is important in modelling the mechanics of soft tissues, since the stress state in the reference configuration has a substantial effect on the subsequent response to external loads, as illustrated by the application of nonlinear elasticity theory. Thus, an appropriately estimated residual stress at particular time instants could provide useful information about the growth history of living tissues. However, how best to include the important effect of residual stress in cardiovascular applications presents a modelling challenge.

For G&R of living organs, changes of tissue structure and volume are important determinants for organ development. This raises academic challenges for the understanding of the evolution of material properties and mechanical response of living tissues within an dynamic environment. For instance, the fibre structure in heart myocardium is remodelled by fibroblast migration, since individual fibres are deposited and rotated by fibroblasts. To investigate the biomechanical response of a organ during remodelling, complex multiple-scale calculations will be involved. Besides, since remodelling is influenced by different environment cues (like chemical or mechanical cues), multi-physics calculations are also involved.

In this thesis, we focus on three new developments of soft tissue modelling. Firstly, a multiple cut model is developed to estimate residual stress in the heart, which helps to explain recent experiments on residual stress. Secondly, a multiscale three-dimensional heart model is developed for simulating the remodelling process after heart infarction. This model captures the interaction and information exchange processes between the mechanical behaviour and the collagen tissue remodelling guided by bio-environmental cues. Finally, a volumetric growth approach is developed for simulating the inhomogeneous growth in residually-stressed current configurations of living tissues.

1.1 Residual Stress and Opening-cut Method

To estimate the stress state in organs, traditionally, one of the fundamental ideas is to assume the existence of a (stress-free) reference configuration [57], which coincides with the unloaded configuration. However, according to experimental observation [23], the unloaded configuration is not stress free, but is residually stressed. Obviously, residual stress affects the subsequent mechanical response of the tissues to external loads. Therefore, it is of importance to estimate the residual stress state in tissues. The residual stress can be estimated using the so-called *opening angle* method [23], in which an opening angle indicative of the extent of the residual strain can be measured after a single radial cut on intact arterial ring (fig. 1.1). Using the open-angle configuration as the reference configuration, the residual stress of a cylindrical artery model can be estimated [77]. This methodology has been extended to multiple cuts by Taber and Humphrey [78], and used in the two-layered arterial models by Holzapfel et al. [34].

Residual stress in the reference configuration is important in modelling the mechanics of soft tissues when using nonlinear elasticity theory to determine the stress state. And omission of the residual stress leads to significantly different total stress predictions [71].

However, work that includes residual stress in complex organs, such as the heart, remains rare. A few existing models for the left ventricle that take account of residual stress are based on the assumption that a simple radial cut can release all the residual stresses [90], but this assumption

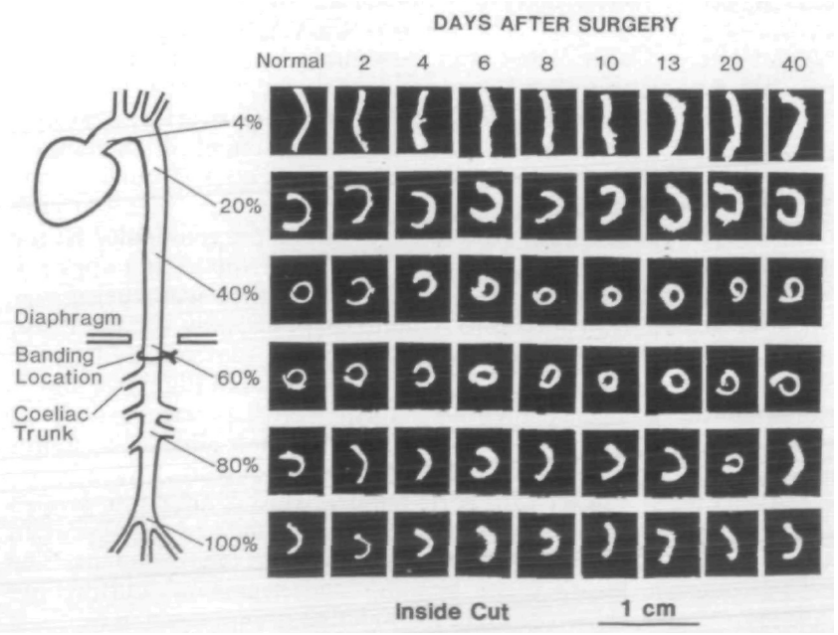

FIGURE 1.1: Photographs of cross sections at different locations of aorta trees after radial cuts: the open angle is observed after a radial cut, which helps to estimate the residual strain in the aorta wall [23].

is not supported by all experiments. For example, Omens et al. [59] showed that residual stress in a mouse primary heart can be further released by a circumferential cut following the initial radial cut, as illustrated in fig. 1.2. This implies that the single-cut opening angle configuration does not correspond to the stress free configuration.

Inspired by the experiments [59], in this thesis, we develop multi-cut models in order to estimate the residual stress distribution across the wall of an intact mature heart based on a simplified heart model.

1.2 Coupled Agent-based and Elastic Modelling of Remodelling of Left Ventricle Post-myocardial Infarction

Changes of micro-collagen structure and material properties are important determinants for the bio-environment during heart healing after a myocardial infarction (MI). This is because remodelling (or healing) will adjust the material properties and mechanical behaviour of organs, which process in the heart poses a complex multiscale soft tissue problem.

At the cellular level, micro-collagen structure remodelling is regulated by fibroblast cell alignment. Environmental cues, such as mechanical and chemical cues, have been shown to influence cell migration. Fibroblasts regulate the collagen fibre deposition and rotation process (fig. 1.3). Therefore, fibroblast migration, induced by environmental information, will modify the micro

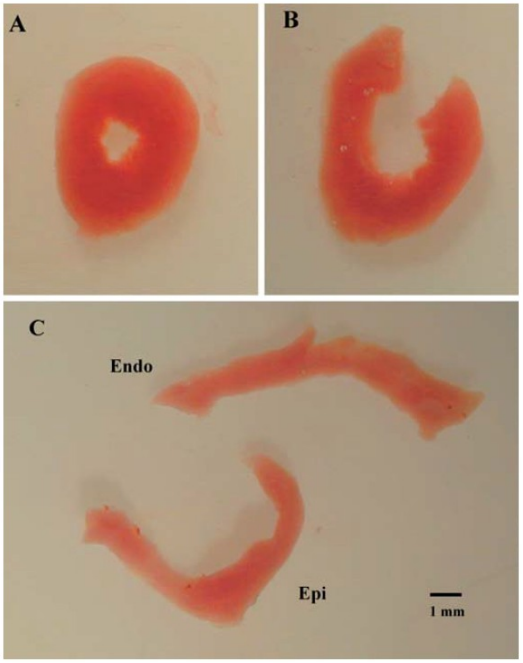

FIGURE 1.2: A typical short-axis apical segment of a mouse heart before and after cuts. [59] The initial intact segment, shown in A, was about 2 mm thick. The same segment after a single radial cut and a further circumferential cut are shown in B and C, respectively. In particular, the endocardial segment has reversed its curvature, in C. Notice that the definition of opening angle in [59] follows that in Fung, [7] which is different from that used in the present thesis.

(collagen) fibre structures locally [12]. Hence, agent-based models that account for these effects have been developed and used to study a 2D slab model of the myocardium infarction [66].

To embed the micro fibre structure within a tissue constitutive law, a commonly used up-scaling method is based on volumetric averaging [83] to get the constitutive parameters for soft tissues of the LV from an agent-based model.

In this thesis, we combine an agent-based approach and a structure-based fibre-reinforced constitutive law to study MI in the left ventricle for the first time. We modify the original Holzapfel–Ogden (HO) constitutive model [35] by employing a distributed fibre model [38]. The specific fibre distribution is determined using an agent-based model similar to that of [9, 18].

We embed the combined model within a mechanical finite element (FE) framework for a 3D cylindrical tube and real LV model. These new models are used to predict the evolution of the (regional) mechanical response of infarcted heart and simulate the myocardium remodelling in terms of the fibre structure and density.

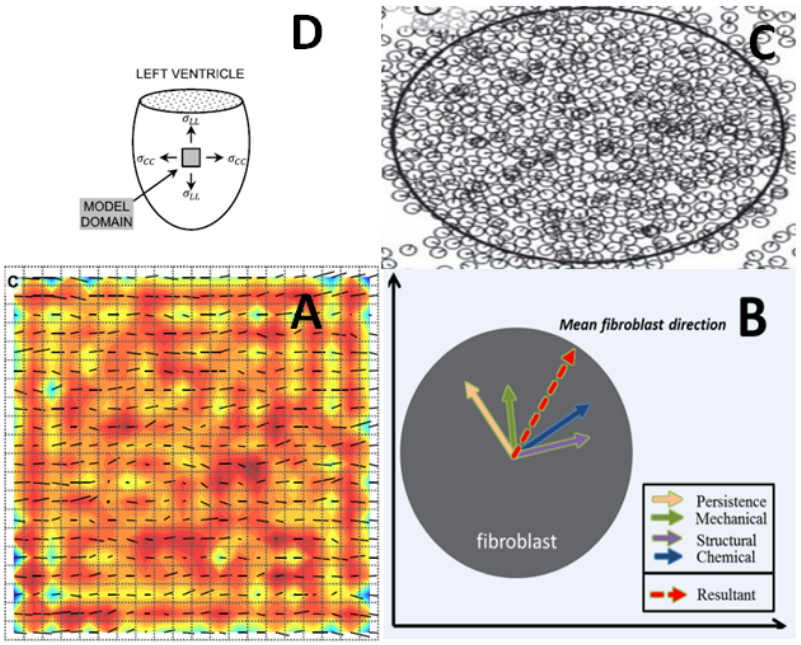

FIGURE 1.3: Coupled agent-based model and finite-element model for a 2D slab: A) FE elements of a 2D slab; B) fibroblast migration determined by external cues; C) fibroblasts infiltrated the LV infarction by migrating; D a two-dimensional slab representing a tissue cut from infarcted LV wall [59].

1.3 Volumetric Growth from a Residually-stressed (Current) Configuration

Referring to G&R theories, volumetric growth is a key ingredient in organ development. Recently, if the idea of growth is applied to study the evolution of organ formation, it is usually assumed that the growth occurs in the natural (reference) configuration. For instance, in studies by Ellen Kuhl and her colleagues [25, 68], it is assumed myocardium growth occurs in a fixed reference configuration. Avoiding (1) re-meshing of the grown heart for FE computation, and (2) updating of the stress-free configuration to compute the mechanical response, it is computationally convenient for studying the stress or growth evolution in the heart by assuming growth from a fixed (stress-free) configuration. And a similar approach was also employed by Kerckhoffs [46, 47].

In some studies, it is stated that they investigated the growth from the updated reference configuration. For instance, in Kroon [50], inhomogeneous volumetric growth was studied using 3D simulation of heart growth. However, in this study, it assumed that **the growth could release all the residual stress, and the further growth will start from the updated but stress-free configuration**. Accordingly, the current stress state could be obtained by applying external loading in the updated stress free configuration. However, in reality, the empirical evidence suggests the existence of residual stress in living organs.

Besides, in the study by Ben Amar [3, 26], growth is assumed to occur in the current configuration along the local principal directions. This assumption leads to a simplified growth deformation tensor as $\mathbf{G}^i = \mathrm{diag}(g_1, g_2, g_3)$. Due to the geometric symmetry, the elastic deformation tensor is also diagonal, since the living body was assumed as a sphere in this research. Thus, the ith elastic deformation (gradient) tensor $\mathbf{F}_e^i = \mathrm{diag}(\lambda_1, \lambda_2, \lambda_3)$.
For the consequent G&R process, the overall deformation could be stated as

$$\mathbf{A}^k = \mathbf{G}^k \cdot \mathbf{F}_e^k \cdot \mathbf{G}^{k-1} \cdot \mathbf{F}_e^{k-1} \cdots \mathbf{G}^1 \cdot \mathbf{F}_e^1,$$

$$\mathbf{A}^k = \mathbf{F}_g^k \cdot \mathbf{F}_e^k \cdot \mathbf{F}_g^{k-1} \cdot \mathbf{F}_e^{k-1} \cdots \mathbf{F}_g^1 \cdot \mathbf{F}_e^1,$$

which, due to the symmetry of the growth and deformation tensors, could be rearranged as

$$\mathbf{A}^k = \underbrace{\mathbf{G}^k \cdot \mathbf{G}^{k-1} \cdots \mathbf{G}^1}_{\text{overall growth}} \mathbf{F}_e^k \cdot \mathbf{F}_e^{k-1} \cdots \mathbf{F}_e^1.$$

Here, the contributions of a simplified growth law and the elastic deformation give an equivalent growth in the fixed reference configuration. The overall growth tensor could directly update the stress configurations. This approach is computationally convenient and avoids considering the residual stress due to incompatible G&R processes in living organs, which makes it possible to compute the stress from a stress-free configuration. However, living organs are actually exposed to complex boundary conditions all the time, while the (volumetric) growth should occur from the residually-stressed current configuration. This thesis tries to draw a sketch of how to calculate the mechanical behaviour of soft tissue after introducing inhomogeneous growth in the residually-stressed current configuration.

1.4 Research Aims

Major research aims include to 1) develop a multiple-cut models to estimate the residual stress in the LV; 2) develop a multiple-scale model to investigate the evolution of tissue structure and mechanical behaviour of the heart during G&R processes of the LV after MI:

The details of aim (1) are presented as

Referring to previous researches, the residual stress is mostly estimated by a single-cut model based on the 'opening-angle' approach. However, as a result of complex G&R processes in living organs, distributions of residual stresses are more complicated. Inspired by the experiments [59], multiple models are developed to estimate the residual stress distribution across the wall of an intact mature heart based on a simplified heart model.

The details of aim (2) are presented as

a) The fibre structure and material properties will be significantly changed in the heart after MI. At the cell level, those changes are regulated by fibroblast migration, which can be simulated by an agent-based model. At the tissue level, the modified material response will change the bio-mechanical environment of the LV and feed back to the G&R processes. In this paper, a simple cylindrical model is used to study the evolution of the mechanical behaviour of the LV, with certain biomechanical consequences for the infarcted LV.

Besides, for more reality, a 3D left ventricle model is developed within a finite element (FE) framework to study the G&R process for an infarcted heart within a FE LV model coupled with an agent-based fibroblast cell model.

b) Volumetric growth of the LV is another important factor affecting the heart formation process and function. In previous research, the growth is assumed to occur in the fixed (and residual-stressed) configuration. However, sustained growth actually occurs in the evolving current configuration. A volumetric growth approach is needed to calculate the mechanical behaviour of soft tissue after introducing inhomogeneous growth in the residually-stressed (current) configuration.

1.5 Outline of Thesis

The basic theory of nonlinear elasticity is summarized in Chapter 2. Chapter 3 provides a review of existing contributions to research with particular focus on 1) residual stress in soft tissues and

the opening angle method, and 2) the interactions between the G&R process and the biomechanical response of living organs. Multiple-cut models are developed in Chapter 4, and are used to estimate residual stress distribution in the LV with respect to cut-induced configurations. To investigate the evolution of the biomechanical environment and material properties of the heart (tissues) after MI, an agent-based model, describing the fibroblast migration, is coupled with an elastic LV model as a cylindrical tube and FE LV model (Chapter 5). The mechanism of MI development is explained by these models in Chapter 6. A new approach is developed to investigate inhomogeneous volumetric growth in the stressed (current) configuration in Chapter 7. Finally, limitations, conclusions and future works are discussed in Chapter 8. intro

Chapter 2

Basic Nonlinear Elastic Deformation Theory

In this project, the fundamental mathematical theory is 'nonlinear elasticity', which is suitable for analyzing the material properties and mechanical behaviour of soft tissues. The basic concepts about deformation and motions will be introduced in this section. Most of the attention will be be paid to quasi-static problems, while the dynamic and time-dependent problems will be only slightly touched on here.

The basic kinematics of deformation and motion will be described first. The concepts of stress will be defined, as well as the stress equilibrium state (balance equations). The stress-deformation relation will be given by the material constitutive laws. In this thesis, the strain energy function (SEF), as a special form of constitutive law, is defined to describe the elastic behaviour of soft materials. In general, the SEF can be defined in any arbitrary configuration, while the most popular way is to use the SEF referring to the natural (and stress-free) configuration. The general form of SEF is used in this thesis. Besides, the SEF is also defined to describe soft tissues with more than one constituent here.

2.1 Deformation and Strain

2.1.1 Observers and Frame of Reference

To mathematically describe phenomena in the real world, a framework (or set of coordinates) is defined by the notion of an observer o. From the view of observer o, a certain event could be recorded as $(\mathbf{x},t)$, where $\mathbf{x}$ is position vector and t is time. If the same event is recorded by another observer o^*, it will be named as event $\mathbf{x}^*$ in new framework. And the connection

between $\mathbf{x}^*$ and $\mathbf{x}$ is

$$\mathbf{x}^* = \mathbf{c}(t) + \mathbf{Q}(t)\mathbf{x}, \tag{2.1}$$

where $\mathbf{c}(t)$ is the distance vector, describing the observed position between two observers ($\mathbf{c}(t) = \mathbf{x}^* - \mathbf{Q}(t)\mathbf{x}$); $\mathbf{Q}$ is a tensor, transforming the vector observed by o into vector observed by o^*. If two observers are under rectangular Cartesian coordinates, $\mathbf{Q}$ is an orthogonal tensor.

Transformation of basis: Normally, different observers will select different base to mathematically record the event. Now, we consider the basis for observer o to be $\{\mathbf{e}_i\}$ and $\{\mathbf{e}'_i\}$ (i=1,2,3) for the second observer (o^*). Then, the transformation tensor $\mathbf{Q}$ could help to express the new basis $\mathbf{e}'_i$ respect to $\mathbf{e}_i$ as

$$\mathbf{e}'_j = \mathbf{Q}\mathbf{e}_j, \tag{2.2}$$

i.e. if $\{\mathbf{e}_i\}$, $\left\{\mathbf{e}'_j\right\}$ are basis for Cartesian coordinates, $Q_{ij} = \mathbf{e}'_j \cdot \mathbf{e}_i$ ($j = 1,2,3$).

Moreover, eq. (2.2) gives

$$\cos\theta'_{ij} = \mathbf{e}'_i \cdot \mathbf{e}'_j = \mathbf{Q}\mathbf{e}_i \cdot \mathbf{Q}\mathbf{e}_j, \tag{2.3}$$

where θ'_{ij} is the angle between $\mathbf{e}'_i$ and $\mathbf{e}'_j$.

The change of the base could be expressed as

$$\mathbf{e}'_i \otimes \mathbf{e}'_j = \mathbf{Q}\ \mathbf{e}_i \otimes \mathbf{e}_j\ \mathbf{Q}^T. \tag{2.4}$$

Assumingly here, we try to transform basis $\mathbf{e}'_i$ back to basis $\mathbf{e}_i$, the expression could be similarly obtained as

$$\mathbf{e}_i = \mathbf{Q}^T \mathbf{e}'_i. \tag{2.5}$$

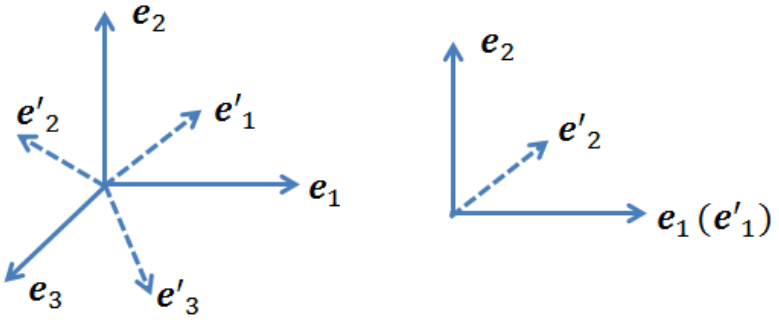

FIGURE 2.1: Change of basis (2D case): left, orthonormal basis $\mathbf{e}_i$ to orthonormal basis $\mathbf{e}'_j$; right, orthonormal basis $\mathbf{e}_i$ to oblique basis $\mathbf{e}'_j$.

The simplest (and most popular) case is to transform an orthonormal basis $\{\mathbf{e}_i\}$ to a second orthonormal basis $\{\mathbf{e}'_j\}$, which gives the relations as

$$\delta_{ij} = \mathbf{e}'_i \cdot \mathbf{e}'_j = \mathbf{e}_i \cdot \mathbf{e}_j \quad \text{or} \quad \mathbf{I} = \mathbf{e}'_i \otimes \mathbf{e}'_i = \mathbf{e}_i \otimes \mathbf{e}_i. \tag{2.6}$$

where $\mathbf{I}$ is the unit tensor.

Application of eqs. (2.3), (2.4) and (2.6), it gives tensor $\mathbf{Q}$ as an orthogonal matrix, where

$$\mathbf{I} = \mathbf{Q}\mathbf{Q}^T \quad \text{and} \quad \det(\mathbf{Q}) = \pm 1. \tag{2.7}$$

It is worth to emphasize that eq. (2.7) of tensor $\mathbf{Q}$ is only valid for the transformation between two orthonormal bases. In general cases, $\mathbf{Q}$ is not necessarily orthonormal.

2.1.2 Configuration and Deformation Gradient

To consider the relative deformation (and motion) of a 'body' with continuously distributed material, the configurations should be pre-defined. A configuration is a one-to-one mapping to describe the places occupied by all material points of body $\mathscr{B}$. If suppressing the dependence of deformation on time t, the position of material point $\mathbf{X}$ could be expressed as

$$\mathbf{x} = \mathscr{X}(\mathbf{X}), \tag{2.8}$$

where $\mathscr{X}$ is the one-to-one mapping of position in current configuration for material point X.

Considering the deformation from configuration $\mathscr{B}_0$ to $\mathscr{B}_1$, the differential on mapping $\mathscr{X}$ gives

$$\mathrm{d}\mathbf{x} = \mathbf{F}\mathrm{d}\mathbf{X} \quad \text{and} \quad \mathbf{F} = \mathrm{Grad}\mathscr{X}(\mathbf{X}) = \nabla \otimes \mathscr{X}(\mathbf{X}), \tag{2.9}$$

where 'Grad' is the gradient operation with respect to $\mathbf{X}$, and $\mathbf{F}$ is the deformation gradient.

Differential in curvilinear coordinate: In most previous researches, the differential operations are analyzed in Cartesian coordinate, which is computationally convenient for the derivations. However, in general, the differential operation should be analyzed in curvilinear coordinate, while Cartesian coordinates are special cases of curvilinear coordinates with the fixed orthonormal basis.

In the reference configuration, the *natural basis vectors* are defined as $\mathbf{G}_I = \frac{\partial \mathbf{X}}{\partial X^I}$, while the reciprocal basis is defined as $\{\mathbf{G}^I(\mathbf{X})\}$ such that

$$\delta^I_J = \mathbf{G}^I(\mathbf{X}) \cdot \mathbf{G}_J(\mathbf{X}).$$

The gradient operator using reference coordinates is

$$\mathrm{Grad} = \mathbf{G}^J(\partial/\partial X^J).$$

In current configuration, the *natural basis* are defined as $\mathbf{g}_i = \frac{\partial \mathbf{x}}{\partial x^i}$, while the reciprocal basis is defined as $\{\mathbf{g}^i(\mathbf{x})\}$ such that

$$\delta^i_j = \mathbf{g}^i(\mathbf{x}) \cdot \mathbf{g}_j(\mathbf{x}).$$

The position vector in current configuration for material point $\mathbf{X}$ is expressed as

$$\mathbf{x} = x_i \mathbf{g}^i(\mathbf{x}) \quad \text{or} \quad \mathbf{x} = x_I \mathbf{G}^I, \tag{2.10}$$

where the component x_I is expressed as

$$x_I = x_i Q^i_I,$$

and Q^i_I are the components of the tensor $\mathbf{Q}$ ($Q^i_I = \mathbf{g}^i \cdot \mathbf{G}_I$).
Recalling the gradient operator in the current coordinates and eq. (2.9), the deformation tensor is obtained as

$$\mathbf{F} = \text{Grad}\,(x_I \mathbf{G}^I) = \nabla \otimes (x_I \mathbf{G}^I) = \frac{\partial x_I}{\partial X^J} \mathbf{G}^I \otimes \mathbf{G}^j + x_I \frac{\partial \mathbf{G}^I}{\partial X^J} \otimes \mathbf{G}^J, \tag{2.11}$$

Introducing the Christoffel symbols as

$$\frac{\partial \mathbf{G}^I}{\partial X^J} = -\mathbf{\Gamma}^I_{JK} \mathbf{G}_K \text{ and } \mathbf{\Gamma}^K_{IJ} = \frac{\partial \mathbf{G}_I}{\partial X^J} \cdot \mathbf{G}^K = -\mathbf{G}_I \cdot \frac{\partial \mathbf{G}^K}{\partial X^J} \tag{2.12}$$

Inserting eq. (2.12) into (2.13), it yields

$$\mathbf{F} = \frac{\partial x_I}{\partial X^J} \mathbf{G}^I \otimes \mathbf{G}^J - (x_I \mathbf{\Gamma}^I_{JK} \mathbf{G}^K \otimes \mathbf{G}^J). \tag{2.13}$$

Eq. (2.13) is the general expression for deformation tensor from eq. (2.9). Considering the deformation tensor is described within fixed Cartesian coordinates for current and reference configurations, it gives the component of Christoffel symbols yields

$$\Gamma^k_{ij} = 0 \quad \text{and} \quad \mathbf{Q} = \mathbf{I}. \tag{2.14}$$

Then,

$$\mathbf{F} = \frac{\partial x^i}{\partial X^j} \mathbf{e}^i \otimes \mathbf{E}_j. \tag{2.15}$$

where $\mathbf{e}^i$ and $\mathbf{E}_j$ are the orthonormal basis vectors for the current and reference configurations, respectively.

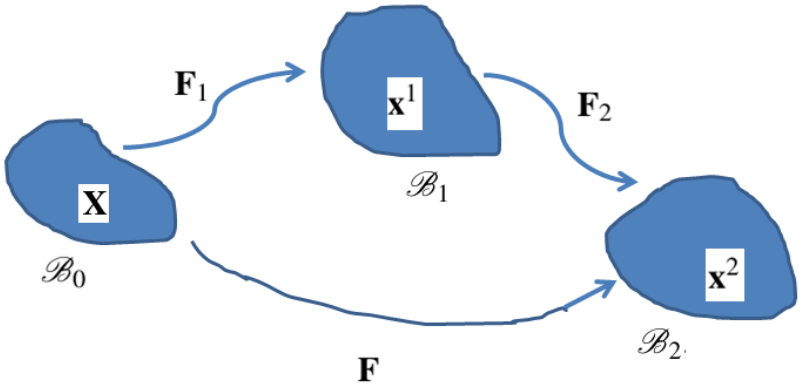

FIGURE 2.2: The cumulative deformation and intermediate deformations.

2.1.3 Cumulative Deformation and Polar Decomposition of Deformation Tensor

2.1.3.1 Cumulative Deformation

The general deformation path can be described as: the body deforms from a reference configuration $\mathscr{B}_0$ to the generic configuration $\mathscr{B}_2$, via the intermediate configurations $\mathscr{B}_1$. The relations will be shown between the cumulative deformation and intermediate deformations. Applying eq. (2.13) in the Cartesian coordinates (fig. 2.2), The intermediate deformation gradients are

$$\begin{cases} \mathbf{F}_1 = \dfrac{\partial \mathbf{x}^1}{\partial \mathbf{X}} = \dfrac{\partial x_i^1}{\partial X_j} \mathbf{e}_i^1 \otimes \mathbf{E}_j \ (\mathscr{B}_0 \to \mathscr{B}_1) \\ \mathbf{F}_2 = \dfrac{\partial \mathbf{x}^2}{\partial \mathbf{x}^1} = \dfrac{\partial x_i^2}{\partial x_j^1} \mathbf{e}_i^2 \otimes \mathbf{e}_j^1 \ (\mathscr{B}_1 \to \mathscr{B}_2), \end{cases} \tag{2.16}$$

where $\mathbf{X}, \mathbf{x}^1$ and $\mathbf{x}^2$ are the positions in $\mathscr{B}_0, \mathscr{B}_1$ and $\mathscr{B}_2$; $\{\mathbf{E}_j\}$, $\{\mathbf{e}_i^1\}$ and $\{\mathbf{e}_i^2\}$ are the bases for $\mathscr{B}_0, \mathscr{B}_1$ and $\mathscr{B}_2$.

The cumulative deformation gradient is directly expressed as

$$\mathbf{F} = \frac{\partial \mathbf{x}^2}{\partial \mathbf{X}} = \frac{\partial x_i^2}{\partial X_j} \mathbf{e}_i^2 \otimes \mathbf{E}_j. \tag{2.17}$$

Applying the chain rule to rewrite eq. (2.17), it yields

$$F_{ij} = \frac{\partial x_i^2}{\partial X_j} = \frac{\partial x_i^2}{\partial x_k^1} \frac{\partial x_k^1}{\partial X_j} = F_{2,ik} F_{1,kj} \ \Rightarrow \mathbf{F} = \mathbf{F}_2 \mathbf{F}_1. \tag{2.18}$$

This relation could be extended to calculate the cumulative deformation gradients with any number of intermediate stages. The cumulative deformation gradient could be obtained as the product of intermediate deformation gradients with sequential order (fig. 2.3):

$$\mathbf{F} = \mathbf{F}_n \cdots \mathbf{F}_j \cdots \mathbf{F}_1, \tag{2.19}$$

where $\mathbf{F}_j$ is intermediate deformation gradient at the jth step.

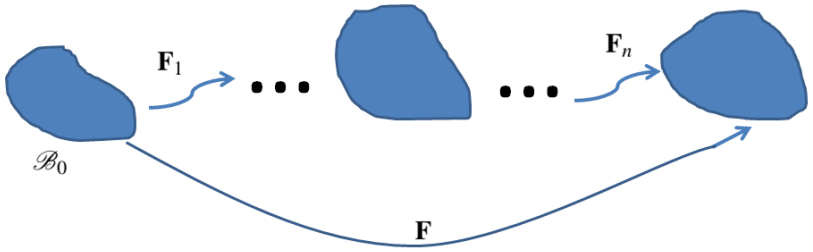

FIGURE 2.3: The cumulative deformation with a series of intermediate deformations.

2.1.3.2 Polar Decomposition of Deformation Tensor

In general, we assume condition $\mathbf{F}d\mathbf{X} \neq \mathbf{0}$ is always satisfied, which indicates the length of non-zero material line ($d\mathbf{X} \neq \mathbf{0}$) will not be reduced to zero by the deformation. It indicates the non-singularity of $\mathbf{F}$ as

$$\det \mathbf{F} > \mathbf{0}. \tag{2.20}$$

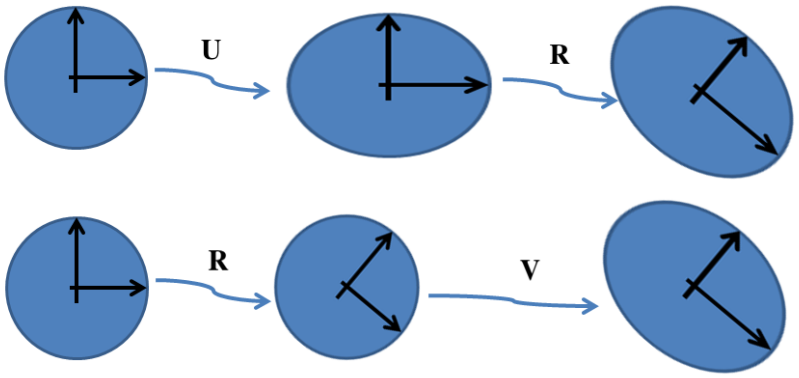

FIGURE 2.4: The polar decompositions of the deformation gradient: up, the left polar decomposition; down, the right polar decomposition.

For the non-singular $\mathbf{F}$, the polar decomposition theorem indicates the existence of unique positive definite symmetric tensors $\mathbf{U}$ and $\mathbf{V}$, and the orthogonal tensor $\mathbf{R}$ giving

$$\mathbf{F} = \mathbf{RU} = \mathbf{VR}. \tag{2.21}$$

The deformation path $\mathbf{F} = \mathbf{VR}$ could be understood as the body is rotated first with $\mathbf{R}$ and then stretched along principal directions of $\mathbf{V}$ (fig. 2.4 (down)). The deformation path $\mathbf{F} = \mathbf{RU}$ could be understood as the body is stretched along principal directions of $\mathbf{U}$ and then rotated with $\mathbf{R}$ (fig. 2.4 (up)). And the relation between the pure stretches $\mathbf{U}$ and $\mathbf{V}$ could be obtained from eq. (2.21) as

$$\mathbf{V} = \mathbf{RUR}^T. \tag{2.22}$$

2.1.4 Deformation of Volume and Surface

We introduce three incremental lines $\mathbf{dX}^1$, $\mathbf{dX}^2$ and $\mathbf{dX}^3$ in the reference configuration $\mathscr{B}_0$. The volume of the infinitesimal parallelepiped with these lines could be expressed as

$$\mathrm{d}V = \mathrm{d}\mathbf{X}^1 \cdot (\mathrm{d}\mathbf{X}^2 \wedge \mathrm{d}\mathbf{X}^3) = \det(\mathrm{d}\mathbf{X}^1, \mathrm{d}\mathbf{X}^2, \mathrm{d}\mathbf{X}^3). \tag{2.23}$$

After deforming, the incremental lines are labeled as $\mathrm{d}\mathbf{x}_i (= \mathbf{F}\mathrm{d}\mathbf{X}_i, i = 1,2,3)$. The volume of the parallelepiped element in deformed configuration could be expressed as

$$\mathrm{d}v = \mathrm{d}\mathbf{x}^1 \cdot (\mathrm{d}\mathbf{x}^2 \wedge \mathrm{d}\mathbf{x}^3) = \det(\mathrm{d}\mathbf{x}^1, \mathrm{d}\mathbf{x}^2, \mathrm{d}\mathbf{x}^3) = \det(\mathbf{F})\mathrm{d}V \quad \Rightarrow J\mathrm{d}V = \mathrm{d}v. \tag{2.24}$$

The local volume ratio is defined as $J = \det(\mathbf{F})$. Now we introduce the infinitesimal vector elements ($\mathrm{d}\mathbf{S} = \mathbf{N}\mathrm{d}S$, $\mathrm{d}\mathbf{s} = \mathbf{n}\mathrm{d}s$) to describe the surface neighborhood around $\mathbf{X}$ in $\mathscr{B}_0$ and $\mathscr{B}_1$, while $\mathbf{N}$ and $\mathbf{n}$ are the unit normal vectors to the surface. The surface vector elements could be connected with applications of eq. (2.23) and (2.24) as

$$\begin{cases} \mathrm{d}V = \mathrm{d}\mathbf{X} \cdot \mathrm{d}\mathbf{S} \\ \mathrm{d}v = \mathrm{d}\mathbf{x} \cdot \mathrm{d}\mathbf{s} \end{cases} \Rightarrow \quad J\mathrm{d}\mathbf{X} \cdot \mathrm{d}\mathbf{S} = \mathrm{d}\mathbf{x} \cdot \mathrm{d}\mathbf{s}. \tag{2.25}$$

Recalling eq. (2.9), eq. (2.25) is rewritten as

$$\mathrm{d}\mathbf{s} = J\mathbf{F}^{-T}\mathrm{d}\mathbf{S}. \tag{2.26}$$

2.1.5 Strains and Stretch

For the information, some definitions of strain tensors are given here. The Green (or Lagrange) strain is defined as

$$\mathbf{E} = \frac{1}{2}(\mathbf{F}^T\mathbf{F} - \mathbf{I}), \tag{2.27}$$

which is to describe the strain of body deformed from reference to deformed configurations.

The Eulerian strain is defined as

$$\mathbf{e} = \frac{1}{2}\left[\mathbf{I} - (\mathbf{F}\mathbf{F}^T)^{-1}\right], \tag{2.28}$$

which is to measure the strain from deformed to reference configurations.

Considering an arbitrary line element vector $\mathbf{M}$ in the reference configuration, it will deform into element vector $\mathbf{m}$ in deformed configuration. The stretch of line element is written as

$$\lambda(\mathbf{M}) = \frac{|\mathbf{m}|}{|\mathbf{M}|} = \frac{(\mathbf{m}\cdot\mathbf{m})^{1/2}}{(\mathbf{M}\cdot\mathbf{M})^{1/2}} = (\frac{\mathbf{M}\cdot(\mathbf{F}^T\mathbf{F})\mathbf{M}}{\mathbf{M}\cdot\mathbf{M}})^{1/2}. \tag{2.29}$$

2.2 Stress and Balance Laws

2.2.1 Conservation of Mass

In this thesis, masses of bodies are constant for observers with different velocities. Moreover, if we don't consider growth of the body, no new material will be added into $\mathscr{B}$. Thus, the mass function should be independent from t as

$$\frac{\mathrm{d}m(\mathscr{B})}{\mathrm{d}t} = 0,$$

which is called as the '*mass conservation*'.

In arbitrary configuration $\mathscr{B}_t$, the mass density function $\rho(\mathbf{x},t)$ could be defined as

$$m(\mathscr{B}_t) = \int_{\mathscr{B}_t} \rho(\mathbf{x},t)dv.$$

Recalling the statement of *mass conservation*, the connection between density functions for different configurations is expressed as

$$\int_{\mathscr{B}_t} \rho(\mathbf{x},t)dv = \int_{\mathscr{B}_0} \rho_0(\mathbf{X})dV, \tag{2.30}$$

where ρ_0 is the density function, $\mathrm{d}V$ is the local volume element, both independent of time t and in reference configuration. If $\mathrm{d}V$ depends on t ($\frac{\partial}{\partial t}\mathrm{d}V \neq 0$), it indicates '*mass conservation*' is not satisfied and body is growing. This case will be discussed in the section of 'Volumetric growth'.

Considering $\mathscr{B}_t$ is an arbitrary configuration, it suggests the connection of density (eq. (2.24)) is also valid for any sub-domain of $\mathscr{B}_t$. Then, the relation between densities can be written as

$$\rho = J\rho_0. \tag{2.31}$$

2.2.2 Momentum Balance Equation

The momentum of body $\mathscr{B}$ (in current configuration) is defined as

$$\int_{\mathscr{B}_t} \rho(\mathbf{x},t)\mathbf{v}(\mathbf{x},t)\mathrm{d}v, \tag{2.32}$$

where $\mathbf{v}(\mathbf{x},t)$ is the velocity ($\mathbf{v}(\mathbf{x},t)$ is expressed as $\dot{\mathscr{X}}(\mathbf{X},t)$, when $\mathbf{x}=\mathscr{X}(\mathbf{X},t)$) and $(\dot{\bullet})$ means the time derivative.

If rewriting this into a Lagrangean form, it gives

$$\int_{\mathscr{B}_t} \rho(\mathbf{x},t)\mathbf{v}(\mathbf{x},t)dv = \int_{\mathscr{B}_0} \rho_0(\mathbf{X})\mathbf{v}(\mathscr{X}(\mathbf{X}),t)\mathrm{d}V. \tag{2.33}$$

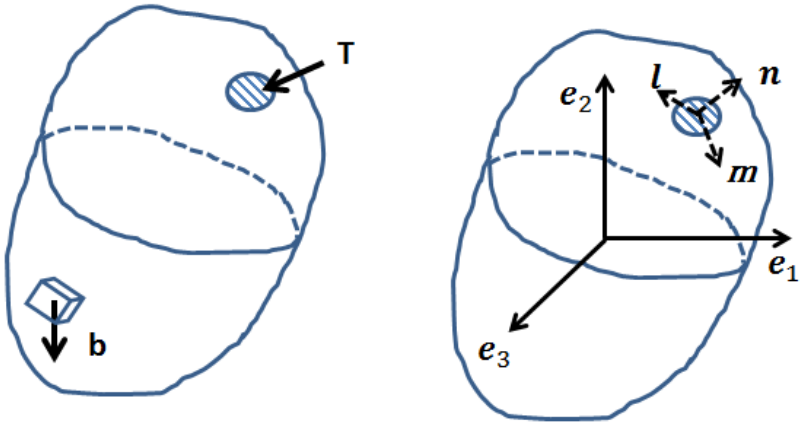

FIGURE 2.5: Schematic of body force and contact force: left, the body force density **B** and contact force density **t**; right, the global coordinates and local coordinates for local surface.

The body force (such as gravity) is expressed as

$$\int_{\mathscr{B}_t} \rho(\mathbf{x},t)\mathbf{b}(\mathbf{x},t)\mathrm{d}v, \tag{2.34}$$

where $\mathbf{b}$ is the body force density defined on the body in $\mathscr{B}_t$.

Similarly, the contact force is

$$\int_{\partial\mathscr{B}_t} \mathbf{t}(\mathbf{x},t)\mathrm{d}a, \tag{2.35}$$

where $\mathbf{t}$ is the contact force density at local surface.

Then, the balance of linear momentum is expressed in Eulerian form as (fig. 2.5)

$$\int_{\mathscr{B}_t} \rho(\mathbf{x},t)\mathbf{b}(\mathbf{x},t)\mathrm{d}v + \int_{\partial\mathscr{B}_t} \mathbf{t}(\mathbf{x},t)\mathrm{d}a = \frac{\mathrm{d}}{\mathrm{d}t}\left(\int_{\mathscr{B}_t} \rho(\mathbf{x},t)\mathbf{v}(\mathbf{x},t)\mathrm{d}v\right). \tag{2.36}$$

The application of eq. (2.33) gives

$$\begin{aligned}\frac{\mathrm{d}}{\mathrm{d}t}\left(\int_{\mathscr{B}_t}\rho(\mathbf{x},t)\mathbf{v}(\mathbf{x},t)\mathrm{d}v\right) &= \frac{\mathrm{d}}{\mathrm{d}t}\left(\int_{\mathscr{B}_0}\rho_0(\mathbf{X})\mathbf{v}(\mathscr{X}(\mathbf{X},t))\mathrm{d}V\right.\\ &= \int_{\mathscr{B}_0}\rho_0(\mathbf{X})\frac{\mathrm{d}}{\mathrm{d}t}\mathbf{v}(\mathscr{X}(\mathbf{X},t))\mathrm{d}V\\ &= \int_{\mathscr{B}_t}\rho(\mathbf{x},t)\frac{\mathrm{d}}{\mathrm{d}t}\mathbf{v}\mathrm{d}v.\end{aligned} \tag{2.37}$$

With help of eq. (2.37), eq. (2.36) is rewritten as

$$\int_t\rho(\mathbf{x},t)\mathbf{b}(\mathbf{x},t)\mathrm{d}v+\int_{\mathscr{B}_t}\mathbf{t}(\mathbf{x},t)\mathrm{d}a=\frac{\mathrm{d}}{\mathrm{d}t}\left(\int_{\mathscr{B}_t}\rho(\mathbf{x},t)\mathbf{v}(\mathbf{x},t)\mathrm{d}v\right)=\int_{\mathscr{B}_t}\rho(\mathbf{x},t)\frac{\mathrm{d}}{\mathrm{d}t}\mathbf{v}\mathrm{d}v. \tag{2.38}$$

2.2.3 Stress Tensors and Motions

2.2.3.1 Cauchy Stress Tensor

Cauchy's theorem states that: the stress vector $\mathbf{t}(\mathbf{x})$ linearly dependent on the direction vector $\mathbf{n}$ and there therefore exists a second-order tensor field such that

$$\mathbf{t}(\mathbf{x})=\boldsymbol{\sigma}(\mathbf{x})\mathbf{n}, \tag{2.39}$$

where $\boldsymbol{\sigma}(\mathbf{x})$ is the Cauchy stress tensor.

Applying the balance of angular momentum, it indicates that the tensor of Cauchy stress is symmetric, i.e.

$$\boldsymbol{\sigma}=\boldsymbol{\sigma}^T. \tag{2.40}$$

(*the proof can be found in [57].)

Applying eq. (2.39), the linear balance equation could be rewritten as

$$\int_{\mathscr{B}_t}\rho(\mathbf{x},t)\mathbf{b}(\mathbf{x},t)\mathrm{d}v+\int_{\partial\mathscr{B}_t}\boldsymbol{\sigma}\mathbf{n}(\mathbf{x},t)\mathrm{d}a=\int_{\mathscr{B}_t}\rho(\mathbf{x},t)\frac{\mathrm{d}}{\mathrm{d}t}\mathbf{v}\mathrm{d}v. \tag{2.41}$$

This is then rewritten by applying the divergence theorem as

$$\int_{\mathscr{B}_t}\{\rho(\mathbf{x},t)\mathbf{b}(\mathbf{x},t)+\mathrm{div}\boldsymbol{\sigma}^T-\rho(\mathbf{x},t)\frac{\mathrm{d}}{\mathrm{d}t}\mathbf{v}\}\mathrm{d}v=\mathbf{0}. \tag{2.42}$$

This equation is valid for arbitrary region $\mathscr{B}_1$, which indicates

$$\rho\mathbf{b}+\mathrm{div}\boldsymbol{\sigma}^T-\rho\frac{\mathrm{d}}{\mathrm{d}t}\mathbf{v}=\mathbf{0}. \tag{2.43}$$

2.2.3.2 Nominal Stress and Lagrangean Balance Equation

Recalling the relation between surface elements in different configurations (eq. (2.25)), the resultant contact force of body **b** is written as

$$\int_{\partial\mathscr{B}_t} \boldsymbol{\sigma}\mathbf{n}\mathrm{d}a = \int_{\partial\mathscr{B}_0} J\boldsymbol{\sigma}\mathbf{F}^{-T}\mathbf{N}\mathrm{d}A,$$

where **N** is the normal vector of surface element in $\partial\mathscr{B}_0$.
Accordingly, the nominal stress (tensor) is defined as

$$\mathbf{S} = J\mathbf{F}^{-1}\boldsymbol{\sigma}. \tag{2.44}$$

With the helps of eqs. (2.31), (2.37) and (2.44), the linear balance equation (2.45) is pushed back into $\mathscr{B}_0$ as

$$\int_{\mathscr{B}_0} \rho_0(\mathbf{X})\mathbf{b}_0(\mathbf{X},t)\mathrm{d}V + \int_{\partial\mathscr{B}_0} \mathbf{S}^T\mathbf{N}\mathrm{d}A = \int_{\mathscr{B}_0} \rho_0\frac{\mathrm{d}}{\mathrm{d}t}\mathbf{v}\mathrm{d}V, \tag{2.45}$$

where $\mathbf{b}_0$ is the body force density in $\mathscr{B}_0$.
Application of the divergence theorem indicates

$$\rho_0\mathbf{b}_0 + \mathrm{Div}\mathbf{S} - \rho_0\frac{\mathrm{d}}{\mathrm{d}t}\mathbf{v} = \mathbf{0}. \tag{2.46}$$

Besides nominal and Cauchy stresses, another stress tensors are also widely used. For information, the first and second Piola-Kirchhoff stresses are introduced here as

$$\mathbf{K} = \mathbf{S}^T \quad \text{(first P-K stress)}, \tag{2.47}$$

$$\mathbf{P} = \mathbf{F}^{-1}\mathbf{K} \quad \text{(second P-K stress)}. \tag{2.48}$$

2.3 Constitutive Laws and Strain-energy Functions

2.3.1 Constitutive Laws

To analyze the motion of the body based on eqs. (2.43) or (2.46), we require to determine the relation between stresses and motions. The constitutive law is generally used to describe the mechanical behaviours of material, which can address the relation between stresses and motions. In this project, only purely mechanical behavior will be focused, which implicitly indicates that the thermodynamic variables don't contribute to the material properties. In this thesis, only the elastic behaviors will be discussed.

For a *simple material*, the stress could be solely determined by the motion history, which gives the constitutive relation as

$$\boldsymbol{\sigma}(\mathbf{x},t) = \mathbf{G}(\mathscr{X}^t;X,t), \tag{2.49}$$

where $\mathbf{G}$ is the function to describe the constitutive relation relation, $\mathscr{X}^t(X,t)$ is the motion history as

$$\mathscr{X}^t(X,s) = \mathscr{X}(X,t-s) \quad t \geq s \geq 0.$$

Concerning the constitutive law for an elastic material, the stress state could be directly determined by the deformation relative to an arbitrary reference configuration, with the helps of the stress state in the reference configuration. Thus, for a uniform material, the constitutive law is independent of material particle X. Therefore, the constitutive law could be written as

$$\boldsymbol{\sigma}(\mathbf{x},t) = \mathbf{G}(X;\mathbf{F}_e,\boldsymbol{\tau}) \quad \Rightarrow \quad \boldsymbol{\sigma}(\mathbf{x},t) = \mathbf{G}(\mathbf{F}_e,\boldsymbol{\tau}). \tag{2.50}$$

where $\boldsymbol{\tau}$ is the Cauchy stress in the reference configuration, and $\mathbf{F}_e$ is the elastic deformation.

Considering the mechanical behaviours are observed by a new observer o^* (eq. (2.1)), the deformation gradient and Cauchy stress could be rewritten with the helps of eqs. (2.2) and (2.9) as

$$\mathbf{F}_e^* = \mathbf{Q}\mathbf{F}_e, \quad \boldsymbol{\sigma}^* = \mathbf{Q}\boldsymbol{\sigma}\mathbf{Q}^T. \tag{2.51}$$

If the stress-deformation relation is unaffected by the selection of observer, eq. (2.51) gives

$$\boldsymbol{\sigma}^* = \mathbf{G}(\mathbf{F}_e^*,\boldsymbol{\tau}). \tag{2.52}$$

Applying eqs. (2.51) and (2.52), it gives

$$\mathbf{G}(\mathbf{Q}\mathbf{F}_e,\boldsymbol{\tau}) = \mathbf{Q}\mathbf{G}(\mathbf{F}_e,\boldsymbol{\tau})\mathbf{Q}^T. \tag{2.53}$$

2.3.2 Strain-energy Function

The scalar product of eq. (2.43) with velocity $\mathbf{v}$ gives

$$\rho\mathbf{b}\cdot\mathbf{v} + \mathrm{div}\boldsymbol{\sigma}\cdot\mathbf{v} - \rho(\frac{\mathrm{d}}{\mathrm{d}t})\mathbf{v}\cdot\mathbf{v} = 0. \tag{2.54}$$

This could be rearranged with the product rule of differentiation as

$$\rho\mathbf{b}\cdot\mathbf{v} + \mathrm{div}(\boldsymbol{\sigma}\mathbf{v}) - \mathrm{tr}(\boldsymbol{\sigma}\boldsymbol{\Gamma}) - \rho(\frac{\mathrm{d}}{\mathrm{d}t}\mathbf{v})\cdot\mathbf{v} = 0. \tag{2.55}$$

where $\boldsymbol{\Gamma}$ is the velocity gradient as $\boldsymbol{\Gamma} = \mathrm{grad}\mathbf{v}(\mathbf{x},t)$, and 'grad' is gradient operation in the current configuration with respect to $\mathbf{x}$.

With the help of the divergence theorem and conservation of mass (eq. (2.30)), the energy balance equation could be obtained from the integration of last equation as

$$\int_{\mathscr{B}_t} \rho \mathbf{b} \cdot \mathbf{v} dv + \int_{\mathscr{B}_t} \mathbf{t} \cdot \mathbf{v} \mathrm{d}a = \int_{\mathscr{B}_t} \mathrm{tr}(\boldsymbol{\sigma}\boldsymbol{\Gamma}) \mathrm{d}v + \frac{\mathrm{d}}{\mathrm{d}t} \int_{\mathscr{B}_t} \frac{1}{2} \rho \mathbf{v} \cdot \mathbf{v} \mathrm{d}v. \tag{2.56}$$

In the last equation, the left sides are the (body force and contact force) rates of working done by external forces. For the right side of the equation, the term

$$\frac{\mathrm{d}}{\mathrm{d}t} \int_{\mathscr{B}} \frac{1}{2} \rho \mathbf{v} \cdot \mathbf{v} \mathrm{d}v$$

is the rate of kinetic energy. And the term

$$\int_{\mathscr{B}} \mathrm{tr}(\boldsymbol{\sigma}\boldsymbol{\Gamma}) \mathrm{d}v.$$

is the rate of working of the Cauchy stress.
And the energy balance equation (2.56) could also be written in Lagrangian form as

$$\int_{\mathscr{B}} \rho_0 \mathbf{b}_0 \cdot \mathbf{v} \mathrm{d}V + \int_{\mathscr{B}} \mathbf{S}^T \mathbf{N} \cdot \mathbf{v} \mathrm{d}A = \int_{\mathscr{B}} \mathrm{tr}(\mathbf{S} \frac{\mathrm{d}}{\mathrm{d}t} \mathbf{F}_e) \mathrm{d}V + \frac{\mathrm{d}}{\mathrm{d}t} \int_{\mathscr{B}} \frac{1}{2} \rho_0 \mathbf{v} \cdot \mathbf{v} \mathrm{d}V. \tag{2.57}$$

Besides, after scalar product with velocity on both sides of the Lagrangean force balance equation (eq. 2.46) the Lagrangean energy balance equation (2.57) could also be obtained by directly using the Lagrangean divergence theorem. However, the derivation with the Eulerian form holds a more obvious physical meaning.

Actually, the term

$$\mathrm{tr}(\mathbf{S} \frac{\mathrm{d}}{\mathrm{d}t} \mathbf{F}_e) \tag{2.58}$$

is the rate of the change of the elastic energy (volumetric) density. In general, given that a function $\bar{W}$ exists such that

$$\dot{\bar{W}}(\mathbf{F}_e, \boldsymbol{\tau}) = \mathrm{tr}(\mathbf{S}\dot{\mathbf{F}}_e), \quad \text{then } \mathbf{S} = \frac{\partial \bar{W}(\mathbf{F}_e, \boldsymbol{\tau})}{\partial \mathbf{F}_e}, \tag{2.59}$$

where $\boldsymbol{\tau}$ is residual stress in $\mathscr{B}_1$.
Then, $\bar{W}$ is the strain-energy function (per unit volume) with respect the configuration $\mathscr{B}_1$. In general, stress exists in $\mathscr{B}_1$ and it will affect the mechanical behaviour of the material; therefore, it indicates the form of strain-energy function depends on the selection of reference configuration (fig. 2.6) and residual stress in the selected configuration.

Considering a natural configuration ($\mathscr{B}_0$), in which no (residual) stress exists ($\boldsymbol{\tau} = \mathbf{0}$), the total elastic energy could be expressed as

$$\int_{\mathscr{B}_0} W \mathrm{d}V. \tag{2.60}$$

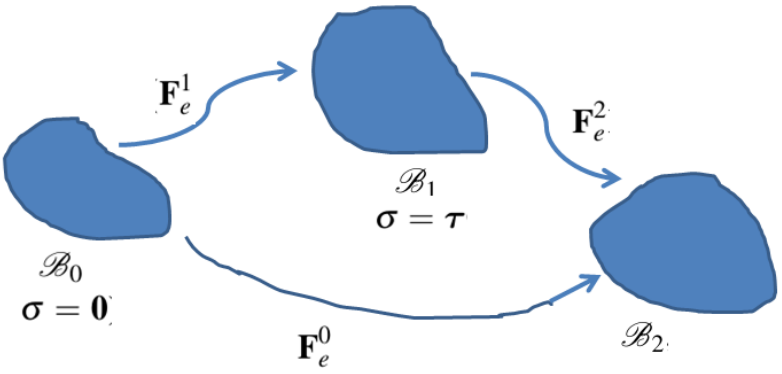

FIGURE 2.6: The strain energy function defined in an arbitrary configuration $\mathscr{B}_1$. $\mathscr{B}_0$ is the stress-free reference configuration, $\mathscr{B}_1$ is the residually-stressed configuration. The elastic deformation $\mathbf{F}_e^2$ takes body into the current configuration $\mathscr{B}_2$

Assuming the elastic body deforms into $\mathscr{B}_2$ via the intermediate configuration $\mathscr{B}_2$, the relation between deformation gradients could be given by application of eq. (2.18) as

$$\mathbf{F}_e^0 = \mathbf{F}_e^2 \mathbf{F}_e^1, \tag{2.61}$$

where $\mathbf{F}_e^0$ is the elastic deformation gradient from $\mathscr{B}_0$ to $\mathscr{B}_2$, $\mathbf{F}_e^1$ is the deformation gradient from $\mathscr{B}_0$ to $\mathscr{B}_1$, and $\mathbf{F}_e^2$ is the deformation gradient from $\mathscr{B}_1$ to $\mathscr{B}_2$.

The application of elastic energy conservation gives

$$\int_{\mathscr{B}_0} W(\mathbf{F}_e^0)\mathrm{d}V - \int_{\mathscr{B}_0} W(\mathbf{F}_e^1)\mathrm{d}V = \int_{\mathscr{B}_1} \bar{W}(\mathbf{F}_e^2, \boldsymbol{\tau})\mathrm{d}v, \tag{2.62}$$

This could be rewritten with the help of eq. (2.25) as

$$\int_{\mathscr{B}_0} W(\mathbf{F}_e^0)\mathrm{d}V - \int_{\mathscr{B}_0} W(\mathbf{F}_e^1)\mathrm{d}V = \int_{\mathscr{B}_0} J_1 \bar{W}(\mathbf{F}_e^2, \boldsymbol{\tau})\mathrm{d}V, \tag{2.63}$$

where $J_1 = \det \mathbf{F}_e^1$.
Since eq. (2.63) is valid for arbitrary volumes, it gives

$$\bar{W}(\mathbf{F}_e^2, \boldsymbol{\tau}) = (J_1)^{-1}\{W(\mathbf{F}_e^0) - W(\mathbf{F}_e^1)\}. \tag{2.64}$$

Referring to $\mathscr{B}_0$, the Cauchy stress in $\mathscr{B}_2$ is computed as

$$\boldsymbol{\sigma} = J_0^{-1} \mathbf{F}_e^0 \frac{\partial W}{\partial \mathbf{F}_e^0}. \tag{2.65}$$

Referring to $\mathscr{B}_1$ (eq. (2.64)), the Cauchy stress in $\mathscr{B}_2$ is computed as

$$\bar{\boldsymbol{\sigma}} = J_2^{-1}\mathbf{F}_e^2\frac{\partial \bar{W}}{\partial \mathbf{F}_e^2} = J_2^{-1}\mathbf{F}_e^2\frac{\partial}{\partial \mathbf{F}_e^2}\{J_1^{-1}\left[W(\mathbf{F}_e^0) - W(\mathbf{F}_e^1)\right]\}. \tag{2.66}$$

Obviously, $W(\mathbf{F}_e^1)$ and J_1 are independent of $\mathbf{F}_e^2$, then

$$\bar{\boldsymbol{\sigma}} = J_2^{-1}J_1^{-1}\mathbf{F}_e^2\frac{\partial}{\partial \mathbf{F}_e^2}\left[W(\mathbf{F}_e^0)\right]. \tag{2.67}$$

Application of the chain rule and eq. (2.61), then gives

$$\bar{\boldsymbol{\sigma}} = J_2^{-1}J_1^{-1}\mathbf{F}_e^2\mathbf{F}_e^1\frac{\partial}{\partial \mathbf{F}_e^2}\left[W(\mathbf{F}_e^0)\right] = J_0^{-1}\mathbf{F}_e^0\frac{\partial W}{\partial \mathbf{F}_e^0} = \boldsymbol{\sigma}. \tag{2.68}$$

2.3.2.1 Deformation Constraints

The elastic body sometimes will deform with local constraints, for example, the body is constrained to be inextensible in a certain direction. The constraint will mathematically reduce the number of independent components of the elastic deformation tensor. For instance, a rigid rod is assumed to be inextensible along its axial direction. The elastic deformation and energy will be both zero along axial direction, no matter how huge the force is applied at both ends of the rod.

We consider a deformation constraint to be defined by a scalar function

$$C(\mathbf{F}_e) = 0. \tag{2.69}$$

Then, the strain energy function with respect to $\mathscr{B}_0$ will be modified by the contribution of constraints as

$$\bar{W}(\mathbf{F}_e, \boldsymbol{\tau}, C) = \bar{W}(\mathbf{F}_e, \boldsymbol{\tau}) - pC(\mathbf{F}_e), \tag{2.70}$$

where p is a Lagrange multiplier.
Applying eq. (2.59), the nominal stress is given as

$$\mathbf{S} = \frac{\partial \bar{W}(\mathbf{F}_e, \boldsymbol{\tau})}{\partial \mathbf{F}_e} - p\frac{\partial C}{\partial \mathbf{F}_e}, \tag{2.71}$$

The application of the connection between Cauchy and nominal stresses gives

$$\boldsymbol{\sigma} = J^{-1}\mathbf{F}_e\frac{\partial \bar{W}(\mathbf{F}_e, \boldsymbol{\tau})}{\partial \mathbf{F}_e} - pJ^{-1}\mathbf{F}_e\frac{\partial C}{\partial \mathbf{F}_e}, \tag{2.72}$$

Considering the constraint is incompressibility of elastic body, it indicates constant volume of body after elastic deformation), which gives the constraints function as

$$J(\mathbf{F}_e) \equiv 1 \ \Rightarrow C(\mathbf{F}_e) = J - 1 = 0. \tag{2.73}$$

Recalling the expressions of nominal and Cauchy stresses with constraints, they could be rearranged as

$$\begin{aligned} \mathbf{S} &= \frac{\partial \bar{W}(\mathbf{F}_e, \boldsymbol{\tau})}{\partial \mathbf{F}_e} - p\frac{\partial (J-1)}{\partial \mathbf{F}_e} \\ &= \frac{\partial \bar{W}(\mathbf{F}_e, \boldsymbol{\tau})}{\partial \mathbf{F}_e} - p\mathbf{F}_e^{-1}, \end{aligned} \tag{2.74}$$

and

$$\boldsymbol{\sigma} = J^{-1}\mathbf{F}_e\frac{\partial \bar{W}(\mathbf{F}_e, \boldsymbol{\tau})}{\partial \mathbf{F}_e} - p\mathbf{I}, \tag{2.75}$$

where $\frac{\partial J}{\partial \mathbf{F}_e} = J\mathbf{F}_e^{-1}$.

2.3.2.2 Strain Energy Function with Invariants

Recalling the definitions for the SEF for arbitrary configurations in eq. (2.64), it shows that this SEF could be directly pushed back into the SEF of (fixed) stress-free configurations, even though stress-free configuration does not really exist for particular bodies.

Considering the SEF for a stress-free configuration, it is a scalar function with respect to the elastic deformation. Moreover, recalling the polar decomposition of the deformation gradient, it suggests that the scalar function should be independent of rotation of elastic body and be objective as

$$W(\mathbf{F}_e) = W(\mathbf{R}\mathbf{U}_e) = W(\mathbf{U}_e) = \hat{W}(\lambda_1, \lambda_2, \lambda_3), \tag{2.76}$$

where λ_i is the ith principal value of $\mathbf{U}_e$ (eq. (2.21)).
For an isotropic material, the mechanical responses are the same for deformation along arbitrary directions, which indicates

$$\hat{W}(\lambda_1, \lambda_2, \lambda_3) = \hat{W}(\lambda_2, \lambda_1, \lambda_3) = \hat{W}(\lambda_3, \lambda_2, \lambda_1),$$

Furthermore, this could be represented with the invariants of the deformation tensor as

$$\hat{W}(\lambda_1, \lambda_2, \lambda_3) = \Psi(I_1, I_2, I_3), \tag{2.77}$$

where

$$\begin{cases} I_1 = \mathrm{tr}\mathbf{C}_e = \sum \lambda_i^2 \\ I_2 = \frac{1}{2}\{(\mathrm{tr}\mathbf{F}_e^2) - \mathrm{tr}\mathbf{F}_e^2\} = \lambda_1\lambda_2 + \lambda_2\lambda_3 + \lambda_1\lambda_3 \\ I_e = \det \mathbf{C}_e = J, \end{cases} \tag{2.78}$$

and $\mathbf{C}_e = \mathbf{F}_e^T \mathbf{F}_e$.

The proof is not shown here, details seeing in Ogden [57].

2.3.2.3 SEF for Mixture Materials

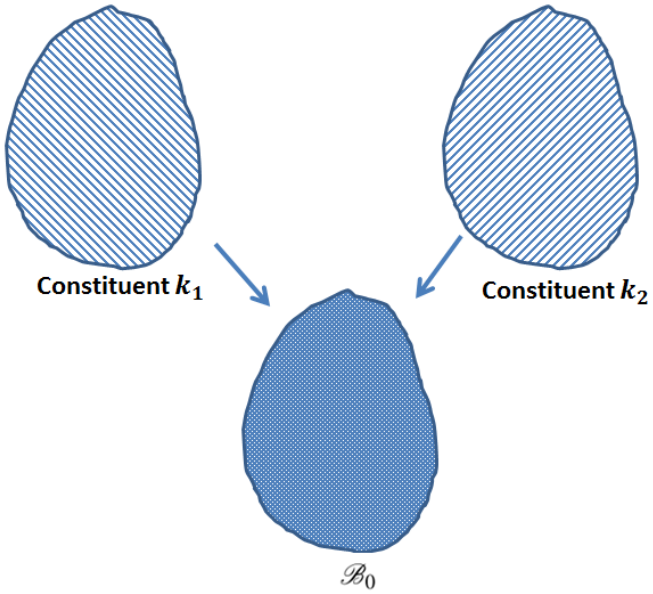

FIGURE 2.7: The configurations for a mixture material with constituents k_1 and k_2. The two materials are assumed to cover the same volume but with different volumetric fractions.

Assuming the elastic body is mixed by two constituents k_1 and k_2 (fig. 2.7), states of residual stresses are generally different for two constituents. The total elastic strain-energy with respect to this configuration could be obtained as

$$\int_{\mathscr{B}} W(\mathbf{F}_e, \boldsymbol{\tau}) \mathrm{d}V + \int_{\mathscr{B}^*} W^*(\mathbf{F}_e, \boldsymbol{\tau}^*) \mathrm{d}V, \tag{2.79}$$

where * indicates the variable for new material, and $\mathscr{B}_0 = \mathscr{B} \cup \mathscr{B}^*$.

To obtain the mechanical behaviours of the mixture with respect to configuration $\mathscr{B}_0$, the local average deformation is defined to describe the overall elastic deformation for the mixture as

$$\int_{\mathscr{B}_0} \mathbf{F}_e \mathrm{d}V = \int_{\mathscr{B}} \mathbf{F}_e \mathrm{d}V + \int_{\mathscr{B}^*} \mathbf{F}_e \mathrm{d}V. \tag{2.80}$$

Then, the total elastic energy for mixture material is written as

$$\int_{\mathscr{B}_0} W_0(\mathbf{F}_e)\mathrm{d}V = \int_{\mathscr{B}} W(\mathbf{F}_e,\boldsymbol{\tau})\mathrm{d}V + \int_{\mathscr{B}^*} W^*(\mathbf{F}_e,\boldsymbol{\tau}^*)\mathrm{d}V. \tag{2.81}$$

Applying eq. (2.80) and (2.81), the total elastic energy could be re-written as

$$\int_{\mathscr{B}_0} W_0(\mathbf{F}_e)\mathrm{d}V = \int_{\mathscr{B}} \{\Phi W(\mathbf{F}_e,\boldsymbol{\tau}) + \Phi^* W^*(\mathbf{F}_e,\boldsymbol{\tau}^*)\}\mathrm{d}V, \tag{2.82}$$

where Φ and Φ^* are the volumetric fractions for materials ($\Phi + \Phi^* = 1$).
Since this integration is valid for any volume, the SEF for the mixture is given as

$$W_0(\mathbf{F}_e) = \Phi W(\mathbf{F}_e,\boldsymbol{\tau}) + \Phi^* W^*(\mathbf{F}_e,\boldsymbol{\tau}^*). \tag{2.83}$$

The state of residual stress will affect the mechanical behaviors of individual constituent. In turn, it will influence the overall mechanical behaviors of the mixture body, which indicates the importance of the residual stress in soft tissues to determine the mechanical behaviors of mixture body under external loading. However, in a biomaterial mixture or living organ, the residual stress is hard to determine, due to the complexity of its formation. For instance, living tissues are usually composed by different constituents. The growth of different constituents are usually incompatible. In turn, the residual stress will be induced by the deformations to get the compatible configuration for living organ. Till now, how to accurately predict and measure residual stress is still a open challenge for the study of the mechanical behaviours of living organs.

Besides, the residual stress could also affect the expression of the SEF for the mixture. However, for a mixture, the stress-free configuration usually doesn't exist, while the individual stress-free configurations exist for each constituent. If considering the mixture material as a whole body, the stress-deformation relation could be given by the SEF for the mixture (eq. (2.83)) and could be pushed into any arbitrary configuration.

Furthermore, the SEF for a body is given for n constituents as

$$W_0 = \sum \Phi^i W(\mathbf{F}_e^i,\boldsymbol{\tau}^i), \tag{2.84}$$

where index i indicates variables for ith constituent and $\sum_i \Phi^i = 1$.

2.3.2.4 The SEF for a Fibre-reinforced Material

Considering the fibre-reinforced material, the fibres are embed into matrix materials, while the interactions are ignored between fibres here. Moreover, it is assumed that fibres only contribute to mechanical response along their axial directions. Then, the SEF for a fibre could be written

as

$$W_f(\mathbf{F}_e^f, \boldsymbol{\tau}_f) = \hat{W}_f(\lambda_f, \boldsymbol{\tau}_f), \tag{2.85}$$

where $\mathbf{F}_e^f$ is elastic deformation for fibre, λ_f is stretch of fibre and $\boldsymbol{\tau}_f$ is residual stress.
The residual stress in fibres has been studied by many researches (e.g. Taber & Humphrey [78]). In this section, the residual stress is assumed to be zero to reduce the complexity.

Applying eq. (2.29), then

$$\lambda_f = (\mathbf{N} \cdot (\mathbf{F}_e^T \mathbf{F}_e)\mathbf{N})^{1/2}, \tag{2.86}$$

where $\mathbf{N}$ is the unit vector along fibre direction.
Application of eqs. (2.77), (2.80), (2.81) and (2.85), the SEF for a material reinforced by one fibre family could be written as

$$W_0(I_1, I_2, I_3, \lambda_f) = \Phi W(I_1, I_2, I_3) + \Phi^* W^*(\lambda_f). \tag{2.87}$$

Fiber dispersion in fibrous tissues has been recognized as being important in the mechanical response of the tissue. Considering the 3-dimension fibre family, the orientation density function $\hat{\varphi}(\Theta, \Upsilon)$ could be defined to satisfy the normalization condition

$$\iint_\Omega \hat{\varphi}(\Theta, \Upsilon) \mathrm{d}\Theta \mathrm{d}\Upsilon = 1.$$

where Θ and Υ are the spherical polar angles, and $\Omega = \{(\Theta, \Upsilon) \in (0 \leq \Theta \leq \pi, 0 \leq \Upsilon \leq 2\pi)\}$.

In this thesis, only the 2-dimension fibre family is used. Here, the 2-dimension orientation density function ($\hat{\varphi}$) is employed to describe the fibre structure

$$\int \hat{\varphi}(\Theta) \mathrm{d}\Theta = 1. \tag{2.88}$$

where Θ is the fibre angle to the vector along mean direction of fibre family.
And the volumetric fraction for fibre family along a particular direction could be obtained as

$$\Phi_f \int \hat{\varphi}(\Theta) \mathrm{d}\Theta, \tag{2.89}$$

where Φ_f is total volumetric fraction of fibres.
For a material with dispersed fibre families, the SEF could be given with the orientation density function

$$W_0(I_1, I_2, I_3, \lambda_f) = \Phi W(I_1, I_2, I_3) + \Phi_f \int \hat{\varphi}(\Theta) W^*(\lambda_f) \mathrm{d}\Theta, \tag{2.90}$$

where Θ is the angle between fibre and certain directions in reference configuration, $\hat{\varphi}(\Theta)$ is the orientation density function.
In this project, the crosslinks and interactions between fibres are ignored. It is supposed that fibres can not take compressive loads. To exclude the mechanical contributions of compressed

fibre, the fibre 'switch' is employed as

$$\lambda_f(\Theta) > 1.$$

Then, the SEF (eq. 2.90) is modified as

$$W_0(I_1,I_2,I_3,\lambda_f) = \Phi W(I_1,I_2,I_3) + \Phi_f \int_\Sigma \hat{\varphi}(\Theta) W^*(\lambda_f) \mathrm{d}\Theta, \tag{2.91}$$

where Σ is the solution of fibre 'switch' (if $\lambda_f(\Theta) > 1, \Theta \in \Sigma$).

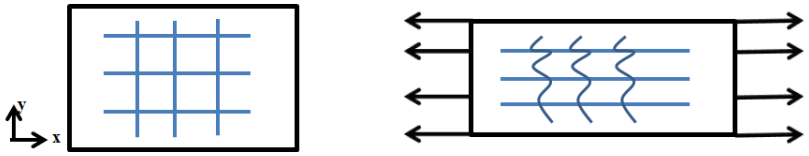

FIGURE 2.8: The single-axis tension applied to a fibre-reinforced tissue with orthogonal fibre families.

Example to test the SEF for a fibre-reinforced material

To validate the SEF for a fibre-reinforced material, an analytical solution will be shown for mechanical behaviour of the fibre-reinforced material with simple boundary conditions.

Considering a tissue with rectangular shape defined by,

$$0 \le X \le A, 0 \le Y \le B, 0 \le Z \le C.$$

The single-axial tension, along the x-axis, is applied on the incompressible and fibre reinforced tissue (fig. 2.8). Assuming a plane-strain condition, the deformation gradient could be simply given as $\mathbf{F}_e = \mathrm{diag}(\lambda_1, \lambda_2, 1)$. And the incompressibility ($\lambda_1\lambda_2\lambda_3 = 1$) gives $\mathbf{F}_e = \mathrm{diag}(\lambda_1, \frac{1}{\lambda_1}, 1)$.

The force boundary condition gives

$$\sigma_y = 0. \tag{2.92}$$

where x and y are coordinates (fig. 2.8), z is the direction othogonal to directions x and y.
A square tissue is assumed to be reinforced by two independent and orthogonal fibre families. The orientation density function could be reduced as

$$\hat{\varphi} = \begin{cases} +\infty, & \text{if } \Theta = 0; \\ +\infty, & \text{if } \Theta = 90; \\ 0, & \text{if } \Theta \neq 0 \text{ or } 90. \end{cases} \tag{2.93}$$

And

$$\begin{cases} \int_{-\infty}^{0} \hat{\varphi}(\Theta)\mathrm{d}\Theta = \frac{1}{2}; \\ \\ \int_{90}^{+\infty} \hat{\varphi}(\Theta)\mathrm{d}\Theta = \frac{1}{2}. \end{cases} \tag{2.94}$$

The volumetric fractions are selected as:

$$\begin{cases} \Phi = 0.97, \quad \text{(matrix)} \\ \Phi_f = 0.03, \quad \text{(fibre)} \end{cases} \tag{2.95}$$

The HGO model is selected as the SEF for the tissue, it gives

$$W = \frac{c}{2}(I_1 - 3), \quad W^* = \frac{k_1}{2k_2}\{\exp k_2(I_4 - 1)^2 - 1\}, \tag{2.96}$$

where

$$I_1 = \mathrm{tr}(\mathbf{F}_e^T \mathbf{F}_e), \tag{2.97}$$

and I_4 is written as

$$I_4 = \mathbf{N} \cdot (\mathbf{F}_e^T \mathbf{F}_e)\mathbf{N} = \lambda_f^2; \tag{2.98}$$

c, k_1 and k_2 are material constants, here using $c = 3$kPa, $k_1 = 78.67$kPa and $k_2 = 0.84$.
Recalling the SEF (eq. 2.90) and the fibre orientation density function (eq. 2.94), the SEF here is written as

$$W_0 = \Phi\frac{c}{2}(I_1 - 3) + \frac{\Phi_f}{2}\frac{k_1}{2k_2}\{\exp k_2(I_4(\mathbf{N}_1) - 1)^2 - 1\} + \frac{\Phi_f}{2}\frac{k_1}{2k_2}\{\exp k_2(I_4(\mathbf{N}_2) - 1)^2 - 1\}, \tag{2.99}$$

where $\mathbf{N}_i$ is the direction vector for ith fibre family ($\mathbf{N}_1 = \mathbf{e}_x$ and $\mathbf{N}_2 = \mathbf{e}_y$).

Solution:
If compressed fibre are included, the Cauchy stress could be obtained from eq. (2.99) as

$$\begin{aligned} \boldsymbol{\sigma} = & -p\mathbf{I} + (\Phi c)\mathbf{F}_e\mathbf{F}_e^T \\ & + \Phi_f k_1\{(I_4(\mathbf{N}_1) - 1)\exp(k_2(I_4(\mathbf{N}_1) - 1)^2\}\mathbf{e}_x \otimes \mathbf{e}_x \\ & + \Phi_f k_1\{(I_4(\mathbf{N}_2) - 1)\exp(k_2(I_4(\mathbf{N}_2) - 1)^2\}\mathbf{e}_y \otimes \mathbf{e}_y, \end{aligned} \tag{2.100}$$

with the help of the definitions of deformation tensor and stress tensor (eq. (2.100)), the components of Cauchy stress are expressed as

$$\begin{cases} \sigma_x = -p + \Phi c\lambda_x^2 + \Phi_f k_1(\lambda_x^2 - 1)exp\{k_2(\lambda_x^2 - 1)^2\} \\ \sigma_y = -p + \Phi c\lambda_y^2 + \Phi_f k_1(\lambda_y^2 - 1)exp\{k_2(\lambda_y^2 - 1)^2\} \\ \sigma_z = -p + \Phi c\lambda_z^2. \end{cases} \tag{2.101}$$

Recalling the boundary condition (eq. (2.92)), eq. $(2.101)_2$ gives

$$\sigma_y = 0 \;\Rightarrow\; p = \Phi c\lambda_y^2 + \Phi_f k_1(\lambda_y^2 - 1)\exp\{k_2(\lambda_y^2 - 1)^2\}. \tag{2.102}$$

With the help of the deformation tensor and boundary condition (2.102), the relations are obtained from eq. (2.101) for '$\lambda_x - \sigma_x$'.

With help of eq. (2.98), $I_4(\mathbf{N}_1) = \lambda_1^2 \geq 1$ and $I_4(\mathbf{N}_2) = \lambda_2^2 \leq 1$, if applying single axis tension along x axis. Therefore, if the compressed fibres are excluded ($I_4(\mathbf{N}_2) = \lambda_2^2 \leq 1$), the SEF could be rewritten as

$$W_0 = \Phi\frac{c}{2}(I_1 - 3) + \frac{\Phi_f}{2}\frac{k_1}{2k_2}\{\exp k_2(I_4(\mathbf{N}_1) - 1)^2 - 1\}. \tag{2.103}$$

If the compressed fibres are excluded by fibre switch ($\lambda_f > 1$), the Cauchy stress could be obtained from eq. (2.103) as

$$\begin{aligned}\boldsymbol{\sigma} =& -p\mathbf{I} + (\Phi c)\mathbf{F}_e\mathbf{F}_e^T \\ &+ \Phi_f k_1\{(I_4(\mathbf{N}_1) - 1)exp(k_2(I_4(\mathbf{N}_1) - 1)^2\}\mathbf{e}_x \otimes \mathbf{e}_x,\end{aligned} \tag{2.104}$$

which gives

$$\begin{cases}\sigma_x = -p + \Phi c\lambda_x^2 + \Phi_f k_1(\lambda_x^2 - 1)exp\{k_2(\lambda_x^2 - 1)^2\} \\ \sigma_y = -p + \Phi c\lambda_y^2 \\ \sigma_z = -p + \Phi c\lambda_z^2.\end{cases} \tag{2.105}$$

Recalling the boundary condition (2.92), eq. $(2.105)_2$ gives

$$\sigma_y = 0 \;\Rightarrow\; p = \Phi c\lambda_y^2. \tag{2.106}$$

With the helps of the deformation tensor and boundary condition (2.106), the relations are obtained from eq. (2.105) for '$\lambda_x - \sigma_x$'.

Fig. 2.9 shows the differences of mechanical behaviours between the SEF with and without the fibre switch: the stresses, obtained from the SEF without fibre switch, are bigger. The differences are bigger with the increasing fibre stretch (λ_x). The results suggest that the stress prediction is not accurate if the compressed fibres are not excluded. In this project, **the fibre switch will be included to describe the mechanical behaviours for fibre-reinforced materials**.

2.4 Summary

In this section, the concepts of deformation and motions are explained. In general, the deformation is to describe the shape change of a body respect to a certain configuration. Then, the deformation gradient (tensor) is introduced to measure the changes of shape. From a perspective

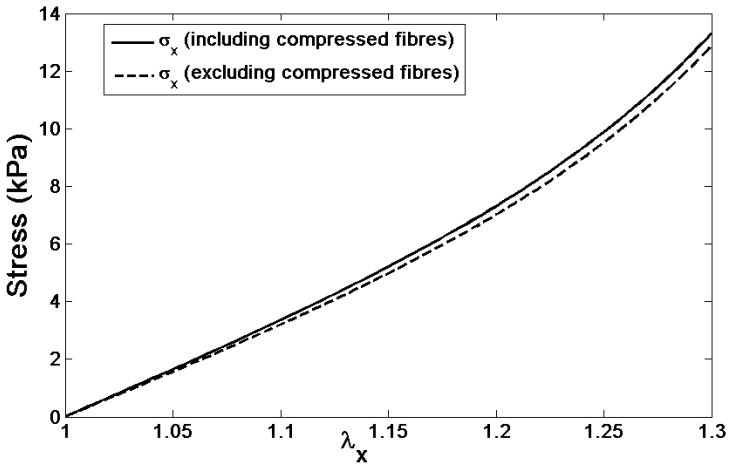

FIGURE 2.9: The comparison of Cauchy stresses from different SEFs: the comparison between σ_x, dash line is σ_x obtained from SEF including the compressed fibre, solid line is σ_x obtained from SEF excluding the compressed fibre.

of mechanism, the stress could induce the (relative) deformation. To solve the mechanical behaviours of a body, a stress-deformation relation is required. The relation between deformation and stress is mathematically described by a constitutive law. The basic form of constitutive law is used as the SEF in this project. Focusing the soft tissue composed with biomaterials, most biomaterials are fibre-reinforced materials. If assuming the fibre can't bear compressive loading, the fibre switch will be used to exclude the compressed fibres.

Chapter 3

Literature Review: Theories of Residual Stress in Living Organs Estimated by the Opening-angle Method

A basic physical description is needed to understand and predict the mechanical behaviour of soft tissues (or organs) in circulatory physiology. Generally, referring to small-deformation and linear theories, the moduli of elasticity and Poisson's ratios are originally employed to describe the material properties for soft tissues, before the well-developed theories of large deformation. However, in order to accurately describe the complex mechanical behaviours of soft tissue, large deformation theories were introduced by researchers (like Bergel [6] or Fung [21]). Referring to large deformation theories, the most popular method is to use the *strain energy function* (SEF) or *energy density function* (EDF) to describe the material properties for soft tissue, which is based on the laws of thermodynamics and the Gibbs-Duhem entropy inequality. At least to the author, between nonlinear and linear theories, one of biggest differences is whether the consequent mechanical behaviour of an elastic body is influenced by the stress states in the reference configurations.

For nonlinear theories, the (natural) stress-free configuration is implicitly important to identify the stress–deformation relation, even though the SEF could be defined with respect to the arbitrary reference configuration. In the early stages of large deformation theories, the unloaded configuration of soft tissues were selected as the stress-free one, which fact might introduce theoretical errors in estimating the mechanical behaviours of soft tissues or living organs if residual stress exists in the selected configuration. This includes why the theories of residual stresses are important.

In this section, the theories and models for estimating residual stress in organs will be summarized and reviewed.

3.1 Residual Stress Estimated by an One-cut Model

Von Maltzahn [87] reported experimental measurements of the elastic properties of different layers of bovine carotid arteries, based on the perspective of large deformation theories. In [87], assuming the unloaded configuration to be stress-free, the linkage between deformation and stress was obtained for an artery (with the SEF defined by Fung [21]), for a thick-wall tube model with the cylindrical coordinates. Afterwards, comparison of the geometries of atria were presented between experimental data and predicted results. The obvious differences suggest a problematical selection of the stress-free configuration, though the estimates were significantly better than results estimated by small-deformation theories (seeing Bergel [5]). As least to the author, one of the most important error sources is the inappropriate selection of the stress-free configuration, which fact in turn gives the inappropriate estimations of (Cauchy) stress.

To investigate the stress states (residual strain or residual stress) of living organs, Fung published a series of papers based on observations of artery-slice-cutting experiments. In [23], a radial cut was done on an aorta slice, and then the opening angles were measured. The experimental results showed that the arterial slices would spring open after cutting along the radial directions, while the opening angles varied with the locations on the aorta trees.

The residual strain, which is the elastic strain between zero-stress and no-load states, indicates the existence of residual stress after removal of the external loads. An important influences of the residual stress is that it affects the homeostatic stress distribution in the tissues. It contributes a definite influence on the elastic behaviours of the tissue, since the stiffness of soft tissue varies with the states of stress. It's also pointed out the unsatisfactory calculations in previous researches (like [87], [79] and etc.), since they were derived from states that ignore the effects of residual stress.

The another important implication from [23] is that one radial-cut is sufficient to release all the residual stress (fig. 3.1).

The aorta slices were further cut into smaller parts at different circumferential positions and assembled into a whole specimen, which is to test whether the specimen could reproduce the shapes before cutting out. The experimental observations presented a good resemblance, indicating no further deformation after more radial cuts. Therefore, it was concluded that one radial cut could deform tissue into the stress-free configuration from the intact tube configuration. However, the logic behind this conclusion might be problematic. If the organ is in the

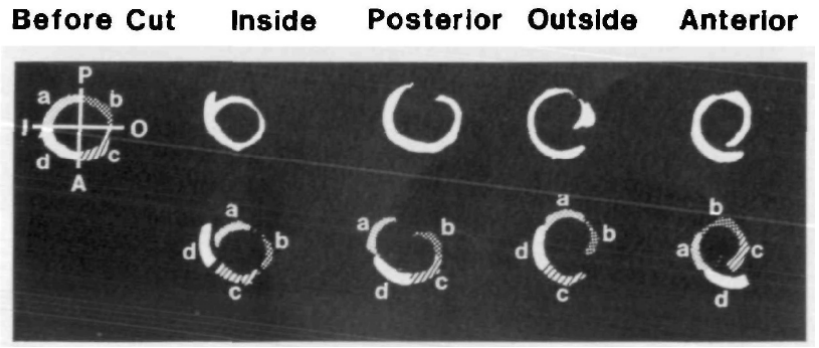

FIGURE 3.1: Photographs of cross sections at different locations of aorta trees after cut ([23]).

stress-free configuration, any further cut will not introduce any further elastic deformation. This logic is reasonable and rational. However, even if no further deformation occurs after the additional cut, the organ could still be in residually-stressed configuration before the cut, while the possible explanations could be: 1) a further cut is not sufficient to release the residual stress from the one-cut configuration. If the residual stress distribution is symmetric and independent of angular position, more radial cuts can not release any more residual stress. Therefore, in this case, a radial cut does not induce elastic deformation from a residually-stressed configuration. 2) the organ went into a newly stressed configuration. For example, if the SEF is not mathematically convex.

Accurate biomechanical analysis is required to identify the stress-free configuration. The first step is to experimentally quantify the residual strain for living organs. Before Omens [60], no experimental measurement existed to identify the residual strain in heart tissue (myocardium). Most peer researchers (like Huisman [42], or Yin [96]) used the unloaded configuration as the stress-free configuration, and the results show the extraordinarily huge stress concentration at the endocardial wall. In [60], the residual strain was measured and was used to recover a real stress-free configuration, which could be expected to reduce the estimation of stress concentration at the endocardial wall.

In the results of [60], the circumferential stretches were less than one at the endocaridal wall, which indicated a compressive (residual) stress at the specified location. Therefore, this important feature could explain the huge stress concentration at the endocadial wall estimated by the non-residual stress approach. Besides, additional deformation occurred after the second cut, which indicates that the one-cut configuration is still a residually-stressed one for rat heart. However, due to the obviously small magnitude of additional deformation, the stress-free configuration could be represented by slices with one cut.

The radial cut and opening angle methods were applied to measure the residual strain in porcine

and canine trachea (Han [28]). Results suggest that: (1) the opening angles were obviously different in trachea induced by single radial cuts at different locations, especially for canine trachea. It indicated the residual strains are not uniformly distributed in the trachea wall. (2) The sections from anterior cuts, made by additional radial cuts, could represent the opening angle configuration made by posterior cuts. It indicated that the additional cuts did not induce more elastic deformation. And similar with conclusions on aorta or hearts ([28], [23], [60]), one radial cut is sufficient to release all the residual stress. However, to the author, the statement – one cut configuration is stress-free configuration– is not sufficiently proved due to the listed reasons.

The residual strain could be generated by different growths ([28], [60], [23]). Then, the measurements of the residual strain (by opening angle method), could relieve the information about history of growth and heart formation. Besides the researches of residual strain in mature cardiovascular or heart systems, the changes of residual strain was speculated during the development of embryonic heart ventricle [77]. In [77], the embryonic hearts were obtained from chicks at different growth stages. The radial cuts were made to measure the residual strain in heart.

The results suggested that the opening angle decreased along with the heart formation [77]. For the heart, the growth was faster in the outer layer of the myocardium. Besides, stress-driven growth laws were proposed with explanations as: mechanical computation in [77] presented that the peak stress occurred at the same location (epicardium) with highest growth rate, while the strain peak was at endocardium; since living heart will never actually 'know' what are elastic strains from the natural configuration, however, the stress in current configuration could be 'felt' by the heart. It supports that the growth is regulated by stress.

After (incompatible) growth, residual strain occurred in elastic body to keep the body continuous without holes or overlaps in tissues. In [77], the stress-driven growth was proposed. Following this idea, Rodiguez [65] introduced a continuum formulation to figure out the relation between residual stress and stress-driven growth, with a simple tube model.

In [77], the relation between growth and stress was analyzed with a thick-wall heart model with a simple growth tensor. For simple volumetric growth, the growth was assumed to occur in the principal directions of the heart tube. With the diagonal growth tensor, the growth rate $\dot{\mathbf{U}}_g$ (represented in matrix form) and overall growth tensor $\mathbf{F}_g$ were defined as

$$\dot{\mathbf{U}}_g(t) = \begin{bmatrix} K_x[T_{zz}(t) - T_{zz}^*] & 0 & 0 \\ 0 & K_y[T_{zz}(t) - T_{zz}^*] & 0 \\ 0 & 0 & 0 \end{bmatrix} \Rightarrow \mathbf{F}_g(t) = \int_0^t \mathbf{U} \mathrm{d}t \tag{3.1}$$

where K_x, K_y are the growth rate constants, T_{zz} is the axial stress, T_{zz}^* is the criteria value.

In [77], it was suggested to explain how the residual stress might arise with incompatible growth and how residual stress helps to reduce the stress concentration in the ventricular wall. Meanwhile, it indicates that growth and elastic deformations are decoupled during the continuous growth. Moreover, the commutation law between growth and elastic deformation tensors was implicitly included in [65] as

$$\begin{aligned}\mathbf{F}_{eg} &= \mathbf{F}_{e,t_n}\mathbf{F}_{g,t_n}\mathbf{F}_{e,t_{n-1}}\mathbf{F}_{g,t_{n-1}}\mathbf{F}_{e,t_{n-2}}\mathbf{F}_{g,t_{n-2}}\cdots \\ &= \mathbf{F}_{e,t_n}\mathbf{F}_{e,t_{n-1}}\mathbf{F}_{e,t_{n-2}}\cdots(\mathbf{F}_{g,t_n}\mathbf{F}_{g,t_{n-1}}\mathbf{F}_{g,t_{n-2}}),\end{aligned} \tag{3.2}$$

where $\mathbf{F}_{e,t_n}$, $\mathbf{F}_{g,t_n}$ are the growth and elastic deformation tensors at time step t_n

In this simple model with only diagonal deformation tensors, the commutation laws are sufficient. However, this algorithm is problematic for the general case. For instance, for simple shear, the commutation laws are not satisfied:

$$\mathbf{F}_e = \begin{bmatrix}1 & \lambda & 0\\ 0 & 1 & 0\\ 0 & 0 & 1\end{bmatrix} \Rightarrow \mathbf{F}_e\mathbf{F}_g \neq \mathbf{F}_g\mathbf{F}_e. \tag{3.3}$$

To better characterize the mechanical behaviours of arterial material, the constitutive framework reference of Holzapfel, Gasser and Ogden (HGO) artery model was influenced. With the one-cut and thick-wall model, the computations suggested some important advantages of HGO model, compared with other models. Comparing with Delfino's model, the HGO model gave better prediction of the anisotropic mechanical behaviour in arteries. The HGO model could be applied to more general cases than previous models (Vaishnav [82], Fung [22] and Takamizawa [79]). For instance, those models are not always convex, then, the restrictions on material parameters are required to avoid material instabilities, while the HGO model is convex.

The first attempt to mechanically model the residual stress and growth of developing embryo heart was made by Taber [74]. Experiments were performed to measure the evolution of residual strain and the effects of the volume overload condition on the time course. The embryo chick hearts were banded with nylon loops to introduce the overload condition. The results showed the opening angles slightly decreased in the test group. However, the opening angles were significantly lower after heart banding. With the observations of opening angle, the passive and active zero-stress configuration could be identified (seeing stress equilibrium equation in [75]), with both active and passive stress components.

Olsson [58] developed a thermodynamically consistent (one-layer) model and applied it to analyze the residual stress in arteries after volumetric growth. The total strain energy, including the growth contribution, is

$$\Psi = \int W(\mathbf{F}_e, m)\mathrm{d}V_g = \int \det(\mathbf{G})W(\mathbf{F}_e, m)\mathrm{d}V_0, \tag{3.4}$$

where V_0, V_g are the volumes of the elastic body before and after growth (by tensor $\mathbf{G}$).

To this author, this framework is satisfactory for simple cases, such as the one-layer tube model with a diagonal growth tensor. However, it is not perfectly rational to be applied to more general cases. The energy (refeq27) can be used to calculate the first Piola-Kirchhoff stress, which indicates the stress state is unchanged before and after growth. However, if the residual stress is induced by incompatible growth, the stress states are different before and after growth. Therefore, the residual stress induced by growth will drive the elastic body into a new stress state, which requires to calculate the current stress state related to the growth-updated natural configuration.

To investigate the effects of residual stress on the mechanical behaviours of the heart (or left ventricle), Huiming [90] included the residual stress in a FE model for the LV by the approach introduced by one-cut approach from Shams [71]. In [71], if the initial (or residual) stress is given as $\boldsymbol{\tau}$, the SEF could be defined to this stressed configuration $\mathscr{B}_r$ as

$$W = W(\mathbf{F}_r, \boldsymbol{\tau}), \tag{3.5}$$

where $\mathbf{F}_r$ is the elastic deformation from $\mathscr{B}_r$.

Then, the Cauchy stress could be obtained for the incompressible myocardium as

$$\boldsymbol{\sigma} = \mathbf{F}_r \frac{\partial W_r}{\partial \mathbf{F}}(\mathbf{F}, \boldsymbol{\tau}) - p\mathbf{I}. \tag{3.6}$$

In order to refine the SEF in stressed configuration by above approach, Huiming [90] compared the residual stress obtained by residual strains in the LV measured by Costa [10] and residual stress computed from the opening angle method with one radial cut [1]. The results show obviously different stress distributions. Moreover, this shows the residual stresses influenced the stress distributions significantly after applying external loading, which contradicts with conclusion of Guccione [27].

By reviewing previous research, it is clear that the one-cut configuration might still be a stressed configuration, which makes the estimation of residual stress in intact heart inaccurate.

3.2 Residual Stress Estimated by a Multiple-cut Model

The growth of living tissues will induce residual stress in organs. In general, volumetric growth and mass growth are two key approaches for analyzing the growth and remodelling process in living organs. These two approaches will be reviewed about these two approaches.

3.2.1 Multiple-layer Model Using the Volumetric Growth Approach

In [88], after the radial cut, the bovine aorta was separated into the inner and outer layers by an additional circumferential cut. The opening angles were different for the layers, which indicates that residual stress and residual strains were different. This suggests using the two-layer model to describe the mechanical behaviours of arteries [76].

Taber [76] applied the stress-dependent finite growth method and thick-wall heart tube model for estimating the growth of aorta, with minor modifications of the model in [65]. Rather than the one layer model in [65], the two-layer model was employed to represent the structure of the aorta with both media and adventitia, which idea was inspired by the experimental observation by Vossoughi [88].

In [88], it is assumed that growth is induced by the principal stress. Then, the stress-dependent growth laws were used as

$$\dot{\mathbf{G}}(t) = \begin{bmatrix} \dot{\lambda}_{g1} & 0 & 0 \\ 0 & \dot{\lambda}_{g2} & 0 \\ 0 & 0 & \dot{\lambda}_{g3} \end{bmatrix} \Leftarrow \dot{\lambda}_{gi} = \sum D_{ij}\sigma_i \tag{3.7}$$

where σ_i is the ith principal stress, $\dot{\mathbf{G}}$ is the growth rate tensor, D_{ij} is the growth-rate coefficient measured from experimental data. Referring to the last equation, the growth rate will be bigger at material points with higher principal stress.

In previous experiments, the growth in bone was induced in the direction of stress, which guided the choice of growth law (6.73). However, skeletal muscles were observed empirically to grow in orthogonal directions to the primary stress [76]. To investigate the growth of aorta, two hypotheses were proposed for future study about the stress-driven growth laws [76]: (1) strain-driven law: the longitudinal growth was induced by strain along the associated strain directions, while stress induces transverse growth orthogonal to the stress directions; (2) active stress-dependent law: the active stress could induce the transverse growth. (The listed hypotheses were widely used to study the growth of soft tissues. This will be further discussed in next section.)

To this author, one problem might arise from the calculation of stress equilibrium in [76]. In general, in the multiple layer model, it is always required that the radial stress is continuous at

the interface of contacted layers, which condition was ignored in [76]. For instance, in [39], the stress continuity, ignored by [76], was described as

$$(\sigma_r|_{r=r_m})^+ = (\sigma_r|_{r=r_m})^-, \tag{3.8}$$

where r_m is the radius of interface.

Recently, more experimental observations support to the non-homogeneous distribution of residual strain [63]. Later researchers have started to analytically investigate the residual stress and opening angle in arteries with a multiple-layer model, while considering that the single-cut configuration is residually stressed.

The two-layer and thick-wall tube model was employed by Taber [78]. The predicted opening angles, produced by cuts at different locations, agreed well with experimental observations. This supported the idea that the multiple cut model could be a good direction to analyze the residual strain in arteries.

Compared to the heart function, the active stress in arteries is actually negligible. Taber [75] developed (passive) stress-driven laws to study the residual stress and evolution of vascular growth. In previous experimental studies, it is supported that the growth of organs intends to restore the wall stress and fluid shear stress into the stable states. Therefore, growth law, related with stable stress states, is developed within the thick-wall tube model ([75]). In [75], predicted opening angles matched well with experimental observations.

Though the non-homogeneous distributions of residual strains were accepted, early studies still used the single cut model to estimate the stress distribution in the heart. Omens [59] made the first attempt to experimentally measure the complex distributions of residual strain. The rings of heart were cut from mature rats. A radial cut was first made on each heart. Then, a circumferential cut was made to relieve another residual stress. The results show that additional deformations were induced after the second cuts, which indicates 1) the one-cut configuration is not the stress-free configuration; 2) the complex distribution of residual strains should be taken into consideration for mechanical analysis of the heart tissue.

The finite element method is popular for developing a patient-specific computational model, which is a powerful method for clinical diagnosis and treatment guidance. In analytical models, the residual stress (and opening angle) theories are accepted, while the effects of residual stress were well explored for regulating the growth. However, FE models rarely take account of both residual stress and growth in the study of the bio-mechanical behaviours of soft tissues or living organs. The influence of residual stress had been numerically studied by Holzapfel [33] on the physiological stress state of the arterial wall. In [33], the multiple layer structures of

arteries were developed within a FE geometry, while the opening angles were used to compute the residual stress states in arteries.

Alastrue [1] developed a patient-specific FE model to study adaptive volumetric growth, in which the residual stress states were coupled in. Considering an arbitrary material point $\mathbf{X}$ in the stress-free artery wall (with opening angle), the deformation $\mathbf{F}$ takes $\mathbf{X}$ into the compatible configuration $\mathscr{B}_r$. After applying external loading at $\mathscr{B}_r$, the deformation $\mathbf{F}_e$ drives the material point into the loaded configuration $\mathscr{B}_c$, which gives the overall deformation as $\mathbf{F} = \mathbf{F}_e\mathbf{F}_0$. In other words, if starting from $\mathscr{B}_r$, it required to multiple the deformation with the deformation associated with residual stress to compute the accurate mechanical response for arterial material point. This is the basic idea how Alastrue [1] developed the FE model including residual stress states. The deformation gradient was derivate from the cylindrical artery model with opening angles. After applying pressure on the inner surface, $\mathbf{F}_r$ would be multiplied with further elastic deformation to compute the stress states for arteries. The overall stress will be employed in the stress-driven growth (from [73] with minor modifications) to simulate the diagonal growth tensor. By repeating the growth-stress loop, the FE model could give the evolutions of stress and adaptive growth with the patient-specific arterial geometry.

Ren [64] used the two-layer model to investigate the effects of growth on the stress distribution and deformation. The key features of the two-layer model and growth laws were similar to these models in [78] or [34]: (1) the stress-driven growth laws and diagonal growth tensors employed for each layer; (2) the active stress is generated by smooth muscle. To this author, the key difference in [64] is the selection of the stress-free configuration. In previous studies, the intact ring was used as the stress-free configuration, while the incompatible growth in different layers would modify the stress-free configurations. However, in [64], the growth occurred in the opened angle configuration as stress-free one, which will affect the stress distribution.

With better understanding of the structures of artery wall, the non-homogeneity of the wall structure is well accepted, and represented by three layers: intima, media and adventitia (fig. 3.2).

The fact that the residual strains (opening angles) were different in layers has been experimentally demonstrated (Vossoughi [88], Han [29]). Rachev [63] measured the distribution of residual strains by the opening angle method for a multi-cut model. The first radial cuts were made on the aorta slices of mature rats to introduce the opening angle. Then, the wall components (collagen, elastin and smooth muscle) were grown chemically or thermally along the direction from the inner wall to the outer wall or in the reverse direction. The changes of growth opening angles were recorded to show the distribution of residual strains changing with time.

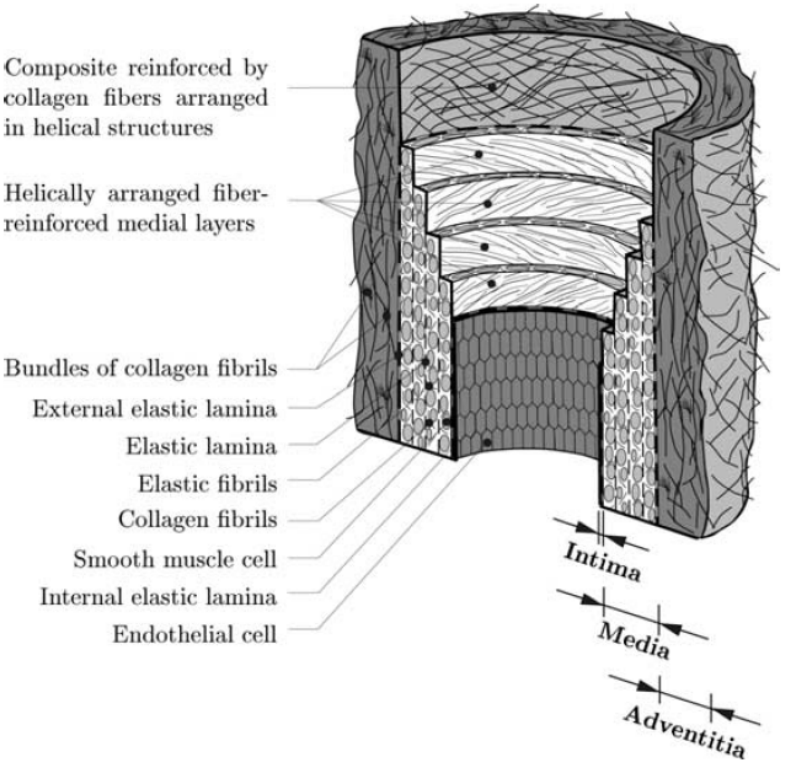

FIGURE 3.2: Components of a healthy artery with three layers: intima (I), media (M), adventitia (A).

The results showed the different opening angles in different layers of artery, which conditions also suggested the existence of non-homogeneous residual strain distributions across the layers. By releasing residual strain, the updated zero-stress configuration could be identified more accurately, which is important for analyzing the mechanical behaviours of aortas. Another important consequence of this research is that it also suggests that one radial cut could release all the residual stress.

The published experiments on residual stress and growth of arteries show several important features: 1) the arteries have at least three layers (intima, media and adventitia). 2) Distributions of residual strains are non-homogeneous, which could be demonstrated by the multiple cut experiments. Therefore, the zero stress configurations were different for different layers. 3) The incompatible natural configuration come from the complex growth processes of components of the arterial structure such as elastin, collagen and smooth muscles. The remodelling of collagen [73] and muscle growth [24] were experimentally measured.

By considering the listed issues, Alford [2] developed a framework with a thick-wall tube model to investigate the remodelling and growth in arteries. In this model, the passive material properties were described for individual components (elastin, collagen and smooth muscle), while the active stress generated by smooth muscle was also included. The remodelling of collagen and

elastin were mathematically described, as well as the growth laws for smooth muscle. For elastin remodelling, it was assumed that the turnover rate is negligible. For collagen remodelling, It was assumed that the old collagen is continuously replaced by new collagen. For smooth muscle, the growth law is used as: the transverse growth is induced by passive stress, while the circumferential growth is regulated by a combination of passive tensile and shear stresses, and active strains. To solve a mechanical equilibrium problem, the governing equations were combined with the previous intact ring model and radial cut slice model.

Besides the circumferential residual strains (measured by opening angles), the axial residual strain was experimentally shown along longitudinal direction of aortas by Holzapfel ([39]), with the axial strips taken from the anterior position of human aortas. After separating the layers from axial strips, further axial deformations occurred, which demonstrated the axial residual strain.

In previous works (like [2]), the residual stress analysis was based on the opening angle method, which does not account for address the 3D residual stress associated with both circumferential and axial residual strains. Holzapfel and Ogden [36] constructed the first 3D model to analyze the residual stresses in multiple layer arteries, considering axial bending.

The key difference from 2D residual stress model was the description of the elastic deformation for media layer, which mathematically explained the deformation from the axial bending configuration into the circumferential bending configuration. With the help of stress equilibrium and continuity of radial stresses at interface (3.8), the mechanical and geometric information could be used to give the residual stress states in aortas.

The structure of an artery with atherosclerosis experimentally was observed with 5 layers: inner intima, necrotic layer, outer intima, media and adventitia. Vandiver [85] analytically developed a 5-layer model to study the growth formulation of an artery with atherosclerosis and studied the effect of growth on peak stress. In [85], the stress-free configurations were unknown, which would be determined from the pressurized artery tube and the residually-stressed configuration with one radial cut. For a pressurized artery tube, the stress equilibrium equation is similar to that in [23], while the continuous a displacement and radial stresses between layers are solved with boundary conditions.

For a residually-stressed artery with an opening angle, the zero-net axial force and bending moment conditions were applied. Then, the zero-stress configuration was solved after growth. By considering different growth tensors, the effects on residual stress and peak stresses were studied [85].

3.2.2 Multiple Layer Model with Mass Growth Approach

Karvsaj [45] employed the constrained mixture growth model [4] to develop a multiple layer model to study pathological arterial adaption. Moreover, the opening angle, induced by the unbalanced growth in the constituents (fig. 3.3), was also considered with a decomposition approach similar with [1].

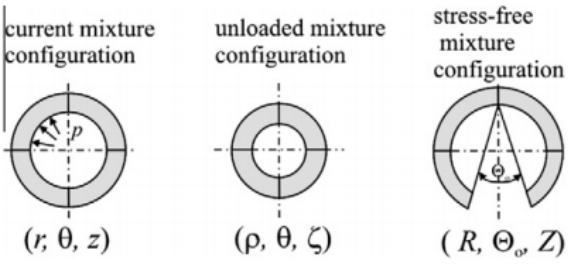

FIGURE 3.3: Configurations of arteries from constrained mixture model: left, the loaded configuration of arteries; middel, after unloading, the arteries deform into a residually-stressed configuration; right, the radial cuts release the residual strains in arteries measured by opening angle.

3.3 Summary

After the opening angle method was firstly introduced by Fung, the existence of residual stress has been well-accepted. More than significantly influencing the material properties of soft tissues, the residual stress is considered to modulate the growth and remodelling process in living organs. The evolution of residual stress could relieve the information about the history of growth, which could help to better the understanding of the formation of organs and the development of diseases. Due to the complex growth process in living organs, the complexity of residual strain is actually a huge challenge to further studies about the mechanical behaviour of living organs.

For arteries, the multiple layer model is developed to analytically study the mechanical response to changes of external loading or chemical environment, while the volumetric and mass (or constrained mixture) growth approaches were used to simulate the growth. However, the theory is still needed to explore how to address the stress-free state.

For the heart, due to its complex structure and geometry, most previous studies used the unloaded configuration or one-cut configuration as the stress-free configuration to estimate the stress state. However, both experimental and theoretical studies were suggested that: 1) residual stress will significantly influence the stress distribution in the heart. 2) simple (or single) cut does not release the residual stress in the heart. Therefore, more work is required to address the effect of residual stress in the heart.

Chapter 4

Literature Review: Theories of Growth and Remodelling for Living Tissues

The interactions between living organs and the bio-environment play important roles in regulating pathological or physiological growth. In general, it has been experimentally demonstrated that environmental factors, such as the chemical, mechanical or genetic stimuluses, could induce growth and remodelling (G&R) processes in living organs. For instance, nutrition concentration will be increased around the tumors, which helps to accelerate cell division and lead to the local growth of tumors at the tissue level (chemical factors). In [76], the experiments show that the myocardium will grow along the direction of principal tensile stress (mechanical factors). During the heart formation, the embryo heart will continuously and instinctively develop the heart structure (genetic factor).

Living organs can re-shape themselves and reset the growth (or turnover) rates of their constituents; in the long run, they will develop volumetric and mass changes to adapt to the pathological or physiological changes in the bio-environment. G&R processes have been observed in different patterns: For embryonic or young organs, they will continuously re-structure themselves to develop specified functions, like heart formation. For mature organs, they are expected to stay in a relatively stable living state and serve as fully functional; however, pathologically, the dynamic impact of bio-environmental changes will induce a quick remodelling process to renovate the functional tissue. For instance, chronic disorder could develop maladaptive G&R, such as the hypertrophic ventricular growth induced by systemic hypertension in the heart; physiologically, body exercises will stimulate reversible growth to strengthen the functions of the living organs. As evidence, the wall-thickness of artery is increased (in other words, eccentric ventricular growth were observed) for animal after more body exercises, which could promote muscle contractions.

After G&R, the functions and life cycles would be modified in living organs. However, the principles governing those mechanism are still not fully understood that could address the relation between external stimuli and growth processes. Obviously, improving the knowledges in this particular field will give huge potential for the design and optimization of clinical treatments to efficiently save more lives. However, in this relatively new field, many challenges exist. As mentioned, the stimulus could be considered as the combined effects of different sources, including mechanical, thermal, electrical and genetic information. These stimuli will simultaneously contribute to the successive growth processes in living organs. In practice, this fact raises the complexity of figuring out the contributions of individual environmental factors. Besides, to understand growth in living organs, the theoretical framework is expected to be based on the coupling factors from multidisciplinary, which is still a gap in the current stages of knowledge.

For the biomechanical or even the mechanical community, the key questions now are: how could the mechanical behaviours of soft tissues be mathematically described? what is the role played by mechanical factor in the regulation of the growth? How would the mechanical functions and behaviours of living organs be modified after the growth? How would the mechanical information feedback and regulate changes of bio-environment during the life cycle? How would the mechanical information be decoupled and coupled with information from other fields to regulate the growth in living tissues?

Recently, significant improvements have been made to build up knowledge about the mechanical behaviour of soft tissues, like theories of the nonlinear elastic deformations. To answer these questions, in early stages of researches in this field, the mechanical stimuli was exclusively extracted. If controlling other stimuluses stable and unchanged, by recording the mechanical stimulus and subsequent growth, the relations could be mathematically described between growth and mechanical information. In the coming sections, the (mainstream) academic works will be reviewed to show the current research stage and potential directions in this field.

It should be clarified that only two key categories about growth and remodelling will be addressed in those sections: (1) the remodelling of fibre-reienforced material; (2) the volumetric and mass growth in living organs. These are closely related with author's research interests,

4.1 Remodelling of (Collagen) Fibre-reinforced Soft Tissues

Considering the formations of living organs, if ignoring other stimuli (like chemical factors), mechanical environment plays an important role for the adaptation of tissues. In other words, the structure and functionality of soft tissues will be structured and optimized to adapt external (mechanical) working environments.

Strain and stress are key indicators for measuring the load level in living organs. Experimental evidence suggests strains and stresses are the mechanical factors inducing adaptations in tissues. For instance, Huiskes [41] found that the strains could contribute to the bone growth. Taber [78] hypothesized the stress-regulated growth in soft tissue. Later researchers studied how these factors affect the fibre architecture.

Strain – driven fibre remodelling

In [14], Driessen et. al. investigated the interrelations between collagen structure and mechanical conditions in arteries via a strain-driven law, with an algorithm introduced in [13, 15]. After applying abnormal loading (hypertension), the elastic deformation is obtained via the constitutive laws of the artery wall. Then, the principal strains are obtain. The fibres are assumed to be re-oriented to the directions of the principal strains in the current configuration as

$$\frac{\mathrm{d}\theta}{\mathrm{d}t} = k(1 - \mathbf{f}_t \cdot \mathbf{e}_p) \tag{4.1}$$

where $\mathrm{d}\theta/\mathrm{d}t$ is the rate of reorientation from fiber direction to the positive principal strain direction ($\mathbf{e}_p$), , $\mathbf{f}_t$ is the fibre orientation in the current configuration at time t.

In a time incremental Δt, with helps of rotation tensor $\mathbf{R}$, the new fibre orientation is given as

$$\mathbf{f}_{t+1} = \mathbf{R}(\Delta\theta, \mathbf{e}_r)\mathbf{f}_t,$$

where $\mathbf{R}$ is the rotation tensor based on $\Delta\theta$ and the normalized rotation axis $\mathbf{e}_r$.

After the fibre rotations by strain, the fibre is pushed back into the unloaded (and natural) configuration, according to

$$\mathbf{f}_{0,t+1} = \frac{\mathbf{F}^{-1}\mathbf{f}_{t+1}}{||\mathbf{F}^{-1}\mathbf{f}_{t+1}||}, \tag{4.2}$$

where $\mathbf{F}$ is the elastic deformation gradient from the initial reference configuration to the current configuration, $\mathbf{f}_{0,t+1}$ is the new orientation of a fibre in updated stress-free configuration.

After the fibre architecture is updated by previous process, the loaded configuration is recomputed with the same loading boundary conditions. Repeating this iterative process, the final fibre architecture is obtained till the reorientation of the fibre converge to a stable stage. Actually, ultimately, the fibre orientations will perfectly align with the directions of principal strains, which agrees with experimental observation.

Stress – driven fibre remodelling

The stress is considered as the driving force for fibre remodelling in some researches (for example, in [78]). Following this hypothesis, Hariton [31] used a thick-wall tube to simulate the fibre reorientations in an artery wall via the stress-driven approach. After applying external loading for an artery wall, the fibre is reoriented in the current configuration by a stress-driven law.

The new fibre orientations in remodelling-updated natural configuration could be obtained by the push-back algorithm similar with eq. (4.2). Then, after the boundary-value problem is solved, the fibre angles is deduced again. The final fibre structure would be obtained by repeating the iteration till the stress field in the artery is stable. The computational results show the predicted fibre structure also agrees with experimental observation.

The stress-driven law and algorithm were also applied to predict the fibre structures at the carotid bifurcation by Hariton, which also gave the reasonable results comparing with experimental data [17].

Summary

Actually, the previous stimulations mentioned in this subsection are more like the mathematical calculations to determine the optimal fibre structure when bearing the external load. The important implications include: (1) the mechanical factors could be employed to explain the remodelling in soft tissues. (2) it demonstrates that the living organs would optimize the fibre structure responding to mechanical-biological environment. (3) In an artery, the fibre structures simulated by stress-driven [31] or strain-driven [14] laws were similar and both relatively agree with experimental data. It also suggested that the stress and strain distributions were coupled or coaxial in arteries in some level.

4.1.1 G&R Process for Fibre-reinforced Tissues (from Cell Level to Tissue Level)

Fibre structure is the key feature for determining the mechanical behaviours of soft tissues. In the real bio-environment, G&R processes are really complex and are usually induced by environmental factors. In general, the fibres will be produced and removed by the fibroblasts. Besides, the existing fibre alignments will be modulated or rotated by fibroblasts as well. Many researchers have focused on what factors influence the activities of fibroblasts and how the fibroblast activities regulate the fibre structure.

Due to the features of the fibre structure, different assumptions are introduced to describe the material properties of collagen fibres: (1) the collagen fibre is considered as the 'rope' in the tissue and doesn't bear the compressive loading. For instance, Holzapfel et. al. [38], [37] used the angular integration (AI) model to describe the mechanical behaviours of the fibre structure, with a switch to properly exclude the influence of compressed fibres. Assuming the dispersed fibre structure is defined by the fibre orientation density function $\rho(\theta)$, the angle range (Σ) of stretched fibre could be determined by the fibre invariance as

$$I_4(\theta) = \mathbf{N} \cdot (\mathbf{C}\mathbf{N}) > 1 \Rightarrow \ \theta \in \Sigma \tag{4.3}$$

where $\mathbf{C}$ is the right Cauchy-Green deformation tensor, Σ is the solution for the inequity $I_4 > 1$.

For the deformation $\mathbf{C}$, the compressed fibres are excluded if $I_4 < 1$.

(2) Actually, the crosslinks between collegan fibres were experimentally observed in many researches (seeing [81]). However, the crosslinks suggested the higher fibre alignment and the interactions between fibres, while it was usually assumed that the fibre responded independently to external loading in previous studies (like [38]). By effects of fibre connections, the entire fibre structure could bear compressive loading, though the individual fibre might not take any compression.

In [49], Kroon used a new SEF to describe the mechanical behaviours of the fibre structure under compressive or tensile loading. If ignoring the crosslinks between fibres, the fibre would act like the 'rope' and don't take any compressive loading. As results, the mechanical contributions of compressed fibres should be removed ([38]). However, with helps of cross-links, the tissue will exhibit a certain stiffness in compression direction as well. Then, the SEF is introduced as

$$\Psi = \frac{k_c}{4a}\int \rho \exp(a(I_4-1)^2-1)\cdot H(I_4-1)\mathrm{d}\Omega + \frac{k_c n}{4}\int \rho(\xi_c - I_4)^2 \cdot H(\xi_c - I_4)\mathrm{d}\Omega, \qquad (4.4)$$

where Ω is the angle domain in which the orientation density function ρ is defined. Constants of k_{cn}, k_c and a are material parameters, I_4 is the stretch along fibre ($I_4 = \mathbf{f}\cdot(\mathbf{Cf})$). ξ_c is the stretch of matrix material along $\mathbf{M}$ direction ($\xi_c = \mathbf{C}:\mathbf{A}$ and $\mathbf{A} = \mathbf{FM}/|\mathbf{FM}| \otimes \mathbf{FM}/|\mathbf{FM}|$); $\mathbf{F}$ is the related elastic deformation tensor; $H(x)$ is the Heaviside step function.

The SEF (eq. 4.4) includes the contributions from fibres in tension (first term) and the matrix material with compressed fibres (second term).

Moreover, accordingly, the crosslinks and interactions between fibres could be modulated by the fibroblasts ([62]). Kroon [49] studies the remodelling process of the fibre structure, with the mentioned constitutive law of soft tissue (eq. 4.4). Results suggest that the fibre orientations and alignments are key features for soft tissues.

After re-structuring the fibre structure in the current configuration, the push-back method [31] was also employed to determine the fibre network in the reference configuration. Interestingly, the remodelling process in [49] ignored fibre degradations. For instance, after remodelling, the orientation density function ρ will be updated. Meanwhile, the overall mass of fibres is changed, which is indicated by the changing mass production rate. Besides, while the volumetric fraction of fibres was implicitly ignored in this research. However, experimentally, it is suggested that the fibroblasts could rotate and produce the fibres [62]. Later researches explore more in this field. Recently, experiments suggested that the activities of fibroblasts could be influenced by: (1) chemokine (chemical) factors; (2) the existing collagen fibre structure; (3) mechanical factors.

Living organs were exposed to the *in vivo* environment, bearing the loading all the time. If the environmental factors changed (for example, the chemical field changes around the wound in the organs), the fibre structure would be modified by the changed fibroblast activities, which in the long run would influence the material properties of the tissues. Besides, mechanical factors (like strain or stress) would be changed since the mechanical behaviours of the tissue would be different. In the life cycle, the mechanical factors will be coupled with G&R processes: the remodelling will modify the material properties of the tissues; the mechanical factors, influenced by the modifications of the material properties, will feedback to the remodelling process. These steps will repeat and subsequently affect the functional activities of living organs.

Rouillard [66] developed an agent based model to study the remodelling of infarct scar tissue and fibroblast behaviour in the complex environment of a healing infarct, by accounting for environmental factors. Here, the preferential directions of fibroblasts were determined by the combination of effects of (environmental) factors . The fibre structure will be modified by fibroblast migration along preferred direction of fibroblast cells, with fibre depositions and rotations by cells. Automatically, the material properties would be modified by assembling the fibre structure into the SEF. Then, after re-solved the boundary problems with the new SEF, the mechanical information would be updated, which will contribute to the subsequent fibre remodelling process. The whole process will be repeated until the end of healing period.

The fibre structure was predicted for the infarcted heart during the healing period, which agreed with the published experimental data in [20]. It is needed to clarify that the mechanical factors were assumed as constants in [66].

Rouillard [67] coupled the agent-based model [66] with FE method to study the evolution of fibre structure in the infarcted heart tissues, in which the altered material properties and mechanical influences were included.

In [67], the material properties were described by the modified Fung-type SEF. Then, the features of the fibre structure could be assembled into Fung-type SEF by computing the Fung-type coefficients. An algorithm was introduce to account for the contributions of every individual fibre to get the coefficients.

The fibre structure will be modified by fibroblast migration in the agent-based model, which will alter the material properties. Then, the mechanical response will be re-solved with the new fibre structure in the FE model. By coupling the agent-based model with the FE method, the evolution of both collagen fiber structure and regional deformation were studied in [67]. To this author, the obvious disadvantages in [67] are: 1) the mechanical behaviours of the stretched and compressed fibres are implicitly the same. In reality, the compressed fibres do not contribute to

the mechanical response of the tissues to external loading. 2) 2D slices of tissues are employed to simulate the G&R process of fibre-reinforced materials. And 3D model is not available. 3) The geometry of living tissues are too simple. The geometry of a real organ is complex and irregular, which makes the simulation more difficult.

4.2 Volumetric Growth of Soft Tissues

Besides the fibre remodelling in soft tissues, other important G&R effects are the mass or volumetric growth of living tissues, associated with an obvious impacts on the mechanical behaviours. To mathematically describe the volumetric or mass growth, two popular approaches have been developed: (1) the growth deformation tensor, similar to an elastic deformation tensor, is used to deform the tissue into the growth-updated configuration. In general, it is assumed that the material properties are unchanged from the initial stress-free configuration to the growth-updated natural configuration. Then, residual stress will be induced by the elastic deformation to make the incompatible configuration (after growth) into the intact (and compatible) tissues. (2) soft tissues are usually composed of different constituents; for instance, the artery walls could be decomposed into smooth muscle, collagen fibres, etc. Then, individual growth laws were used to describe the growth for each constituent. This will give individual reference configurations for each constituent. The residual stresses will come from the interactions between constituents in the compatible configuration.

The later chapters will review the key theories and developments in these two fields. Besides, another key question in the biomechanical field is what is the mechanical by driven factors that induce and regulate growth in tissues: to answer that, two hypotheses were popularly used, which were firstly proposed in [76]: (1) strain-driven law: the growth was induced by strain; (2) stress-dependent law: the stress could induce the growth. The experimental evidences and the applications of those growth driven laws will be reviewed in the coming chapters.

4.2.1 Volumetric Growth with Kinematic Approach

In [65], Rodriguez used the growth deformation gradient to describe the growth in soft tissues. The growth tensor updated the tissue into a new stress-free configuration. Then, the elastic deformation carried the tissue into a compatible configuration with an elastic deformation tensor, causing residual stress. The overall deformation, after growth and elastic deformations, could be expressed as

$$\mathbf{F} = \mathbf{F}_e \mathbf{F}_g. \tag{4.5}$$

If assuming the material properties for tissues are unchanged after growth, the Cauchy stress could be obtained from elastic deformation ($\mathbf{F}_e$) and constitutive laws of tissues.

In work of [65], only growth along principal directions was included, which ensured the rotation tensor $\mathbf{R}_g$ was $\mathbf{I}$ so that

$$\mathbf{F}_g = \mathbf{R}_g\mathbf{U}_g = \mathbf{U}_g = \mathrm{diag}(\lambda_1, \lambda_2, \lambda_3). \tag{4.6}$$

where λ_i is the stretch along ith principal direction.

To further simplify the problem, a tube model was employed in [65], which gives the elastic deformation as the diagonal tensor what is based on cylindrical coordinates as

$$\mathbf{F}_e = \mathrm{diag}(\lambda_r, \lambda_\theta, \lambda_z). \tag{4.7}$$

Then, it gives convenience for calculating the updated stress-free configuration by the overall growth tensor, from eqs. (4.8) to (4.9):

$$\mathbf{F}_{e,t_k}\mathbf{F}_{g,t_k} = \mathbf{F}_{g,t_k}\mathbf{F}_{e,t_k}, \tag{4.8}$$

$$\begin{aligned}
\mathbf{F}_{eg} &= \mathbf{F}_{e,t_n}\mathbf{F}_{g,t_n}\mathbf{F}_{e,t_{n-1}}\mathbf{F}_{g,t_{n-1}}\mathbf{F}_{e,t_{n-2}}\mathbf{F}_{g,t_{n-2}}\cdots \\
&= \underbrace{\mathbf{F}_{e,t_n}\mathbf{F}_{e,t_{n-1}}\mathbf{F}_{e,t_{n-2}}\cdots}\underbrace{\mathbf{F}_{g,t_n}\mathbf{F}_{g,t_{n-1}}\mathbf{F}_{g,t_{n-2}}\cdots} \\
&= \underbrace{\mathbf{F}_{e,t_n}\mathbf{F}_{e,t_{n-1}}\mathbf{F}_{e,t_{n-2}}}\cdots\mathbf{F}_g \\
&= \mathbf{F}_e\mathbf{F}_g,
\end{aligned} \tag{4.9}$$

where $\mathbf{F}_{e,t_k}, \mathbf{F}_{g,t_k}$ are the elastic and growth tensors at time step t_k.

This approach was used to study growth in the left ventricle under a stress-driven law ([76]. However, the commutation laws between growth and elastic tensors are not always satisfied, which state is shown by later researches (like [26]).

In [3], the decomposition (eq. 4.5) was borrowed to study mechanical stability in a spherical body after one-step growth. The nominal stress-deformation relation was derived in the (non-growth) original configuration

$$\mathbf{S} = J\frac{\partial W}{\partial \mathbf{F}_{eg}}(\mathbf{F}_e) = J\mathbf{F}_g^{-1}\frac{\partial W}{\partial \mathbf{F}_e}.(\mathbf{F}_e) \tag{4.10}$$

In a pressurized spherical shell, the symmetric growth and elastic deformations were expressed in spherical coordinates as

$$\mathbf{F}_e = \mathrm{diag}(F_{e1}, F_{e2}, F_{e3}) \quad \mathbf{F}_g = \mathrm{diag}(F_{g1}, F_{g2}, F_{g3}). \tag{4.11}$$

After applying loading, the nominal stress equilibrium is given, referring to original reference

configuration. The mechanical information could be obtained by testing the boundary conditions. The results presented different modes of bifurcation in the spherical body after growth.

The decomposition method was further explored to describe incremental growth in [26]. The elastic body deformed into the intermediate configuration ($\mathbf{F}_1 = \mathbf{A}_1\mathbf{G}_1$). If the subsequent incremental growth occurred in the intermediate configuration, the stress-free configurations before and after growth could be linked by the cumulative growth tensor $\mathbf{G}^{(2)}$. If the residual stress in $\mathscr{V}_2$ could be released by $(\mathbf{R}_2\mathbf{A}_1)^{-1}$, where $\mathbf{R}_2$ is the rotation tensor from the polar decomposition of incremental growth $\mathbf{G}_2$ ($\mathbf{G}_2 = \mathbf{V}_2\mathrm{R}_2$). This process shows that the commutation law is not always satisfied between the growth and elasticity tensors (eq. 4.13). Moreover, it suggests that the commutation law is satisfied in cases with diagonal growth and elastic tensors, which indicates that

$$\mathbf{F}_{e,t_n}\mathbf{F}_{g,t_n} = \mathbf{F}_{g,t_n}\mathbf{F}_{e,t_n} \tag{4.12}$$

For cumulative growth, the growth could be expressed as

$$\mathbf{F}_{eg} = \mathbf{F}_{e,t_n}\mathbf{F}_{g,t_n}\mathbf{F}_{e,t_{n-1}}\mathbf{F}_{g,t_{n-1}}\mathbf{F}_{e,t_{n-2}}\mathbf{F}_{g,t_{n-2}}\cdots \tag{4.13}$$

Applying eq. (4.12), last equation could be rearranged as

$$\begin{aligned}\mathbf{F}_{eg} &= \mathbf{F}_{e,t_n}\mathbf{F}_{e,t_{n-1}}\mathbf{F}_{e,t_{n-2}}\cdots\mathbf{F}_{g,t_n}\mathbf{F}_{g,t_{n-1}}\mathbf{F}_{g,t_{n-2}}\cdots \\ &= \mathbf{F}_e\mathbf{F}_g,\end{aligned} \tag{4.14}$$

where

$$\mathbf{F}_e = \mathbf{F}_{e,t_n}\mathbf{F}_{e,t_{n-1}}\mathbf{F}_{e,t_{n-2}}\cdots\mathbf{F}_{e,t_1}, \tag{4.15}$$

$$\mathbf{F}_g = \mathbf{F}_{g,t_n}\mathbf{F}_{g,t_{n-1}}\mathbf{F}_{g,t_{n-2}}\cdots\mathbf{F}_{g,t_1}, \tag{4.16}$$

To this author, one assumption in previous derivations looks problematic. Referring to the previous explanation, the residual strain could be released by $(\mathbf{R}_2\mathbf{A}_1)^{-1}$. The elastic deformation ($\mathbf{A}_1$) is from the stress-free configuration $\mathscr{V}_1$ to $\mathscr{B}_1$. However, to calculate the residual stress in $\mathscr{V}_2$, the elastic deformation could be obtained from the undated stress-free configuration $\mathscr{V}^{(2)}$ to $\mathscr{V}_2$. Since the stress state and the reference configuration are different, the new elastic deformation $\mathbf{A}_2$ should depend on the boundary condition in $\mathscr{V}_2$ and reference configuration $\mathscr{V}_2$, while it should be independent of $\mathbf{A}_1$. In other words,

$$\mathbf{A}_2' \neq \mathbf{R}_2\mathbf{A}_1, \tag{4.17}$$

where $\mathbf{A}_2'$ is the deformation tensor from $\mathscr{V}^{(2)}$ to $\mathscr{V}_2$.

In previous studies ([3] and [26]), the growth is employed as a constant deformation tensor independent of external factors. However, in reality, growth is regulated by environmental factors, like chemical, mechanical or genetic factors. If focusing on mechanics, it is necessary to answer how the mechanical factors influence the growth. Two driven factors are proposed by Taber: (1) strain-driven law: the longitudinal growth was induced by strain, while stress induces transverse growth. For instance, skeletal muscles were observed to grow in the directions orthogonal to the primary stress [76]. This strain-driven law was employed by by Taber [74] to mechanically model the growth of a developing embryo heart.

(2) active stress-dependent law: the active stress could induce the transverse growth. For instance, in [76], the stress-driven law was employed as

$$\frac{\dot{\lambda}_{gr}}{\lambda_{gr}} = b_r(\sigma_\theta - \sigma_0), \tag{4.18}$$

where b_r is the growth constant, λ_{gr} is the growth stretch along radial direction, σ_θ is the component of Cauchy stress along circumferential direction (orthogonal to radial direction), σ_0 is the critical value.

In some works, the stress and strain driven laws are combined to study growth induced by mechanical information, for example, Taber [76] used the growth laws as

$$\frac{\dot{\lambda}_{g\theta}}{\lambda_{g\theta}} = b_\theta(\sigma_\theta - \sigma_0) - b_\lambda(\lambda_\theta - \lambda_0),$$

where b_θ, b_λ are the growth constants, $\lambda_{\theta g}, \lambda_\theta$ are the growth and elastic stretches along circumferential direction, and σ_θ is the stress along circumferential direction.

Kerchkoffs [46] used the strain-driven laws to model cardiac growth during the post-natal. In that work, the multiplicative decomposition was employed between growth and elastic deformation tensors (eq. (4.5) from [65]). Experimental evidence suggests that the growth of the heart increased the cardiac sarcomere length and diameter. Therefore, for any growth step, the growth tensor was defined as

$$\mathbf{F}_{g,i} = \begin{bmatrix} F_{g,i,rr} & 0 & 0 \\ 0 & F_{g,i,ff} & 0 \\ 0 & 0 & F_{g,i,cc}, \end{bmatrix} \tag{4.19}$$

where $F_{g,i,ff}$ is the growth along (sarcomeres) fibre direction, $F_{g,i,cc}, F_{g,i,rr}$ are the growth along cross-fibre directions.

The strain-driven laws were defined similarly to laws in [76], as

$$F_{g,i,ff} = (b_f(E_{ff} - E_{ff,set})\Delta t + 1), \tag{4.20}$$

$$F_{g,i,cc} = (b_f(E_{cc} - E_{cc,set})\Delta t + 1), \tag{4.21}$$

$$F_{g,i,rr} = F_{g,i,cc}, \tag{4.22}$$

where E_{ii} is the component of Eulerian strain tensor, and $E_{ii,set}$ is the threshold strain. Then, the cumulative growth could be obtained as

$$\mathbf{F}_g^n = \prod_{i=1}^{n} \mathbf{F}_{g,i}. \tag{4.23}$$

For the LV, the mechanical factors (such as strain) could be solved after setting boundary conditions and material properties for the heart tissues in the FE method. Then, the local growth would be induced following growth laws. After the geometric information of the LV is updated by the growth, the mechanical information would be resolved and induce new growth. By repeating this process, the long-term growth could be simulated.

However, one defect of the previous growth laws is that they might allow the 'unbounded' growth. For instance, in eq. (4.20), if the magnitude of fibre strain (E_{ff}) is significantly large, it will induce the 'large' growth step. However, this is almost impossible in real living organs. In [47], the growth laws are modified to exclude the 'unbounded' growth, as

$$F_{g,i,ff} = \begin{cases} k_{ff} \frac{f_{ff,max}\Delta t_{growth}}{1+exp(-f_f(s_l - s_{l,50}))} + 1, & s_l > 0 \\ \frac{-f_{ff,max}\Delta t_{growth}}{1+exp(f_f(s_l + s_{l,50}))} + 1, & s_l < 0, \end{cases} \tag{4.24}$$

$$F_{g,i,cc} = \begin{cases} \sqrt{k_{cc} \frac{f_{cc,max}\Delta t_{growth}}{1+exp(-c_f(s_t - s_{t,50}))} + 1}, & s_l > 0 \\ \sqrt{\frac{-f_{ff,max}\Delta t_{growth}}{1+exp(c_f(s_t + s_{t,50}))} + 1}, & s_l < 0, \end{cases} \tag{4.25}$$

where f_f, c_f are growth constants, and s_i is the growth stimulus defined as

$$s_l = max(E_{ff}) - E_{ff,set}, \; s_c = min(E_{cc,max}) - E_{cc,set}. \tag{4.26}$$

Referring to eq. (4.25), the growth rate is actually bounded with upper limit value. For instance, recalling eq. (4.25),

$$\lim_{s_l = \infty} F_{g,i,ff} = k_{ff} f_{ff,max} \Delta t_{growth} + 1.$$

By applying this growth law, the heart growth was studied under pressure and volumetric overloads.

In [25], different growth laws were employed to study pathological and physiological growth processes in the heart: it is assumed the driven factors are different for wall-thickening (stress-driven) and ventricular dilation (strain-driven).

The adaptation in an athlete's heart gives the increased heart pressure and volume. The stress-driven growth law for the heart is given as

$$\mathbf{F}^g = \upsilon^g \mathbf{I}, \tag{4.27}$$

where υ^g is the growth multiplier which is determined by

$$\upsilon^g = k^g(\upsilon^g) \cdot \phi^g(\dot{\mathbf{M}}^e) \begin{cases} k^g = \frac{1}{\tau}(\frac{\tau^{max}-\tau^g}{\tau^{max}-1})^\gamma \\ \phi^g = tr(\mathbf{M}^e) - M^{e\ \text{crit}}, \end{cases} \tag{4.28}$$

where τ, γ are the growth constants, $\mathbf{M}^e$ is the the Mandel stress ($\mathbf{M}^e = \mathbf{C}^e\mathbf{P}^e$) and $M^{e\ \text{crit}}$ is the criteria value.

This growth law induced isotropic cardiomyocyte growth, which increased the volume and wall thickness of the LV.

The experimental observations suggest a transversely-isotropic growth during cardiac dilation. The strain-driven growth law was defined as

$$\mathbf{F}^g = \mathbf{I} + (\upsilon^g - 1)\mathbf{f}_0 \otimes \mathbf{f}_0, \tag{4.29}$$

where $\mathbf{f}_0$ is the unit vector along the (sarcomere) fibre direction in the (fixed) reference configuration. ϕ^g is the growth multiplier which is determined by

$$\dot{\upsilon}^g = k^g(\upsilon^g) \cdot \phi^g(\dot{\mathbf{F}}^e) \begin{cases} k^g = \frac{1}{\tau}(\frac{\tau^{max}-\tau^g}{\tau^{max}-1})^\gamma \\ \phi^g = tr(\mathbf{M}^e) - M^{e\ crit}, \end{cases} \tag{4.30}$$

where τ, γ are the growth constants.

This growth law induced transversely-isotropic growth which increased the volume of the LV with constant wall thickness.

The experimental observations also suggest a transmural growth of heart muscle under pressure overload. The stress-driven growth law was defined as

$$\mathbf{F}^g = \mathbf{I} + (\upsilon^g - 1)\mathbf{s}_0 \otimes \mathbf{s}_0, \tag{4.31}$$

where $\mathbf{s}_0$ is the unit vector orthotropic to the (sarcomere) fibre direction in the (fixed) reference configuration, ϕ^g is the growth multiplier which is determined by

$$\upsilon^g = k^g(\upsilon^g) \cdot \phi^g(\dot{\mathbf{M}}^e) \begin{cases} k^g = \frac{1}{\tau}(\frac{\tau^{max}-\tau^g}{\tau^{max}-1})^\gamma \\ \phi^g = tr(\mathbf{M}^e) - M^{e\ crit} \end{cases} \tag{4.32}$$

where τ, γ are the growth constants.

This listed growth law induced the growth which increased the wall thickness of LV with constant cavity size.

The smallest functional unit of a cardiac cell is a sarcomere, which structures the cardiomyocyte. Responding to volume-overload, the sarcomeres would be added in series to increase the cardiomyocyte length. If under pressure-overload, the sarcomeres would be added in parallel to increase the myocyte cross-section. A multiscale model [48] was developed to study the cardiac growth which are the results of sarcomere additions. The growth is similar to the growth in [25], but at the sarcomere level [48]. Referring to the experimental observations [80], the overall volume of the heart tissue remains constant after the heart infarction. Therefore, the isochoric growth tensor ($J(\mathbf{F}^g) = 1$) was used to describe the growth of healthy tissue as

$$\mathbf{F}^g = \upsilon^g \mathbf{f}_0 \otimes \mathbf{f}_0 + \frac{1}{\sqrt{\upsilon^g}}(\mathbf{I} - \mathbf{f}_0 \otimes \mathbf{f}_0), \tag{4.33}$$

The stress-driven growth law was similar to eq. (4.32) for the healthy tissues, while the infarcted tissues are assumed to be ingrown. The growth is simulated for the patient-specific LV.

Alternatively, Kroon [50] used a 'updated reference' method to determine the new stress-free configuration and to calculate the successive mechanical behaviours of living organs after incremental growth.

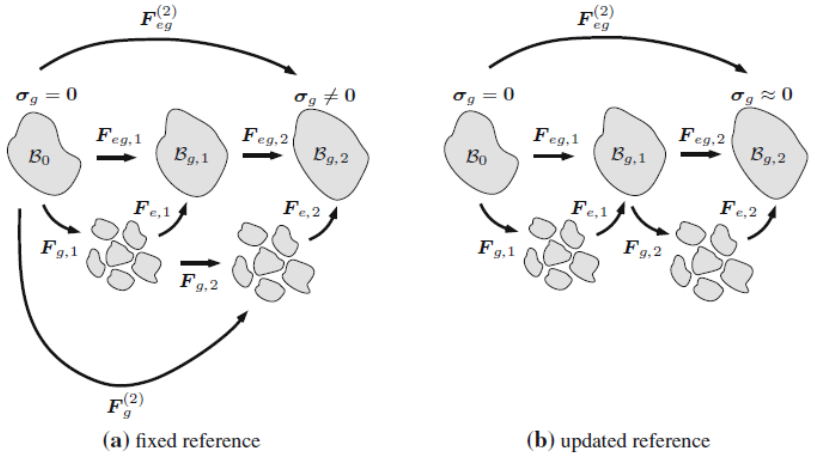

FIGURE 4.1: Configurations during the incremental growth: left, $\mathscr{B}_0$ is used as the fixed reference, the incremental growth ($\mathbf{F}_{g,i}$) updates the virtual stress-free configuration; right, the updated current configuration ($\mathscr{B}_{g,2}$) is used as the stress-free one, where Cauchy stress is small ($\boldsymbol{\sigma}_g \approx 0$).

In [50], the approach to determine the stress free configuration by cumulative growth is named as the 'fixed reference'. Here, the incremental growth is assumed to occur in the initial 'stress-free' configuration, while the growth-elastic mixed deformation connects to the new compatible

configuration. For instance, in fig. 4.1 (left), the incremental growth occurs in the loaded configuration $\mathscr{B}_{g,1}$, which simultaneously induces the elastic deformation to make the soft body compatible. Therefore, the growth-elastic mixed deformation ($\mathbf{F}_{eg,2}$) connects two compatible configurations $\mathscr{B}_{g,1}$ and $\mathscr{B}_{g,2}$. The real (or pure) incremental growth is assumed to occur in the previous stress-free configuration and connects to the new stress-free configuration. Finally, the new stress-free configuration could be obtained by cumulative growth $\mathbf{F}_n^{(2)}$ related to the initial configuration $\mathscr{B}_0$.

This 'updated-reference' approach links the new stress-free configuration with the stressed configuration via pure incremental growth. In this approach, the internal stresses are assumed to be fully relaxed by the growth (or turnover), or saying, the incremental growth directly connects to the new stress-free configuration. For instance, in fig. 4.1 (right), the incremental growth occurs in the loaded configuration $\mathscr{B}_{g,1}$. If the growth could relax all internal stress, the new stress-free configuration could be determined by the growth increment $\mathbf{F}_{g,2}$.

In summary, the listed researches usually assumed the incremental growth occurs in the reference (stress-free) configuration. It is mathematically convenient to obtain the new stress free configuration and the stress distributions after growth. For instance, the cumulative growth tensor could be obtained directly from previous incremental growth (eq. (4.23)), while the stress free configuration could be identified simultaneously by a cumulative growth tensor. However, the growth generally occurs in the current or residually-stressed configuration. The existence of the residual stress might inspire researchers to develop new approaches to calculate the cumulative growth tensor and give different stress-free configurations.

The decomposition of growth and the elastic deformation have been been used in previous researches. In most studies, pure growth is assumed to occur in a stress-free configuration, which is mathematical convenient to determine the updated stress-free configuration. However, in living organs, the residual stress usually exists and will influence the successive growth and remodelling process. Since growth occurs in the (residually) stressed configuration, the approach to determine the updated stress-free configuration should include the effects of residual stress on the stress states after growth. Recently, some researches started to focus on the influences of residual stress on mechanical behaviours of soft tissues after growth. However, the understanding is still relatively poor, in the perspective of nonlinear elastic theories.

4.2.2 Mass Growth

The 'volumetric growth' approach was used to describe the growth when the volume increases in soft tissues; and the related works have been reviewed in the last subsection. Some researches used the 'mass growth' approach to describe the growth and remodelling process in living organ.

Baek [4] used the 'constrained mixture model' to study the growth of the aneurysms, which model was initially developed by Humphrey [44]. The living organs are usually composed of different constituents which continuously turnover during the life cycle. For an individual constituent, the material or micro-structures are also turning over. For instance, the arteries are composited by three key materials: smooth muscle, collagen and elastin; and the collagen is continuously deposited and removed by fibroblast cells. Referring to nonlinear deformation theories, the elastic states should be obtained by calculating the elastic deformation of arteries, referring to the reference configurations of each constituent during turnover.

In the constrained mixture model, the reference (natural) configurations are different for old and new material even for the same constituents. In [4], it is only turnover (growth and remodelling) of collagen fibres in arteries is considered and the turnovers of elastin and muscle are ignored. The newly-produced collagen (kth constituent of arteries) could be assembled into the loaded configuration ($\mathscr{K}_\tau$) of artery from its own stress-free configuration $\mathscr{K}_n^k(\tau)$ at time t. If the prestretch of new collagen was defined as a constant $\mathbf{G}^k(\tau)$, the total elastic deformation here is

$$\mathbf{F}^k_{n(\tau)}(t) = \mathbf{F}(t)\mathbf{F}^{-1}(\tau)\mathbf{G}^k(\tau), \tag{4.34}$$

where $\mathbf{F}(t)$, $\mathbf{F}(\tau)$ are the deformation tensors connected with subsequent configurations at time t and τ from a universal reference configuration.

The total mass for individual constituent k was changed due to the local production and removal of material, as

$$M^k(t) = M^k(0)Q^k(t) + \int^t m^k(\tau)q^k(t-\tau)\mathrm{d}\tau, \tag{4.35}$$

where $Q^k(t)$ and $q^k(t)$ are the survival rates of constituents, m^k is the rate of production, M^k is the initial mass for constituent k. It is assumed that the density is constant for each individual constituent, which means the mass changes of the constituents are proportional to the volumetric changes.

The overall strain energy per unit volume could be obtained by

$$w^k(t) = \frac{M^k(0)}{\rho^k}Q^k(t)W^k(\mathbf{F}_t) + \int^t \frac{m^k(\tau)}{\rho^k}q(t-\tau)W^k(\mathbf{F}^k_{n(\tau)})\mathrm{d}\tau. \tag{4.36}$$

Then, the total strain energy per reference volume could be expressed

$$W(t) = \sum_k w^k(t). \tag{4.37}$$

Then, Cauchy stress could be obtained from the SEF related with time-dependent mass fractions of the constituents. After solving the stress states for the boundary value problem with the helps

of the SEF (eq. 4.37), the collagen production could be obtain via a stress-driven G&R as

$$m^k(t) = M(t)(K_g(\sigma^k(t) - 1) + m_h^k), \tag{4.38}$$

where K_g is the growth parameter, m_h^k is the homeostatic value of mass for constituent k, $M(t)$ is the total mass at time t.

In [4], this approach was employed to study a developing aneurysm, in which the changed constituent is collagen only.

As mentioned, the artery wall is composed of three key constituents: smooth muscle, collagen and elastin. In [2], the constrained mixture model is used to analysis the growth and remodelling in an artery wall, while G&R processes occurred in all the key constituents. For elastin, the experimental observations [11] suggests the turnovers of elastic are negligible. Then, the additional stretch λ is assumed as 1 after turnover (no growth or remodelling). For collagen, the stress-driven turning over is similar to that in [4] (eq. (4.38)). For smooth muscle, the used growth laws indicates 1) the stress-driven growth of muscle along the radial direction, and 2) the circumferential growth is induced by both strain and stress factors. By assembling the growth laws into the SEF of an artery wall (eq. (4.37)), the SEF is obtained to describe the mechanical behaviours of the artery under the framework of constrained mixture growth approach. In [2], the stress state could be obtained to solve the boundary problems for a thick-wall artery tube model. Coupling with the constrained mixture growth for artery constituents, the growth and remodelling process is simulated for artery.

In previous researches from the Humphrey group ([4], [2]), the loads on living organs were used as static and constant forces applied on the inner surface of the artery wall. Actually, the loading and boundary conditions are dynamic and more complex than the constant loads, which are induced by the interactions between the fluid (blood) and solid (artery walls) during life cycle. By coupling the constrained mixture model with the fluid-solid interaction model, the fluid-solid-growth is developed to study the cardiovascular growth and remodelling during the cardiac cycle.

Applying the traction and stress continuity conditions at the fluid-solid interface, stress equilibrium equations are solved for both the fluid and solid domains. Then, combined with the constrained mixture model, the growth and remodelling process could be computed for the cardiovascular vessel under fluid-solid-interaction conditions.

Most previous researches used the constrained mixture model, in which the studied cases are relatively too simple in some sense: for example, using the thick-wall tube model describing the mechanical behaviors of artery. However, from that clinical view, the problems are more

complex and challenging, which includes the hypodynamic or irregular geometry of the heart and the boundary conditions. Valentin [84] implemented the constrained mixture model into a FE model to simulate the growth and remodelling of an artery with a multilayer structure.

The evolution of the mechanical behaviours and growth in different artery layers were simulated, which is a more-general tool to analyze the complex boundary problem associated with patient-specific geometries ([4, 43]).

Watton [92, 94] also employed different configurations to describe the growth and remodelling in different constituents of living organs. In [94], the artery wall is assumed to be composed of two constituents: extracellular matrix (ECM) and collagen. For ECM, the degradation of elastin is fitted from experimental data.

For collagen: 1) all collagen fibres will be deposited into the recruitment configuration with different recruitment stretches. Recruitment stretch, firstly introduced in [93], is to describe the onset stretch of recruitment of fibres to bear loads. 2) the strain-driven growth law of collagen could be also obtained from experimental data as

$$\frac{dm^C}{dt} = (\xi_1 m^C + \xi_2 |\frac{dm^E}{dt}|)(E^C - E^C_{AT}) \tag{4.39}$$

where ξ_i is the remodelling constant.

By coupling the remodelling-growth laws and the SEF, the evolution of remodelling and the mechanical behaviours are obtained by solving the boundary problem for the thick-wall artery model. However, to author, the remodelling-growth framework is only suitable for limited cases, and is not satisfactory for solving general problems. For instance, it is assumed all collagen fibres are deposited in the fixed recruitment configuration. However, the fibres, deposited by fibroblast cells, are usually produced in the current configuration, while cells don't 'know' the recruitment configuration. Besides, from the mechanical perspective, the SEF used in [94] is defined for per volume for artery tissues (eq. (4.40)). Then, the sum of weights from the constituents (collagen and ECM) should be one, which guarantees the SEF for tissues is always defined for unit volume as

$$m^C + m^E \equiv 1.$$

However, the volumetric fractions of constituents are independently regulated by their own remodelling-growth laws. If $m^C + m^E \neq 1$, the SEF might not give the proper stress-strain relation. Moreover, other limitations are also included in that framework.

The different formulations of artery wall were experimentally observed ([69]): for an individual constituent, the material density remains constant during life, which is named as 'constant

individual density' (CID). If the material density is changing, it is called 'adaptive individual density' (AID). Eriksson [16] modified the remodelling-growth laws (eq. 4.39) and the SEF with the material density factors to describe the mechanical behaviours of an artery and applied them in the FE method. The SEF is modified as

$$\Psi = \hat{\rho}_e \hat{\Psi}^E + \hat{\rho}_C \hat{\Psi}^C, \tag{4.40}$$

where $\hat{\rho}_e, \hat{\rho}_C$ are density factors for elastin and collagen.

If the density ρ_ξ is constant for constituent ξ (CID), the density factor at time τ is expressed as

$$\hat{\rho}_\xi(\tau) = \frac{\rho_\xi(\tau)}{\rho_\xi(\tau_0)} = \frac{\hat{v}_\xi(\tau)}{\hat{v}(\tau)} \tag{4.41}$$

where $\hat{v}_\xi(\tau)$ is the volumetric factor of constituent ξ, $\hat{v}(\tau)$ is the volumetric fraction of tissue.

If the density ρ_ξ is adaptive for constituent ξ (AID), the density factor at time τ is expressed as

$$\hat{\rho}_\xi(\tau) = \frac{\rho_\xi(\tau)}{\rho_\xi(\tau_0)} = \hat{\rho}_\xi 0(\tau) \frac{\hat{v}_\xi(\tau)}{\hat{v}(\tau)}, \tag{4.42}$$

where $\hat{\rho}_\xi(\tau)$ is the individual (unnormalized) density.

Combining with the growth laws of collagen and elastin, the SEF is obtained for artery tissues during the remodelling-growth process. This framework is assembled into the FE method to simulate the evolution of the artery structure during the life cycle with different growth patterns (CID or AID).

Volokh [86] used a phenomenological theory of tissue growth and develop a toy-like model to describe tumor growth. In [86], the growth is explained as: considering a regular initial tissue, the new tissue elementary components (cells, molecules) are supplied, which is seen as a result of injection. And it could be constructed physically into a model of tissue growth. In this model, the stress-strain relation is redefined as

$$\mathbf{P} = \mathbf{F}(\partial W / \partial \mathbf{E} - (\rho - \rho_0)\boldsymbol{\eta}), \tag{4.43}$$

where W is the SEF for non-growing tissue, $\mathbf{P}$ is the first Piola-Kirchohoff stress, $\boldsymbol{\eta}$ is the grown moduli tensor, which is related to the tissue growth and independent from mechanical factors.

This growth law is obviously different from other researches ([2], [4]). In [86], the tumor is simulated as a multi-layer spheroid. The simulation of tumor growth agreed with in vitro experimental observation.

4.3 Summary and Theoretical Gaps

Understanding of G&R is obviously improved in previous researches. The fibre remodelling is simulated with different regulators. It is analytically demonstrated that the fibre structure is optimized to bear the external loading. However, the limitations are also obvious in those works. To this author, the most important problem is: in real living tissues, the fibre turnover usually includes two key processes: the fibre deposition and re-orientation. In most of researches, the remodelling is decoupled from volumetric growth. Then, if the fibre is deposited in the current configuration, the push-back method is employed to obtain the fibre structure in the stress free configuration, i.e.

$$\mathbf{f}_0' = \mathbf{F}_e^{-1}\mathbf{f},$$

where $\mathbf{f}_0', \mathbf{f}$ are fibre vectors in stress free and loaded configurations.

However, if the tissues experience both turnover of the fibres and volumetric growth, the method is more complex to obtain the fibre structure in the stress-free configuration. In general, if the fibre rotation and volumetric growth occur in the current configuration, the fibre structure should be carried into the grown configuration according to

$$\mathbf{f}' = \mathbf{G}\mathbf{f},$$

where $\mathbf{f}', \mathbf{f}$ are the fibre vectors in loaded and grown configurations.

After the previous step, assuming the updated stress-free configuration could be obtained by fully releasing the residual stress, the fibre vector is updated as

$$\mathbf{f}_0' = \mathbf{F}_\tau^{-1}\mathbf{f},$$

where $\mathbf{f}_0'$ is the fibre vector in the updated stress-free configuration, and $\mathbf{F}_\tau$ is the elastic deformation tensor connecting the updated stress-free and residually-stress configurations.

The coupled remodelling and volumetric model for the fibre structure is really needed for determining the evolution of the fibre structure and the material properties.

Another theoretical gap is: For the volumetric growth, currently, it is assumed that the growth occurs in the stress-free or unloaded configuration, which is computationally convenient. However, in real organs, the stress is always existing which condition requires to assuming the growth occurs in the stressed configuration. Then, the material properties will obviously differ from the tissue with growth in stress-free configuration. In some works, the importance of investigating the growth in stressed configuration is addressed. However, in those researches, the framework is not given to properly compute the growth. It is important for investigating the influence of

growth on the mechanical behaviours, which is fundamental for really understanding the mechanisms of G&R in living organs.

From a general perspective mechanics to investigate the G&R process in living tissues, the questions are: How does the residual stress influence the fibre remodelling and the material properties of entire organs? How to determine the combined effects of growth (in the stressed configuration) and remodelling on the fibre structure? How to develop a framework for investigating G&R processes occurring in the stressed configuration?

Chapter 5

Residual Stress from Multi-cut Opening Angle Models of the Left Ventricle

5.1 Introduction

Living tissues in the heart continuously interact with the external bio-environment, reshape and rearrange their constituents under chemical, mechanical or genetic stimuli during their life cycles. In the mature period, these processes remain in a homeostatic state. However, heart diseases will disrupt the balance, and the tissues will grow and remodel in response to an insult. Physiologically, exercise may also induce healthy and reversible growth and remodelling. An important ingredient in evaluating the mechanics involved in the cardiovascular system is knowledge of the solid mechanical properties of the soft tissues involved, including the components of the heart (such as the left ventricle). A particular aspect is that the soft tissues possess residual stress in vivo, so that when the external loading is removed, residual stresses remain in the material. However, residual stresses, which are generally considered to result from growth and remodelling, are imprecisely characterized (experimentally) at present, and how best to include the important effect of residual stress in cardiovascular applications therefore presents a modelling challenge.

Over the last century [40], various hypotheses on the growth and remodelling response to mechanical loading have been put forward, with particular success in arteries. Traditionally, one of the fundamental ideas is to assume the existence of a (stress-free) reference configuration [57], which coincides with the unloaded configuration. In the present context, however, the unloaded configuration is not stress free, but is residually stressed. The residual stress can be estimated using the so-called *opening angle* method [8, 52], in which an opening angle indicative of the

extent of the residual stress can be measured after a single radial cut of an unloaded arterial ring. Using the opened configuration as the reference configuration, the residual stress of a cylindrical artery model can be estimated[8, 77]. This methodology has been extended to multiple cuts by Taber and Humphrey [78], and used in the two-layered arterial models by Holzapfel et al. [34].

Residual stress is important in modelling the mechanics of soft tissues for a number of reasons: (a) in nonlinear elasticity theory the stress state in the reference configuration has a substantial effect on the subsequent response to the loads, and omission of the residual stress leads to significantly different total stress predictions [55], for example, the stress distribution in mice heart is simulated under hear pressure [90]. The estimation of maximal principal stress increased about 40% after introducing the residual stress; (b) in biological tissues, the residual stress is a result of growth [54]; (c) while the detailed process of local growth is difficult to measure, residual stress, on the other hand, may be estimated from experiments, as demonstrated by the opening angle measurement. Thus, a properly estimated residual stress at particular time instants could provide useful information about the growth history of living tissues.

However, work that includes residual stress in complex organs, such as the heart, remains rare. A few existing models for the left ventricle that take account of residual stress are based on the assumption that a simple radial cut can release all the residual stresses [90], but this assumption is not supported by all experiments. For example, Omens *et al.* [59] showed that residual stress in a mouse primary heart can be further released by a circumferential cut following the initial radial cut, as illustrated in fig. 5.1. This implies that the single cut opening angle configuration does not correspond to the stress-free configuration.

Inspired by the experiments [59], in this chapter, we develop multi-cut models in order to estimate the residual stress distribution across the wall of an intact mature heart based on a simplified heart model.

5.2 Methodology

For the material model of incompressible heart tissues, we use a reduced version of the invariant-based constitutive law for the myocardium developed by Holzapfel and Ogden [35], subsequently referred to as the HO model, namely

$$\Psi = \Psi_{\mathrm{m}} + \Psi_{\mathrm{f}}, \tag{5.1}$$

where

$$\Psi_{\mathrm{m}} = \frac{a}{2b}\{\exp[b(I_1-3)]-1\}, \quad \Psi_{\mathrm{f}} = \frac{a_{\mathrm{f}}}{2b_{\mathrm{f}}}\{\exp[b_{\mathrm{f}}(I_4-1)^2]-1\}, \tag{5.2}$$

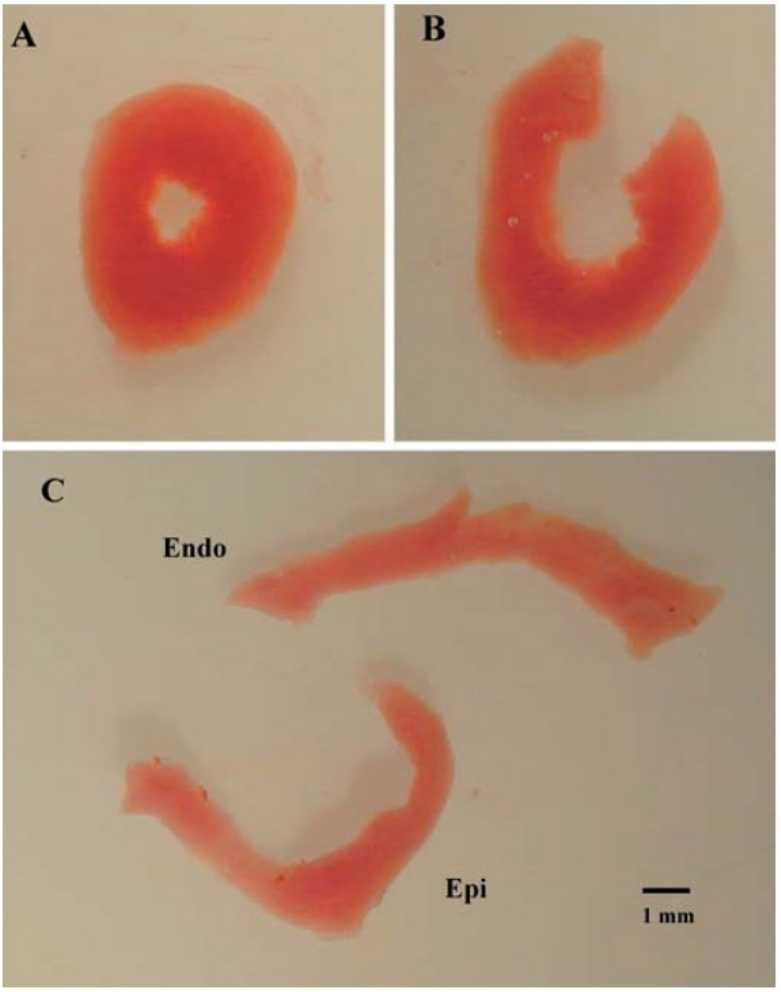

FIGURE 5.1: A typical short-axis apical segment of a mouse heart before and after cuts [59]. The initial intact segment, shown in A, was about 2 mm thick. The same segment after a single radial cut and a further circumferential cut is shown in B and C, respectively. In particular, the endocardial segment has reversed its curvature, in C. Notice that the definition of opening angle in [59] follows that in Fung, [8] which is different from that is used in the present paper.

$a, b, a_{\mathrm{f}}, b_{\mathrm{f}}$ are material constants, and

$$I_1 = \mathrm{tr}\mathbf{C}, \quad I_4 = \mathbf{f}_0 \cdot (\mathbf{C}\mathbf{f}_0), \tag{5.3}$$

I_1 and I_4 being the invariants corresponding to the matrix and fibre structure of the myocardium, $\mathbf{I}$ the identity tensor, $\mathbf{C} = \mathbf{F}^{\mathrm{T}}\mathbf{F}$, $\mathbf{F}$ the deformation gradient tensor, $\mathbf{f}_0$ a unit vector along the fibre direction in the stress-free reference configuration. In this paper, the heart is considered as thick–wall cylindrical tube, while the coordinate bases $\{\mathbf{e}_r, \mathbf{e}_\theta, \mathbf{e}_z\}$ are corresponding to local radial, circumferential and longitudinal directions. Then, collagen fibres distributed in local 'circumferential–longitudinal' plane, described by fibre vector $\mathbf{f}_0$ with components $(0, \cos\gamma, \sin\gamma)$. γ is the angle between the fibre and circumferential directions. The fibre 'switch' is not considered in this chapter, since the fibres are always extended after applying pressure on

the internal wall of LV.

The Cauchy stress tensor is then

$$\boldsymbol{\sigma} = -p\mathbf{I} + 2\frac{\partial \Psi_{\mathrm{m}}}{\partial I_1}\mathbf{B} + 2\frac{\partial \Psi_{\mathrm{f}}}{\partial I_4}\mathbf{f}\otimes\mathbf{f}, \tag{5.4}$$

where $\mathbf{B} = \mathbf{F}\mathbf{F}^{\mathrm{T}}$ is the left Cauchy–Green deformation tensor, and $\mathbf{f} = \mathbf{F}\cdot\mathbf{f}_0$ is the stretched fibre vector in the deformed configuration. Note that we only employ one family of fibres since only circumferential and axial tests on mice primary hearts were reported in [59]. Based on the experimental observation of the fibre structure of the heart, in [90], it was assumed that the fibre orientation rotates linearly across the transmural (radial) direction in the intact-heart configuration (i.e. $\mathscr{B}_3$ in fig. 5.2) from $-\pi/3$ at the endocardial surface to $\pi/3$ at the epicardial surface, the angle γ is measured relative to the circumferential direction in the $(\mathbf{e}_\theta, \mathbf{e}_z)$ plane. The pre-image of the deformed fibre vector $\mathbf{f}$ in the reference configuration is

$$\mathbf{f}_0 = \frac{\mathbf{F}^{-1}\mathbf{f}}{|\mathbf{F}^{-1}\mathbf{f}|}. \tag{5.5}$$

5.2.1 1-Cut Model

For simplicity, we model the left ventricle (LV) as an incompressible single-layered cylindrical tube. We use different models based on a different number of cuts and assume that the residual stress in the unloaded tube can be released by either a single (radial) cut or multiple cuts (a radial cut followed by one or three circumferential cuts). We also assume that all the cut segments retain their cylindrical configurations, each with its own opening angle.

For the single cut model, this approach has been well described [34], but is briefly summarized here for completeness. Let the geometry of the right-hand panel in fig. 5.2 represent a stress-free configuration $\mathscr{B}_2$, which can be described by cylindrical polar coordinates $\{R, \Theta, Z\}$ as

$$R^{(\mathrm{i})} \leqslant R \leqslant R^{(\mathrm{o})}, \quad \frac{\alpha_2}{2} \leqslant \Theta \leqslant (2\pi - \frac{\alpha_2}{2}), \quad 0 \leqslant Z \leqslant L, \tag{5.6}$$

where $R^{(\mathrm{i})}$, $R^{(\mathrm{o})}$, and L denote the inner and outer radii, and the tube length, respectively, and α_2 is the opening angle.

The isochoric deformation from $\mathscr{B}_2$ to the intact configuration $\mathscr{B}_3$ is then expressed as

$$\mathbf{x} = r\mathbf{e}_r + z\mathbf{e}_z. \tag{5.7}$$

Material incompressibility gives

$$r = \sqrt{\frac{R^2 - {R^{(\mathrm{i})}}^2}{k\lambda_z^{(3)}} + {r^{(\mathrm{i})}}^2}, \quad \theta = k(\Theta - \alpha_2/2), \quad z = \lambda_z^{(3)} Z, \tag{5.8}$$

where $r^{(\mathrm{i})}$ is the inner radius in the configuration $\mathscr{B}_3$, $\lambda_z^{(3)} = l/L$ is the constant axial stretch, where l is the cylinder length in $\mathscr{B}_3$, while $k = 2\pi/(2\pi - \alpha_2)$ is a measure of the opening angle in $\mathscr{B}_2$. The outer radius in $\mathscr{B}_3$ is

$$r^{(\mathrm{o})} = \sqrt{\frac{{R^{(\mathrm{o})}}^2 - {R^{(\mathrm{i})}}^2}{k\lambda_z^{(3)}} + {r^{(\mathrm{i})}}^2}. \tag{5.9}$$

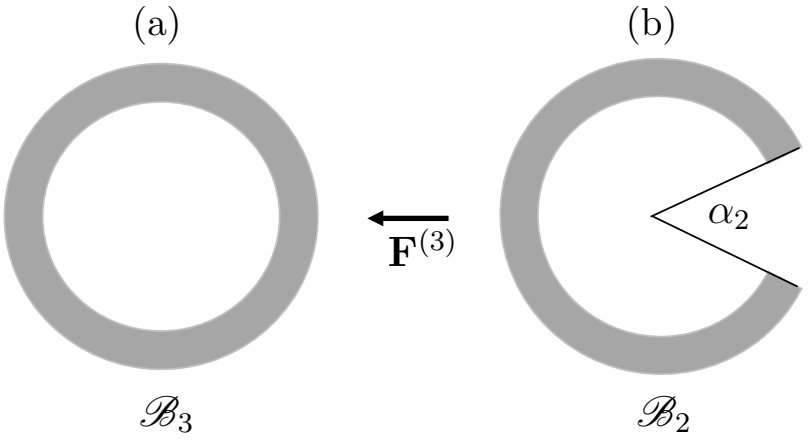

FIGURE 5.2: 1-cut model: cylindrical model of the LV after a single radial cut of the intact unloaded configuration $\mathscr{B}_3$ into a stress-free sector $\mathscr{B}_2$.

The corresponding deformation gradient (from $\mathscr{B}_2$ to the intact ring configuration $\mathscr{B}_3$), denoted $\mathbf{F}^{(3)}$, is given by

$$\mathbf{F}^{(3)} = \lambda_1^{(3)} \mathbf{e}_r \otimes \mathbf{E}_R + \lambda_2^{(3)} \mathbf{e}_\theta \otimes \mathbf{E}_\Theta + \lambda_z^{(3)} \mathbf{e}_z \otimes \mathbf{E}_Z, \tag{5.10}$$

where

$$\lambda_1^{(3)} = \frac{R}{rk\lambda_z^{(3)}}, \quad \lambda_2^{(3)} = \frac{kr}{R} \tag{5.11}$$

the superscript $(i = 1,2,3)$ indicates the variable related to the target configuration $\mathscr{B}_i$ and $\{\mathbf{E}_R, \mathbf{E}_\Theta, \mathbf{E}_Z\}$ are cylindrical polar axes in $\mathscr{B}_2$.

It follows that the invariants I_1 and I_4 (with the superscript $^{(3)}$ omitted temporarily for simplicity) are given by

$$I_1 = \lambda_1^2 + \lambda_2^2 + \lambda_z^2, \quad I_4 = \lambda_2^2 \cos^2\gamma + \lambda_z^2 \sin^2\gamma, \tag{5.12}$$

where the components of $\mathbf{f}_0$ and $\mathbf{f}$ are $(0, \cos\gamma, \sin\gamma)^{\mathrm{T}}$ and $(0, \lambda_2\cos\gamma, \lambda_z\sin\gamma)^{\mathrm{T}}$, respectively, and γ is the angle defining the fibre orientation with respect to the circumferential direction in

$\mathscr{B}_2$.

The components of the Cauchy stress tensor in $\mathscr{B}_3$ are then

$$\sigma_{rr} = -p+2\frac{\partial\Psi_{\mathrm{m}}}{\partial I_1}\lambda_1^2, \tag{5.13}$$

$$\sigma_{\theta\theta} = -p+2\frac{\partial\Psi_{\mathrm{m}}}{\partial I_1}\lambda_2^2+2\frac{\partial\Psi_{\mathrm{f}}}{\partial I_4}\lambda_2^2\cos^2\gamma, \tag{5.14}$$

$$\sigma_{zz} = -p+2\frac{\partial\Psi_{\mathrm{m}}}{\partial I_1}\lambda_z^2+2\frac{\partial\Psi_{\mathrm{f}}}{\partial I_4}\lambda_z^2\sin^2\gamma, \tag{5.15}$$

$$\sigma_{\theta z} = 2\frac{\partial\Psi_{\mathrm{f}}}{\partial I_4}\lambda_2\lambda_z\sin\gamma\cos\gamma, \tag{5.16}$$

$$\sigma_{r\theta} = 2\frac{\partial\Psi_{\mathrm{f}}}{\partial I_4}(0*\lambda_2\cos\gamma)=0, \tag{5.17}$$

$$\sigma_{rz} = 2\frac{\partial\Psi_{\mathrm{f}}}{\partial I_4}(0*\lambda_z\sin\gamma)=0. \tag{5.18}$$

The stress components σ_{rr} and $\sigma_{\theta\theta}$ in $\mathscr{B}_3$ satisfy the equilibrium equation $\nabla\cdot\boldsymbol{\sigma}=\mathbf{0}$, which, for the considered geometry, reduces to

$$\frac{\mathrm{d}\sigma_{rr}}{\mathrm{d}r}+\frac{\sigma_{rr}-\sigma_{\theta\theta}}{r}=0, \tag{5.19}$$

while the zero-traction boundary conditions are $\sigma_{rr}=0$ for $r=r^{(\mathrm{i})},r^{(\mathrm{o})}$. Strictly $\boldsymbol{\sigma}$ is not a residual stress since the presence of the components σ_{zz} and $\sigma_{\theta z}$ requires appropriate non-zero boundary conditions.

On integration and use of the latter boundary conditions equation (5.19) gives

$$\int_{r^{(\mathrm{i})}}^{r^{(\mathrm{o})}}\frac{\sigma_{\theta\theta}-\sigma_{rr}}{r}\mathrm{d}r=0, \tag{5.20}$$

which, on substitution from eqs. (5.13) and (5.14), can be used to obtain $r^{(\mathrm{i})}$ in $\mathscr{B}_3$ (and $r^{(\mathrm{o})}$ from eq. (5.9)) when the initial radii $R^{(\mathrm{i})}$ and $R^{(\mathrm{o})}$ and k and γ are known. Hence all the Cauchy stress components can be obtained explicitly.

The axial force N in the deformed configuration $\mathscr{B}_3$ can then be calculated as [34]

$$N=2\pi\int_{r^{(\mathrm{i})}}^{r^{(\mathrm{o})}}\sigma_{zz}r\mathrm{d}r=\pi\int_{r^{(\mathrm{i})}}^{r^{(\mathrm{o})}}(2\sigma_{zz}-\sigma_{rr}-\sigma_{\theta\theta})r\mathrm{d}r. \tag{5.21}$$

5.2.2 2-Cut Model

Now we have a new starting point, with $\mathscr{B}_1$ stress free, but $\mathscr{B}_2$ is not now stress free, so going from $\mathscr{B}_2$ to $\mathscr{B}_3$ is different from the 1-cut case. In particular, a different constitutive equation would be required that takes account of the stress in $\mathscr{B}_2$, unless the constitutive law is based

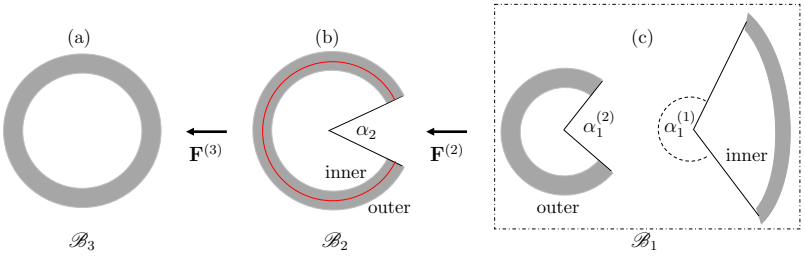

FIGURE 5.3: The 2-cut model: (a) cylindrical model of the LV as the intact ring in $\mathscr{B}_3$, (b) after a radial cut to $\mathscr{B}_2$, and (c) followed by a circumferential cut to $\mathscr{B}_1$. Notice that the inner segment in $\mathscr{B}_1$ has a negative curvature, as in [59]. The red curve, at the mid-wall radius $\bar{R} = (R^{(\mathrm{i})} + R^{(\mathrm{o})})/2$ in (b), separates the inner and outer sectors which become the separate inner and outer sectors in $\mathscr{B}_1$ after the circumferential cut.

on $\mathscr{B}_1$. In the 2-cut model, following a radial cut, a circumferential cut is performed around the mid-wall in $\mathscr{B}_2$ at radius $\bar{R} = (R^{(\mathrm{i})} + R^{(\mathrm{o})})/2$. It is assumed now that residual stress remains after the radial cut but is removed after the circumferential cut and that no axial deformation is associated with the second cut. The resulting stress-free configuration $\mathscr{B}_1$ is depicted in fig. 5.3. We note, in particular, that following the circumferential cut the inner segment has a negative curvature. The geometry in $\mathscr{B}_1$ is described in terms of cylindrical polar coordinates $\{R, \Theta, Z\}$, with subscripts 1 and 2 corresponding to the inner and outer sectors, respectively. Thus,

$$R_1^{(\mathrm{i})} \leqslant R_1 \leqslant R_1^{(\mathrm{o})}, \quad -(\pi - \frac{\alpha_1^{(1)}}{2}) \leqslant \Theta_1 \leqslant \pi - \frac{\alpha_1^{(1)}}{2}, \quad 0 \leqslant Z_1 \leqslant L, \tag{5.22}$$

$$R_2^{(\mathrm{i})} \leqslant R_2 \leqslant R_2^{(\mathrm{o})}, \quad \frac{\alpha_1^{(2)}}{2} \leqslant \Theta_2 \leqslant 2\pi - \frac{\alpha_1^{(2)}}{2}, \quad 0 \leqslant Z_2 \leqslant L, \tag{5.23}$$

where $R_j^{(\mathrm{i})}$, $R_j^{(\mathrm{o})}$, $\alpha_1^{(j)}$, $j = 1,2$, and L denote the inner and outer radii, the opening angles, and the tube length in $\mathscr{B}_1$. In $\mathscr{B}_2$, $R_1^{(\mathrm{i})}$ and $R_2^{(\mathrm{i})}$ both become $\bar{R}$, while $R_1^{(\mathrm{o})}$ and $R_2^{(\mathrm{o})}$ translate to $R^{(\mathrm{i})}$ and $R^{(\mathrm{o})}$, respectively, the opening angle is α_2 and the axial length l.

For each segment, the isochoric deformation from $\mathscr{B}_1$ to $\mathscr{B}_2$ can be written as

$$\mathbf{X} = R\mathbf{E}_R + Z\mathbf{E}_Z, \tag{5.24}$$

with

$$R = \sqrt{\frac{{R_1^{(\mathrm{i})}}^2 - R_1^2}{k_1 \lambda_z^{(21)}} + \bar{R}^2}, \quad \Theta = \pi - k_1\Theta_1, \quad Z = \lambda_z^{(21)} Z_1 \tag{5.25}$$

$$R = \sqrt{\frac{R_2^2 - {R_2^{(\mathrm{i})}}^2}{k_2 \lambda_z^{(22)}} + \bar{R}^2}, \quad \Theta = k_2(\Theta_2 - \pi) + \pi, \quad Z = \lambda_z^{(22)} Z_2 \tag{5.26}$$

for the inner and outer sectors, respectively, where $\lambda_z^{(2j)}$ is taken to be 1 for both segments and $k_j = (2\pi - \alpha_2)/(2\pi - \alpha_1^{(j)})$, $j = 1,2$. Note that the negative curvature of the inner segment in $\mathscr{B}_1$

depicted in fig. 5.3 is captured by the expression for R in (5.25), and that structural compatibility is ensured since the two expressions for R match at $\bar{R}$.

As indicated in fig. 5.3 the deformation gradient from $\mathscr{B}_1$ to $\mathscr{B}_2$ is denoted $\mathbf{F}^{(2)}$, which is shorthand notation for the two separate deformation gradients from the two sectors in $\mathscr{B}_1$ to $\mathscr{B}_2$. These are denoted $\mathbf{F}^{(2j)}$, $j = 1,2$, and given by

$$\mathbf{F}^{(2j)} = \lambda_1^{(2j)} \mathbf{e}_r \otimes \mathbf{E}_R + \lambda_2^{(2j)} \mathbf{e}_\theta \otimes \mathbf{E}_\Theta + \lambda_z^{(2j)} \mathbf{e}_z \otimes \mathbf{E}_Z, \tag{5.27}$$

where

$$\lambda_1^{(2j)} = \frac{R_j}{k_j R \lambda_z^{(2j)}}, \quad \lambda_2^{(2j)} = \frac{k_j R}{R_j}, \quad \lambda_z^{(2j)} = 1.14, \quad j = 1,2. \tag{5.28}$$

Similarly to the 1-cut model, and with the same notation for the stress components, the equilibrium equation in $\mathscr{B}_2$ yields

$$\frac{\mathrm{d}\sigma_{rr}}{\mathrm{d}r} + \frac{\sigma_{rr} - \sigma_{\theta\theta}}{r} = 0, \quad \int_{R^{(\mathrm{i})}}^{R^{(\mathrm{o})}} \frac{\sigma_{\theta\theta} - \sigma_{rr}}{r} \mathrm{d}r = 0. \tag{5.29}$$

Equation $(5.29)_1$ can be rearranged as

$$\sigma_{\theta\theta} = \frac{\mathrm{d}}{\mathrm{d}r}(r\sigma_{rr}), \tag{5.30}$$

from which it follows, on use of the zero-traction boundary conditions on $R^{(\mathrm{i})}$ and $R^{(\mathrm{o})}$, that

$$\int_{R^{(\mathrm{i})}}^{R^{(\mathrm{o})}} \sigma_{\theta\theta} \mathrm{d}r = 0, \tag{5.31}$$

i.e. the mean value of $\sigma_{\theta\theta}$ is zero.
It's assumed that is there is no bending moment on the faces $\Theta = \alpha_2/2$ and $\Theta = 2\pi - \alpha_2/2$ in $\mathscr{B}_2$, which yields

$$\int_{R^{(\mathrm{i})}}^{R^{(\mathrm{o})}} \sigma_{\theta\theta} r \mathrm{d}r = 0. \tag{5.32}$$

Substitution of $\sigma_{\theta\theta}$ from (5.30) into this equation followed by integration by parts and a further application of the zero-traction boundary conditions leads to

$$\int_{R^{(\mathrm{i})}}^{R^{(\mathrm{o})}} \sigma_{rr} r \mathrm{d}r = 0. \tag{5.33}$$

Equations $(5.29)_2$, (5.31) and (5.33) are solved with equations (5.25) and (5.26) to obtain the radius $R^{(\mathrm{i})}$, and the angle α_2 of the segment in $\mathscr{B}_2$. In $\mathscr{B}_2$, the radial traction σ_{rr} is continuous across interface $\bar{r}$, since the deformation gradient, Lagrangian multiplier p and the other stress

components are continuous. The continuity of hoop stress yields

$$(\sigma_{\theta\theta}|_{r=\bar{r}})^{+} = (\sigma_{\theta\theta}|_{r=\bar{r}})^{-}, \tag{5.34}$$

where $\bar{r}$ are the radial positions of the interfaces ($\bar{r} = \frac{r^{(o)}+r^{(i)}}{2}$).
The stress continuity will help to exclude the redundant solutions of $R^{(i)}$ and the angle α_2 from equations $(5.29)_2$ and (5.33).

Once $R^{(i)}$, $R^{(o)}$ and α_2 are obtained, the 1-cut approach is used to estimate the residual stress of the intact-ring configuration.
It's worthy to emphasize that asymmetry in local fibre structure leads to the non-zero torsion boundary condition in $\mathscr{B}_2$, which yields

$$\int_{R^{(i)}}^{R^{(o)}} \sigma_{\theta z} dr \neq 0.$$

However, actually, comparing with σ_{rr} or $\sigma_{\theta\theta}$, the shear component at cross-section of the tube is ignorably small. Then, the mechanical contributions of shear stress are assumed to be ignorable to stress equilibrium and the shape changing of cylindrical geometry of heart tube. And this assumption will also be mathematically applied in our 4-cut model later.

Essentially, this is equivalent to calculating the deformation gradient from $\mathscr{B}_1$ to $\mathscr{B}_3$ by multiplication as $\mathbf{F}^{(3)}\mathbf{F}^{(2)}$, where $\mathbf{F}^{(3)}$ is given by eq. (5.10) and $\mathbf{F}^{(2)}$ is either $\mathbf{F}^{(21)}$ or $\mathbf{F}^{(22)}$ and determined from eq. (5.27).

An expression for the axial load N is obtained from a formula similar to that in eq. (5.21).

It suggests that 'infinite cuts' are efficient to release all residual stress in living organs, since residual stress is induced by the complex (inhomogeneous) growth. Therefore, 4-cut model may give better estimations for residual stress.

The mechanical behaviors of LV are calculated with the single fibre family. According to the discussion about the effect of shear stress on the mechanical response of LV tube, it shows that the geometric shape doesn't change much by the shear stress. Therefore, the effects of shear stress are really ignorable, while the values of shear stresses are really small.

The stress distributions in 1-cut configuration are obtained from both stress and deformation continuity conditions. And it shows that stress continuity is almost equivalent with deformation continuity in multiple-cut model.

The computation results explain experimental observation by Fung [23]. In the residually stressed configuration of an artery, the subsequent radial cuts don't introduce any more elastic deformations. Moreover, no solid evidence supports that the 1-*cut* configuration is the stress

free configuration for living organs. More cuts are needed to release the residual stress and address the stress-free configuration for living organs [36].

5.2.3 4-Cut Model

The effect of two further circumferential cuts, one in each of the two separated segments, is now considered in order to assess if there is any significant change in the resulting calculated residual stress compared with that obtained with a single circumferential cut, although this is not a test that has been carried out experimentally. For definiteness we consider taking a circumferential cut along the mid-wall of each of the two sectors of the 2-cut model, leading to the four separate sectors depicted in fig. 5.4. We assume that the resulting configuration $\mathscr{B}_0$ is stress-free with no further reversal of the curvature.

Each of the four sectors in $\mathscr{B}_0$ is described in terms of cylindrical polar coordinates $\{\rho,\phi,\zeta\}$ according to

$$\rho_1^{(\mathrm{i})} \leqslant \rho \leqslant \rho_1^{(\mathrm{o})}, \quad -(\pi - \frac{\alpha_0^{(1)}}{2}) \leqslant \phi \leqslant \pi - \frac{\alpha_0^{(1)}}{2}, \quad 0 \leqslant \zeta \leqslant L \quad (\text{inner } I), \tag{5.35}$$

$$\rho_2^{(\mathrm{i})} \leqslant \rho \leqslant \rho_2^{(\mathrm{o})}, \quad -(\pi - \frac{\alpha_0^{(2)}}{2}) \leqslant \phi \leqslant \pi - \frac{\alpha_0^{(2)}}{2}, \quad 0 \leqslant \zeta \leqslant L \quad (\text{inner } II), \tag{5.36}$$

$$\rho_3^{(\mathrm{i})} \leqslant \rho \leqslant \rho_3^{(\mathrm{o})}, \quad \frac{\alpha_0^{(3)}}{2} \leqslant \phi \leqslant (2\pi - \frac{\alpha_0^{(3)}}{2}), \quad 0 \leqslant \zeta \leqslant L \quad (\text{outer } I), \tag{5.37}$$

$$\rho_4^{(\mathrm{i})} \leqslant \rho \leqslant \rho_4^{(\mathrm{o})}, \quad \frac{\alpha_0^{(4)}}{2} \leqslant \phi \leqslant (2\pi - \frac{\alpha_0^{(4)}}{2}), \quad 0 \leqslant \zeta \leqslant L \quad (\text{outer } II), \tag{5.38}$$

where $\rho_n^{(\mathrm{i})}$, $\rho_n^{(\mathrm{o})}$, $\alpha_0^{(n)}$, $n = 1,2,3,4$, and L are the internal radii, the external radii, opening angles, and the lengths of the four segments in $\mathscr{B}_0$, and I and II refer to fig. 5.4.

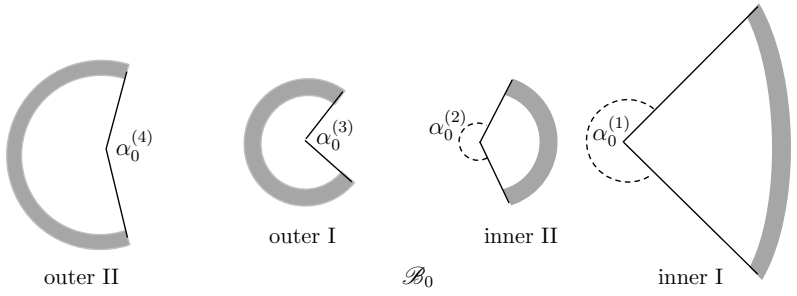

FIGURE 5.4: The stress-free configuration $\mathscr{B}_0$ consisting of the four sectors obtained by circumferential cuts of the two sectors in $\mathscr{B}_1$.

In $\mathscr{B}_1$, the geometries of the two segments are described in terms of polar coordinates R,Θ,Z, with indices 1 and 2, as in (5.22) and (5.23). Next, in $\mathscr{B}_2$, $R^{(\mathrm{i})}$, $R^{(\mathrm{o})}$, α_2, l denote the internal and external radii, the opening angle and the length of the single sector according to (5.25)–(5.26).

The deformations from the four sectors in $\mathscr{B}_0$ to the two sectors in $\mathscr{B}_1$ are described by

$$R_1 = \sqrt{\frac{\rho^2 - \rho_1^{(\mathrm{i})^2}}{k_{11}\lambda_z^{(11)}} + \bar{R}_1^2}, \quad \Theta_1 = k_{11}\phi, \quad Z_1 = \lambda_z^{(11)}\zeta, \quad \text{(inner I)}, \tag{5.39}$$

$$R_1 = \sqrt{\frac{\rho^2 - \rho_2^{(\mathrm{o})^2}}{k_{12}\lambda_z^{(12)}} + \bar{R}_1^2}, \quad \Theta_1 = k_{12}\phi, \quad Z_1 = \lambda_z^{(12)}\zeta, \quad \text{(inner II)}, \tag{5.40}$$

$$R_2 = \sqrt{\frac{\rho^2 - \rho_3^{(\mathrm{o})^2}}{k_{23}\lambda_z^{(23)}} + \bar{R}_2^2}, \quad \Theta_2 = k_{23}(\phi - \pi) + \pi, \quad Z_2 = \lambda_z^{(23)}\zeta, \quad \text{(outer I)}, \tag{5.41}$$

$$R_2 = \sqrt{\frac{\rho^2 - \rho_4^{(\mathrm{i})^2}}{k_{24}\lambda_z^{(24)}} + \bar{R}_2^2}, \quad \Theta_2 = k_{24}(\phi - \pi) + \pi, \quad Z_2 = \lambda_z^{(24)}\zeta, \quad \text{(outer II)}, \tag{5.42}$$

where

$$k_{1n} = (2\pi - \alpha_1^{(1)})/(2\pi - \alpha_0^{(n)}), \quad n = 1,2, \quad k_{2n} = (2\pi - \alpha_1^{(2)})/(2\pi - \alpha_0^{(n)}), \quad n = 3,4,$$

$$\lambda_1^{(1n)} = \frac{R_1}{\rho k_{1n}\lambda_z^{(1n)}}, \quad \lambda_2^{(1n)} = \frac{k_{1n}\rho}{R_1}, \quad n = 1,2,$$

and

$$\lambda_1^{(2n)} = \frac{R_2}{\rho k_{2n}\lambda_z^{(2n)}}, \quad \lambda_2^{(2n)} = \frac{k_{2n}\rho}{R_2}, \quad n = 3,4.$$

The deformation gradients from $\mathscr{B}_0$ in fig. 5.4 to $\mathscr{B}_1$ in fig. 5.3 are

$$\mathbf{F}^{(1n)} = \lambda_1^{(1n)}\mathbf{E}_R \otimes \mathbf{e}_\rho + \lambda_2^{(1n)}\mathbf{E}_\Theta \otimes \mathbf{e}_\phi + \lambda_z^{(1n)}\mathbf{E}_Z \otimes \mathbf{e}_\zeta, \quad n = 1,2, \tag{5.43}$$

$$\mathbf{F}^{(1n)} = \lambda_1^{(2n)}\mathbf{E}_R \otimes \mathbf{e}_\rho + \lambda_2^{(2n)}\mathbf{E}_\Theta \otimes \mathbf{e}_\phi + \lambda_z^{(2n)}\mathbf{E}_Z \otimes \mathbf{e}_\zeta, \quad n = 3,4. \tag{5.44}$$

In $\mathscr{B}_1$, the radial direction for each of the two segments yields

$$\int_{R_j^{(\mathrm{i})}}^{R_j^{(\mathrm{o})}} \frac{\sigma_{\Theta\Theta} - \sigma_{RR}}{R}\mathrm{d}R = 0, \quad j = 1,2. \tag{5.45}$$

The radial traction σ_{RR} should be continuous across each interface $\bar{R}_j$, $j = 1,2$, and hence, since the deformation gradient is continuous, p is continuous and the other stress components are also continuous. The continuity of hoop stress yields

$$(\sigma_{\Theta\Theta}|_{R=R_k})^+ = (\sigma_{\Theta\Theta}|_{R=R_k})^-, \quad k = 1,2, \tag{5.46}$$

where R_k are the radial positions of the interfaces ($R_k = \frac{R_j^{(\mathrm{o})} + R_{j+1}^{(\mathrm{i})}}{2}, j = 1,2$)

TABLE 5.1: Transformation of the radii between configurations.

$\mathscr{B}_0$		$\mathscr{B}_1$		$\mathscr{B}_2$		$\mathscr{B}_3$
$\rho_1^{(\mathrm{i})}$	$\to$	$\bar{R}_1$				
$\rho_1^{(\mathrm{o})}$	$\to$	$R_1^{(\mathrm{o})}$	$\to$	$R^{(\mathrm{i})}$	$\to$	$r^{(\mathrm{i})}$
$\rho_2^{(\mathrm{i})}$	$\to$	$R_1^{(\mathrm{i})}$	$\to$	$\frac{1}{2}(R^{(\mathrm{i})}+R^{(\mathrm{o})})$		
$\rho_2^{(\mathrm{o})}$	$\to$	$\bar{R}_1$				
$\rho_3^{(\mathrm{i})}$	$\to$	$R_2^{(\mathrm{i})}$	$\to$	$\frac{1}{2}(R^{(\mathrm{i})}+R^{(\mathrm{o})})$		
$\rho_3^{(\mathrm{o})}$	$\to$	$\bar{R}_2$				
$\rho_4^{(\mathrm{i})}$	$\to$	$\bar{R}_2$				
$\rho_4^{(\mathrm{o})}$	$\to$	$R_2^{(\mathrm{o})}$	$\to$	$R^{(\mathrm{o})}$	$\to$	$r^{(\mathrm{o})}$

Also, similarly to the 2-cut model,

$$\int_{R_j^{(\mathrm{i})}}^{R_j^{(\mathrm{o})}} \sigma_{\Theta\Theta} R \mathrm{d}R = \int_{R_j^{(\mathrm{i})}}^{R_j^{(\mathrm{o})}} \sigma_{RR} R \mathrm{d}R = 0, \quad j = 1,2. \tag{5.47}$$

The corresponding deformation gradient from $\mathscr{B}_1$ to $\mathscr{B}_2$ is $\mathbf{F}_{0\to 2} = \mathbf{F}^{(2)}\mathbf{F}^{(1)}$ (Table 5.1), and the governing equations for the single sector are

$$\int_{R^{(\mathrm{i})}}^{R^{(\mathrm{o})}} \frac{\sigma_{\theta\theta} - \sigma_{rr}}{r} \mathrm{d}r = 0, \quad \int_{R^{(\mathrm{i})}}^{R^{(\mathrm{o})}} \sigma_{\theta\theta} r \mathrm{d}r = \int_{R^{(\mathrm{i})}}^{R^{(\mathrm{o})}} \sigma_{rr} r \mathrm{d}r = 0, \tag{5.48}$$

as in eqs. $(5.29)_2$, (5.32) and (5.2.2).

This model consists of 8 independent equations (5.45)–(5.48), and eight unknown geometrical parameters in $\mathscr{B}_0$: $\rho_n^{(\mathrm{i})}, \alpha_0^{(n)}$, $n = 1,2,3,4$. The required external axial force are then calculated by means of the formulas (5.21).

Once we obtain all the details in $\mathscr{B}_0$, we estimate the residual stress components σ_{rr} and $\sigma_{\theta\theta}$ in the intact-ring configuration $\mathscr{B}_3$, with the total deformation gradient $\mathbf{F}_{0\to 3} = \mathbf{F}^{(3)}\mathbf{F}^{(2)}\mathbf{F}^{(1)}$ (Table 5.1).

5.3 Results

5.3.1 Modelling Parameters

The reference configuration changes with the different models, so we need to define the parameters according to the specific model we use. For $\mathscr{B}_2$ of the 1-cut model, we assume that the axial stretch has the constant value $\lambda_z^{(3)} = 1.14$, and $R^{(\mathrm{i})} = 2.06$, $R^{(\mathrm{o})} = 3.20$ $\alpha_2 = 65^\circ$ are estimated from the experiments [59].

TABLE 5.2: Measured geometrical input for the 4-cut model, estimated from [59].

configuration $\mathscr{B}_1$	configuration $\mathscr{B}_2$
$R_1^{(\mathrm{i})} = 5.28$	$\frac{1}{2}(R^{(\mathrm{i})} + R^{(\mathrm{o})})$
$R_1^{(\mathrm{o})} = 6.29$	$R^{(\mathrm{i})} = 2.06$
$\alpha_1^{(1)} = 268^\circ$	$\alpha_2 = 65^\circ$
$R_2^{(\mathrm{i})} = 1.97$	$\frac{1}{2}(R^{(\mathrm{i})} + R^{(\mathrm{o})})$
$R_2^{(\mathrm{o})} = 3.04$	$R^{(\mathrm{o})} = 3.20$
$\alpha_1^{(2)} = 180^\circ$	$\alpha_2 = 65^\circ$

For the 2-cut model, in addition to the parameters used in the 1-cut model, we use additional measurements in $\mathscr{B}_1$ of the 2-cut model [59]: $R_1^{(\mathrm{i})} = 5.28$, $R_2^{(\mathrm{i})} = 1.97$, $\alpha_1^{(1)} = 268^\circ$ and $\alpha_1^{(2)} = 180^\circ$, and that there is same axial stretch in the transformation from $\mathscr{B}_1$ to $\mathscr{B}_2$, i.e. $\lambda_z^{(2j)} = 1.14$, j=1,2.

For the 4-cut model, in addition to the parameters used in the 2-cut model, we need more geometrical information in $\mathscr{B}_1$, which is again estimated from the measurements [59] as listed in Table 6.2. We also assume that $\lambda_z^{(1n)} = 1$ from $\mathscr{B}_0$ to $\mathscr{B}_1$, i.e. no axial deformation after the first circumferential cuts.

Initially, we consider a homogeneous myocardium model, for which the material parameters of the HO constitutive law (5.1) and (5.2) are fitted to the data of mice [61]. This gives $a = 2.21$kPa, $b = 1.8$, $a_\mathrm{f} = 3.96$ kPa and $b_\mathrm{f} = 3.45$ (fig. 5.5).

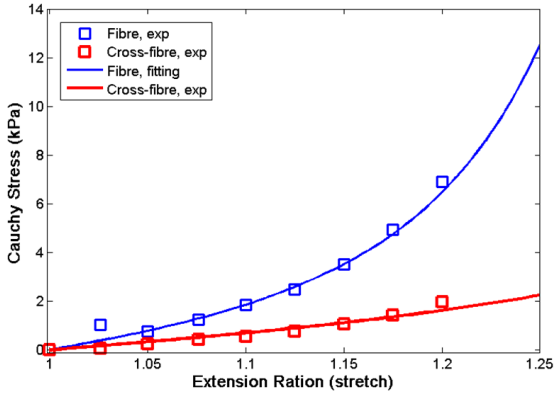

FIGURE 5.5: Fit of parameters of the HO model (5.1) to the experimental data (squares; from [61]) for the loading curves: The axial loading curve along fibre direction (blue); the axial loading curve along cross-fibre direction (red).

However, the dramatic difference in the maximum hoop stress between the single cut and multiple cuts models raises concerns over the rationale of the homogeneous models we adopted. Novak *et al.* [56] showed that canine myocardium is heterogeneous and the material properties are strongly location dependent. We also consider an inhomogeneous myocardium model, and fit the data from [56] with the HO strain energy function (5.1) and (5.2).

The parameters are spatially dependent, as shown in fig. 5.6. Since our model is for mice, and there are no experimental data on the heterogeneous properties of the mice myocardium, we take the spatial variation of the canine data, but keep the mean values of the mice data from our fitted parameters, and implement these into our models.

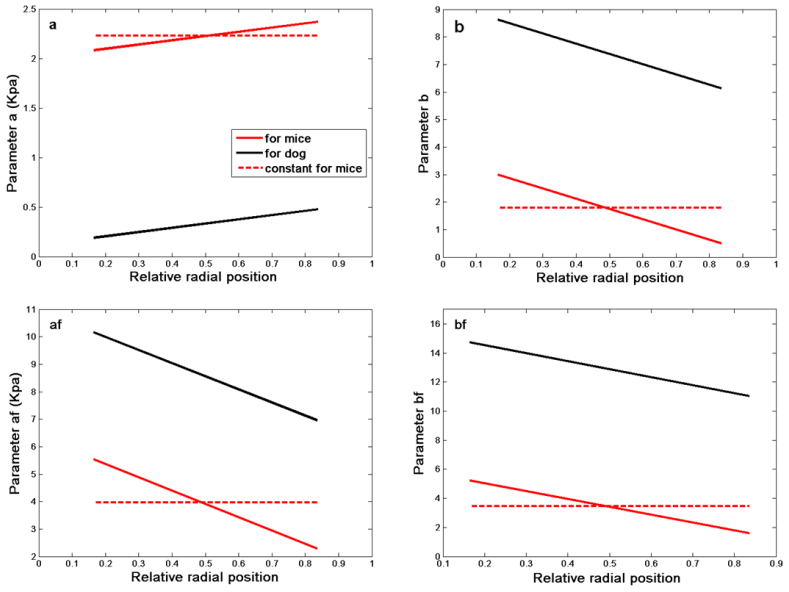

FIGURE 5.6: The heterogeneous material parameters fitted to canine data from [56] (black solid lines). The red dashed lines indicate the constants used for the homogeneous models, and the red solid lines are for the heterogeneous mice model.

5.3.2 Results for the Homogeneous Myocardium Model

The geometry of the intact ring predicted by the three different models is summarized in Table 6.3, and compared with the measured data in [59].

TABLE 5.3: Computed intact ring from the homogeneous models, compared to measurements [59].

Measurements (mm)	1-cut model	2-cut model	4-cut model
$r^{(\mathrm{i})} = 0.388$	0.557	0.482	0.403
$r^{(\mathrm{o})} = 2.13$	2.167	2.148	2.133
$r^{(\mathrm{o})} - r^{(\mathrm{i})} = 1.742$	1.61	1.667	1.73
Difference in thickness	8.2%	4.74 %	0.7%

It is clear that the agreement of the estimated radius and thickness of the unloaded configuration gets better as the number of cuts increases. Although in principle the true zero-stress configuration requires infinite cuts, Table 6.3 suggests that 2 or 4 cuts provides a good approximation of the zero-stressed configuration, given that the measured geometry is not exactly circular as assumed by the models.

The components of the residual stress distribution in the unloaded configuration $\mathscr{B}_3$, from the different models are shown in fig. 5.7. Although the overall distributions are similar in all these models, there is marked difference in the magnitudes of the residual (hoop) stress. In particular, the maximum $\sigma_{\theta\theta}$ is 2.58 kPa, 207.5 kPa, and 214.9kPa, respectively, for the single cut, 2-cut, and 4-cut models. In other words, ratio of the maximum hoop stresses over the single cut is about 80 times for the 2-cut model, and 83.3 times for the 4-cut model. We also notice that the 4-cut model gives much smoother stress distribution. However, the 2-cut model leads to a similar magnitude of the maximum hoop stress as the 4-cut model. This suggests that the significant rise in the residual stress is due to the negative curvature at the first circumferential cut.

5.3.3 Results for the Heterogeneous Myocardium Model

The geometry of the intact ring from the heterogeneous myocardium model is computed and compared with the experiments, as shown in Table 5.4. This model provides much better agreement with experimental observations. The agreements of the 2-cut and 4-cut models are excellent, using either the homogeneous or the heterogeneous materials, with an error of less than 2%.

TABLE 5.4: Computed intact ring from the heterogeneous models, compared to measurements [59].

Measurements (mm)	1-cut model	2-cut model	4-cut model
$r^{(\mathrm{i})} = 0.388$	0.517	0.403	0.39
$r^{(\mathrm{o})} = 2.13$	2.157	2.113	2.13
$r^{(\mathrm{o})} - r^{(\mathrm{i})} = 1.742$	1.64	1.73	1.74
Difference in thickness	5.8%	0.7%	0.011%

The corresponding stress distributions are plotted in fig. 5.8, which shows that the maximum $\sigma_{\theta\theta}$ is 5.52 kPa, 218.5 kPa, and 230.9kPa, respectively, for the single cut, 2-cut, and 4-cut models. The ratio of the maximum hoop stresses over the single cut is reduced significantly in the heterogenous model, about 39 times for the 2-cut model, and 41.6 times for the 4-cut model.

5.4 Discussion

The issue of multiple cuts has been studied before. In particular, Fung suggested that one radial cut might be sufficient to release all the residual stress. This was supported his experiments which showed that after two or more radial cuts, no obvious deformation occurs from the one-radial-cut configuration of the arteries [23]. Using our models we can show, however, that multiple radial cuts indeed do not release more residual stress, since due to the symmetry of the

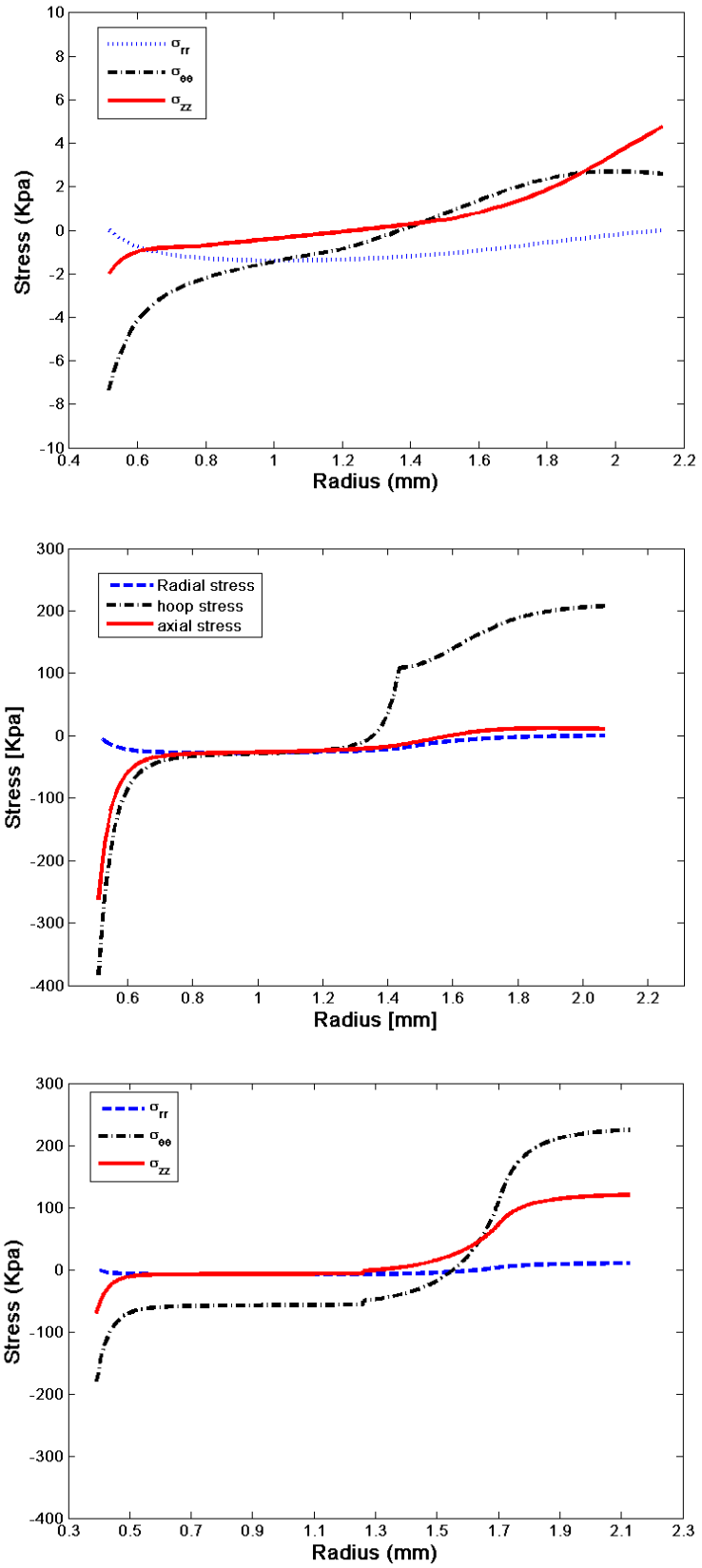

FIGURE 5.7: Distribution of the residual stress components in the intact ring from (a) single cut, (b) 2-cut, and (c) 4-cut models based on homogenous material assumption.

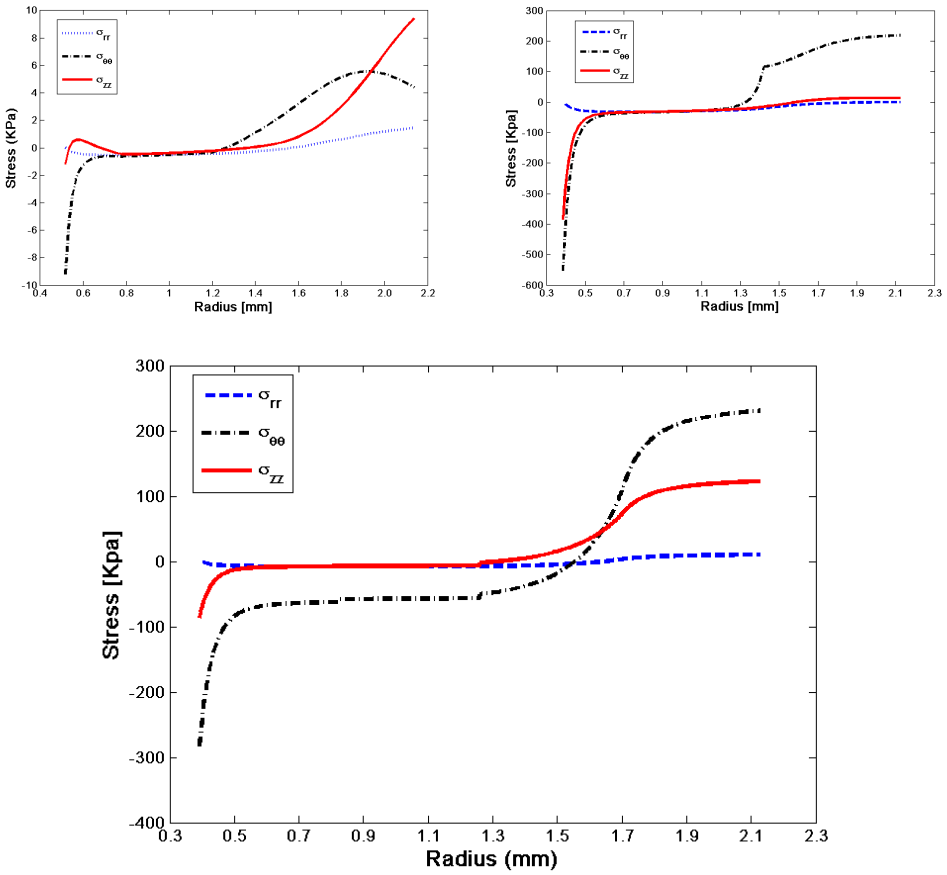

FIGURE 5.8: Distribution of the residual stress components from (a) single cut, (b) 2-cut, and (c) 4-cut models based on heterogeneous myocardium assumption.

considered geometry, once a radial cut is made, no further elastic deformation can occur after more radial cuts.

In other words, the deformation gradient in each of our models is independent of the azimuthal angle and the solutions are also independent of this angle. However, this does not indicate that the one-cut configuration is a stress-free one. To further release residual stress circumferential cuts following a radial cut are necessary.

The fact that our 2-cut and 4-cut models predict a much higher (40 times!) hoop stress is surprising, but is not unexpected given the large negative curvature revealed by the experiments [59]. However, the significant stress underestimate of the radial cut model does not just occur in the heart models. In the residual stress modelling of arteries, by treating the artery wall as three separate layers (intima, media and adventitia), and measuring the opening angles for each of the three layers, Holzapfel and Ogden [36] have essentially developed a 3-cut model (one radial cut followed by two circumferential cuts, in this case separating the layers with different properties). Their model is also heterogeneous, as different material parameters are used for different layers. The residual stress distribution across the wall from the arterial model is shown in fig. 5.9 for both the 3-cut and 1-cut models, all other parameters being the same. The maximum values of

the hoop stress in different layers of the 3-cut model are listed in Table 5.5. Table 5.5 shows that the ratio of the hoop stress in the different layers ranges from 24 to 50 times. This is similar to that for the mouse hearts.

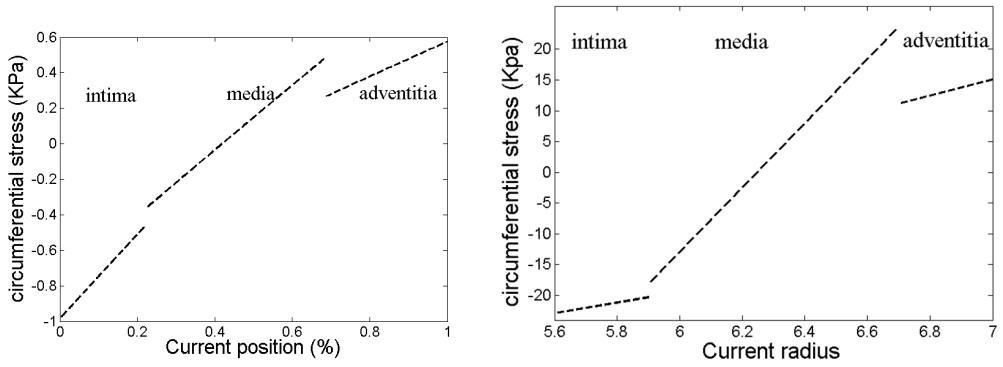

FIGURE 5.9: Residual stress distributions through the intima, media and adventitia of the artery wall as functions of the radial coordinate r, (a) without layer separation, and (b) the original result with layer separations from [36].

TABLE 5.5: Residual stress in the arteries computed using single-cut and original HO model [36]

Max hoop stress (kPa)	single-cut for HO model	original HO model [36]	Ratio of the stresses
Adventitia	0.57	15.08	26.45
Media	0.47	23.74	50.51
intima	-0.97	-23.20	23.91

5.4.1 Effect of Shear Stress

As mention in section '1-cut model', we assume LV and all the cut segments remain their cylindrical configuration before and after cutting. Furthermore, the geometric symmetry indicates that the distribution of (Cauchy) stress is also symmetric to the z-axis. And stress distribution is independent from angle position as

$$\mathbf{Q}\boldsymbol{\sigma}(\theta)\mathbf{Q}^T = \boldsymbol{\sigma}(\theta+\alpha) \tag{5.49}$$

where $\mathbf{Q}$ describes a rotation about the axis of tube about the angle α.
Further, last equation gives

$$\sigma_{r\theta} = 0, \ \frac{\partial \sigma_{rr}}{\partial \theta} = 0, \ \frac{\partial \sigma_{\theta\theta}}{\partial \theta} = 0.$$

And the stress is obviously independent from z as

$$\boldsymbol{\sigma}(z) = \boldsymbol{\sigma}(z+z_0) \tag{5.50}$$

where z_0 is an arbitrary constant and $0 \leq z + z_0 \leq l$).
Further, last equation gives

$$\frac{\partial \sigma_{zr}}{\partial z} = 0, \ \frac{\partial \sigma_{z\theta}}{\partial z} = 0, \ \frac{\partial \sigma_{zz}}{\partial z} = 0.$$

Stress equilibrium equation ($\nabla \cdot \boldsymbol{\sigma}$=$\mathbf{0}$) under cylindrical coordinates $\{r, \theta, z\}$, it gives

$$\begin{cases} \frac{\partial \sigma_{rr}}{\partial r} + \frac{1}{r}\frac{\partial \sigma_{\theta r}}{\partial \theta} + \frac{\partial \sigma_{zr}}{\partial z} + \frac{1}{r}(\sigma_{rr} - \sigma_{\theta\theta}) = 0 \\ \frac{\partial \sigma_{r\theta}}{\partial r} + \frac{1}{r}\frac{\partial \sigma_{\theta\theta}}{\partial \theta} + \frac{\partial \sigma_{z\theta}}{\partial z} + \frac{1}{r}(\sigma_{r\theta} + \sigma_{\theta r}) = 0 \\ \frac{\partial \sigma_{rz}}{\partial r} + \frac{1}{r}\frac{\partial \sigma_{\theta z}}{\partial \theta} + \frac{\partial \sigma_{zz}}{\partial z} + \frac{1}{r}(\sigma_{rz}) = 0. \end{cases} \tag{5.51}$$

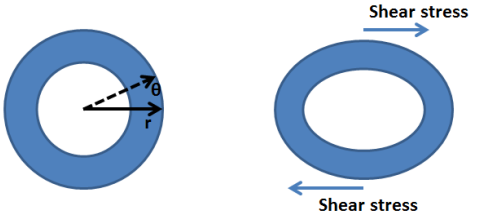

FIGURE 5.10: The change of shape of heart tube with shear stress σ_{xy}.

Combining (5.49) and (5.50), (5.51) gives (5.19), while the rest equations will be satisfied automatically. Obviously, if the geometry of heart is not symmetric to z-axis, the stress will not be symmetric to z-axis, which will cancel (5.49) and (5.50) and change the expression for stress equilibrium equation. Moreover, if the shear stress is non-zero, the overall geometry of heart will not remain cylindrical. For instance, if shear stress σ_{xy} is non-zero, it indicates the cylindrical tube deforming into a elliptic cylinder. Due to the antisymmetry to z-axis, the stress is not independent from angle position θ in intact-tube configuration

$$\frac{\partial \boldsymbol{\sigma}}{\partial \theta} \neq \mathbf{0}. \tag{5.52}$$

Then, the first stress equilibrium equation in eq. (5.51) is replaced by

$$\frac{\partial \sigma_{rr}}{\partial r} + \frac{1}{r}\frac{\partial \sigma_{\theta r}}{\partial \theta} + \frac{1}{r}(\sigma_{rr} - \sigma_{\theta\theta}) = 0. \tag{5.53}$$

It indicates that the existence of shear stress could change the shape of heart tube and change the expression for the stress equilibrium equation. Therefore, our calculation will be different with multiple-cut model with existence of shear stress.

Recalling expression of the Cauchy stress (5.4), the term $\mathbf{f}\otimes\mathbf{f}$ could be obtained with help of fibre vector $\mathbf{f}=(0,\lambda_2\cos\gamma,\lambda_z\sin\gamma)^{\mathrm{T}}$ as

$$\begin{bmatrix} 0 & 0 & 0 \\ 0 & \lambda_\theta^2\cos^2\theta & \lambda_\theta\lambda_z\cos\theta\sin\theta \\ 0 & \lambda_\theta\lambda_z\cos\theta\sin\theta & \lambda_z^2\sin^2\theta \end{bmatrix}. \tag{5.54}$$

Then, it indicates the shear stress $\sigma_{\theta z}$ is not zero, and this fact might change the shape of intact heart tube.

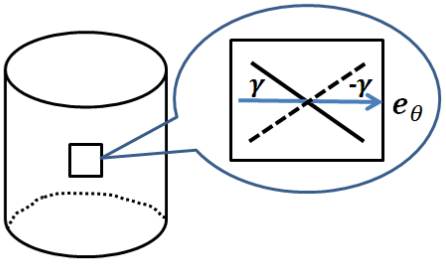

FIGURE 5.11: The heart tube model with two symmetric fibre families: the dash line indicates new fibres with fibre angle $(-\gamma)$ to circumferential direction $\mathbf{e}_\theta$.

Moreover, if we introduce another fibre family ($\mathbf{f}'=(0,\lambda_2\cos(-\gamma),\lambda_z\sin(-\gamma))^{\mathrm{T}}$), which is symmetric to the existing fibre family. Then, the shear stress will be canceled (details will be shown later). And the stress equilibrium equation (6.43) could be satisfied.

So *how mechanical behaviors of intact heart model will be influenced by the shear stress induced by the single family? What's the difference between mechanical responses from tissues with a fibre family and tissues with symmetric fibre families in the multiple-cut models?*

If assuming the material properties are same for two fibre families, the SEF could be given by modifying HO model (5.1) as

$$\Psi=\Psi_{\mathrm{m}}+\Psi_{\mathrm{f}_1}+\Psi_{\mathrm{f}_2} \tag{5.55}$$

where

$$\Psi_{\mathrm{m}}=\frac{a}{2b}\{\exp[b(I_1-3)]-1\},\ \Psi_{\mathrm{f}_1}=\frac{a_{\mathrm{f}}}{2b_{\mathrm{f}}}\{\exp[b_{\mathrm{f}}(I_4-1)^2]-1\},\ \Psi_{\mathrm{f}_2}=\frac{a_{\mathrm{f}}}{2b_{\mathrm{f}}}\{\exp[b_{\mathrm{f}}(I_6-1)^2]-1\}, \tag{5.56}$$

$a,b,a_{\mathrm{f}},b_{\mathrm{f}}$ are material constants, and

$$I_1=tr\mathbf{C},\quad I_4=\mathbf{f}_0\cdot(\mathbf{C}\mathbf{f}_0),\quad I_6=\mathbf{f}_0'\cdot(\mathbf{C}\mathbf{f}_0'), \tag{5.57}$$

$\mathbf{f}_0'$ is the unit fiber vector for new fibre family ($\mathbf{f}=(0,\cos(-\gamma),\sin(-\gamma))^{\mathrm{T}}$).

The Cauchy stress tensor is then

$$\boldsymbol{\sigma} = -p\mathbf{I} + 2\frac{\partial \Psi_{\mathrm{m}}}{\partial I_1}\mathbf{B} + 2\frac{\partial \Psi_{\mathrm{f}_1}}{\partial I_4}\mathbf{f}\otimes\mathbf{f} + 2\frac{\partial \Psi_{\mathrm{f}_2}}{\partial I_4}\mathbf{f}'\otimes\mathbf{f}', \tag{5.58}$$

Recalling (5.10), the invariants I_1, I_4 and I_6 are given by

$$I_1 = \lambda_1^2+\lambda_2^2+\lambda_z^2,\ I_4 = \lambda_2^2\cos^2\gamma+\lambda_z^2\sin^2\gamma,\ I_6 = \lambda_2^2\cos^2(-\gamma)+\lambda_z^2\sin^2(-\gamma), \tag{5.59}$$

where the components of $\mathbf{f}$ and $\mathbf{f}'$ are $(0,\lambda_2\cos\gamma,\lambda_z\sin\gamma)^{\mathrm{T}}$ and $(0,\lambda_2\cos(-\gamma),\lambda_3\sin(-\gamma))^{\mathrm{T}}$, respectively). The components of the Cauchy stress tensor in $\mathscr{B}_3$ are then

$$\begin{aligned}
\sigma_{rr} &= -p+2\frac{\partial \Psi_{\mathrm{m}}}{\partial I_1}\lambda_1^2, && (5.60)\\
\sigma_{\theta\theta} &= -p+2\frac{\partial \Psi_{\mathrm{m}}}{\partial I_1}\lambda_2^2+4\frac{\partial \Psi_{\mathrm{f}}}{\partial I_4}\lambda_2^2\cos^2\gamma, && (5.61)\\
\sigma_{zz} &= -p+2\frac{\partial \Psi_{\mathrm{m}}}{\partial I_1}\lambda_z^2+4\frac{\partial \Psi_{\mathrm{f}}}{\partial I_4}\lambda_z^2\sin^2\gamma, && (5.62)\\
\sigma_{\theta z} &= 2\frac{\partial \Psi_{\mathrm{f}}}{\partial I_4}\lambda_2\lambda_z\sin\gamma\cos\gamma+2\frac{\partial \Psi_{\mathrm{f}}}{\partial I_4}\lambda_2\lambda_z\sin(-\gamma)\cos(-\gamma)=0. && (5.63)
\end{aligned}$$

1-cut model with symmetric fibre families The shear stress is zero and independent from angle position θ, it indicates the validations of (5.49) and (5.50). Therefore, with help of zero-traction boundary condition, the stress equilibrium equation is obtained from (5.51) as

$$\frac{\partial \sigma_{rr}}{\partial r}+\frac{1}{r}(\sigma_{rr}-\sigma_{\theta\theta})=0 \ \Rightarrow\ \int_{r^{(\mathrm{i})}}^{r^{(\mathrm{o})}}\frac{\sigma_{\theta\theta}-\sigma_{rr}}{r}\mathrm{d}r=0. \tag{5.64}$$

On substitution from (5.61) and (5.62), (5.64) can be used to obtain $r^{(\mathrm{i})}$ in $\mathscr{B}_3$ (and $r^{(\mathrm{o})}$ from (5.8)) when the initial radii $R^{(\mathrm{i})}$ and $R^{(\mathrm{o})}$ and k and γ are known. Hence all the Cauchy stress components can be obtained explicitly.

1-cut model with one fibre family To test the effect of shear stress on the heart tube model, we still assume LV and all the cut segments remain their cylindrical configurations, and then the shear stress will be determined via stress equilibrium. This calculation will show magnitude of shear stress and implicate the possible change of shape from a cylindrical model.

If LV and all the cut segments remain their cylindrical configurations, the components of Cauchy stress is obtained as (5.13) to (5.16). Obviously, (5.49) and (5.49) are satisfied, which indicates the stress equilibrium equation could be written as eq. (6.44). On substitution from ((5.13)) and ((5.14)), (5.8) can be used to obtain $r^{(\mathrm{i})}$ in $\mathscr{B}_3$ (and $r^{(\mathrm{o})}$ from (5.8)) when the initial radii $R^{(\mathrm{i})}$ and $R^{(\mathrm{o})}$ and k and γ are known. Hence all the Cauchy stress components can be obtained explicitly.

2-cut model with symmetric fibre families Similarly to the 1-cut model, and with the same notation for the stress components for tissues with symmetric fibre families (5.61 - 5.63), the the

equilibrium equation in $\mathscr{B}_2$ yields as eq. (5.29_2). Moreover, the zero-moment condition gives (5.32). Then, (($5.29)_2$), ((5.32)) and ((5.33)) are solved with equations (5.25) and (5.26) to obtain the radius $R^{(\mathrm{i})}$, and the angle α_2 of the segment in $\mathscr{B}_2$. Once $R^{(\mathrm{i})}$, $R^{(\mathrm{o})}$ and α_2 are obtained, the 1-cut approach is used to estimate the residual stress of the intact-ring configuration.

2-cut model with a single fibre family The solution method is shown in section '2-cut model'. Briefly, the stress equilibrium equation and zero-moment boundary condition are solved to give the radius $R^{(\mathrm{i})}$, and the angle α_2 of the segment in $\mathscr{B}_2$. Then, the 1-cut approach is used to estimate the residual stress of the intact-ring configuration.

5.4.1.1 Results to Compare the Solutions for Tissues with One and Symmetric Fibre Families

Comparison between results from tissues with one and symmetric fibre families (1-cut model) The geometric informations are used same as the information for 1-cut model, as well as the selection of values for material parameters, such as a, b (seeing in 'Modeling parameters' section). fig. 5.12 shows the radius and residual stresses in intact-ring configuration $\mathscr{B}_3$ estimated from tissue with symmetric fibre families and single fibre family. The estimated radius of the intact heart tubes are 0.502 mm from tissues from symmetric fibres, while it's 0.557 mm from tissues with single fibre (4.5% of difference). The material is stiffer for tissues with symmetric families, while gives the bigger values of stress components. However, it shows the closely similar shapes of curves for principal stresses. More important, the values of shear stress ($\sigma_{\theta z}$) are obviously smaller than the other stresses. The maximum absolute value of shear stresses is about 0.74 kPa, comparing 3 kPa for circumferential stress ($\sigma_{\theta\theta}$) and 4.9 kPa for axis stress (σ_{zz}) (fig. 5.12, right). It's concluded that: 1) the geometric sizes are almost same for estimations from tissues with symmetric families or single family. 2) the shapes and trends of curves are closely similar from tissues with symmetric families or single family. 3) the shear stress is canceled in estimated results from tissues with symmetric families, while the values of shear stresses are really smaller than principal stresses. According to this evidence, it suggests that: 1) the geometric shape doesn't change much by the shear stress, 2) **the effects of shear stress are really ignorable**, while the values of shear stresses are really small.

Comparison between results from tissues with one and symmetric fibre families (2-cut model) The geometric informations are used same as the information for 2-cut model, as well as the selection of values for material parameters, such as a, b (seeing in 'Modeling parameters' section). Recalling the comparison between estimated geometric and mechanical information estimated from 1-cut mode, similar phenomena are observed. fig. 5.13 shows the radius and residual stresses in intact-ring configuration $\mathscr{B}_3$ estimated from tissue with symmetric fibre families and single fibre family. The estimated radii are close from tissues from symmetric fibres (0.482

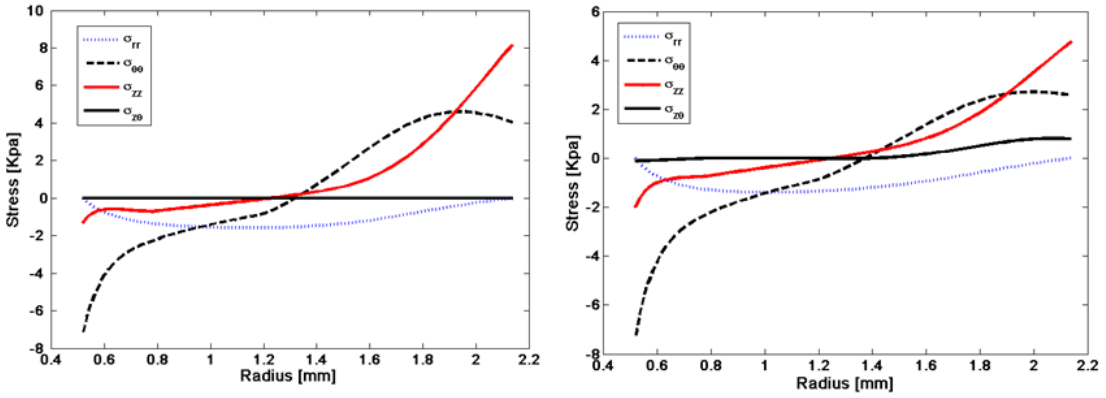

FIGURE 5.12: Distribution of residual stresses components form: left, the symmetric fibre families; right, the single family

mm) or from tissues with single fibre (0.480 mm). Principal stress components are estimated bigger from tissues with symmetric fibre due to the higher stiffness. Again, the closely similar shapes of curves for principal stresses are observed. The relative values of shear stresses are even smaller than one from 1-cut model. The maximum absolute value of shear stresses is about 3.5 kPa, comparing 207 kPa for circumferential stress (fig. 5.13, right). It's concluded that: 1) the geometric sizes are almost same for estimations from tissues with symmetric families or single family. 2) the shapes and trends of curves are closely similar from tissues with symmetric families or single family. 3) the shear stress is canceled in estimated results from tissues with symmetric families, while the relative values of shear stresses are even smaller than principal stresses. According to this evidence, it suggests that: 1) the geometric shape doesn't change much by the shear stress, 2) **the effects of shear stress are really ignorable**, while the values of shear stresses are really small.

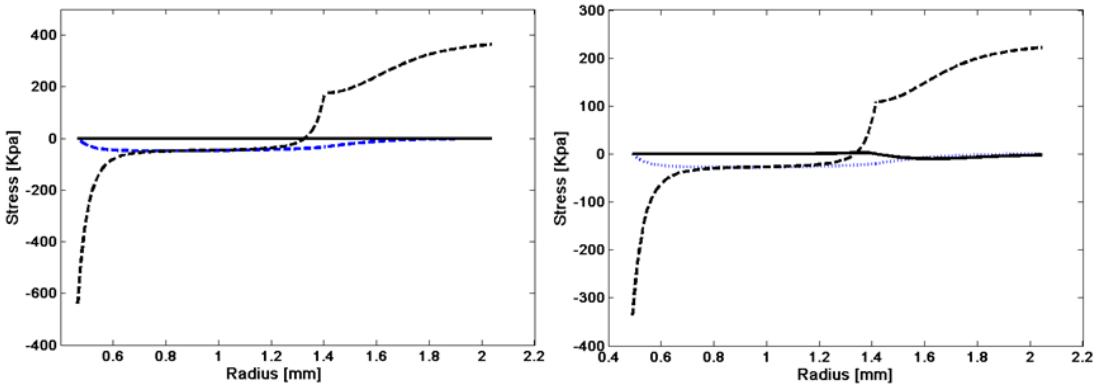

FIGURE 5.13: Distribution of residual stresses components form: left, the symmetric fibre families; right, the single family.

5.4.2 Deformation Continuity and Stress Continuity

As mentioned in '2-cut model' section, the deformation continuity leads to the stress continuity (5.34) in 1-cut configuration ($\mathscr{B}_2$). In this sectoin, it will explain the relation between the stress continuity and deformation continuity conditions.

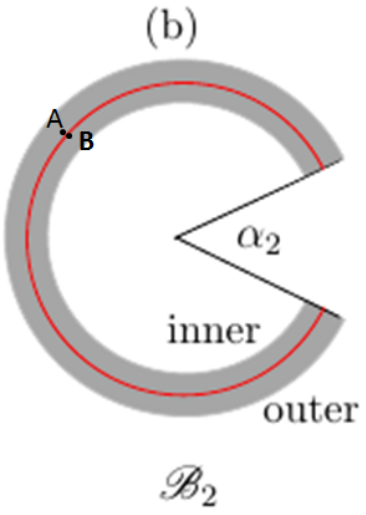

FIGURE 5.14: Two contacted material points at the interface of $\mathscr{B}_2$. **A** is the material point $\mathbf{x}_A$, while **B** is the material point $\mathbf{x}_B$

Considering two contacted material points ($\mathbf{P}_1(\mathbf{x}_A)$ and $\mathbf{P}_2(\mathbf{x}_B)$) at the interface of $\mathscr{B}_2$ (fig. 5.14), while $\mathbf{P}_1(\mathbf{x}_A)$ is point in outer layer and $\mathbf{P}_2(\mathbf{x}_B)$ is the point in inner layer. As a intact slice from heart, the deformation should be continuous as well as elastic energy across the interface, which gives

$$\begin{cases} \mathbf{F}_A^{(2)} = \mathbf{F}_B^{(2)} \\ W_A(\mathbf{F}_A^{(2)}) = W_B(\mathbf{F}_B^{(2)}) \end{cases} \quad \text{while } r_A = r_B. \tag{5.65}$$

Recalling (5.4), the Cauchy stresses from point A and B are

$$\begin{cases} \boldsymbol{\sigma}_A = J_A^{-1}\mathbf{F}_A^{(2)}\frac{\partial W_A}{\partial \mathbf{F}_A^{(2)}} - p_A\mathbf{I} \\ \boldsymbol{\sigma}_B = J_B^{-1}\mathbf{F}_B^{(2)}\frac{\partial W_B}{\partial \mathbf{F}_B^{(2)}} - p_B\mathbf{I}. \end{cases} \tag{5.66}$$

The expressions of SEF (5.1) indicates W_A or W_B are monotonic increasing along with the increasing of deformation gradient, which gives the one-to-one mapping between stress and deformation. With the help of deformation continuity (5.65), this stress-deformation relation gives the stress continuity as

$$\begin{cases} p_A = p_B \\ \frac{\partial W_A}{\partial \mathbf{F}_B^{(2)}} = \frac{\partial W_B}{\partial \mathbf{F}_B^{(2)}} \end{cases} \quad \Rightarrow \ \boldsymbol{\sigma}_{\theta\theta(A)} = \boldsymbol{\sigma}_{\theta\theta(B)}. \tag{5.67}$$

It concludes that the stress continuity is equivalent with the deformation continuity in '2-cut' model. To validate this conclusion, the results will be shown for the residual stress distributions obtained from deformation and stress continuity.

Results from the 2*cut model with stress continuity*

Recalling '2cut' model, Equations $(5.29)_2$, (5.31) and (5.33) are solved with equations (5.25) and (5.26) to obtain the radius $R^{(i)}$, and the angle α_2 of the segment in $\mathscr{B}_2$. The stress continuity will help to exclude the redundant solutions of $R^{(i)}$ and the angle α_2 from Equations $(5.29)_2$ and (5.33). Hence all the Cauchy stress components can be obtained explicitly in $\mathscr{B}_2$ with $R^{(i)}$ and α_2 (fig. 5.15, left).

Results from the 2*cut model with deformation continuity*

Similar with previous solution, Equations $(5.29)_2$, (5.31) and (5.33) are solved with equations (5.25) and (5.26) to obtain the radius $R^{(i)}$, and the angle α_2 of the segment in $\mathscr{B}_2$. Here, deformation continuity, rather than stress continuity, will help to exclude the redundant solutions of $R^{(i)}$ and the angle α_2 from Equations $(5.29)_2$ and (5.33). Hence all the Cauchy stress components can be obtained explicitly in $\mathscr{B}_2$ with $R^{(i)}$ and α_2 (fig. 5.15, right).

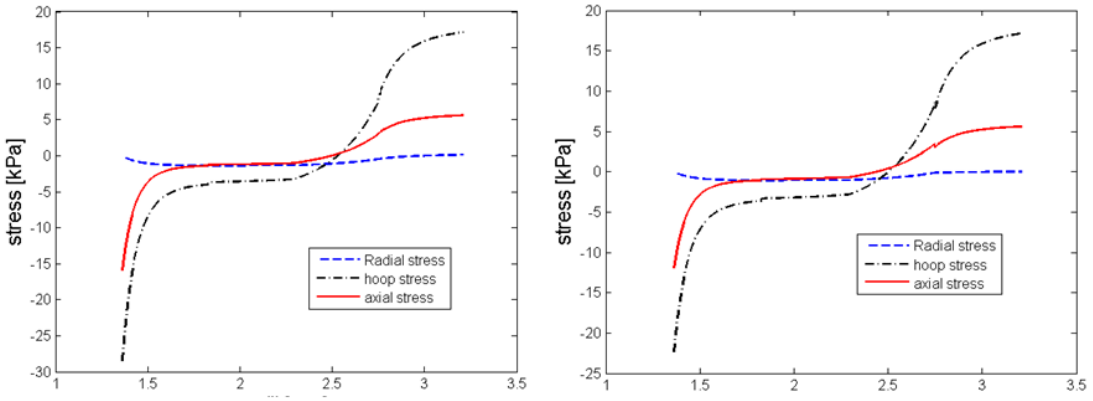

FIGURE 5.15: The residual stress distributions in $\mathscr{B}_2$: left, the solution from stress continuity; right, the solution from deformation continuity.

The results show that the residual stress distribution obtained from stress continuity is almost same for the one obtained from the deformation continuity. Or saying, in multiple-cut model, **residual stresses estimated with stress continuity (as boundary condition) is similar to the ones estimated with deformation continuity.**.

5.4.3 Subsequent Elastic Deformation after Radial Cut on 1 *cut* Configuration

As mentioned in 'Literature review of residual stress theories', Fung [23] firstly introduces the 'opening angle' method to estimate the residual stress in living organs based on the observations of artery slice cutting experiments. In experiments, the radial cut was done on aorta slice,

then, the slices will spring open. It suggests that the intact organs are the residually-stressed configurations and the residual stress will affect the mechanical behaviors of organs.

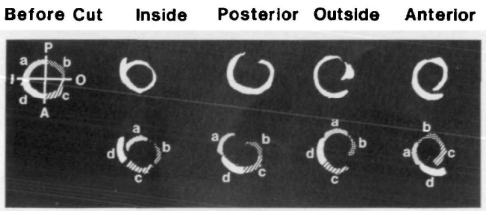

FIGURE 5.16: No observable deformations occur after additional radial cuts [23].

Moreover, the aorta slices were radially cut into smaller parts at different circumferential positions and assembled back into a whole specimen (fig. 5.16), which is to test whether the specimen could reproduce the pre-cut shape [23]. The experimental observations presented a good resemblance. Since on elastic deformation occurs after more radial cuts, it's concluded that one radial cut could help tissue to deform into the stress. Referring to configurations defined in our models (fig. 5.2), this suggestion indicates that 1-*cut* configuration ($\mathscr{B}_2$) is stress-free as

$$\boldsymbol{\tau} = \mathbf{0}. \tag{5.68}$$

where $\boldsymbol{\tau}$ is the residual stress in $\mathscr{B}_2$.
However, in our multiple-cut model, it's assumed that the 1-*cut* configuration ($\mathscr{B}_2$) is residually stressed configuration as

$$\boldsymbol{\tau} \neq \mathbf{0}. \tag{5.69}$$

This contradiction will be explained in this section. And it will give answers to following questions as: is the 1-cut configuration residually-stressed configuration? what's elastic deformation occurring from the residually stressed configuration? If no elastic deformation occurs after cutting tissues from a certain configuration, is this the sufficient condition to address that this configuration is stress free?

Mechanical response of the heart slice after subsequent radial cuts
As defined in 2cut model section, the geometry of the right-hand panel in fig. 5.2 represent a 1-*cut* configuration $\mathscr{B}_2$, which can be described by cylindrical polar coordinates $\{R,\Theta,Z\}$ as (5.75). The slices are assumed to remain their cylindrical configurations. Therefore, due to symmetry in geometries, it indicates the stress distributions are also symmetric to z-axis and independent from angle position Θ.

$$\frac{\partial \boldsymbol{\sigma}_0}{\partial \Theta} = \mathbf{0}, \tag{5.70}$$

where $\boldsymbol{\sigma}_0$ is the Cauchy stress in $\mathscr{B}_2$.
The configuration is at stress equilibrium state ($\nabla \cdot \boldsymbol{\sigma} = \mathbf{0}$), which yields balance equation (5.29) with help of (5.70). Since no load is applied on this configuration, the distributions of Cauchy

stress components should satisfy the boundary conditions as:
zero-circumferential-stress boundary condition gives

$$\int_{r^{(\mathrm{i})}}^{r^{(\mathrm{o})}} \sigma_{0\theta\theta}\mathrm{d}r = 0, \tag{5.71}$$

Zero-bending-moment on the surfaces of cross-section yields

$$\int_{r^{(\mathrm{i})}}^{r^{(\mathrm{o})}} \sigma_{0\theta\theta} r\mathrm{d}r = 0. \tag{5.72}$$

Zero-traction boundary conditions leads to

$$\int_{r^{(\mathrm{i})}}^{r^{(\mathrm{o})}} \sigma_{0rr} r\mathrm{d}r = 0. \tag{5.73}$$

where σ_{0ij} is the component of $\boldsymbol{\sigma}_0$.
As mentioned in 2-*cut* section, only zero-bending-moment equation is independent control equation.

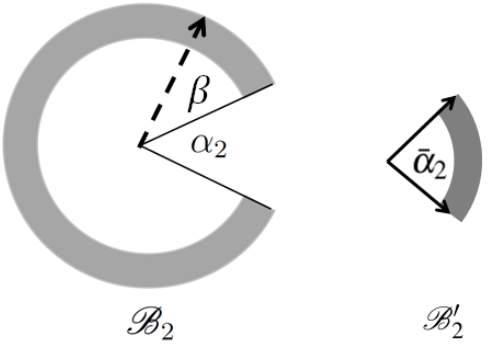

FIGURE 5.17: Radial cut on 1-cut configuration: a radial cut at of 1-cut configuration $\mathscr{B}_2$. The slice will deform into new configuration $\mathscr{B}'_2$.

Assuming one more radial cut is made on 1*cut* slice, the new slices are assumed to remain cylindrical configurations. To investigate the mechanical behavior of one of two slices, the configuration (fig. 5.17) of target slice before cutting could be represented as

$$r^{(\mathrm{i})} \leqslant r \leqslant r^{(\mathrm{o})}, \quad \frac{\alpha_2}{2} \leqslant \theta \leqslant (\beta + \frac{\alpha_2}{2}), \quad 0 \leqslant z \leqslant l, \tag{5.74}$$

where β is the angle position for cutting.

Let the geometry of the right-hand panel in fig. 5.17 represent the new configuration $\mathscr{B}'_2$ of target slice, which can be described by cylindrical polar coordinates $\{\bar{r}, \bar{\theta}, \bar{z}\}$ as

$$\bar{r}^{(\mathrm{i})} \leqslant \bar{r} \leqslant \bar{r}^{(\mathrm{o})}, \quad \frac{\bar{\alpha}_2}{2} \leqslant \bar{\theta} \leqslant (2\pi - \frac{\bar{\alpha}_2}{2}), \quad 0 \leqslant \bar{z} \leqslant \bar{l}, \tag{5.75}$$

where $R^{(\mathrm{i})}$, $R^{(\mathrm{o})}$, and L denote the inner and outer radii, and the tube length, respectively, and α_2 is the opening angle.

To study stress distribution in $\mathscr{B}_2'$, symmetry in geometry indicates the stress distributions are also symmetric to z-axis and independent from angle position $\bar{\theta}$.

$$\frac{\partial \bar{\sigma}_0}{\partial \bar{\theta}} = \mathbf{0} \tag{5.76}$$

where $\bar{\sigma}_0$ is the Cauchy stress in $\mathscr{B}_2'$.
Stress equilibrium state ($\nabla \cdot \bar{\sigma}_0 = 0$) yields balance equation (5.29) with help of (5.76).

$$\int_{\bar{r}^{(\mathrm{i})}}^{\bar{r}^{(\mathrm{o})}} \frac{\sigma_{\bar{\theta}\bar{\theta}} - \sigma_{\bar{r}\bar{r}}}{\bar{r}} \mathrm{d}\bar{r} = 0, \tag{5.77}$$

Similarly with previous stress state, zero load condition is applied on $\mathscr{B}_2'$, the distributions of Cauchy stress components should satisfy the boundary conditions as:
zero-circumferential-stress boundary condition gives

$$\int_{\bar{r}^{(\mathrm{i})}}^{\bar{r}^{(\mathrm{o})}} \bar{\sigma}_{0\theta\theta} \mathrm{d}\bar{r} = 0, \tag{5.78}$$

Zero-bending-moment on the surfaces of cross-section yields

$$\int_{\bar{r}^{(\mathrm{i})}}^{\bar{r}^{(\mathrm{o})}} \bar{\sigma}_{0\theta\theta} \bar{r} \mathrm{d}\bar{r} = 0. \tag{5.79}$$

Zero-traction boundary conditions leads to

$$\int_{\bar{r}^{(\mathrm{i})}}^{\bar{r}^{(\mathrm{o})}} \bar{\sigma}_{0rr} \bar{r} \mathrm{d}\bar{r} = 0. \tag{5.80}$$

where $\bar{\sigma}_{0ij}$ is the component of $\bar{\sigma}_0$.

The stress distribution could be obtained by solving (5.79) and (equ745). The stress equilibrium (5.29) and boundary conditions (5.72-5.73) in $\mathscr{B}_2$ hold the same expressions with stress equilibrium (5.29) and boundary conditions (5.78-5.80) in $\mathscr{B}_2'$. Therefore, obviously, the stress distribution in $\mathscr{B}_2$ is same as one in $\mathscr{B}_2'$, which gives

$$\bar{\sigma}_0 = \sigma_0. \tag{5.81}$$

The stress energy function, respect to $\mathscr{B}_2$, is defined as

$$\bar{\Psi} = \bar{\Psi}(\bar{\mathbf{F}}, \sigma_0), \tag{5.82}$$

where $\bar{\mathbf{F}}$ is elastic deformation gradient from $\mathscr{B}_2$ to $\mathscr{B}_2'$.
Recalling (5.4), Cauchy stress in $\mathscr{B}_2'$ is given as

$$\bar{\sigma}_0 = J^{-1}\bar{\mathbf{F}}\frac{\partial\bar{\Psi}(\bar{\mathbf{F}},\boldsymbol{\sigma}_0)}{\partial\bar{\mathbf{F}}} - p\mathbf{I}. \tag{5.83}$$

Since the defined SEF gives the one-to-one mapping between stress and strain, recalling (5.81), it gives

$$\bar{\mathbf{F}} = \mathbf{I}. \tag{5.84}$$

Therefore, no elastic deformation occurs after more radial cuts at 1-cut configuration. Moreover, obviously, this phenomenon is independent from the cutting position. In other words, it gives that no elastic deformation occurs after cutting at an arbitrary angle position. And this conclusion could explain the experimental observation by Fung [23]. In the residually stressed configuration of artery, the subsequent radial cuts don't introduce any more elastic deformations. Moreover, no solid evidence supports that the 1-*cut* configuration is the stress free configuration for living organs. More cuts are needed to release the residual stress and address the stress-free configuration for living organs.

If referring the non-linear elastic deformation theories to determine the stress-free configuration, it's safe to conclude that: if the body is at the stress-free configuration, the cuts on body will not introduce the elastic deformation and the cut slices could perfectly reassembled back to the previous configuration, but not vice versa; if no elastic deformation occurs after some cuts on the body, the initial configuration is not necessary to be the stress-free one.

5.5 Conclusion

Based on experimental observations, it shows that a single radial cut does not release all residual stress. We have developed multiple cuts models to estimate the residual stress distributions in a mouse LV model. Our results show that both radial cuts and circumferential cuts are required to release the residual stresses in the left ventricle. Remarkably, using radial cuts alone leads to significantly underestimated residual stress, which will be around 40 times greater if estimated properly. We show that similar findings apply to arteries [36].

Comparing the stress distritubtions in intact rings, it shows stresses estimated by 4-cut model are smoother than by 2-cut model. In real heart, the stresses should smoothly distribute for intact heart, which indicates 4-cut model is more reasonable. Moreover, as mentioned in previous researches, it suggests 'infinite cuts' are efficient to release all residual stress in living organs, since residual stress is induced by the complex (inhomogeneous) growth. Therefore, 4-cut model may give better estimations for residual stress.

The mechanical behaviors of LV are calculated with the single fibre family. According to the discussion about effect of shear stress on the mechanical response of LV tube, it shows that the geometric shape doesn't change much by the shear stress. Therefore, the effects of shear stress are really ignorable, while the values of shear stresses are really small.

The stress distributions in 1cut configuration are obtained from both stress and deformation continuity conditions. And it shows that stress continuity is almost equivalent with deformation continuity in multiple-cut model.

The computation results explain experimental observation by Fung [23]. In the residually stressed configuration of artery, the subsequent radial cuts don't introduce any more elastic deformations. Moreover, no solid evidence supports that the 1-*cut* configuration is the stress free configuration for living organs. More cuts are needed to release the residual stress and address the stress-free configuration for living organs.

Moreover, magnitude of hoop stress is estimated to be larger than the order of active tension (200 kPa from this work VS 100 kPa for normal active tension for human heart). It might be explained by: 1) the selection of the material properties. The constitutive parameters are fitted from the experiments on rice [61], while the opening angles are obtained from the experiments [59]. Considering the diversity of mechanical behaviors of soft tissues, the constitutive parameters might be different between two mentioned works, even though these are the closest data according to author's best knowledge. With lower values for constitutive parameters, the magnitudes of hoop stress will be significantly lower. For instance, if a_{f} is used as value of 2.00kPa in equation (5.2) (rather than 3.96kPa from parameter fitting), the max hoop stress is reduced to 114 kPa (53% lower than estimation from previous results). 2) the time effects on the opening angle; as mentioned in [30], the opening angle will be enlarged under the viscoelasticity effects of (in vitro) artery tissues after the arterial samples are separated from the living organs. In experiments [59], the opening angles after circumferential cuts are not immediately measured after heart harvesting, which might introduce the enlarged opening angle. This fact (enlarged opening angle) leads to the overestimated residual stresses.

This work gives a new direction to estimate the residual stress in LV by using the multiple cut model. As shown in previous experiments (like [59]), single cut can release all the residual stress in LV, since further deformations are observed after more cuts. By simply estimating the residual with one-cut model, the residual stress will be significantly underestimated. To increase the accuracy of the residual stress estimations. More experimental data are needed to describe the material properties of in vitro tissues. Besides, the constitutive law, involving the viscoelasticity in soft tissues, could be employed to estimate the residual stress in living organs.

Chapter 6

A Coupled Agent-based and Hyperelastic Modelling of the Left Ventricle Post Myocardial Infarction

6.1 Introduction

Myocardial infarction (MI), commonly known as a heart attack, occurs when blood flow decreases or stops to a part of the heart, causing damage to the heart muscle. The healing process in the heart poses a complex multiscale soft tissue problem, invovling cardiac growth and remodelling (G&R). Cellular growth is often considered to be the cause for residual stress [72]. The myocardial stress and constitutive properties are the two key factors in myocardial G&R [91]. There are typically two types of G&R modelling approaches at the continuum level. One is the volumetric growth (the density remains unchanged) following the G&R, and the other is the density growth (volume remains unchanged). In the volumetric approach, G&R can be modelled using the growth tensor first introduced by Rödriguez *et al*. [65]. For example, Göketepe *et al*. [25] developed a multi-scale framework to study myocardial growth via alignment of myocytes and parallel additional of sarcomere units. Their model was extended to study the mechanical effects on remodelling patterns of left ventricle (LV) after certain surgical procedures. Kerckhoffs *et al*. [47] developed a strain-driven growth laws to explain how the grown cardiac myocytes increased the fibre and cross-fibre strains . Density growth, on the other hand, focuses on changing the constitutive properties of myocaridum in healthy remote and infarcted cardiac tissues, the latter being characterised with stiffer constitutive properties, simulating the replacement of fibrosis by collagen fibres. For example, in a study, the stiffness in the infarct zone is increased significantly compared to functional myocardium in a patient-specific infarcted LV model.

There are very few combined volumetric and density growth models for G&R, particularly for the heart. Eriksson *et al*. [16] developed a framework to study the G&R process of fibre-reinforced arteries, while the evolution of constitutive properties was simulated via a density-and-volumetric growth approach for a mixture of constituents. However, the remodelling of the fibre structure was not included. Indeed, it is not clear how the collagen fibre structure is modified during the post-MI healing process, and how the macro-mechanical response of the infarcted LV changes post-MI.

Recent developments in soft tissue modelling in parallel with advances in experimental techniques have enabled us to predict mechanical states at, and obtain images of, the small scales relevant to biology. For example, the structure-based fibre-reinforced Holzapfel–Ogden model (HO) [35] for myocardium was developed based on simple shear experiments, and has catalysed much of the recent activities in soft tissue modelling.

At the cellular level, collagen deposition and remodelling are regulated by fibroblast cell alignment. Environmental cues, such as mechanical and chemical cues, have been shown to influence cell migration and regulate the micro-fibre structures [12]. Recently, agent-based models that account for these effects have been developed and used to study a two-dimensional slab model of the myocardium infarction [18, 66]. However, the extension of this approach to a three-dimensional LV model has not been reported.

In this paper, we combine the agent-based approach by [18, 66] with a structure-based fibre-reinforced constitutive law to study MI healing in a three-dimensional left ventricular model for the first time. To account for the necessarily dispersed fibre structure post-MI, we modify the original Holzapfel–Ogden (HO) constitutive law [35] by employing a distributed fibre model [37]. The specific fibre distribution is determined using an agent-based model similar to that of [18]. We then incorporate the agent-based model within a finite element (FE) LV model. This new multiscale model is used to simulate the myocardium remodelling in terms of the collagen fibre structure and density. To account for the micro-fibre structure in the tissue constitutive laws, a commonly used up-scaling method is based on volumetric averaging [83]. However, since these micro-fibres in the soft tissue do not support compression, a switch is required to exclude the compressed fibres. For dispersed fibre structure, however, such a 'switch' is often applied inappropriately due to the volumetric averaging [37]. In our model, we describe the fibre structure using angular integration over a local coordinate system, which allows an analytical expression of the fibre on-off switch to be implemented in the constitutive model.

6.2 Methodology

6.2.1 Geometry of LV Model

An idealized half ellipsoid geometry (with 28mm of the long aixs, 5mm of internal radius for base surface and 10mm of external radius for base surface) is used to construct FE model for a rat LV, with 2100 hexahedral elements and 2375 nodes (fig. 6.1). The global Cartesian coordinates (X,Y,Z) are used to describe the material point in the undeformed reference configuration, with the basis denoted as $\{\mathbf{E}_X,\mathbf{E}_Y,\mathbf{E}_Z\}$.

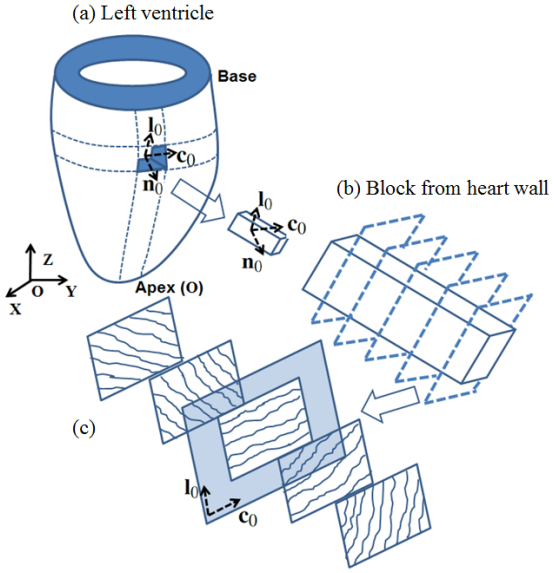

FIGURE 6.1: (a) The LV geometry with 28mm long axis, internal radius of 5mm and external radius of 10mm at the base, and a block cut from the LV wall. The basis vectors at the reference configuration are ($\mathbf{c}_0$, $\mathbf{l}_0$, $\mathbf{n}_0$) for local coordinates, where $\mathbf{c}_0$, $\mathbf{l}_0$, and $\mathbf{n}_0$ are the local circumferential, longitudinal and transmural unit vectors. The basis vectors at the reference configuration are (**X**, **Y**, **Z**) for global Cartesian coordinates, with origin **O** at the LV apex. (b) The fibre structure through the thickness of the LV wall. (c) Five longitudinal–circumferential sections through the wall thickness. Collagen fibres lie in the $\mathbf{c}_0$–$\mathbf{l}_0$ plane.

Myocardium is considered to be a fibre-reinforced material mostly composed of collagen fibres and myocytes [35]. A local coordinate system with the circumferential, longitudinal, and transmural basis ($\mathbf{c}_0$, $\mathbf{l}_0$, $\mathbf{n}_0$), is introduced to describe the layered fibre structure within the ventricular wall, as shown in fig. 6.1. Note that

$$\mathbf{c}_0 = \mathbf{E}_Z \times \mathbf{n}_0/(||\mathbf{E}_Z \times \mathbf{n}_0||), \quad \mathbf{l}_0 = \mathbf{n}_0 \times \mathbf{c}_0/(||\mathbf{n}_0 \times \mathbf{c}_0||). \tag{6.1}$$

The myofibre architecture is generally described by a 'fibre-sheet-normal' system (**f**, **s**, **n**) [89] in the current configuration. Here, we assume that the fibre direction **f** always lies in the $\mathbf{c}-\mathbf{l}$ plane, the sheet direction is transmural, and the sheet-normal $\mathbf{n} = \mathbf{f} \times \mathbf{s}$, where **c** and **l** are the

current circumferential and longitudinal directions: $\mathbf{c} = \mathbf{F}\mathbf{c}_0/(||\mathbf{F}\mathbf{c}_0||), \mathbf{l} = \mathbf{F}\mathbf{l}_0/(||\mathbf{F}\mathbf{l}_0||)$, and $\mathbf{F}$ is the deformation gradient.

6.2.2 Agent-based Model

6.2.2.1 Chemokine Concentration

Fibroblast cells adjust the micro-structure of heart tissue, including the density and orientation of the collagen fibre bundles, which determine the material properties of infacted tissues. The collagen fibres are aligned along the myocytes in healthy tissues. Following an acute MI, sudden changes of the chemokine concentration and mechanical environment in and around the infarct area activate the fibroblasts, which will remodel the micro-collagen structure of heart tissues by changing the collagen orientations and its volumetric fraction thorough deposition and degradation. Subsequently, the material properties and mechanical behaviors are modified at the tissue level. In this study, we extend the 2D agent-basedmodel developed in [18], to 3D, to describe the collagen remodelling post-MI. The modified 3D agent-based model is explained in the coming section.

We assume a circular myocardial infarction with its centre at $\mathbf{X}_c$. The static chemokine concentration at point $\mathbf{X}$, representing the milieu of cytokines and chemokine surroundings, is described by a chemical diffusion equation as:

$$D_c \nabla^2 C(\mathbf{X}) = \begin{cases} k_{\mathrm{c,deg}} C(\mathbf{X}) - k_{\mathrm{c,gen}}, & \mathbf{X} \in \Omega_b \\ k_{\mathrm{c,deg}} C(\mathbf{X}), & \mathbf{X} \notin \Omega_b \end{cases} \tag{6.2}$$

where Ω_b is the infarct region, D_c is the diffusion coefficient, C is the chemokine concentration equation, and $k_{\mathrm{c,gen}}$, $k_{\mathrm{c,deg}}$ are the chemokine generation and degradation rates, respectively.

The boundary condition for the chemokine concentration equation is

$$C(\mathbf{X}) = 0, \quad \text{if } ||\mathbf{X} - \mathbf{X}_c|| \to \infty, \tag{6.3}$$

Experimental data suggest that the infarct-induced chemical concentration reduces rapidly from the infarct area, and drops to nearly zero away from the infarct centre. Hence, In practice, we choose $C(\mathbf{X}) = 0$, when $||\mathbf{X} - \mathbf{X}_c||$ is ten times of the infarct zone in order to approximate diffusion into an infinite space, following [66]. The continuity of the chemokine field requires that

$$(C_{|\mathbf{X}\in\Omega_b})^+ = (C_{|\mathbf{X}\in\Omega_b})^-, \quad (\frac{\partial C}{\partial \mathbf{X}})^+_{|\mathbf{X}\in\Omega_b} = (\frac{\partial C}{\partial \mathbf{X}})^-_{|\mathbf{X}\in\Omega_b} \tag{6.4}$$

For a spherical infarct zone of radius r_0, (6.2) has an analytical solution,

$$C(r) = \begin{cases} \frac{a_1 \exp(a_2 r) - a_1 \exp(-a_2 r)}{r} + a_0, & r \leq r_0 \\ \frac{a_3 \exp(-a_2 r)}{r}, & r > r_0 \end{cases} \tag{6.5}$$

where $a_0 = k_{\text{c,gen}}/k_{\text{c,deg}}$, $a_1 = -\frac{a_0(r_0+1/a_2)}{2\exp(a_2 r_0)}$, $a_2 = \sqrt{k_{\text{c,deg}}/D_c}$ and $a_3 = \frac{1}{2}(r_0 - 1/a_2)\exp(a_2 r_0) - a_1$.

The fibroblast activation parameters, including cell migration speed, collagen degradation rate, collagen deposition rate and collagen reorientation rate, all are modulated by the local chemokine concentration $C(r)$. To compute the activation parameters in the agent based model, the local fibroblast activation parameters are assumed to vary linearly with C as

$$P_i(\mathbf{X}) = \left(\frac{P_{i,\max} - P_{i,\min}}{C_{\max} - C_{\min}}\right)[C(\mathbf{X}) - C_{\min}] + P_{i,\min} \tag{6.6}$$

where P_i is the ith rate parameter, $P_{i,\max}$ and $P_{i,\min}$ are the maximum and minimum rates, and $C_{\max}, C_{\min}$ are the maximum and minimum chemokine concentrations.

6.2.2.2 Fibroblast Migrations Regulated by Environmental Cues

According to the experimental observations in [18], the infarct area is stretched only into longitudinal and circumferential directions and developed the scar tissues with collagen fibres. In this thesis, it's assumed that the new collagen fibres are disposed in the **c**-**l** plane, along with the fibroblast migrations regulated by local environmental cues. These include the chemical, mechanical, persistent and structural cues ([12], [18], [66]. We further assume the fibroblasts are rigid discs with radius R_{cell}, and there is no interaction between fibroblasts [66].

Chemical Cues

We define chemokine vector as the production of chemokine concentration and the outward normal vector at the fibroblast boundary. The chemical cue $\mathbf{v}_c$is obtained from

$$\mathbf{v}_{\text{c}} = \frac{1}{2\pi}\int_{-\pi}^{\pi} C(r)\mathbf{n}(\theta)\mathrm{d}\theta, \tag{6.7}$$

where $\mathbf{n}(\theta)$ is the unit outward normal vector of the cell boundary in the current configuration, r is the distance at the boundary of a fibroblast cell to the infarction centre $\mathbf{X}_{\text{c}}$.

Mechanical Cues

The mechanical cue $\mathbf{v}_m$ is defined as

$$\mathbf{v}_{\mathrm{m}} = \frac{1}{2\pi}\int_{-\pi}^{\pi} \varepsilon_n(\xi)\mathbf{n}(\theta)\,\mathrm{d}\theta \tag{6.8}$$

where $\varepsilon_n = \mathbf{n}\cdot\mathbf{Dn}$ is the normal strain, and

$$\mathbf{D} = \frac{1}{2}(\mathbf{I} - \mathbf{F}^{-T}\mathbf{F}^{-1}),$$

is the Eulerian strain tensor, $\mathbf{F}$ is the deformation gradient, ξ is the material point at the cell boundary, and $\mathbf{I}$ is the identify matrix.

Structural Cues

The structural cue $\mathbf{v}_s$ is defined as

$$\mathbf{v}_{\mathrm{s}} = \frac{\int N(\theta)\mathbf{f}(\theta)\,\mathrm{d}\theta}{\int N(\theta)\mathrm{d}\theta}, \tag{6.9}$$

where $N(\theta)$ is the number of collagen fibres along angle θ, $\mathbf{f}(\theta)$ is the unit vector along θ in the current configuration, $\mathbf{f} = \mathbf{F}\mathbf{f}_0/||\mathbf{F}\mathbf{f}_0||$ and $\mathbf{f}_0 = \cos(\theta)\mathbf{c}_0 + \sin(\theta)\mathbf{l}_0$.

Persistence Cue

The persistent cue $\mathbf{v}_p$, is defined as the fibroblast cell migration velocity

$$\mathbf{v}_{\mathrm{p}} = S_{\mathrm{cell}}(\mathbf{X})\mathbf{u}(\Theta), \tag{6.10}$$

where Θ is the angle of fibroblast migration at time t, S_{cell} is the value of the fibroblast migration speed, and $\mathbf{u}(\Theta)$ is the unit vector along Θ in the current configuration, $\mathbf{u} = \mathbf{F}\mathbf{u}_0/||\mathbf{F}\mathbf{u}_0||$ and $\mathbf{u}_0 = \cos\Theta\,\mathbf{c}_0 + \sin\Theta\,\mathbf{l}_0$.
The fibroblast position at time t is tracked from

$$\mathbf{x}(t) = \int_{t_0}^{t} \mathbf{v}_{\mathrm{p}}\mathrm{d}t. \tag{6.11}$$

Resultant Cue

The fibroblast resultant cue $\boldsymbol{\rho}$ is a weighted and normalised sum of all the cues (6.7 – 6.10),

$$\boldsymbol{\rho} = \frac{\sum \mathbf{c}_i}{\eta + \sum ||\mathbf{c}_i||}, \quad \mathbf{c}_i = \frac{W_i}{M_i}\mathbf{v}_i, \tag{6.12}$$

where $\mathbf{v}_i$ is the ith cue vector, $\mathbf{c}_i$ is the ith normalized and weighted cue vector, M_i and W_i are ith scaling and weighting factors, and η is the persistent tuning factor, which is constant fitted from experimental observations [66]. The orientation of $\boldsymbol{\rho}$ provides the mean fibre angle $\bar{\Theta}$. We assume that the fibroblasts obey a Von mises distribution,

$$\varphi_{\text{VM}}(\Theta|\bar{\Theta},\sigma) = \frac{e^{\sigma\cos(\Theta-\bar{\Theta})}}{I_0(\sigma)}, \quad \sigma^2 = -2\ln||\boldsymbol{\rho}||, \sigma^2 = -2\ln||\boldsymbol{\rho}||, \tag{6.13}$$

where I_0 is the Bessel function of the first kind of order zero.

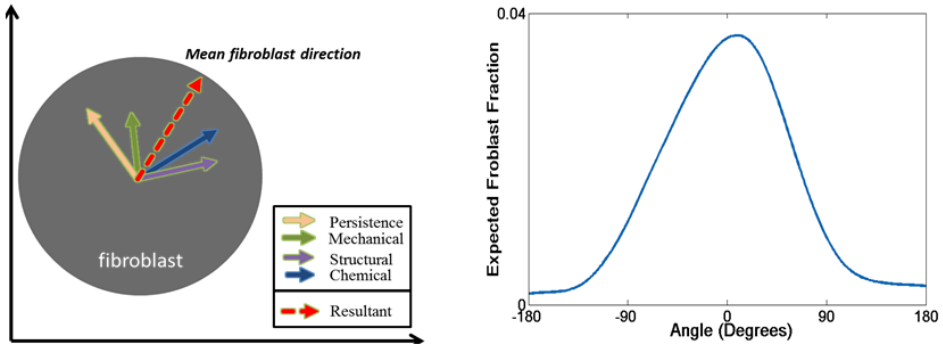

FIGURE 6.2: A) The resultant cue that represents the mean fibroblast direction is computed from a weighted combination of all cues; B) the von Mises distribution of the fibroblast orientation.

6.2.2.3 Remodeling of the Collagen Fibre Structure

The collagen structure of healthy tissue is described by the quantity of collagen fibres (N^0_{tot}) and the fibre angles. And the statistical feature of fibre angles can be described by a fibre orientation density function (φ_0). Then, during the healing process of infarction, more collagen fibres will be deposed by fibroblast cells, while the fibre angles are also updated. The numerical strategy is explained in this section how to mathematically describe the evolution the statistical features of fibre family at the arbitrary material point in infarction region.

The local collagen fibre distribution in the current configuration are remodelled by fibroblasts in the following way.

1. Deposition and degradation: The total collagen fibre number at time t is

$$N_{\text{tot}} = \int_{-\pi/2}^{\pi/2} N(\theta) \mathrm{d}\theta. \tag{6.14}$$

The rate of change of the number of collagen fibres along θ direction $N(\theta)$ is determined from

$$\frac{\partial N(\theta)}{\partial t} = k_{\text{cf,gen}}(C)\beta\pi R_{\text{cell}}^2 \delta(\Theta - \theta) - k_{\text{cf,deg}}(C)N(\theta), \tag{6.15}$$

where β is the maximum collagen fibre number per area, R_{cell} is the radius of the fibroblast cell, δ is the delta function indicating the new fibre is aligned with the fibroblast migration orientation, $k_{\text{cf,gen}}$ and $k_{\text{cf,deg}}$, estimated from (6.6), are the rates of generation and degradation of collagen fibres, respectively.

2. Rotation: The angle of a collagen fibre changes according to

$$\frac{d\theta}{dt} = \begin{cases} k_{\text{cf,rot}}(C)||\sin(\Theta-\theta)||, \ \Theta-\theta \in (0,\frac{\pi}{2}) \cup (\pi,\frac{3\pi}{2}) \cup (2\pi,\frac{5\pi}{2}) \\ -k_{\text{cf,rot}}(C)||\sin(\Theta-\theta)||, \ \Theta-\theta \in (\frac{\pi}{2},\pi) \cup (-\frac{\pi}{2},0) \cup (\frac{3\pi}{2},2\pi) \end{cases}, \tag{6.16}$$

where $k_{\text{cf,rot}}$ is the rate of rotation estimated from eq. (6.6).

Since the material properties are the same about $\mathbf{f}$ and $-\mathbf{f}$, we only need to consider the values of $\theta \in (-\pi/2, \pi/2)$. To achieve this, the following transformation is used:

$$\begin{cases} \theta \Leftarrow \theta, & \theta \in (-\frac{\pi}{2}, \frac{\pi}{2}), \\ \theta \Leftarrow \theta - \pi, & \theta < \frac{\pi}{2}, \\ \theta \Leftarrow \theta + \pi, & \theta < -\frac{\pi}{2}. \end{cases} \tag{6.17}$$

The deformed and remodelled fibre structure needs to be pushed back to the reference configuration ([31]),

$$\mathbf{f}_0(\theta) = \frac{\mathbf{F}^{-1}\mathbf{f}(\theta)}{||\mathbf{F}^{-1}\mathbf{f}(\theta)||}. \tag{6.18}$$

where $\mathbf{F}$ is the deformation gradient and $\mathbf{f}_0$ is the fibre vector in the reference configuration.

6.2.2.4 Upscaling the Fibre Structure from the Fibre Level to the Tissue Level

The updated volumetric fraction Φ_{cf} is

$$\Phi_{\text{cf}} = \frac{N_{\text{tot}}}{N_{\text{tot}}^0} \Phi_{\text{cf}^0}, \tag{6.19}$$

where Φ_{cf^0} and and N_{tot}^0 are the volumetric fraction and numbers of the fibres at the reference configuration.

The fibre orientation density function, when pushed back to the reference configuration, is estimated from

$$\varphi(\theta) = \pi \frac{N(\theta)}{N_{\text{tot}}}. \tag{6.20}$$

6.2.3 Constitutive Laws for Myocardium

6.2.3.1 Modified HO Model with Fibre Orientation Density Function

For the remote healthy myocardium ($r(\mathbf{X}) > r_0$), we use the standard HO model [35], i.e.

$$\Psi = \Psi_{\text{m}} + \Psi_{\text{cf}}, \tag{6.21}$$

where

$$\Psi_{\text{m}} = \frac{a}{2b}\left\{\exp\ [b(I_1 - 3] - 1\right\}, \quad \Psi_{\text{cf}} = \frac{a_{\text{cf}}}{2b_{\text{cf}}}\left\{\exp\left[b_{\text{cf}}(I_4(\theta) - 1)^2\right] - 1\right\}, \tag{6.22}$$

in which a, b a_{cf}, b_{cf} are material parameters, and I_1, I_4 are the invariants of the right Cauchy–Green tensor $\vec{C} = \vec{F}^{\text{T}}\vec{F}$,

$$I_1 = \vec{C} : \mathbf{I}, \quad I_4 = \mathbf{u}_0(\theta) \cdot \mathbf{C}\mathbf{u}_0(\theta), \tag{6.23}$$

Here ':' denotes a double contraction, and $\mathbf{u}_0(\theta) = \cos\theta\ \mathbf{c}_0 + \sin\theta\ \mathbf{l}_0$.

To describe the mechanical behavior of the infarcted tissue ($r(\mathbf{X}) \leq r_0$), we modify the HO model as

$$\Psi = \Phi_{\text{m},t}\Psi_{\text{m}} + \Phi_{\text{cf},t}\Psi_{\text{cf}}, \tag{6.24}$$

where $\Phi_{\text{m},t} (= 1 - \Phi_{\text{cf},y})$ is the volume fraction of the ground matrix, Ψ_{m} is the same as in (6.22) but Ψ_{cf} is changed to

$$\Psi_{\text{cf}} = \frac{1}{\pi}\frac{a_{\text{cf}}}{2b_{\text{cf}}}\int_{\Sigma}\left\{\exp\left[b_{\text{cf}}(I_4(\theta) - 1)^2\right] - 1\right\}\varphi_t(\theta)\ \mathrm{d}\theta. \tag{6.25}$$

Notice that the integration in (6.25) is over a domain Σ in which the fibres are in tension, not $(-\pi/2, \pi/2)$. This is because collagen fibres bear load only when they are stretched. We will address this point in Section 2.3.2.

A rule-based myocardium fibre generation algorithm is adopted to describe the local mean fibre angle. We first calculate the normalized distance parameter d for an arbitrary material point $\mathbf{X}$ as

$$d = \frac{d_{\text{endo}}}{d_{\text{endo}} + d_{\text{epi}}}, \tag{6.26}$$

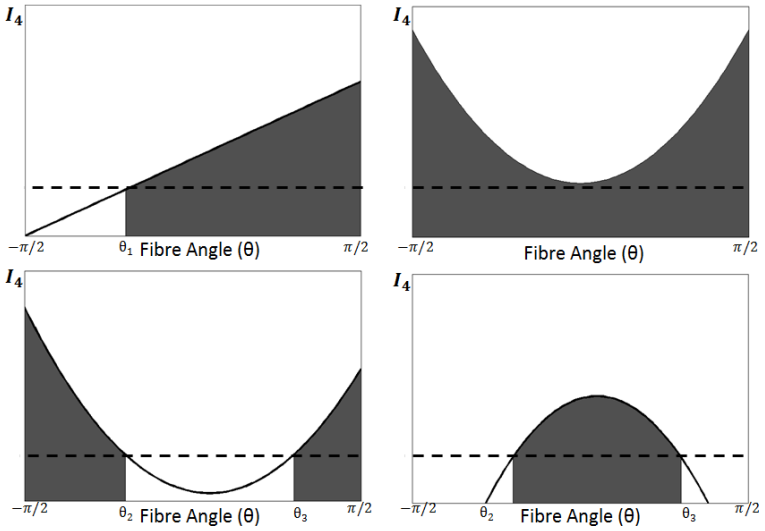

FIGURE 6.3: The shadowed areas show the range of Σ of stretched collagen fibres within $-\frac{\pi}{2} < \theta < \frac{\pi}{2}$ for selected scenarios (dash line denotes $I_4 = 1$): (a) case 1, $C_{23} > 0$; (b) case 2, $C_{33} - 1 > 0, \Delta \leq 0$; (c) case 2, $C_{33} - 1 > 0, \Delta > 0$; (d) case 2, $C_{33} - 1 < 0, \Delta > 0$.

where d_{endo}, d_{epi} are the distances from $\mathbf{X}$ to the endocardial and epicardial surfaces. Then, the local mean fibre angle $\bar{\theta}_0$ at $\mathbf{X}$ is defined as

$$\bar{\theta}_0 = \theta_{\max}(1 - 2d),$$

where $\theta_{\max} = \pi/3$, since it has been observed that the mean angle of fibres in a healthy left ventricle rotates transmurally across the heart wall from $\pi/3$ at the endocardial surface to $-\pi/3$ at the epicardial surface [51].

6.2.3.2 Exclusion of the Compressed Fibres

To exclude the compressed fibres, we choose Σ in eq. (6.25) so that

$$I_4 > 1, \quad \text{or} \quad (C_{22} - 1)\cos^2\theta + 2C_{23}\sin\theta\cos\theta + (C_{33} - 1)\sin^2\theta > 0, \tag{6.27}$$

where C_{ij} are the Cartesian components of $\mathbf{C}$. Eq. (6.27) gives the range of Σ for the stretched collagen fibres in the following two cases.

- Case 1: $C_{33} = 1$,

$$\Sigma = \begin{cases} (\theta_1, \frac{\pi}{2}), & C_{23} > 0 \\ (-\frac{\pi}{2}, \theta_1), & C_{23} < 0 \\ (-\frac{\pi}{2}, \frac{\pi}{2}), & C_{23} = 0, \quad C_{22} > 1 \\ \varnothing, & C_{23} = 0, \quad C_{22} < 1 \end{cases} \tag{6.28}$$

  where $\theta_1 = \arctan\frac{1 - C_{22}}{2C_{23}}$.

- Case 2:

$$\Sigma = \begin{cases} (-\frac{\pi}{2}, \frac{\pi}{2}), & C_{33}-1>0, \quad \Delta \le 0, \\ (-\frac{\pi}{2}, \theta_2) \cup (\theta_3, \frac{\pi}{2}), & C_{33}-1>0, \quad \Delta > 0 \\ (\theta_2, \theta_3), & C_{33}-1<0, \quad \Delta > 0 \\ \varnothing, & C_{33}-1<0, \quad \Delta < 0 \end{cases} \tag{6.29}$$

where $\Delta = (2C_{23})^2 - 4(C_{33}-1)(C_{22}-1)$, and θ_2 and θ_3 are the roots of (6.27).

The Cauchy stress is then

$$\begin{aligned} \boldsymbol{\sigma} &= -p\mathbf{I} + \mathbf{F}\frac{\partial \Psi}{\partial I_1}\frac{\partial I_1}{\partial \mathbf{F}} + \mathbf{F}\frac{\partial \Psi}{\partial I_4}\frac{\partial I_4}{\partial \mathbf{F}} \\ &= -p\mathbf{I} + \Phi_{\mathrm{m},t}\; a \exp[b(I_1-3)]\mathbf{B} \\ &\quad + \frac{1}{\pi}\Phi_{\mathrm{cf}} \int_{\Sigma} 2a_{\mathrm{cf}}(I_4-1)\exp[b_{\mathrm{cf}}(I_4-1)^2]\boldsymbol{\varphi}(\theta)\mathbf{u}(\theta)\otimes\mathbf{u}(\theta)\mathrm{d}\theta, \end{aligned} \tag{6.30}$$

where $\mathbf{B} = \mathbf{F}\mathbf{F}^{\mathrm{T}}$ is the left Cauchy-Green deformation tensor.

6.2.3.3 Change of Basis from Cartesian to Local Coordinates

In numerical simulation, the Cartesian coordinates are usually employed to describe the deformation of material point $\mathbf{X}$, which indicates that the deformation tensor $\mathbf{F}$ is defined with Cartesian base $\{\mathbf{e}_i\}$. However, the fibre family is described by a local coordinate system ($\mathbf{c}_0$, $\mathbf{l}_0$. In order to exclude the compressed fibres, it is convenient to transform the description of fibre orientation between the global Cartesian coordinates and the local polar coordinates, namely,

$$\mathbf{x}^* = \mathbf{Q}\mathbf{x}, \tag{6.31}$$

where * indicates the corresponding variable in the local coordinate, and $\mathbf{Q}$ is the rotation tensor ($\mathbf{Q} = \mathbf{f}\otimes\mathbf{e}_1 + \mathbf{c}\otimes\mathbf{e}_2 + \mathbf{l}\otimes\mathbf{e}_3$).

Then the local deformation gradient and right Cauchy–Green tensor are given as

$$\mathbf{F}^* = \mathbf{Q}\mathbf{F}, \quad \mathbf{C}^* = \mathbf{Q}\cdot(\mathbf{F}^T\mathbf{F})\mathbf{Q}^T. \tag{6.32}$$

TABLE 6.1: fitted material parameters for myocardium from [61, 66].

Initial volumetric fractions	$\Phi_{\mathrm{m},t_0} = 0.97$	$\Phi_{\mathrm{cf},t_0} = 0.03$
Initial concentration parameter	$\sigma_0 = 9.10$	
matrix parameters	$a = 2.28$ kPa	$b = 1.8$
Collagen parameters	$a_{\mathrm{cf}} = 132.0$ kPa	$b_{\mathrm{cf}} = 3.45$

6.2.4 Coupled Agent-based and FE Model

The LV diastolic dynamics is simulated using a coupled agent-based and FE LV model. We assume that mechanical cues are based on end-diastolic state and the remodelling only occurs in the MI region. The computational flowchart is shown in fig. 6.4.

Coupling of the agent-based model and finite element method is operated entirely within the FORTRAN coding environment. The agent-based model enabled one-to-one mapping of the predicted collagen fiber structure and transported the statistical description of fibre structure into to constitutive parameters for each finite element; then the finite element model could inform remodeling in corresponding element with mechanical states and feedback information to agent-based model.
Overall, the cycle of coupled model ran as follows.

- Simulate end-diastolic mechanical states (heart pressure) of the FE model of left ventricle; with helps of the constitutive laws of heart tissues eq. (6.24), the mechanical information, including the stress and strain distributions, will be obtained from the LV FE model after applying boundary conditions.

- Compute mechanical guidance and updated resultant cues for individual fibroblast and import the deformation tensors into agent-based model for FE simulation. The mechanical cue for individual cell will be calculated via eq. (6.8). Then, the resultant cue will be updated via eq. (6.7) – eq. (6.13), which will guide the movements of single cell (eq. (6.11)). At the edges of infarction, the movements of cells are random, while the effects of environmental cues is ignorable to guide the cell moving towards the infarction center. In this thesis, the cell quantity is constant in the infarction region during the healing process. It can be explained as: the cell movement is random at the boundary of infarct. Then, it is assumed that one new cell will move into infarction region across the boundary, when the tracked cell is moving out. Besides, since the feature of collagen fibre structure, such as depositions and degradations of fibres, are stable for healthy tissues. We ignore the fibre modelling for healthy tissue and assume the material parameters are constant.

- Compute the fibre depositions, degradations and rotations. After the cell migration, the collagen fibre family will be modified by the traced cell at the particular material points. The total fibre number will be changed (eq. (6.15)), while the fibre angles will be updated (eq. (6.16) – eq. (6.18)).

- Compute new constitutive parameters. In this paper, the variable constitutive parameters are volumetric fractions for matrix material ($\Phi_{\mathrm{m},t}$) and collagen fibres ($\Phi_{\mathrm{cf},t}$), and the fibre orientation density function φ_t. For healthy tissues, the constitutive parameters are constant as Φ_{cf^0}, Φ_{m^0} and φ_0. And for infarcted tissues, the constitutive parameters

are updated via agent-based model (eq. (6.19) and eq. (6.20)), with helps of the updated statistical feature of fibre family from last step.

- Transport new constitutive parameters into constitutive law of heart tissues for each individual FE element defined by FE method.
- Repeat the entire sequence for next time step till the end of heart healing period.

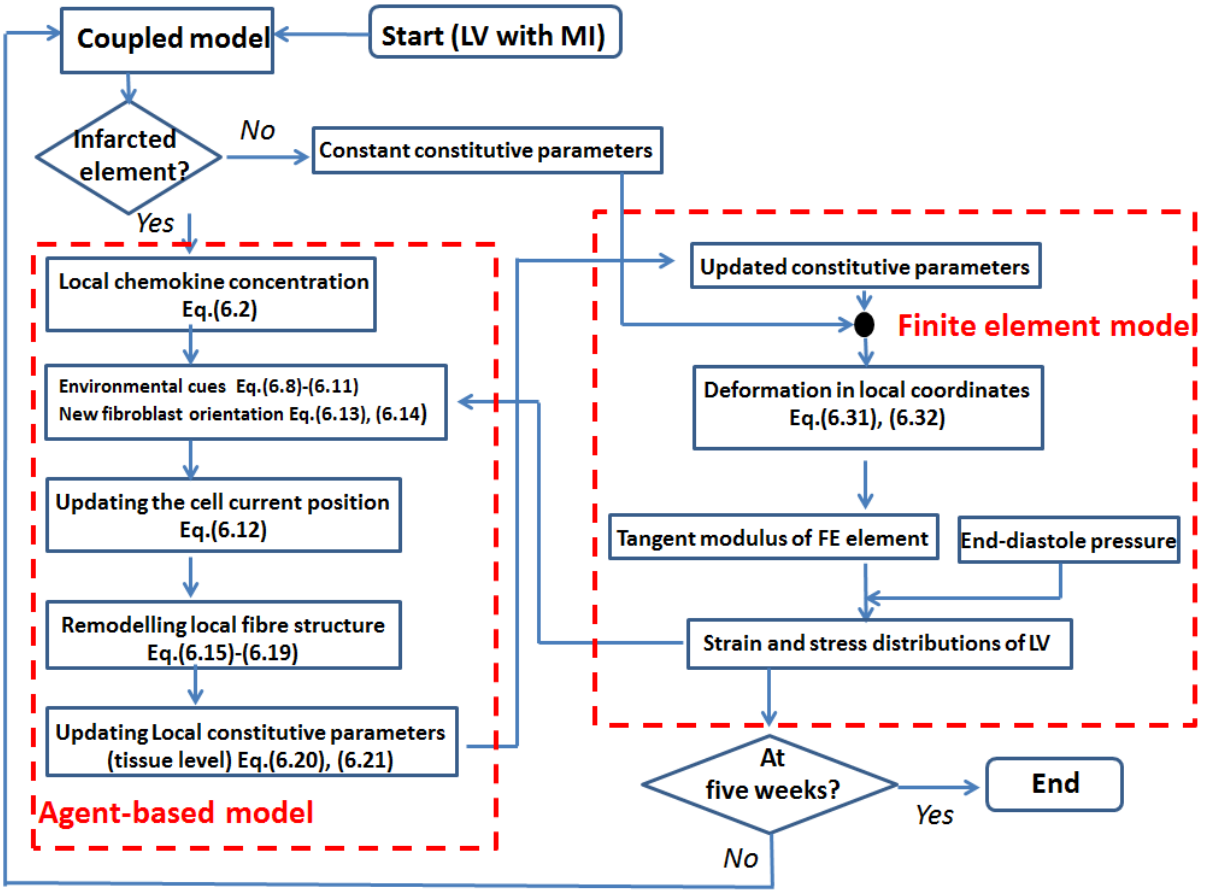

FIGURE 6.4: Flowchart of the coupled agent-based and FE LV model.

6.3 Results

6.3.1 MI Healing Case Studies and Parameters

To validate the model, we follow the experimental study of the infarcted LV of rats by Fonovsky et. al [20], in which cyroinfarctions were created by sewing sonomicrometer crystals into tissues of the epicardial surface of rats' ventricles. After weeks of healing, the hearts were harvested to study the collagen structures at the surface of infarcted zones. We select two cases from [20] to simulate. In the first case, a circular MI is induced in the mid-ventricular anterior wall,

as shown in fig. 6.5(a); In the second case 2, an elliptical MI ($eccentricity \approx 0.8$) is at mid-ventricular anterior wall, as shown in fig. 6.5(b). According to [66], a fibroblast cell is assumed to cover volume of 25X25X25 μm^3. The number of cells in each FM element of infarcted region is determined by the ratio of cell-covered volume to the volume of the FE element. The model time step bigger than 0.5h can reproduce the cell migration data measured in [12]. In this thesis, the maxim time step is employed as 0.5h in order to gain the computational efficiency, by reducing the quantity of time steps in agent-based model to simulate the fibroblast migration.

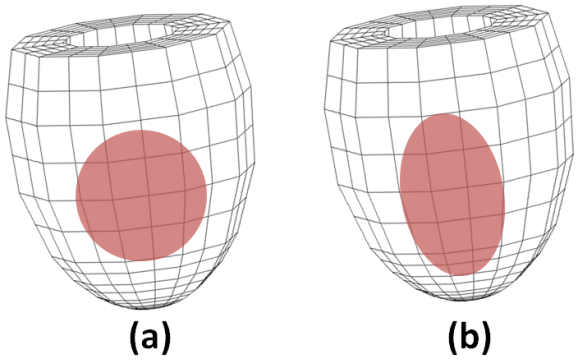

FIGURE 6.5: The FE models of (a) a transmural circular cryoinfarct with $r_0 \approx 5.5$mm and $\mathbf{X_c} = (10.12, 2.82, 0.81)$, and (b) a transmural elliptical cryoinfarct (with long axix $\approx$ 15mm, short axis $\approx$ 5mm and $\mathbf{X_c} = (10.12, 2.82, 0.81)$, in the anterior wall.

We model the healing process for six weeks when the mature scare is formed and the ventricular filling pressure incrased [20]. Hence, a linearly-increasing end-diastolic pressure profile is assumed, with values of 12 mmHg at time 0 to 18 mmHg at 6 weeks. The LV base is constrained in the longitudinal direction, but free movements in radial and circumferential directions are allowed. The model parameters are listed in II, following [20].

6.3.2 Evolution of the Fibre Structure Post-MI

The simulated collagen accumulations for both the circular and elliptical MI shapes in the infarct centre at 0, 1, 2, and 5 weeks post-MI are shown in fig. 6.6. The volume fraction increases from 3% to around 28%. This agrees well with the measured data [18]. We note there is very little difference between the different MI shapes.

The distribution of the collagen fibres at different weeks post-MI is shown in fig.(6.7). At the five weeks post-MI, the simulated result is also compared with the corresponding measurement [18]. Given the large error bars in the measurements, there is a reasonable agreement in terms of the overall distribution and the maximum collagen fibre fraction predicted.

TABLE 6.2: Parameter values related to fibroblast dynamics and collagen remodelling.

Fibroblast dynamics				
Radius of fibroblast cell	R_{cell}	5		μm
maximum collagen fibre number per volume	β	14000		μm^{-3}
chemokine diffusion coefficient	D_c	1.6		$\mu\text{m}^2\text{s}^{-1}$
chemokine degradation rate	$k_{\text{c,deg}}$	0.001		s^{-1}
chemokine generation rate	$k_{\text{c,gen}}$	0.01		nms^{-1}
persistence tuning factor	η	0.175		
Persistence cue weight factor	W_{p}	0.333		
Structural cue weight factor	W_{s}	0.167		
Mechanical cue weight factor	W_{m}	0.167		
Chemical cue weight factor	W_{c}	0.167		
Collagen remodelling				
		Quiescent (min)	activated (max)	
Collagen degradation rate coefficient	$k_{\text{cf,deg}}$	2.4E-4	2.5E-3	h^{-1}
Collagen generation rate coefficient	$k_{\text{cf,gen}}$	7.5E-4	7.3E-2	%volume$\cdot\ \text{h}^{-1}$
chemokine fibre rotation generation rate	$k_{\text{cf,rot}}$	5	5	deg$\cdot\ \text{h}^{-1}$
time step	Δ t	0.5	h	

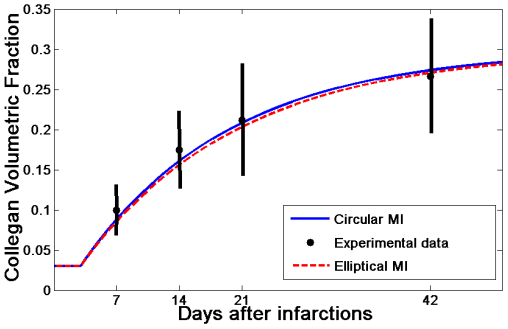

FIGURE 6.6: Comparison of estimated infarct collagen volumetric evolutions with the measurements: the collagen volumetric fractions of infarcted tissues are calculated through the remodelling processes of collagen fibre families via eq. 6.19. Then, the volume average of collagen fibre fractions among all infarcted tissues is employed to describe the evolutions of the collagen fraction. The simulated results (blue for Circular MI and red for Elliptical MI) are compared with evolutions of experimentally-measured collagen fractions in [18] (black dots with error bars).

Fig. 6.8(a) shows that for both MI shapes, the mean collagen angle at 20% of the distance from the epicardium to endocardium surfaces decreases significantly at the fifth week (from the initial 45^o to 22.5^o for the circular MI, and to 10^o for the elliptic MI.

As the anisotropy in collagen fibre structure is a critical determinant for the pump function of LV ([20], [66]), we use the kurtosis of collagen fibre structure to describe the anisotropy level, which is defined as

$$\text{Kurt}(\theta) = \frac{E\left[(\theta-\bar{\theta})^4\right]}{E\left[(\theta-\bar{\theta})^2\right]^2}, \tag{6.33}$$

where $E(\bullet)$ is the expectation of $\bullet$, and $\bar{\theta}$ is the mean fibre angle. A smaller value of kurtosis indicates a lower level of anisotropy. fig 6.8(b) shows that the anisotropy level at the infarcted region decreases in the beginning, but eventually reaches a plateau. It is interesting to see that

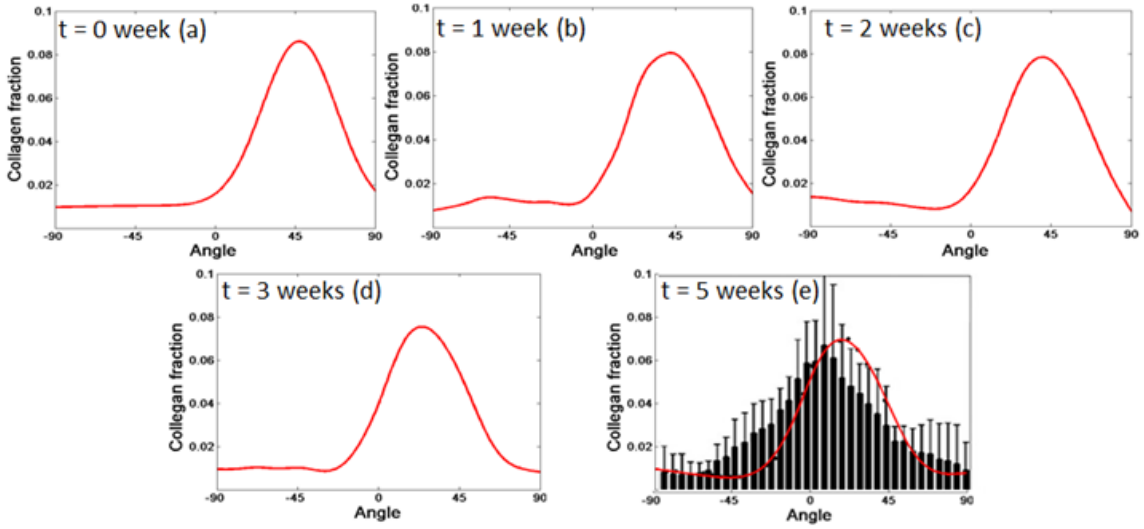

FIGURE 6.7: The evolution of collagen fibre structure for a circular MI: (a) – (e) 0–5 weeks; (f) the overlap of estimated fibre structure with the experimental measurements 5 weeks post-MI [18])

although the fibre volume fraction is similar in both the circular and elliptical MI shapes, the distribution of the fibres is quite different. The evolution of the fibre structure following the elliptical MI is faster than that of the circular MI. The isotropic level of fibre structure, in terms of the kurtosis, decreases from the initial valuve of 3.38 to 3.29 for the circular MI, and to 3.21 for the elliptical MI. In general, the elliptical MI causes greater changes in terms of mean fibre and kurtosis over the healing time. However, in both cases, the volumetric fraction increased to a stable level of around 28% (fig. 6.6) at the fifth week. The decreased anisotropy of the fibre distribution over time is better shown in fig. 6.9, where the local fibre structure near the epicardial surface at different weeks post-MI. Note to make the fibre structure visible, we have averaged the mean values of fibres over much smaller local pockets.

6.3.3 Evolution of the Stress and Strain Level Post-MI

The first principle stress distribution for the circular MI at different time post-MI is shown in fig. 6.10, where the infarcted region is indicated by an arrow. It is evident that the stress distribution is greatly influenced by the evolution of the local collagen fibre structure. The stress increases at the endocardial surface and gradually smears out towards the epicardial surface. The local stress level around the MI region is caused by collagen accumulation and re-orientation, but the overall stress also increases due to the increased end-diastolic pressure.

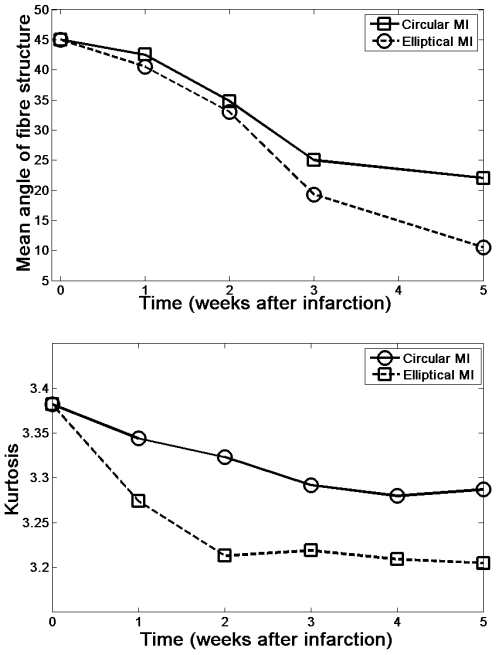

FIGURE 6.8: (a) The mean angle changes during the circular MI, (b) the kurtosis of the fibre structure.

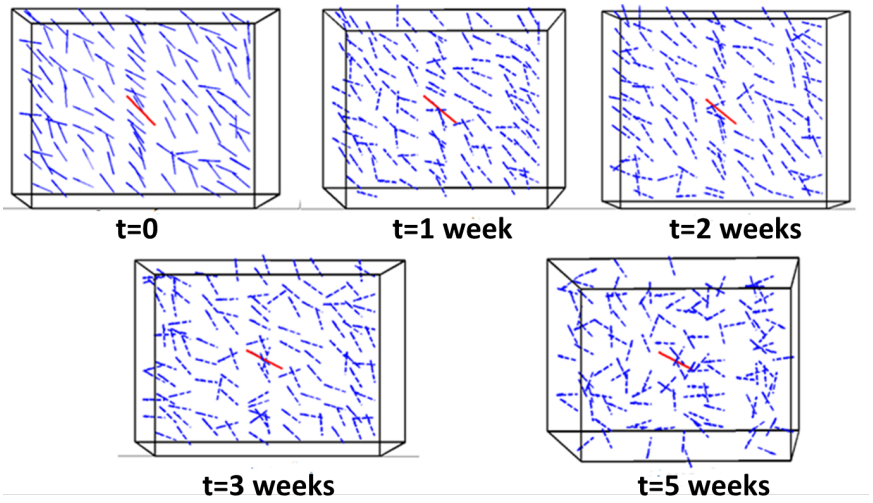

FIGURE 6.9: The evolution of collagen structure at the epicardial surface of the circular infarcted zone: The red arrow is the mean angel of overall fibre structure, while the blue arrows are the mean values of fibres of much smaller local pockets of size.

The involution of the stress level with time is shown in fig. 6.11, the corresponding mean stress values at the infart centre are also listed in Table III. During the healing process, the circumferential stiffness is reinforced by the newly deposited collagen fibres. Hence, the maximum circumferential stresses increases dramatically from 4.3 kPa to 15.1 kPa. The local longitudinal stress has not changed much (from 0.78 kPa to 0.76 kPa at 5 weeks). This is because most of the collagen fibre remodelling happens in the circumferential direction. The elavated circumferential stress level around the MI region can lead to further adverse remodelling in the heart, such

as myocyte apoptosis.

The stress distribution for the elliptical MI is similar to that of the circular MI, but the absolute stress levels are slightly different as shown in Table III.

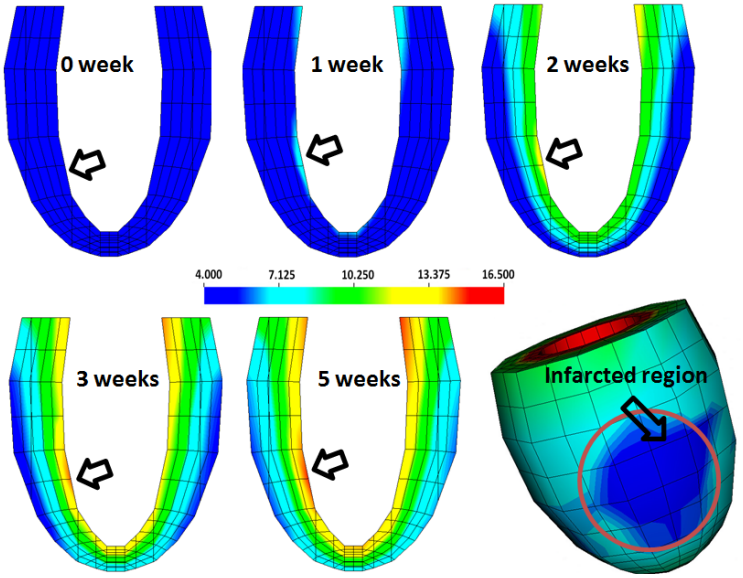

FIGURE 6.10: Evolution of the first principle stress distribution for the circular MI; its location is indicated by the arrow. The bottom right is a 3D plot at 5 weeks post-MI.

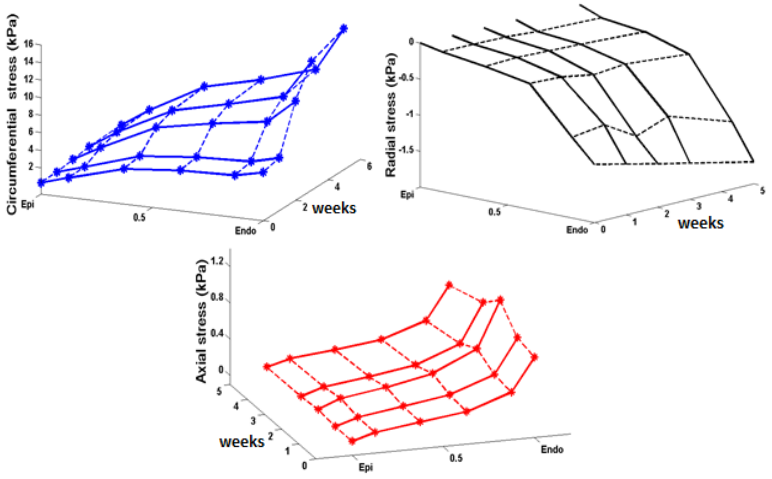

FIGURE 6.11: The evolution of (a) radial stress; (b) circumferential stress; and (c) longitudinal stress, for the circular MI.

Fomovsky et al. [20] also measured the evolution of strain during the healing process in the epicardial surface of the infarcted region. They found that the circumferential strain in the infarct region continuously decreases with an average decrease of 65%, and an average decrease of 13% for the longitudinal strain at six weeks. Our simulation results give similar trends as

TABLE 6.3: Comparison of the mean stress at the infarct centre post-MI

	Circumferential stress (kPa)		**longitudinal stress (kPa)**	
	Cicular MI	Elliptical MI	Cicular MI	Elliptical MI
0 week	4.3	4.5	0.78	0.78
1 week	5	5.8	0.82	0.80
2 weeks	10.2	8.8	1.17	0.84
3 weeks	13.7	13.7	0.91	0.61
5 weeks	15.1	16.3	0.76	0.49

shown in fig. 6.12 for both MI shapes. For example, in the case of the circular MI, the strain shows an average decrease of 49% in the circumferential strain (0.03 $\pm$ 0.01 at 0 weeks, 0.04 $\pm$ 0.024 at 1 weeks, 0.042 $\pm$ 0.01 at 3 weeks, 0.03 $\pm$ 0.02 at 4 weeks, and 0.022 $\pm$ 0.02 at 5 weeks), and an average decrease of 35% in the longitudinal strain at 5 weeks.

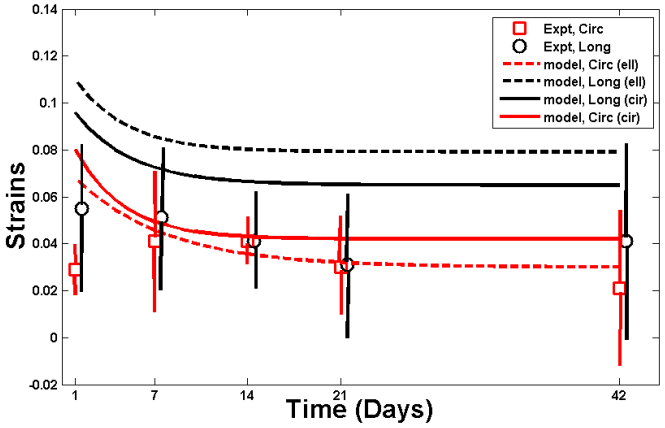

FIGURE 6.12: Strain evolutions over time. (a): preferential accumulation in the circumferential direction reduced strain anisotropy. The predicted strain trends agreed reasonably with the experimentally measured strains 6 weeks after cryoinfarction [18].

The evolution of the strains at endocardial surface of the elliptical MI is similar compared to the circular MI (fig. 6.12). Both circumferential and longitudinal strains decrease to the homeostatic state after healing process, with 31% decrease in the circumferential strain, 43% decrease in the longitudinal strain.

6.3.4 Influence of the Mechanical Cue

We now isolate the effect of the mechanical cue by switching it on and off. The mechanical cue was suggested to be the most important factor of regulating the collagen alignment [66]. fig. 6.13 shows the distribution of the collagen fibres with and without the mechanical cue. The collagen alignment in the infarcted region decreases more quickly when the mechanical cue is switched off. In addition, the mean angle of fibre structure does not change much during the

healing process; it remains more or less unchanged. When the mechanical cue is on, there is much better agreement with the experiments in terms of the fibre distribution and mean angle.

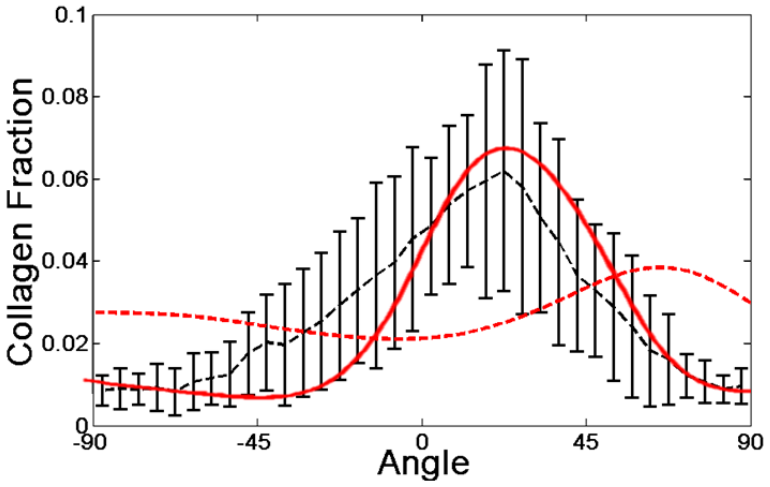

FIGURE 6.13: Fibre structure at 5 weeks post-MI, with (red solid) and without (red dashed) the mechanical cue. The measured data are also shown as dashed line with error bars

6.4 Discussion

Our model is the first to couple an agent-based model with a realistic 3D LV model with local MI and is a significant extention of the previous study based on a 2D FE slab [67]. In particular, a modified HO consititutive law is employed to simulate the mechanical behaviour for myocardium post-MI, where fibre dispersion due to wound healing needs to be accounted for. To exclude the effects of the compressed fibres, an analytical fibre switch is implemented in this FE LV model.

The challenge of developing a multiscale model for the evolutions of collagen fibre structure and mechanical states of infarcted LV is the involvement of many material parameters. In this study, our parameters are pooled from published cryoinfarction measurements [18] and the predictions from our model showed good quantitative agreement. The only parameter not based on the measurements is the persistance tuning factor η (Table II). To see how much effect this has, we also ran the model with the value of η increased. Our results (not shown) suggest that an increased η leads to a greater standard derivation σ, reducing the randomness of the new fibroblast angles through (6.13). The fibre structure reaches the steady state faster, and matured at around 4 weeks if η is doubled, which is one week earlier than using the default value of η. The final fibre structures, however, are very similar.

Environmental cues, such as the chemical, the mechanical and the persistence cues, play important roles on regulating collagen fibre structures during MI healing. Our results show a poor

agreement with measurements if the mechanical cue is switched off. McDougall et al. suggested that the distribution of the chemical gradient established by the chemokines generated around dermal wound, determines patterns of local collagen alignment [53]. In our simulations, different chemokine distributions are realised through the MI shapes; the chemokine field is mostly flat inside the infarction, but with a sudden drop near the infarct border. The influences of chemical gradient are greater in the region near infarcted border. Therefore, the mean angle and kurtosis of the fibre distribution for different infarct shapes are different. Our simulations are also supported by the observations in [66].

Finally, we mention the limitations of this study. Firstly, the transmural fibroblast migration is not considered. Secondly, our model only consider the diastolic dynamics without active contraction. Therefore the mechanical cue is simplified. Furthermore, no transient chemokine concentration is included. Finally, we understand that myocardial infarction in the human heart may have different biological processes and parameters compared to cryoinfarction in the rat heart. Estimation of these parameters for paticent-specific human hearts post-MI, therefore, remains a daunting task.

6.5 Conclusion

We have developed a multiscale MI model by coupling an agent-based model for collagen remodelling to a three-dimensional LV model in diastole. To describe the remodelled material properties of myocardium in the infarted region, a collagen fibre tension-compression 'switch' is incorporated in the FE LV model for the first time. The time-dependent model also captures the interaction and information exchange processes between the mechanical behaviour and collagen tissue remodelling guided by various external cues. The model results show the similar trends in collagen cumulation and collagen alignment during the infarct healing for five weeks. The shapes and the locations of infarctions could affect the local collagen accumulation and the LV dynamics. For example, the mean angle of fibre structure decreases from about 45^o to 22.5^o at near the endocardial surface for the circle infarction, but decreases less in the elliptic infarction. Stresses are affected for both the circle and the ellipse infarctions. The reduction of the circumferential strains at five weeks post-MI agrees well with the experimental observations. With further development, we expect that this multiscale approach could provide useful insights in clinical practices for MI patient management.

6.6 Appendix I: Coupled Agent-based and Cylindrical Modelling of LV Post Myocardial Infarction

6.6.1 Introduction

As mentioned in this chapter, at the cellular level, collagen deposition and remodelling are regulated by fibroblast cell alignment. Environmental cues, such as the mechanical and chemical cues, have been shown to influence cell migration and regulate the (collagen) fibre structures [12].

The agent-based models that accounting for these effects have been developed. Here, a 2D slab model of the myocardium infarction [67] is developed to study the trends of remodelling processess after MI.

6.6.2 Methodology

6.6.3 Geometry of LV (Cylindrical Tube Model)

A geometry of LV is constructed as an idealised cylindrical tube. This geometry will be used to simulate the mechanical responses of mice LV with regional cyroinfarction at the end-distolate.. Along tube wall, 50 nodes are seeded. The cylindrical coordinates (R, Γ, Z) are used to describe the material point in this undeformed geometry, with basis as $\{\mathbf{E}_r, \mathbf{E}_\Gamma, \mathbf{E}_Z\}$.

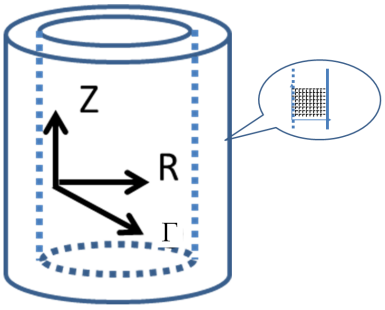

FIGURE 6.14: Depiction to cylindrical model of LV. the dashed area is the cross-section of infarction region with nodes.

The LV is constructed by the fibre-reinforced tissues, which is composed with collagen fibre and myocyte sheet ([35]). As orthotropic material, the (local) fibre direction is assumed to be tangent to LV surface, while the myocyte sheet construction is orthogonal to fibre structure. Therefore, the fibre structure is location-dependent. At an arbitrary material point $\mathbf{X}$, the fibres structure are assumed to be in the local '$\mathbf{E}_\Gamma - \mathbf{E}_Z$' plane in undeformed LV as the (nature) reference configuration.

The infarction is developed respect to the infarction center zone, which is defined as

$$R_{\mathrm{o}} \geq R \geq R_{\mathrm{i}},\ 2\pi \geq \Gamma \geq 0,\ L \geq Z \geq 0$$

where R_{i} and R_{o} are the outer and inner radius of LV cylindrical tube.

6.6.3.1 Agent-based Model

6.6.3.2 MI Healing and Chemokine Concentration

The general form of chemokine concentration is given in eq. (6.2), as well as the boundary conditions in eqs. (6.3) and (6.4). In this simplified model, the chemokine concentration is assumed to only depend on the distance along z-axis from the infarct center. Therefore, the chemokine concentration could be rewritten in cylindrical coordinates $\{R,\Gamma,Z\}$ as

$$D_c \bigtriangledown^2 \hat{C}(Z) = \begin{cases} k_{\mathrm{c,deg}}\hat{C}(Z) - k_{\mathrm{c,gen}} & Z < Z_0, \\ k_{\mathrm{c,deg}}\hat{C}(Z) & Z \geq Z_0, \end{cases} \tag{6.34}$$

where $\hat{C}(Z)$ is the concentration equation in cylindrical coordinate ($\hat{C}(Z) = C(\mathbf{X} - \mathbf{X}_c)$), Z_0 is at the infarct boundary.

The boundary conditions (eqs. (6.3) and (6.4)) are rewritten as

$$\begin{cases} (\frac{\mathrm{d}C}{\mathrm{d}Z}|_{Z=Z_0})^+ = (\frac{\mathrm{d}C}{\mathrm{d}Z}|_{Z=Z_0})^- & \text{if } Z = Z_0, \\ C\,|_{Z=Z_0})^+ = (C\,|_{Z=Z_0})^- & \text{if } Z = Z_0, \\ C = 0 & \text{if } Z = \infty, \\ \frac{\mathrm{d}C}{\mathrm{d}Z} = 0, & \text{at } Z = 0. \end{cases} \tag{6.35}$$

The chemokine equation could be obtained from eq. (6.34) and (6.35) as (fig. 6.15)

$$\hat{C}(Z) = a_1 \exp(a_2 Z) + a_1 \exp(-a_2 Z) + a_0 \quad Z < Z_0, \tag{6.36}$$

where $a_0 = \frac{k_{\mathrm{c,gen}}}{k_{\mathrm{c,deg}}}$, $a_2 = \sqrt{\frac{k_{\mathrm{c,deg}}}{D_c}}$, $a_1 = -\frac{a_0}{2\exp(a_2 Z_0)}$

6.6.3.3 Fibroblast Movement Regulated by Environmental Cues

The fibroblast migrations respond to local environmental cues [19]. Here, the fibroblasts are modelled as rigid discs. The environmental cues for individual cell are defined as: The fibroblast migration are regulated by internal and external environmental cues, such as chemical, mechanical, persistent and structural cues ([12], [19], [66]).

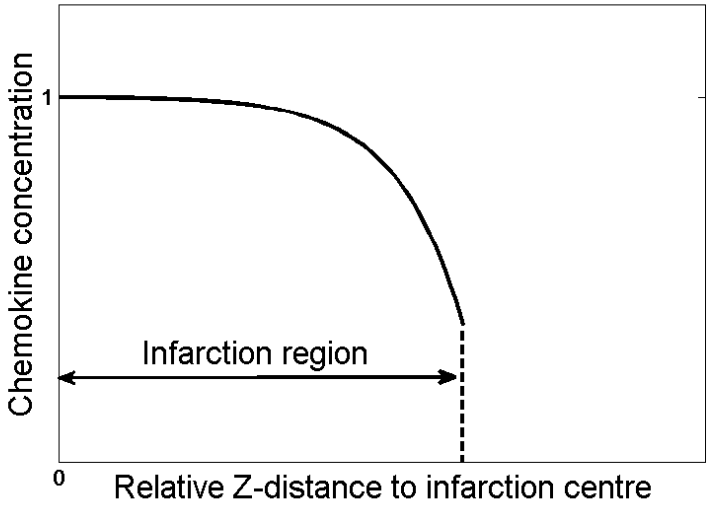

FIGURE 6.15: Depiction to analytical solution of Chemokine concentration: solid line is the Chemokine concentration in the infarction region, while dash line is the one out of infarction.

The chemokine cue is to measure the direction with greatest chemokine concenteration. The indicator of chemokine vector is the production of chemokine concentration and unit outward normal vector at the cell boundary. The distance to infarction could be expressed for the point at boundary of cell ($Z^b_{\text{cell}}(\theta)$) as

$$Z^b_{\text{cell}}(\theta) = Z_{\text{cell}} + \sin(\theta) R_{\text{cell}}, \tag{6.37}$$

where θ is angle to circumferential direction $\mathbf{E}_\Gamma$, Z_{cell} is the Z position of target cell and R_{cell} is radius of cell.

To obtain the local chemical cues, chemokine vector is integrated over the cell boundary in '$\mathbf{E}_\Gamma - \mathbf{E}_Z$' plane as:

$$\mathbf{v}_{\text{c}} = \frac{1}{2\pi} \int_{-\pi}^{\pi} \hat{C}(Z^b_{\text{cell}}) \mathbf{n}(\theta) \mathrm{d}\theta, \tag{6.38}$$

where $\mathbf{v}_c$ is chemical guidance cue vector, $\mathbf{n}$ is unit outward normal vector from cell surface θ.

The mechanical vector and persistent vector are given in eqs. (6.8) and (6.10).

The fibre structural vector can be calculated similar with eq. (6.9), while $\mathbf{u}$ is unit fiber orientational vector as

$$\mathbf{u}(\theta) = \cos(\theta)\mathbf{E}_\Gamma + \sin(\theta)\mathbf{E}_Z.$$

The preferred direction of individual fibroblast is estimated by resultant cue $\boldsymbol{\rho}$ eq. (6.12), current fibroblast orientation is statistically selected from Von mises distribution eq. (6.13), where Θ is

the angle of a single fibroblast cell, $\bar{\Theta}$ is the mean angle of the fibroblast resultant vector $\boldsymbol{\rho}$ in local '$\mathbf{E}_\Gamma - \mathbf{E}_Z$'.

In this reduced agent-based model, the movement of fibroblast is ignored, while it only considers the rotation of fibroblast in '$\mathbf{E}_\Gamma - \mathbf{E}_Z$' plain.

Remodeling of Fibre Structure by Fibroblast Cell

After the fibroblast orientation is statistically determined from eq. (6.13), the structure of the collagen fibres is updated, represented by eqs. (6.15) and (6.16).

6.6.3.4 Upscaling the Fibre Structure from Fibre Level to Tissue Level

In the tissue level, the fibre structure can be described by the fibre volumetric fraction (Φ_{cf}) and fibre orientation density function ($\varphi_t(\theta)$) at time t, which parameters are updated by eqs. (6.19) and (6.20).

6.6.4 Basic Kinematics of Tube Model

Consider LV of heart as an incompressible thick-walled cylindrical tube subjected to external loads. Then, in cylindrical polar coordinates R, Γ, Z, the geometry of heart tube is defined by

$$R_{\text{o}} \geq R \geq R_{\text{i}},\ 2\pi \geq \Gamma \geq 0,\ L \geq Z \geq 0$$

where L is the length of tube.

After applying external loads (heart pressure), in term of (r, γ, z), the geometry of current configuration is given by

$$r_{\text{o}} \geq r \geq r_{\text{i}},\ 2\pi \geq \gamma \geq 0,\ l \geq z \geq 0$$

where r_{i}, r_{o} and l are inner, outer radii and length of deformed tube, respectively.

The isochoric deformation from the undeformed configuration to current configuration is written as

$$\mathbf{x} = r\mathbf{e}_r + z\mathbf{e}_z, \tag{6.39}$$

Material incompressibility gives

$$r = \sqrt{\frac{R^2 - R_{\text{i}}^2}{\lambda_z} + r_{\text{i}}^2}, \quad \gamma = \Gamma, \quad z = \lambda_z Z, \tag{6.40}$$

where $\lambda_z = l/L$ is the constant axial stretch.

The deformation gradient, denoted as $\mathbf{F}$, is given by

$$\mathbf{F} = \frac{\partial \mathbf{x}}{\partial \mathbf{X}} = \lambda_1 \mathbf{e}_r \otimes \mathbf{E}_R + \lambda_2 \mathbf{e}_\gamma \otimes \mathbf{E}_\Gamma + \lambda_z \mathbf{e}_z \otimes \mathbf{E}_Z, \tag{6.41}$$

where

$$\lambda_1 = \frac{R}{r\lambda_z}, \quad \lambda_2 = \frac{r}{R} \tag{6.42}$$

For the tube model, the equilibrium equation $\bigtriangledown \boldsymbol{\sigma} = \mathbf{0}$ is reduced to

$$\frac{\mathrm{d}\sigma_{rr}}{\mathrm{d}r} + \frac{\sigma_{rr} - \sigma_{\gamma\gamma}}{r} = 0, \tag{6.43}$$

With help of pressure boundary condition ($P = -\sigma_{rr}|_{r=r_\mathrm{i}}$), on integration equation (6.43) gives

$$P = \int_{r^\mathrm{i}}^{r^\mathrm{o}} \frac{\sigma_{\gamma\gamma} - \sigma_{rr}}{r} \mathrm{d}r. \tag{6.44}$$

This equation will be used to determine the mechanical response of LV to heart pressure, with help of constitutive laws for passive heart tissues.

6.6.5 Constitutive Laws for LV Tissues

6.6.5.1 Modified HO Model with Fibre Orientation Density Function

The modified HO model is used to describe the constitutive law for heart tissues (eqs. (6.24) - (6.25)).

For the healthy myocardium, the fibre dispersion could be experimentally fitted with a Von mises distribution [38, 70] or a wrapped normal distribution [66]. In this paper, we use the π-periodic Von mises distribution to describe the fibre orientation density function φ_0 for healthy tissue.

$$\varphi_0(\theta) = \frac{e^{\sigma_0 \cos(\theta - \bar{\theta})}}{I_0(\sigma_0)}$$

where σ_0 is the initial concentration parameter, fitted from experimental observation [66], $\bar{\theta}$ is the mean angle of collagen fibre structure. $I_0(\sigma_0)$ is the modified Bessel's function of first kind of order zero [70] as

$$I_0(\sigma_0) = \frac{1}{\pi} \int_0^\pi \exp(\sigma \cos\theta) d\theta.$$

The *in vitro* experimental measurement shows the mean angle of fibre rotates transmurally across the heart wall from $\pi/3$ at the endocardial surface to $-\pi/3$ at the epicardial surface. Here, the myocardium fibre generation algorithm ([89, 95]) is adopted to simulate the local

fibre mean angle. For an arbitrary material point $\mathbf{X}$ of heart tube, the normalized thickness parameter d could be determined by two intramural distances as

$$d = \frac{R_X - R_\mathrm{i}}{R_\mathrm{o} - R_\mathrm{i}} \tag{6.45}$$

The local mean angle of fibre structure could be simulated as

$$\bar{\theta} = \theta_{max}(1 - 2d)$$

where θ_{max} is the maximum fibre angle on the endocardial surface, as $\frac{\pi}{3}$ in this paper.

6.6.5.2 Fibre Switch to Exclude the Compressed Fibre

In the computation of mechanical behavior of myocardium, the undeformed fibre structure is assumed to distribute in the '$\mathbf{E}_\Gamma - \mathbf{E}_Z$' plane. The compressed collagen fibres should be exclued from the mechanical contributions, which requires It requires to solving the inequation of fibre invariance

$$I_4 > 1 \tag{6.46}$$

where I_4 is the fibre invariant; with unit basis $\{\mathbf{E}_R, \mathbf{E}_\Gamma, \mathbf{E}_Z\}$, the right Cauchy–Green tensor ($\mathbf{C} = \mathbf{F}^T\mathbf{F}$) is given with help of eq. (6.41) as

$$\mathbf{C} = \lambda_1^2 \mathbf{E}_R \otimes \mathbf{E}_R + \lambda_2^2 \mathbf{E}_\Gamma \otimes \mathbf{E}_\Gamma + \lambda_z^2 \mathbf{E}_Z \otimes \mathbf{E}_Z. \tag{6.47}$$

Substituting eq. (6.47) into eq. (6.46), it gives

$$I_4 = \lambda_2^2 \cos^2\theta + \lambda_z^2 \sin^2\theta > 1, \tag{6.48}$$

By solving inequality (6.46), the solution is given as:
Case 1:
if $\lambda_2 > 1$, $\theta \in \Sigma = (-\frac{\pi}{2}, \frac{\pi}{2})$.
Case 2:
if $\lambda_2 < 1$,

$$\theta \in \Sigma = (\sqrt{\arctan\frac{1-\lambda_2^2}{\lambda_z^2 - 1}}, \frac{\pi}{2}) \cup (-\frac{\pi}{2}, -\sqrt{\arctan\frac{1-\lambda_2^2}{\lambda_z^2 - 1}}). \tag{6.49}$$

Then, the angel range Σ will be used to describe the stretched collagen fibres in (6.50)

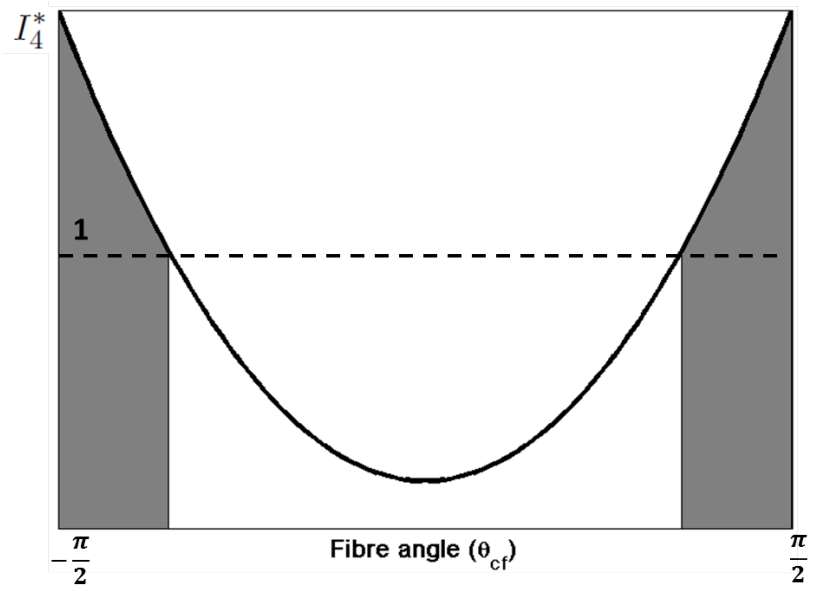

FIGURE 6.16: Depiction of the angel range of stretched fibres: Within the fibre angle range $-\frac{\pi}{2} < \theta < \frac{\pi}{2}$, the shaded regions are computed from eq. (6.48).

The SEF of fibre structure $\Psi_{\mathrm{cf},t}$ at the associated point could be rewritten with help of solution for eq. (6.46) as (fig. 6.17)

$$\Psi_{\mathrm{cf},t} = \Phi_{\mathrm{cf}} \frac{1}{\pi} \frac{a_{\mathrm{cf}}}{2b_{\mathrm{cf}}} \int_{\Sigma} \left[\exp\left(b_{\mathrm{cf}} (I_4(\theta) - 1)^2 - 1 \right) \right] \varphi_t(\theta) \, \mathrm{d}\theta, \tag{6.50}$$

where Σ is the solution of angle domain by inequation (6.46).

Recalling eq. (6.24), for the incompressible myocardium, the Cauchy stress yields as eq. (6.30). Combining eqs. (6.44) and (6.27),the mechanical response of LV will be determined to the given heart pressure.

6.6.5.3 Coupled Agent-based and Tube Model

Coupling of the agent-based model and LV tube model is operated entirely within the MATLAB coding environment. The agent-based model enables one-to-one mapping to regulate local collagen fiber structure by individual cell and transported the statistical description of fibre structure into to constitutive parameters; then the heart tube model uses the new constitutive parameters to determine the mechanical behaviors of LV tube. Overall, the cycle of coupled model runs as follows.

- For infarcted tissues, import the deformation tensors into agent-based model to determine the mechincal cues for fibroblast cells. Compute Other evironmental guidance and updated resultant cues for individual fibroblast.

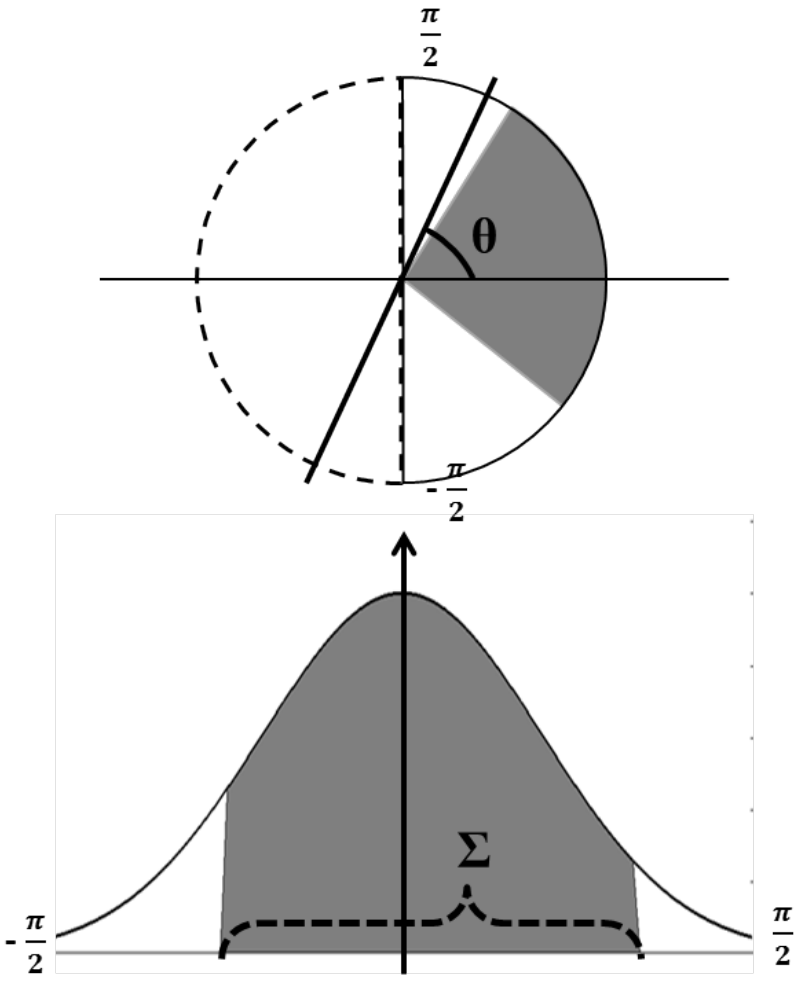

FIGURE 6.17: Depiction of the angel range of stretched fibres in local fibre angle space ($\mathbf{E}_\Gamma - \mathbf{E}_Z$ plane). Within the half circle $-\frac{\pi}{2} < \theta < \frac{\pi}{2}$, the shaded regions are computed from eq. (6.46). The blew figure depicts the associated fibre density function for the fractions of extended collagen fibres.

- Compute the cell rotation and the fibre structure remodeling process for individual fibroblast, with help of resultant cues from the last step.
- Compute new constitutive parameters. In this paper, the variable constitutive parameters are volumetric fractions for matrix material ($\Phi_{\mathrm{m},t}$) and collagen fibres (Φ_{cf}), and the fibre orientation density function φ_t.
- Simulate end-diastolic mechanical states of left ventricle after transporting new constitutive parameters into constitutive law of heart tissues.
- if the healing process doesn't stop, go back the simulation.
- repeat the entire sequence.

6.6.5.4 MI Healing Case Studies

The evolutions of fibre structure and mechanical behaviors of LV have been experimentally investigated by Holmes [20]. In [20], the Cyroinfarctions are created by sewing sonomicrometer crystals into tissues of the epicardial surface of rats' LV. Then, after weeks, the hearts are harvested to study the local strain and the fibre structures of infarcted tissues, which information are collected from the tissues at surface of infarction zone.

In this chapter, it will simulate the remodeling processes of infarcted LV. The constant end-diastole pressure 1.6 (Kpa) is applied on the inner surface. After running the coupled model, the evolutions of collagen volumetric fraction, strains, and stress are simulated over 6 weeks after infarction. To show the influences of the healing process at different location from LV infarction, it investigates the evolutions of stresses and fibre structure for tissues from different locations (fig. 6.19), with different infarction level: (1) the center of infarction, this position is at the center of infarction under highest chemokine effects ($Z = 0$); (2) middle of the infarction, this position is at the middle of infarction center to the infarction edge ($Z = \frac{L}{2}$); (3) edge of infarction, this is the remote region for infarction ($Z = L$).

6.6.6 Results

After introducing a regional infarction to the coupled agent-based and elastic tube model, the change of the collagen structure and mechanical behaviors of LV are simulated.

6.6.6.1 Results for Tissues at Center of Infarction Region

The impacts of infarction occur 3 days after the coronary ligation, while the healing process of heart will start simultaneously with same lag. In this paper, the lengths of collagen fibres are assumed to be constant and stable. Then, the volumetric fraction evolution in infarct myocardium tissue could be directly estimated by the quantitative changes of the total collagen numbers (eq. (6.19)). The value ranges of collagen deposition ($k_{\text{cf,deg}}$) and generation ($k_{\text{cf,gen}}$) rates (table 6.2) are fitted from the published experimental data ([12]) by Holmes [66]. The collagen accumulations are measured at 1, 2, 3, 6 weeks after coronary ligation [18] (from 0.028 to around 0.3), which match well with our calculation (fig. 6.18). Along with the changes of the fibre structure, the mean angle of fibre is also changed. At the epi surface, the mean angle decreases from 60^o at 0 week to 20^o at six weeks (fig. 6.18_b).

The fibre structure is also measured by the collagen fraction for fibre angles. As shown in fig. 6.19, the anisotropic level of fibre structure is decreased, with the decreasing fibre angle

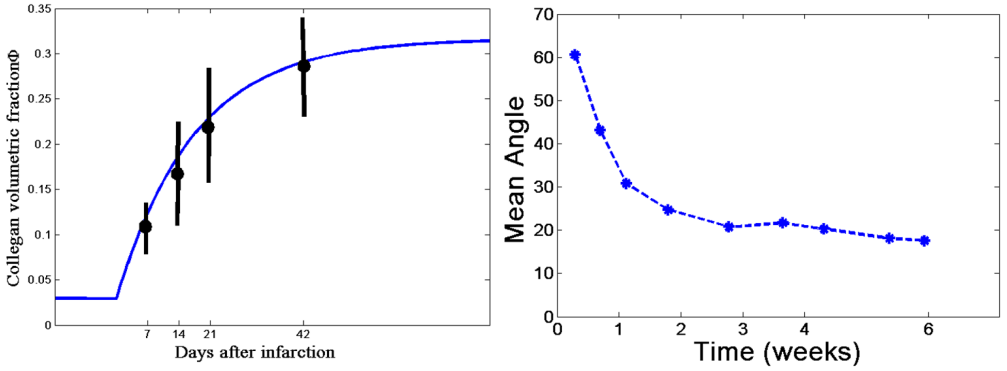

FIGURE 6.18: Estimated infarct collagen volumetric and mean angle evolution at epi surface of infarction heart (Center): Left, the collagen volumetric accumulations are measured by Fomevsky [18] (black dots with error bars), comparing with the estimation by coupled model (blue line); Right, the changes of mean angle during healing process

concentration. The results suggest that the fibre structure will be more isotropic at the infarction, which phenomenon is also experimentally observed [66].

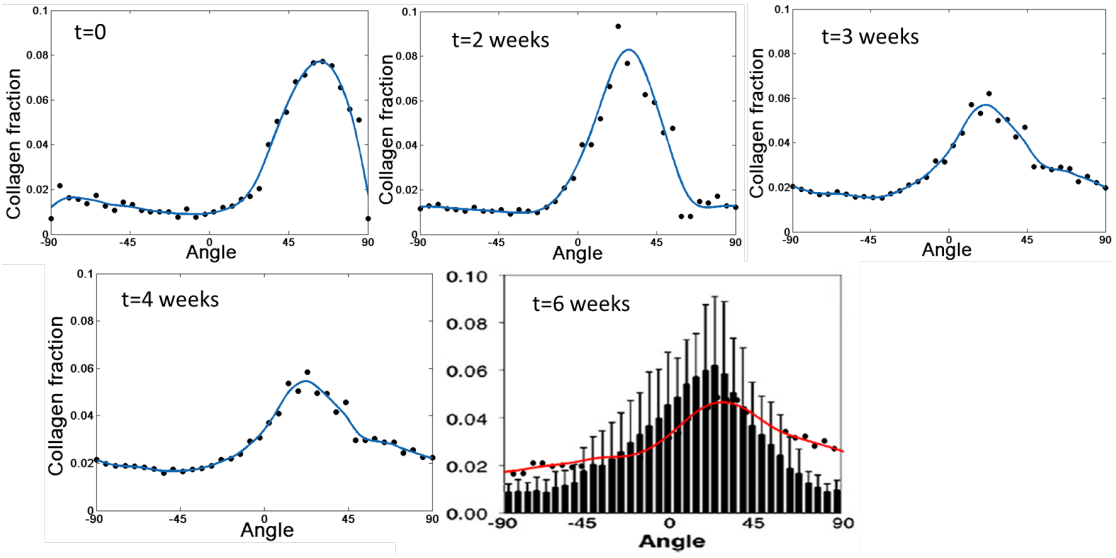

FIGURE 6.19: The evolution of collagen fibre structure: (a) – (e) 0–5 weeks.

At the infarct zone, collagen accumulation caused stiffening of the infarct area. However, the matrix material is volumetrically replaced by the collagen fibres. In contrast to the fibre-reinforcement along fibre directions, the stiffness is negligibly decreased along transmural direction. The stress distributions suggest that the radial stress doesn't change too much during the development of infarction at the infarction center (fig. 6.20$_a$). The max circumferential stresses ($\sigma_{\gamma\gamma}$) are continuously increased (3.8 Kpa at 0 week to 5.3 Kpa at 6 weeks at endo surface, fig. 6.20$_b$). The local longitudinal stress (σ_{zz}) is decreased (2.3 Kpa at 0 week to 0.4 Kpa at 6 weeks at the endo surface fig. 6.20$_c$). Obviously, the concentration of first principal stress, as

the combination of σ_{zz} and $\sigma_{\gamma\gamma}$, is increasing at endo sure during healing process.

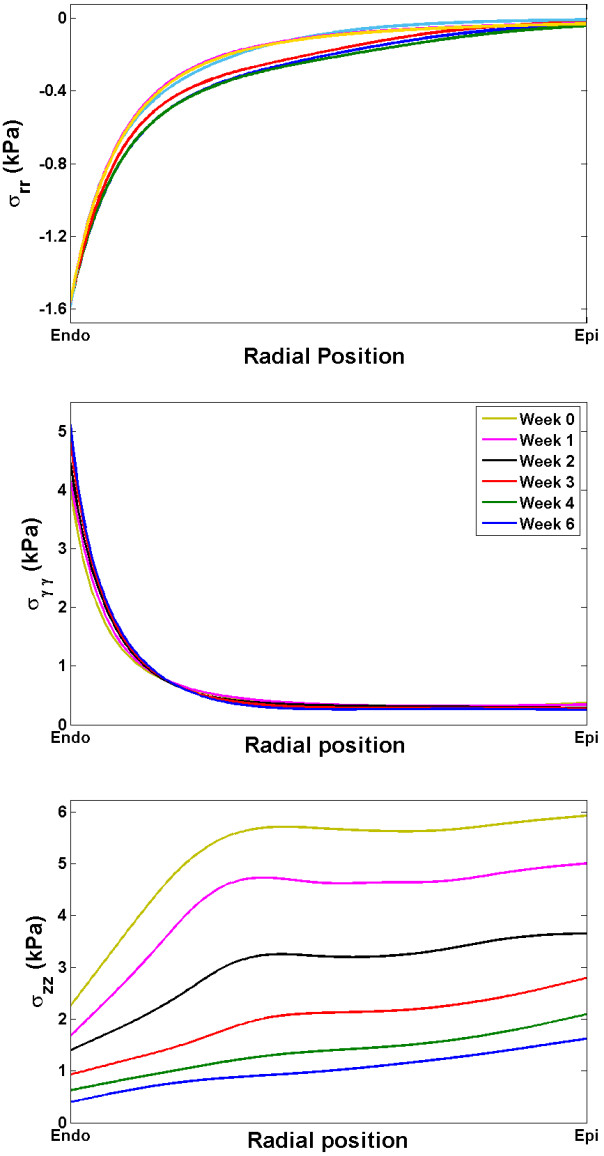

FIGURE 6.20: The evolution of stress: a) radial stress; b) circumferential stress; c) longitudinal stress

6.6.6.2 Results for Tissues at Middle of Infarction Region

The collagen accumulations have similar trends with previous case, but increasing much slower. The volumetric fraction is increase from 0.03 at 0 weeks to 0.22 at 6 weeks (fig. 6.21_a). Along with the changes of the fibre structure, the mean angle of fibre is also decreased less in this case. At the epi surface, the mean angle decreases from 60^o at 0 week to 25^o at six weeks (fig. 6.21_b).

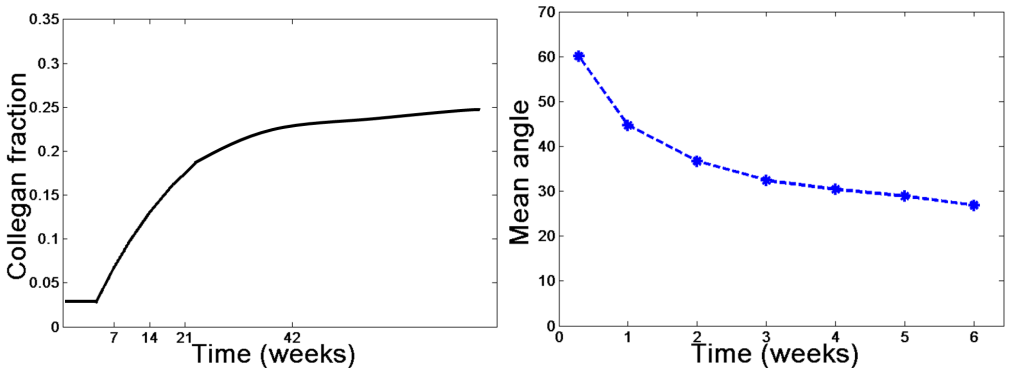

FIGURE 6.21: Estimated infarct collagen volumetric and mean angle evolution at epi surface of infarction heart (middle): Left, the collagen volumetric accumulations; Right, the changes of mean angles.

The fibre structure is also measured by the collagen fraction for fibre angles. As shown in fig. 6.22, the anisotropic level of fibre structure is also decreased less than previous case.

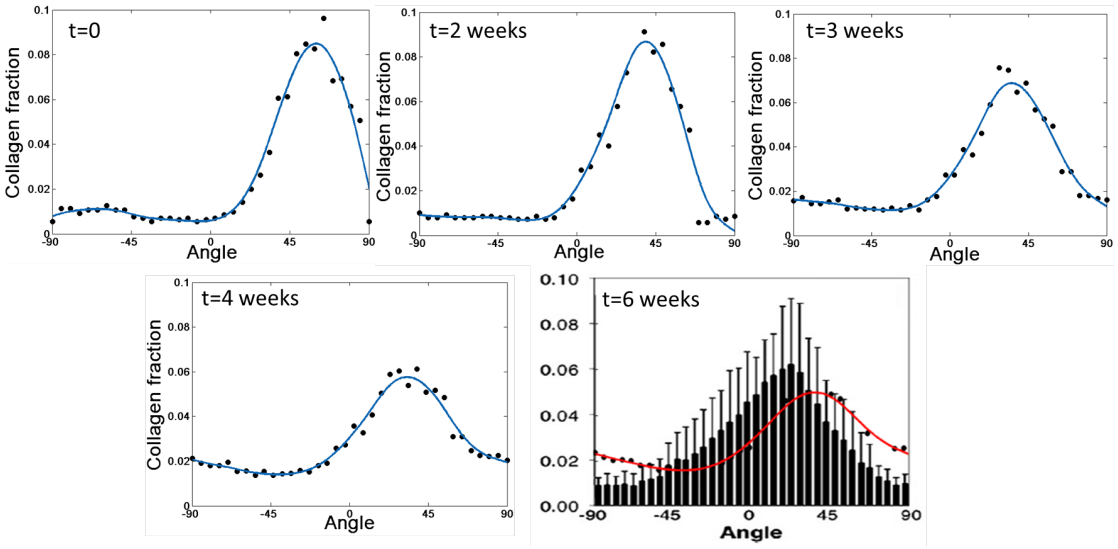

FIGURE 6.22: The evolution of collagen fibre structure: (a) – (e) 0–6 weeks.

Comparing with previous case, the changes of stress distribution are reduced. The max circumferential stresses ($\sigma_{\gamma\gamma}$) are increased less than this stress in previous case. The concentration of first principal stress is also smaller (not shown).

6.6.6.3 Results for Tissues at Edge of Infarction Region

The collagen accumulations are relatively constant, with slightly increase. The volumetric fraction is increase from 0.03 at 0 weeks to 0.031 at 6 weeks. Along with the changes of the fibre structure, the mean angle of fibre is also relatively constant. At the epi surface, the mean angle

decreases from 61^o at 0 week to 58^o at six weeks.

At the edge of infarct zone, the stiffness is negligibly increased. The evolutions of stress distributions suggest that the stress doesn't change too much during the development of infarction at this location. The max circumferential stresses ($\sigma_{\gamma\gamma}$) are decreased (5.7 Kpa at 0 week to 5.6 Kpa at 6 weeks). The local longitudinal stress (σ_{zz}) is slightly increased (1.2 Kpa at 0 week to 1.8 Kpa at 6 weeks). Obviously, the first principal stress is almost constant during healing process.

6.6.7 Changes of the Geometry of LV Tube During Healing Process

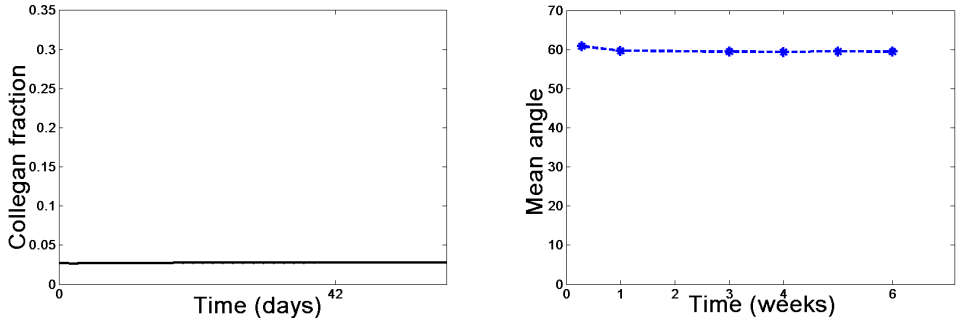

FIGURE 6.23: Estimated infarct collagen volumetric and mean angle evolution at epi surface of infarction heart (edge): Left, the collagen volumetric accumulations; Right, the changes of mean angles

Due to the remodeling of fibre structure regulated by the fibroblast cells after infarction, the local mechanical response of heart tissues will be significantly influenced. Moreover, comparing to the healthy tissues, the changes of material properties will be more obvious for tissues at the infarction center, where the chemokine concentrations are higher with stronger healing effects.

The healing process will generate the activations of fibroblast, resulting more fibres produced by cells. In turn, the collagen fraction will be higher at the position where the cell activations are stronger. It indicates the material will be stiffer at the center of infarction and the stiffness will decrease along the direction from center to the edge of infarction, since the cell activation and healing process is highest at the MI center.

In the loaded LV configuration, the radii are smaller in the center and increases to the normal level at the edge of infarction, with a homogeneous heart pressure at inner surface. Again, this result suggests the deformation will be decreased at the infarction due to the collagen depositions at the infraction region (fig. 6.19).

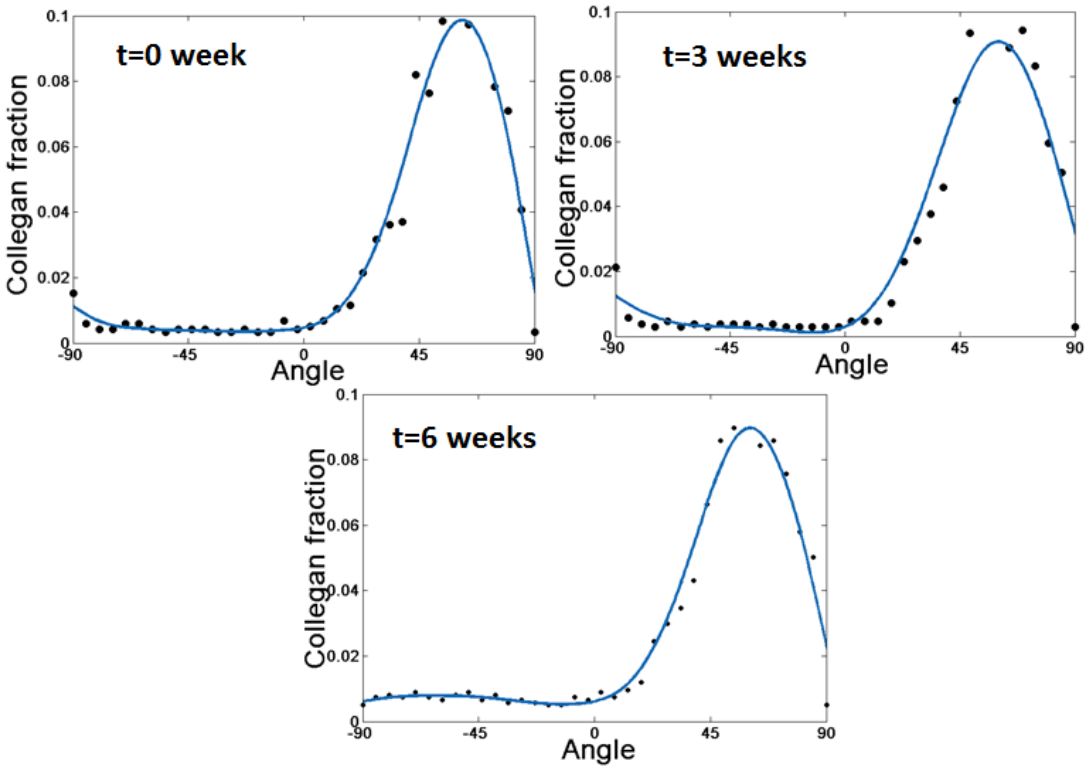

FIGURE 6.24: The evolution of collagen fibre structure: (a) – (e) 0–5 weeks.

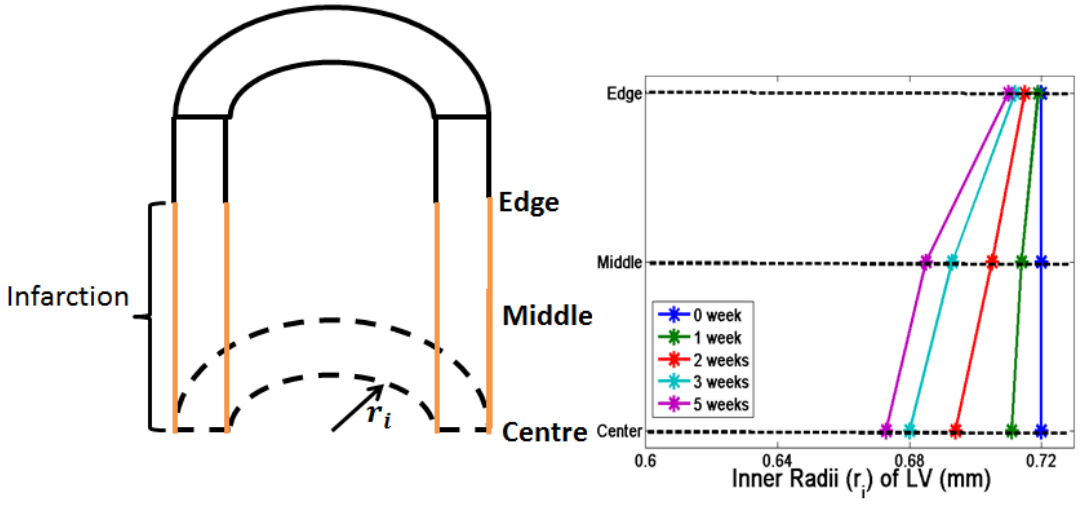

FIGURE 6.25: Geometric changes of infarted LV during the healing prcess: left, deciption of the infarction position; Right, the radii changes of the LV tube.

6.6.8 Summary

A multiscale model, by coupling an agent-based model with a simplified left ventricle tube, is developed. To simulate the appropriate material properties for myocardium, a fibre tension-compression 'switch' is employed as well. The time-dependent model also captures the interaction and information exchange process between mechanical behaviour and collagen tissue remodelling guided by various external cues. The predicted results show the collagen cumulations differ with the location in infraction region. By studying locations of infarctions, it shows the location affects the mechanical behaviors of total LV and the fibre structure.

For fibre structure, the observed fibre changes decrease along distance to infarction center during MI process. The fibre volumetric fraction increases from 0.03 to around 0.3 at the infarction center, while it only increases from 0.03 to 0.031. For mean angle of fibre structure, it decreases from about 60^o 20^o at endosurface at infarction center, while only small change of mean angle is shown for fibre structure at infarction edge. Therefore, the trends of evolutions of fibre structures are significantly influenced by the distance to infraction center.

For stress state, in this simplified tube model, the trends of stress distributions are similar during MI process at different heart locations. However, the stress concentration is obviously changes. At infarction center, the stress concentration is obviously increased at endosurface during MI, while it's almost constant for stress evolution at infarction center. Moreover, the higher fibre fraction indicates tissues are stiffer at infarction center, which gives the smaller radius of heart tube. During MI process, after applying passive heart pressure, the shape of heart tube is changed, while the radius of cylinder is reduced along LV axis.

6.7 Appendix II: Tangent Stiffness

If we want to solve the LV dynamics, the tangent stiffness (4th order) matrix $\mathbb{C}$ is needed in FEAP software. We start from the moduli matrix $\mathscr{C}$ for the second Piola-Krirchoff stress $\mathbf{P}$ at the reference configuration, then push forwards the moduli matrix $\mathscr{C}$ into the current configuration.

$$\text{if } \mathscr{C} = 2\frac{\partial \mathbf{P}}{\partial \mathbf{C}} \text{ then } \mathbb{C} = J^{-1}\mathbf{FFFF}\mathscr{C}, \tag{6.51}$$

$$\text{or } C_{ijkl} = J^{-1}F_{iI}F_{jJ}F_{kK}F_{lL}\mathscr{C}_{IJKL}.$$

The myocardial constitutive law consists of the matrix $\bar{\Psi}_{\mathrm{m}}(\bar{\mathbf{C}})$, collagen fibre $\bar{\Psi}_{\mathrm{cf}}(\bar{I}_4)$ and pure volumetric penalty $\Psi_{\mathrm{v}}(J)$ to ensure the material incompressibility, that is

$$\Psi = \Psi_{\mathrm{v}}(J) + \bar{\Psi}_{\mathrm{m}}(\bar{\mathbf{C}}) + \bar{\Psi}_{\mathrm{cf}}(\bar{I}_4), \tag{6.52}$$

in which $\bar{\Psi}$ is a purely isochoric contribution. The volumetric penalty term is

$$\Psi_{\mathrm{v}} = \frac{k}{2}(J-1)^2,$$

the term for the matrix material is

$$\bar{\Psi}_{\mathrm{m}} = \Phi_{\mathrm{m},t}\frac{a}{2b}\left[\exp b(\bar{I}_1 - 3) - 1\right],$$

and the term of the collagen structure is:

$$\bar{\Psi}_{\mathrm{cf},t} = \Phi_{\mathrm{cf},t}\frac{1}{\pi}\frac{a_{\mathrm{cf}}}{2b_{\mathrm{cf}}}\int \left[\exp b_{\mathrm{cf}}(\bar{I}_4(\theta) - 1)^2 - 1\right]\varphi_t(\theta)\,\mathrm{d}\theta,$$

in which $\bar{I}_1 (= \bar{\mathbf{C}} : \mathbf{I})$ is the modified first invariance, $\bar{I}_4 (= \mathbf{f}_0^T \cdot \bar{\mathbf{C}}\mathbf{f}_0)$ is the modified fibre invariance.

The second Piola-Krirchoff stress is

$$\mathbf{P} = 2\frac{\partial \Psi}{\partial \mathbf{C}} = 2\frac{\partial(\Psi_{\mathrm{v}}(J) + \bar{\Psi}_{\mathrm{m}}(\bar{\mathbf{C}}) + \bar{\Psi}_{\mathrm{cf}}(\bar{\mathbf{C}}))}{\partial \mathbf{C}},$$

then the stiffness matrix in eq. (6.51) becomes

$$\mathscr{C} = 2\frac{\partial \mathbf{P}}{\partial \mathbf{C}} = 4\left(\frac{\partial^2 \Psi_{\mathrm{v}}}{\partial \mathbf{C}^2} + \frac{\partial^2 \bar{\Psi}_{\mathrm{m}}}{\partial \mathbf{C}^2} + \frac{\partial^2 \bar{\Psi}_{\mathrm{cf}}}{\partial \mathbf{C}^2}\right). \tag{6.53}$$

Finally the Cauchy stress is expressed as

$$\begin{aligned}\boldsymbol{\sigma} = & k(J-1)\mathbf{I} + \Phi_{\mathrm{m},t}\; a\exp[b(\bar{I}_1-3)]\mathrm{dev}\bar{\mathbf{b}} \\ & + \frac{1}{\pi}\Phi_{\mathrm{cf},t}\int_{\Sigma} 2a_{\mathrm{f}}(\bar{I}_4-1)\exp[b_{\mathrm{f}}(\bar{I}_4-1)^2]\varphi_t(\theta)\;\mathrm{dev}(\mathbf{f}\otimes\mathbf{f})\mathrm{d}\theta,\end{aligned} \tag{6.54}$$

in which the operator dev(•) is

$$\mathrm{dev}(\bullet) = (\bullet) - \frac{1}{3}[(\bullet):\mathbf{I}]\mathbf{I}$$

The tangent moduli $\mathbb{C}$ can be deduced for each individual contributions, respectively.

6.7.1 Second Order Derivation for Penalty Function

6.7.1.1 First Order Derivation ($\frac{\partial\Psi_{\mathrm{v}}}{\partial\mathbf{C}}$)

By definition, it gives

$$\frac{\partial\Psi_{\mathrm{v}}}{\partial\mathbf{C}} = \frac{\partial\Psi_{\mathrm{v}}}{\partial J}\frac{\partial J}{\partial\mathbf{C}} = \frac{k}{2}(J^2-J)\mathbf{C}^{-1}, \tag{6.55}$$

where $\frac{\partial J}{\partial\mathbf{C}} = \frac{1}{2}J\mathbf{C}^{-1}$.

6.7.1.2 Second Order Derivation ($\frac{\partial^2\Psi_{\mathrm{v}}}{\partial\mathbf{C}^2}$)

With help of eq. (6.55), it gives

$$\begin{aligned}\frac{\partial^2\Psi_v}{\partial\mathbf{C}^2} &= \frac{(\partial\frac{k}{2}(J^2-J)\mathbf{C}^{-1})}{\partial\mathbf{C}} \\ &= \frac{k}{4}\left\{(2J^2-J)\cdot\mathbf{C}^{-1}\otimes\mathbf{C}^{-1} - (J^2-J)\cdot(\mathbf{C}^{-1}_{(IK)}\otimes\mathbf{C}^{-1}_{(JL)} + \mathbf{C}^{-1}_{(IL)}\otimes\mathbf{C}^{-1}_{(JK)})\right\},\end{aligned} \tag{6.56}$$

where the orders of subscripts are 'IJKL' for a normal 4th order tensor, for example, $\mathbf{C}^{-1}_{(IL)}\otimes\mathbf{C}^{-1}_{(JK)} = C^{-1}_{IL}C^{-1}_{JK}\mathbf{E}_I\otimes\mathbf{E}_L\otimes\mathbf{E}_J\otimes\mathbf{E}_K$.

6.7.2 Second Order Derivation for SEF of Matrix

6.7.2.1 First Order Derivation ($\frac{\partial\bar{\Psi}_{\mathrm{m}}}{\partial\mathbf{C}}$)

By $\bar{\Psi}_{\mathrm{m}}$, it gives

$$\frac{\partial\bar{\Psi}_{\mathrm{m}}}{\partial\mathbf{C}} = \Phi_{\mathrm{m},t}\;\frac{a}{2}\exp(b(\bar{I}_1-3))\frac{\partial\bar{I}_1}{\partial\mathbf{C}} = \Phi_{\mathrm{m},t}\;\frac{a}{2}\exp(b(\bar{I}_1-3))\left[-\frac{1}{3}\bar{I}_1\mathbf{C}^{-1} + J^{-2/3}\mathbf{I}\right], \tag{6.57}$$

where $\frac{\partial\bar{I}_1}{\partial\mathbf{C}} = -\frac{1}{3}\bar{I}_1\mathbf{C}^{-1} + J^{-2/3}\mathbf{I}$.

6.7.2.2 Second order derivation ($\frac{\partial^2 \bar{\Psi}_{\mathrm{m}}}{\partial \mathbf{C}^2}$)

With help of eq. (6.57), we have

$$\begin{aligned}\frac{\partial^2 \bar{\Psi}_{\mathrm{m}}}{\partial \mathbf{C}^2} &= \Phi_{\mathrm{m},t} \frac{\partial \left\{ \frac{a}{2} \exp(b(\bar{I}_1 - 3)) \left[-\frac{1}{3}\bar{I}_1 \mathbf{C}^{-1} + J^{-2/3}\mathbf{I} \right] \right\}}{\partial \mathbf{C}} \\ &= \Phi_{\mathrm{m},t} \frac{a\gamma}{2} (b \left[-\frac{1}{3}\bar{I}_1 \mathbf{C}^{-1} + J^{-2/3}\mathbf{I} \right] \otimes \left[-\frac{1}{3}\bar{I}_1 \mathbf{C}^{-1} + J^{-2/3}\mathbf{I} \right] \\ &- \frac{1}{3}\mathbf{C}^{-1} \otimes (-\frac{1}{3}\bar{I}_1 \mathbf{C}^{-1} + J^{-2/3}\mathbf{I}) + \frac{1}{6}\bar{I}_1 (\mathbf{C}^{-1}_{(IK)} \otimes \mathbf{C}^{-1}_{(JL)} + \mathbf{C}^{-1}_{(IL)} \otimes \mathbf{C}^{-1}_{(JK)}) \\ &- \frac{1}{3} J^{-2/3}\mathbf{I} \otimes \mathbf{C}^{-1}),\end{aligned} \tag{6.58}$$

where $\gamma = \exp(b(\bar{I}_1 - 3))$.

6.7.3 Second Order Derivation for SEF of Collagen Structure

6.7.3.1 First Order Derivation $\frac{\partial \bar{\Psi}_{\mathrm{cf}}}{\partial \mathbf{C}}$

By $\bar{\Psi}_f$, it gives

$$\frac{\partial \bar{\Psi}_f}{\partial \mathbf{C}} = \frac{\Phi_{\mathrm{cf},t}}{\pi} \int \varphi \; \Omega'(\bar{I}_4) \cdot \frac{\partial \bar{I}_4}{\partial \mathbf{C}} d\theta = \frac{\Phi_{\mathrm{cf},t}}{\pi} \int \varphi \Omega'(\bar{I}_4) \left[-\frac{1}{3}\bar{I}_4 \mathbf{C}^{-1} + J^{-2/3}\mathbf{f}_0 \otimes \mathbf{f}_0 \right] \mathrm{d}\theta, \tag{6.59}$$

where $\frac{\partial \bar{I}_4}{\partial \mathbf{C}} = -\frac{1}{3}\bar{I}_4 \mathbf{C}^{-1} + J^{-2/3}\mathbf{f}_0 \otimes \mathbf{f}_0$, and $\Omega(\bar{I}_4) = \frac{a_{\mathrm{cf}}}{2b_{\mathrm{cf}}} \exp\ (b_{\mathrm{cf}}(\bar{I}_4 - 1)^2 - 1)$, $\Omega'(\bar{I}_4) = \frac{\partial \Omega}{\partial \bar{I}_4} = a_{\mathrm{cf}}(\bar{I}_4 - 1)(\exp\, b_{\mathrm{cf}}(\bar{I}_4 - 1)^2)$

6.7.3.2 Second Order Derivation ($\frac{\partial^2 \bar{\Psi}_{\mathrm{cf}}}{\partial \mathbf{C}^2}$)

With the help of eq. (6.59), it gives

$$\begin{aligned}\frac{\partial^2 \bar{\Psi}_{\mathrm{cf}}}{\partial \mathbf{C}^2} &= \frac{\partial (\frac{\Phi_{\mathrm{cf},t}}{\pi} \int \varphi \Omega'(\bar{I}_4) \left[-\frac{1}{3}\bar{I}_4 \mathbf{C}^{-1} + J^{-2/3}\mathbf{f}_0 \otimes \mathbf{f}_0 \right] \mathrm{d}\theta)}{\partial \mathbf{C}} \\ &= \frac{\Phi_{\mathrm{cf},t}}{\pi} \int \varphi \Omega'' \left[-\frac{1}{3}\bar{I}_4 \mathbf{C}^{-1} + J^{-2/3}\mathbf{f}_0 \otimes \mathbf{f}_0 \right] \otimes \left[-\frac{1}{3}\bar{I}_4 \mathbf{C}^{-1} + J^{-2/3}\mathbf{f}_0 \otimes \mathbf{f}_0 \right] \mathrm{d}\theta \\ &+ \frac{\Phi_{\mathrm{cf},t}}{\pi} \int \varphi \Omega' \, (-\frac{1}{3}\mathbf{C}^{-1} \otimes (-\frac{1}{3}\bar{I}_4 \mathbf{C}^{-1} + J^{-2/3}\mathbf{f}_0 \otimes \mathbf{f}_0) + \frac{1}{6}\bar{I}_4 (\mathbf{C}^{-1}_{(IK)} \otimes \mathbf{C}^{-1}_{(JL)} + \mathbf{C}^{-1}_{(IL)} \otimes \mathbf{C}^{-1}_{(JK)}) \\ &- \frac{1}{3} J^{-2/3} (\mathbf{f}_0 \otimes \mathbf{f}_0) \otimes \mathbf{C}^{-1}) \, \mathrm{d}\theta,\end{aligned} \tag{6.60}$$

where $\Omega''(\bar{I}_4) = a_{\mathrm{cf}}(\exp\, b_{\mathrm{cf}}(\bar{I}_4 - 1)^2)(1 + 2b_{\mathrm{cf}}(\bar{I}_4 - 1)^2)$

6.7.4 Tangent moduli $\mathbb{C}$

With helps of eq. (6.56), (6.58) and (6.60), the tangent moduli is

$$
\begin{aligned}
\mathbb{C} &= J^{-1}\mathbf{FFFF}\cdots\mathscr{C} = 4J^{-1}\mathbf{FFFF}\cdots(\frac{\partial^2\Psi_v}{\partial\mathbf{C}^2}+\frac{\partial^2\bar{\Psi}_m}{\partial\mathbf{C}^2}+\frac{\partial^2\bar{\Psi}_f}{\partial\mathbf{C}^2}) \\
&= k\left\{(2J-1)\mathbb{I}-(J-1)(\mathbb{I}_{(ikjl)}+\mathbb{I}_{(iljk)})\right\} \\
&+\Phi_{\mathrm{m},t}\frac{2a\gamma}{J}(b\left[-\frac{1}{3}\bar{I}_1\mathbf{I}+\bar{\mathbf{b}}\right]\otimes\left[-\frac{1}{3}\bar{I}_1\mathbf{I}+\bar{\mathbf{b}}\right] \\
&-\frac{1}{3}\mathbf{I}\otimes(-\frac{1}{3}\bar{I}_1\mathbf{I}+\bar{\mathbf{b}})+\frac{1}{6}\bar{I}_1(\mathbb{I}_{(ikjl)}+\mathbb{I}_{(iljk)}) \\
&-\frac{1}{3}(\bar{\mathbf{b}}\otimes\mathbf{I})) \\
&+\Phi_{\mathrm{cf},t}\frac{4}{J\pi}\int\varphi\Omega''\left[-\frac{1}{3}\bar{I}_4\mathbf{I}+J^{-2/3}\mathbf{f}\otimes\mathbf{f}\right]\otimes\left[-\frac{1}{3}\bar{I}_4\mathbf{I}+J^{-2/3}\mathbf{f}\otimes\mathbf{f}\right]\,\mathrm{d}\theta \\
&-\Phi_{\mathrm{cf},t}\frac{4}{3J\pi}\int\varphi\Omega'\,(\mathbf{I}\otimes(-\frac{1}{3}\bar{I}_4\mathbf{I}+J^{-2/3}\mathbf{f}\otimes\mathbf{f})-\frac{1}{2}\bar{I}_4(\mathbb{I}_{(ikjl)}+\mathbb{I}_{(iljk)}) \\
&+J^{-2/3}(\mathbf{f}\otimes\mathbf{f})\otimes\mathbf{I})\,\mathrm{d}\theta,
\end{aligned}
\tag{6.61}
$$

where $\mathbb{I}$ is the forth order unit tensor rooting all its feet in current configuration.

Volumetric Growth from a Residually-stressed (Current) Configuration

In general, 'growth' is mentioned about changes in volume and material properties of soft tissues. In this report, to distinguish the volume changes and changes of material properties (especially for fibre-reinforced material), the term '(volumetric) growth' is used to describe the changes of volume and mass in tissues, while (fibre) remodelling is to describe the changes of material properties by changing the micro-fibre structure.

Recently, if the idea of growth is applied to study the evolution of organ formations, it's usually assumed that growth always occurs in the natural (reference) configuration. For instance, referring to studies by Kuhl [25], it's assumed the growth occurs in some fixed reference configurations. With this assumption, it's convenient to calculate the new stress states of tissue after growth for the following reasons: 1) in general, the shape or geometry of organ will be changed after volumetric growth. However, if it is assumed that growth occurs in a fixed reference configuration, the elastic deformation tensor can be obtained directly from the decomposition of the overall deformation tensor. For instance, referred to the initial reference configuration, the overall deformation tensor $\mathbf{F}$ is decomposed as

$$\mathbf{F} = \mathbf{F}_e \mathbf{F}_g,$$

where $\mathbf{F}_g$ is the growth tensor referred to the initial fixed configuration, and $\mathbf{F}_e$ is the pure elastic deformation tensor referred to the growth-updated configuration.
The elasticity tensor could be directly determined by the overall deformation and growth tensors. To compute the current stress state, the stress can be computed from the pure elastic deformation. Therefore, assuming that growth occurs in the reference configuration, it's not necessary to update the geometry of tissues after growth to compute the stress state, since the elastic tensor (referred to the growth-updated configuration) can be obtained for the deformation and growth tensors directly. (2) Besides, as mentioned, in general, it is required to determine the natural

(stress-free) configuration for a tissue to compute the stress state after tissue growth. However, assuming growth occurs in the fixed reference configuration, the natural configuration is implicitly given with the help of the growth tensor. Therefore, it is really convenient to study the stress or growth evolution of heart with this assumption. And a similar approach is also employed by Kerckhoffs [46, 47].

Actually, in some studies, it's stated that they investigated the growth evolution of organs from the updated reference configuration after each incremental growth step. For instance, inhomogeneous volumetric growth is studied within a 3D simulation on heart growth (Kroon [50], fig. 6.26). However, in this study, it is assumed that **the growth could release all the residual stress, and that further growth will start from the updated but stress-free configuration**. According to this assumption, the updated natural configurations can be determined directly by cumulative incremental growth (or growth history), which approach leads to a similar method to calculate the mechanical behaviours of organs as in Kuhl's approach [25].

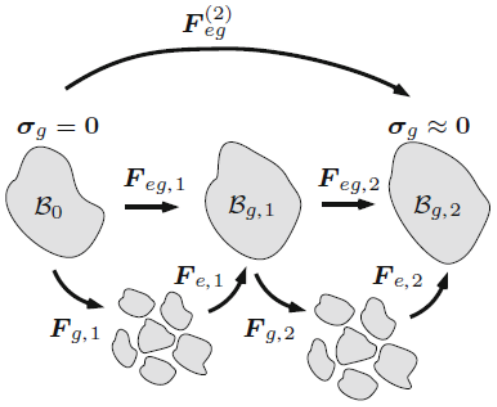

FIGURE 6.26: Updated stress free configuration after growth: Here, the, initial growth step occurs in a stress-free configuration ($\mathscr{B}_0$). Then, the elastic deformation $\mathbf{F}_{e,1}$ assembles the body into the compatible but residually-stress configuration $\mathscr{B}_{g,1}$. Then, the residual stress is released by consequent growth step $\mathbf{F}_{g,2}$. Then, elastic deformation $\mathscr{B}_{g,2}$ assembles the tissue into current configuration $\mathscr{B}_{g,2}$. Therefore, the current stress state is only determined by the last elastic deformation tensor $\mathbf{F}_{e,2}$

Furthermore, in some researches, growth is assumed to occur in the current configuration [3, 26]. However, the growth and mechanical behaviours of organs are mathematically simplified into really special cases. For instance, in [26], the geometry of an elastic body is idealized as a sphere, and the growth only occurs along principal directions, and the growth tensor $\mathbf{G}^i$ has matrix representation

$$\mathbf{G}^i = \begin{bmatrix} g_1 & 0 & 0 \\ 0 & g_2 & 0 \\ 0 & 0 & g_3 \end{bmatrix},$$

and with the homogeneous pressure acting on the external surface of the spherical body, the elastic deformation could be described by the diagonal tensor as

$$\mathbf{F}_e^i = \begin{bmatrix} \lambda_1 & 0 & 0 \\ 0 & \lambda_2 & 0 \\ 0 & 0 & \lambda_3 \end{bmatrix}.$$

Then after a sequence of k steps growth, the overall deformation could be stated as

$$\mathbf{A}^k = \mathbf{G}^k \cdot \mathbf{F}_e^k \cdot \mathbf{G}^{k-1} \cdot \mathbf{F}_e^{k-1} \cdots \mathbf{G}^1 \cdot \mathbf{F}_e^1,$$

and due to diagonal form of growth and deformation tensors, it could be re-arranged as

$$\mathbf{A}^k = \mathbf{G}^k \cdot \mathbf{G}^{k-1} \cdots \mathbf{G}^1 \mathbf{F}_e^k \cdot \mathbf{F}_e^{k-1} \cdots \mathbf{F}_e^1.$$

Similarly with Kuhl's approach [25], it is computationally convenient to update the reference configuration by using the cumulative growth tensor in the last equation for the targeted elastic body and to compute the mechanical behaviours of the body from a new natural configuration.

However, living organs are actually exposed to external loading all the time, while the growth should occur from the residually-stressed current configuration. In this section, we try to draw a sketch on 1) how to obtain the constitutive laws of soft tissue after introducing the inhomogeneous growth in the residually-stressed current configuration, 2) how to couple the growth and (fibre) remodelling processes to identify new mechanical behaviours of soft tissue.

6.8 Constitutive laws for Living Organs with Volumetric Growth

In this section, it's assumed that **pure growth doesn't induce any elastic deformation** (H1). In other words, the mechanical properties do not change after growth.

Besides, it's also assumed that **the incremental growth is determined by external environmental cues, which are independent of the subsequent elastic behaviours of tissues.** (H2)

6.8.1 Growth from a Natural Configuration

As an easy start, it's assumed that pure growth, which is pre-determined by a given growth law, occurs in the natural (stress-free) configuration. Then the local growth tensor deforms the elastic body into an incompatible and stress-free configuration $\mathscr{B}_2$. After applying loading, the living organ eventually deforms into a stressed and compatible configuration $\mathscr{B}_3$ (fig. 6.27).

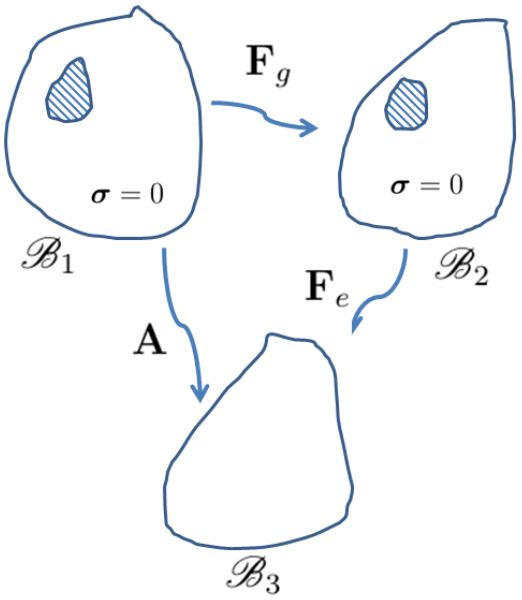

FIGURE 6.27: Growth from the stress-free configuration: It's assumed incremental growth step ($\mathbf{F}_g$) deforms the tissues from the (incompatible) natural configuration $\mathscr{B}_1$ into the updated (and incompatible) configuration $\mathscr{B}_2$. Then, the elastic deformation $\mathbf{F}_e$ assembles the tissues into the compatible configuration $\mathscr{B}_3$.

With help of H1, the overall elastic energy from $\mathscr{B}_1$ to $\mathscr{B}_3$ could be expressed as

$$W_1 = J_g W_2, \tag{6.62}$$

where W_1 is the elastic strain energy from $\mathscr{B}_1$ to $\mathscr{B}_3$ ($W_1 = W_1(\mathbf{A})$), W_2 is the elastic strain energy from $\mathscr{B}_2$ to $\mathscr{B}_3$ ($W_2 = W_1(\mathbf{F}_e)$), and J_g is the determinant of the growth tensor $\mathbf{F}_g$.

To calculate the Cauchy stress From $\mathscr{B}_2$, actually, only pure elastic behaviour is involved (no growth) and the Cauchy stress is expressed as

$$\boldsymbol{\sigma} = J_e^{-1}\mathbf{F}_e\frac{\partial W_2}{\partial \mathbf{F}_e}. \tag{6.63}$$

From $\mathscr{B}_1$, with help of eq. (6.62), the Cauchy stress could be expressed as

$$\boldsymbol{\sigma} = J_A^{-1}\mathbf{A}\frac{\partial W_1}{\partial \mathbf{A}} = J_A^{-1}\mathbf{A}\frac{\partial (J_g W_2)}{\partial \mathbf{A}} = J_A^{-1}J_g\mathbf{A}(\frac{\partial \mathbf{F}_e}{\partial \mathbf{A}} : \frac{\partial W_2}{\partial \mathbf{F}_e}) = J_e^{-1}\mathbf{F}_e\frac{\partial W_2}{\partial \mathbf{F}_e}, \tag{6.64}$$

where $\mathbf{A} = \mathbf{F}_e\mathbf{F}_g$.

It's worth to emphasize that the growth tensor is determined by certain growth laws (related to external environmental cues), which indicates that the pure growth tensor is independent of the elastic deformation tensor,

$$\frac{\partial \mathbf{F}_g}{\partial \mathbf{F}_e} = \mathbf{0}.$$

6.8.2 Growth from a Residually-stressed Configuration

Here, the more general case is raised to discuss the effects of updating the reference configuration by new growth steps. The elastic body is initially in the residually-stressed and compatible configuration $\mathscr{B}_2$. It's assumed the state of residual stress is known and the associated elastic deformation is $\mathbf{F}_\tau$ (fig. 6.28).

If the pure growth occurs in the residually-stressed configuration $\mathscr{B}_2$, the elastic body deforms into the incompatible configuration $\mathscr{B}_3$. After applying loading, the elastic body eventually deforms into a stressed and compatible configuration $\mathscr{B}_4$. If considering pure growth, the equivalent growth tensor $\mathbf{F}'_g$ updates the natural configuration from $\mathscr{B}_0$ to $\mathscr{B}_1$, which approach also indicates the equivalent elastic deformation for residual stress $\mathbf{F}'_\tau$ (the method will be explained later to capture $\mathbf{F}'_g$ and $\mathbf{F}'_\tau$ from $\mathbf{F}_g$ and $\mathbf{F}_\tau$).

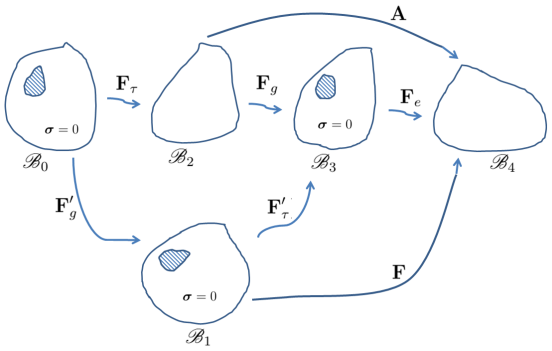

FIGURE 6.28: Growth from the Residually-stressed Configuration: $\mathscr{B}_1$ is the natural but incompatible configuration. The elastic deformation tensor $\mathbf{F}_\tau$ takes the tissue into the compatible and residually-stress configuration $\mathscr{B}_2$. The pure growth occurs in $\mathscr{B}_2$ with tensor $\mathbf{F}_g$, carrying tissue into the incompatible configuration $\mathscr{B}_3$. The subsequent elastic deformation $\mathbf{F}_e$ deforms tissue into the compatible configuration $\mathscr{B}_4$. The equivalent growth $\mathbf{F}'_g$ connects the initial ($\mathscr{B}_0$) and growth-updated ($\mathscr{B}_1$) natural configurations.

With help of H1, the elastic energy (W_2) from $\mathscr{B}_2$ to $\mathscr{B}_4$ could be expressed as

$$W_2 = J_g W_3, \tag{6.65}$$

where W_3 is the elastic energy from $\mathscr{B}_3$ to $\mathscr{B}_4$
Similarly with eq. (6.62), the elastic energy (W_3) from $\mathscr{B}_3$ to $\mathscr{B}_4$ could be obtained by

$$W_3 = (J'_\tau)^{-1}(W_1(\mathbf{F}) - W_1(\mathbf{F}'_\tau)), \tag{6.66}$$

where W_1 is the elastic energy from $\mathscr{B}_1$, $\mathbf{F} = \mathbf{F}_e \cdot \mathbf{F}'_\tau$.
On inserting eq. (6.66) into eq. (6.65), it gives

$$W_2 = J_g (J'_\tau)^{-1}(W_1(\mathbf{F}) - W_1(\mathbf{F}'_\tau)) \tag{6.67}$$

Two methods are employed here to compute the Cauchy stress in $\mathscr{B}_4$:
(1) From $\mathscr{B}_1$,

$$\boldsymbol{\sigma} = J_F^{-1}\mathbf{F}\frac{\partial W_1}{\partial \mathbf{F}} \tag{6.68}$$

(2) From $\mathscr{B}_2$, with help of eq. (6.67), the Cauchy stress is given as

$$\begin{aligned}\boldsymbol{\sigma} &= J_A^{-1}\mathbf{A}\frac{\partial W_2}{\partial \mathbf{A}} = J_A^{-1}\mathbf{A}\frac{\partial\left[J_g J_\tau'^{-1}(W_1(\mathbf{F}) - W_1(\mathbf{F}'_\tau))\right]}{\partial \mathbf{A}} \\ &= J_A^{-1}\mathbf{A}\frac{\partial\left[J_g J_\tau'^{-1}(W_1(\mathbf{F}))\right]}{\partial \mathbf{A}} - J_A^{-1}\mathbf{A}\frac{\partial\left[J_g J_\tau'^{-1}(W_1(\mathbf{F}'_\tau))\right]}{\partial \mathbf{A}} \\ &= J_F^{-1}\mathbf{A}\{(\frac{\partial \mathbf{F}}{\partial \mathbf{A}}) : (\frac{\partial W_1(\mathbf{F})}{\partial \mathbf{F}})\} = J_F^{-1}\mathbf{F}\frac{\partial W_1}{\partial \mathbf{F}}\end{aligned} \tag{6.69}$$

where $\mathbf{A} = \mathbf{F}_e\mathbf{F}_g$, $\mathbf{F} = \mathbf{F}_e\mathbf{F}'_\tau$.
The simplified Cauchy stresses give the same expressions as in eq. (6.68) and (6.69), which indicates that the new SEF (eq. (6.67)) is appropriate.

Then, the only undefined terms are the equivalent growth $\mathbf{F}'_g$ and elastic deformation $\mathbf{F}'_\tau$. To determine $\mathbf{F}'_g$, the polar decomposition of $\mathbf{F}_\tau$ is needed:

$$\mathbf{F}_\tau = \mathbf{V}_\tau\mathbf{R}_\tau. \tag{6.70}$$

Here, it is considered that an arbitrary material point of elastic body is rotated with tensor $\mathbf{R}_\tau$, then, the rotated configuration $\mathscr{B}_R$ is deformed into $\mathscr{B}_1$ by tensor $\mathbf{V}_\tau$. For pure growth, the growth tensor could be decomposed as

$$\mathbf{F}_g = \mathbf{R}_g\mathbf{U}_g. \tag{6.71}$$

Growth tensor $\mathbf{F}_g$ is with respect to $\mathscr{B}_1$. However, if considering the effect of growth in changing the shape of initial body, it could give an equivalent growth occurs before elastic deformation, by rotating the growth tensor back into the initial configuration $\mathscr{B}_0$ with the tensor $\mathbf{R}_\tau$ the decomposition of $\mathbf{F}_g$ could help to raise the form of $\mathbf{F}'_g$, with help of eq. (6.71), as

$$\mathbf{F}_g = \mathbf{R}_g\mathbf{U}_g \;\Rightarrow\; \mathbf{F}'_g = \mathbf{R}_\tau^{-1}\mathbf{R}_g\mathbf{U}_g(\mathbf{R}_\tau^{-1})^T. \tag{6.72}$$

And with rotations between orthogonal coordinates ($\mathbf{R}_\tau^T\mathbf{R}_\tau = \mathbf{I}$), eq. (6.72) could be re-written as

$$\mathbf{F}'_g = \mathbf{R}_\tau^T\mathbf{R}_g\mathbf{U}_g\mathbf{R}_\tau. \tag{6.73}$$

The deformation path ($\mathscr{B}_0 \to \mathscr{B}_1 \to \mathscr{B}_3$) is equivalent to path ($\mathscr{B}_0 \to \mathscr{B}_2 \to \mathscr{B}_3$), so that

$$\mathbf{F}_g\mathbf{F}_\tau = \mathbf{F}'_\tau\mathbf{F}'_g \tag{6.74}$$

and hence

$$\mathbf{F}'_\tau = \mathbf{F}_g \mathbf{F}_\tau (\mathbf{F}'_g)^{-1} \tag{6.75}$$

Example (*2D growth*) A living body is deformed with the elastic deformation tensor $\mathbf{F}_e$ from initial configuration $\mathscr{B}_0$ (fig. 6.29). Considering here, the material point is firstly rotated by $\mathbf{R}_e$ and then stretched by $\mathbf{V}_e$ as

$$\mathbf{F}_e = \mathbf{V}_e \mathbf{R}_e.$$

If the initial basis vectors $(\mathbf{e}_1, \mathbf{e}_2)$ of coordinates are rotated to new ones $(\mathbf{e}'_1, \mathbf{e}'_2)$ with rotation angle $\frac{\pi}{3}$, then the matrix form of the rotation tensor is given as

$$\mathbf{R}_e = \begin{bmatrix} \cos\frac{\pi}{3} & \sin\frac{\pi}{3} \\ -\sin\frac{\pi}{3} & \cos\frac{\pi}{3} \end{bmatrix}.$$

where component $R_{\mathbf{e}ij} = \mathbf{e}'_i \cdot \mathbf{e}_j$.

Assuming the body is stretched into $\mathscr{B}_3$ with $\mathbf{V}_e$ as

$$\mathbf{V}_e = \mathbf{I} + (\lambda_e - 1)\mathbf{e}'_1 \otimes \mathbf{e}'_1.$$

then, the body grows along the $\mathbf{e}'_2$ direction in $\mathscr{B}_V$ as

$$\mathbf{F}_g = \mathbf{I} + (\lambda_g - 1)\mathbf{e}'_2 \otimes \mathbf{e}'_2.$$

$$\mathbf{F}_{gi} = \lambda_{gf}\hat{\mathbf{f}} \otimes \hat{\mathbf{f}} + \lambda_{gs}\hat{\mathbf{s}} \otimes \hat{\mathbf{s}} + \lambda_{gn}\hat{\mathbf{n}} \otimes \hat{\mathbf{n}}$$

What's the equivalent growth for this living body?

Solution Obviously, if skipping the elastic deformation, equivalently saying, the living body grows along the $\mathbf{e}_2$ direction with growth tensor from $\mathscr{B}_0$ as

$$\mathbf{F}'_g = \mathbf{I} + (\lambda_g - 1)\mathbf{e}_2 \otimes \mathbf{e}_2 = \begin{bmatrix} 1 & 0 \\ 0 & \lambda_g \end{bmatrix}.$$

giving the updated stress-free configuration $\mathscr{B}_1$.

Recalling eq. (6.73), the equivalent growth tensor is given as

$$\mathbf{F}'_g = \mathbf{R}_e^T \mathbf{F}_g \mathbf{R}_e = \mathbf{I} + (\lambda_g - 1)\mathbf{e}_2 \otimes \mathbf{e}_2$$

Comparing last two equations describing the equivalent growths, it shows a good validation for algorithm from eq. (6.71) to (6.73).

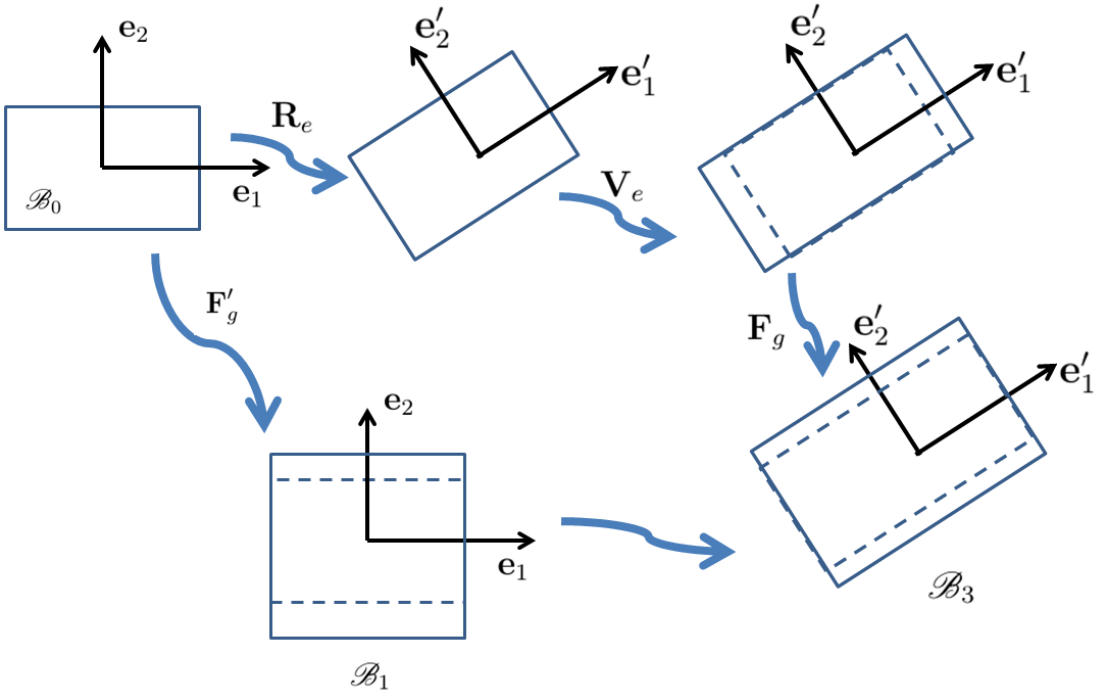

FIGURE 6.29: Description of growth path for example: the rectangular tissue is rotated with $\mathbf{R}_e$ from $\mathscr{B}_0$. Then, tissues are stretched with $\mathbf{V}_e$. The growth then occurs and takes tissues into configuration $\mathscr{B}_3$. The equivalent growth $\mathbf{F}_g$ updates the initial natural configuration to updated configuration $\mathscr{B}_1$; then the equivalent elastic deformation takes tissues into current configuration $\mathscr{B}_3$

In summary, the previous definition of SEF (eq. (6.62) and (6.67)), indicating the updated natural configuration after growth, is computationally convenient for calculating the mechanical behaviours of an elastic body. The major benefits are

1) Under this framework, the growth could be rationally assumed to occur from the residually-stressed configuration.

2) The natural configuration is updated after each incremental growth.

3) Differing from Humphrey's 'constrained mixture models' [83], no new material point is mathematically introduced after growth.

4) By including the growth deformation tensor into the SEF, growth deformation will be automatically included when computing any further elastic behaviours. This is therefore convenient for avoiding remeshing of the elastic body for using the FE method to simulate the evolution of the mechanical behaviours for living tissues after growth.

6.9 (Fibre) Remodelling

In the following section, we will define the remodelling process focusing on evolution of fibre structures in tissues.

As mentioned in Holmes' work [66], the remodelling of the fibre structure is regulated by fibroblasts. Fibres are deposited and rotated by fibroblasts, which change the overall micro-fibre structure. We make a further step and assume that the fibres are deposited and rotated in the current and loaded configuration. This indicates that the fibre structure should be 'pushed-back' into the stress-free configuration to calculate the mechanical behaviours of tissues after the fibre remodelling process. For instance, if the SEF for fibre-reinforced tissue is employed as

$$\Psi = \Phi_{\mathrm{m}} \frac{a}{2b} \left[\exp b(I_1 - 3) - 1\right] + \Phi_{\mathrm{cf}} \frac{1}{\pi} \frac{a_1}{2b_1} \int \left[\exp b_1 (I_4(\theta) - 1)^2 - 1\right] \varphi(\theta, t)\, \mathrm{d}\theta, \tag{6.76}$$

then the 2 fibre structure is mainly described by the fibre volumetric fraction Φ_{cf} and the fibre orientation density function $\varphi(\theta)$. Then after a remodelling incremental step in the tissue (i.e. from agent based model [66]), the fibroblasts deposit new collagen fibres along the cell direction, while they rotate the existing fibres with a certain angle in the current and loaded configuration. The fibre directions will be 'pushed-back' into the reference configuration, which will give the updated fibre orientation density function $\varphi(\theta)_t$ by accounting for the new angles of each fibre.

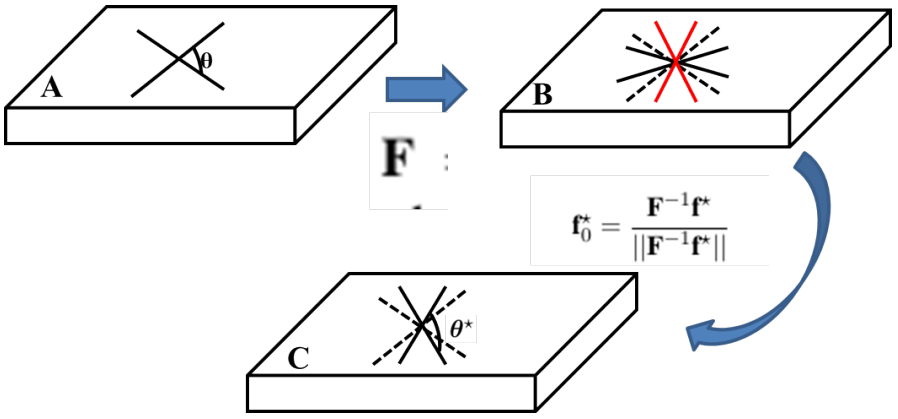

FIGURE 6.30: Example of the updated collagen fibre structure by fibroblast remodelling. A) the initial reference configuration. In this configuration, the fibre structure is presented by the solid lines. B) the fibre modulation by fibroblasts in current configuration, after applying external loading, the fibre structures are updated by the elastic deformation ($\mathbf{F}$) (dash lines). Then, the fibre remodelling processes are induced in this configuration. Then, the fibre structures are regulated by the fibroblast migration (red lines) C) the updated reference configuration and fibre structure via a 'push-back' algorithm: after releasing the external loading, the body will deform into the updated configuration (C) with deformation tensor ($\mathbf{F}^{-1}$). Then, the 'push-back' algorithm is used to calculate the fibre structure from configuration B.

To simplify the problem, we assume that all collagen fibres have the same length. Then, the fibre volumetric fraction is given as

$$\Phi_{\mathrm{cf},t} = \frac{N_{\mathrm{cf},t}}{N_{\mathrm{cf},t_0}} \Phi_{\mathrm{cf},t_0} \tag{6.77}$$

where N_{cf,t_0} and Φ_{cf,t_0} are the initial overall fibre number and volumetric fraction at time t_0, $N_{\mathrm{cf},t}$ and $\Phi_{\mathrm{cf},t}$ are the initial overall fibre number and volumetric fraction at time t

For each individual fibre, the fibre angle in the updated configuration C is obtained by 'push-back' as

$$\mathbf{f}_t = \frac{\mathbf{F}^{-1}\mathbf{f}^{\star}}{||\mathbf{F}^{-1}\mathbf{f}^{\star}||}, \tag{6.78}$$

where $\mathbf{F}$ is the elastic deformation gradient from the reference configuration (A) and intermediate configuration (B), $\mathbf{f}$ and $\mathbf{f}^{\star}$ are the fibre vectors in the updated reference configuration and in the intermediate configuration after fibre remodelling.
The fibre orientation density function will be determined by accounting for each individual fibre angle.

However, if interacting with the mechanism of fibre remodelling growth, it's more complex to determine the fibre angles and the orientation density function in the reference configuration. In the following section, the approach will be discussed in detail in order to explain the 'push-back' method with different G&R processes.

In summary, if the fibre remodelling also occurs in the current and loaded configuration, the updated natural configuration should be determined by 'pushing-back' the fibre structure into the reference configuration.

6.10 Coupling the Volumetric Growth and Fibre Remodelling

As mentioned in the last two sections, the volumetric growth and fibre remodelling both occur in the current and loaded configuration. However, a simple combination of the two processes is not a rational way to determine the updated configuration. Different ways of coupling growth and remodelling (G&R) processes will be considered to determine the fibre structure of tissues.

6.10.1 Quick Remodelling vs Slow Growth

In this section, the case will be discussed about how to couple the remodelling and volumetric growth for living tissues to give an updated SEF if the speed of fibre remodelling is obviously faster than volumetric growth. For instance, for local heart infarction, the volume or shape of heart is relatively constant, while the fibre structure clearly changes [25]. In this section, it's assumed that the volume and shape aren't changed during G&R, which gives

$$\mathbf{F}_g \equiv \mathbf{I}.$$

Actually, if the volumetric growth is ignorable in each G&R loop, the fibre structure is the only determinant to update the natural configuration and SEF for soft tissues. In other words, for the modified HGO model (6.76), the changed fibre volumetric fraction Φ_{cf} and the changed fibre

orientation density function $\varphi(\theta,t)$ are the parameters to describe the new SEF related with the updated natural configuration after G&R process. For details of this process, we refer to the last section.

6.10.2 Quick Growth vs Slow Remodelling

In this section, the case will be discussed about coupling the remodelling and volumetric growth for living tissues to give an updated SEF if the speed of volumetric growth is obviously faster than fibre remodelling. Here, we assume the fibre structure is not actively modulated by fibroblasts but responds passively to the volumetric growth of the matrix tissue.

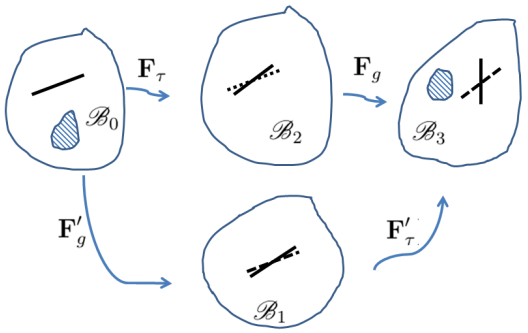

FIGURE 6.31: Quick growth vs slow remodelling: the fibre orientation is modified by the growth. $\mathscr{B}_0$ is the natural (but incompatible) configuration, $\mathbf{F}_\tau$ is the elastic deformation connecting the natural ($\mathscr{B}_0$) and residually-stress configurations ($\mathscr{B}_2$) . Incremental growth step $\mathbf{F}_g$ carries body into $\mathscr{B}_3$. The updated natural configuration $\mathscr{B}_1$ is obtained by the equivalent elastic deformation tensor $\mathbf{F}'_\tau$ between $\mathscr{B}_1$ and $\mathscr{B}_3$. Then, the new fibre angle in $\mathscr{B}_1$ can be obtained by 'push-forwards' old fibre angle from $\mathscr{B}_0$ with equivalent growth tensor $\mathbf{F}'_g$.

The growth of the matrix material is induced for the elastic body from the loaded configuration. If the total number of fibres is constant during growth, the fibre volumetric fraction is updated as

$$\Phi_{\mathrm{cf}} = \frac{\Phi_{\mathrm{cf},t_0}}{J_g}, \tag{6.79}$$

where J_g is the determinant of the growth tensor $\mathbf{F}_g$, Φ_{cf,t_0} is the initial fibre volumetric fraction.

And due to the growing deformation, the fibre angles in the initial natural configuration $\mathscr{B}_0$ should be 'pushed-forward' into the updated natural configuration $\mathscr{B}_1$ (fig. 6.31) as

$$\mathbf{f}_1 = \frac{\mathbf{F}'_g\mathbf{f}_0}{||\mathbf{F}'_g\mathbf{f}_0||}, \tag{6.80}$$

where $\mathbf{f}_1$, $\mathbf{f}_0$ are the fibre vectors in $\mathscr{B}_1$ and $\mathscr{B}_0$.

Moreover, as mentioned in Section 1.2, the SEF is calculated after the volumetric growth from

the residually-stressed configuration. By coupling with the fibre remodelling, the volumetric fraction and the fibre orientation density function are updated (by eq. (6.79), (6.80) and (6.15)) as well.

6.10.3 Quick Growth vs Quick Remodelling

In this section, the growth and remodelling are assumed to take place with similar speeds, i.e. the growth and remodelling processes occur simultaneously from the loaded configuration. This idea is quite similar to the assumption of the mixture of 'constant individual density (CID)' and 'adaptive individual density (AID)' by Watton *et al*. [16]. Besides, here, we also assume the incremental growth step occurs after the incremental fibre remodelling step. And we try to include this G&R process under the coupled G&R framework to describe the evolution of the mechanical behaviours of living tissues.

It's assumed that the volumetric growth and fibre remodelling occur in the loaded configuration $\mathscr{B}_2$ (regulated by different but given G&R laws fig. 6.31). If the overall fibre number is increased to $N_{\mathrm{cf},t}$ from the initial value N_{cf,t_0} by active fibre remodelling (as for the agent-based model [66]), the updated fibre remodelling fraction is

$$\Phi_{\mathrm{cf},t} = \frac{\Phi_{\mathrm{cf},t_0}}{J_g} \frac{N_{\mathrm{cf},t}}{N_{\mathrm{cf},t_0}}, \tag{6.81}$$

where $N_{\mathrm{cf},t}$ is the updated fibre number at time t.

For the individual fibre, the unit fibre vector ($\mathbf{f}_2$) is updated by the fibre remodelling process, (i.e. modified by the fibroblast migration), in intermediate configurations $\mathscr{B}_2$ in fig. 6.28, while the updated fibre vector is given as $\mathbf{f}_2^{\star}$.

Then, the fibre should be 'pushed-back' into the **updated** reference configuration ($\mathscr{B}_1$ in fig. 6.28), which gives

$$\mathbf{f}_1 = \frac{(\mathbf{F}'_\tau)^{-1}\mathbf{F}_g\mathbf{f}_2^{\star}}{||(\mathbf{F}'_\tau)^{-1}\mathbf{F}_g\mathbf{f}_2^{\star}||}, \tag{6.82}$$

where $\mathbf{F}'_\tau$ is the elastic deformation tensor defined in eq. (6.67).

To determine the updated SEF after both fibre remodelling and volumetric growth, the general form of the SEF could be expressed as eq. (6.67) (indicating a volumetric growth from the loaded configuration), but the updated fibre volumetric fraction in eq. (6.81) and fibre orientation density function should be inserted into the SEF to describe the fibre remodelling in the current configuration.

6.11 Tangent Modulus of the Updated SEF for FE Simulation

The theoritical frame is introduced to include the volumetric growth to calculate the mechanical behaviours in living tissues. In practice, the FE model will be emloyed to simulate the growth-mechanic responses of patient-specified organs, while the complex geometry of organs can be implemented. In FE simulations, the tangent modulus is required to compute the Cauchy stress. However, the newly-defined SEF in eq. (6.67), involving the growth tensor, leads to new form of the tangent modulus. In this section, the derivation will be explored for it.

Generally, to obtain the tangent modulus, the referential tensor of elasticities will be figured out with the help of the second Piola-Kirchhoff stress tensor; then, the referential tensor will be pushed forwards into current configuration as the tangent modulus or 'spatial tensor of elasticities' (Holzapfel [32]):

$$\mathbf{P} = 2\frac{\partial W}{\partial \mathbf{C}} \;\Rightarrow\; \mathbb{C} = 2\frac{\partial \mathbf{P}}{\partial \mathbf{C}} \;\Rightarrow\; \mathbf{c}^{(4)} = J^{-1}\mathbf{FFFF}\cdots\cdot\mathbb{C}, \tag{6.83}$$

where $\mathbf{c}^{(4)}$ is the 4th-order spatial tensor of elasticities, $\mathbf{FFFF}\cdots\cdot\mathbb{C}$ is given as $F_{Ii}F_{Jj}F_{Kk}F_{Mm}\mathbb{C}_{ijkm}$ for index form.

The second Piola-Krichhoff stress in $\mathscr{B}_2$ for the SEF is

$$\mathbf{P} = 2\frac{\partial W_2}{\partial \mathbf{C}_A} = 2\frac{\partial\left[J_g(J'_\tau)^{-1}(W_1(\mathbf{F}) - W_1(\mathbf{F}'_\tau))\right]}{\partial \mathbf{C}_A} = 2J_g(J'_\tau)^{-1}\frac{\partial W_1(\mathbf{F})}{\partial \mathbf{C}_A}, \tag{6.84}$$

where $\mathbf{A} = \mathbf{F}_e\mathbf{F}_g$, $\mathbf{F} = \mathbf{F}_e\mathbf{F}'_\tau$ (fig. 6.28) and $\mathbf{C}_A = \mathbf{A}^T\mathbf{A}$.
If the chain rule is applied on the last equation, it yields

$$\begin{aligned}(\mathbf{P})_{IJ} &= 2J_g(J'_\tau)^{-1}\frac{\partial W_1(\mathbf{F})}{\partial \mathbf{C}_A} \\ &= 2J_g(J'_\tau)^{-1}(\frac{\partial W_1(\mathbf{F})}{\partial \mathbf{C}_F})_{KL}\cdot\frac{\partial(\mathbf{C}_F)_{KL}}{(\partial \mathbf{C}_e)_{MN}}\cdot\frac{\partial(\mathbf{C}_e)_{MN}}{\partial(\mathbf{C}_A)_{IJ}},\end{aligned} \tag{6.85}$$

where $\mathbf{C}_e = \mathbf{F}_e^T\mathbf{F}_e$, $\mathbf{C}_F = \mathbf{F}^T\mathbf{F}$.

Also,

$$\begin{aligned}\frac{\partial(\mathbf{C}_F)_{KL}}{(\partial \mathbf{C}_e)_{MN}} &= \frac{\left[\partial(\mathbf{F}'_\tau)^T\mathbf{C}_e\mathbf{F}'_\tau\right]_{KL}}{(\partial \mathbf{C}_e)_{MN}} = \frac{\partial\ (\mathbf{F}'_\tau)^T_{kK}(\mathbf{C}_e)_{kl}(\mathbf{F}'_\tau)_{lL}}{(\partial \mathbf{C}_e)_{MN}} \\ &= \frac{1}{2}(\mathbf{F}'_\tau)^T_{kK}\ (\delta_{kM}\delta_{lN} + \delta_{kN}\delta_{lM})\ (\mathbf{F}'_\tau)_{lL} \\ &= \frac{1}{2}\left[(\mathbf{F}'_\tau)_{MK}(\mathbf{F}'_\tau)_{NL} + (\mathbf{F}'_\tau)_{NK}(\mathbf{F}'_\tau)_{ML}\right],\end{aligned} \tag{6.86}$$

where $\frac{\partial \mathbf{C}_{IJ}}{\partial \mathbf{C}_{KL}} = \frac{1}{2}(\delta_{IK}\delta_{JL} + \delta_{IL}\delta_{JK})$.

Similarly,

$$\frac{\partial(\mathbf{C}_e)_{MN}}{(\partial\mathbf{C}_A)_{IJ}} = \frac{1}{2}\left[(\mathbf{F}_g^{-1})_{IM}(\mathbf{F}_g^{-1})_{JN} + (\mathbf{F}_g^{-1})_{JM}(\mathbf{F}_g^{-1})_{IN}\right], \tag{6.87}$$

where $\mathbf{C}_e = (\mathbf{F}_g^{-1})^T\mathbf{C}_A\mathbf{F}_g^{-1}$.

Inserting eq. (6.86) and (6.87) into eq. (6.85) gives

$$\mathbf{P} = J_g(J'_\tau)^{-1}\mathbb{A}^{(6)}(\frac{\partial W_1}{\partial\mathbf{C}_F})_{KL}, \tag{6.88}$$

where $\mathbb{A}^{(6)} = \frac{1}{2}\left[(\mathbf{F}'_\tau)_{MK}(\mathbf{F}'_\tau)_{NL} + (\mathbf{F}'_\tau)_{NK}(\mathbf{F}'_\tau)_{ML}\right]\left[(\mathbf{F}_g^{-1})_{IM}(\mathbf{F}_g^{-1})_{JN} + (\mathbf{F}_g^{-1})_{JM}(\mathbf{F}_g^{-1})_{IN}\right]$.

Then, referential tensor of elasticities is

$$\begin{aligned}\mathbb{C} &= 2\frac{\partial(\mathbf{P})_{IJ}}{(\partial\mathbf{C}_A)_{PQ}} = 2\frac{\partial(\mathbf{P})_{IJ}}{(\partial\mathbf{C}_F)_{RT}}\cdot\frac{\partial(\mathbf{C}_F)_{RT}}{(\partial\mathbf{C}_A)_{PQ}}\\ &= 2J_g(J'_\tau)^{-1}\mathbb{A}^{(6)}\frac{(\frac{\partial W_1}{\partial\mathbf{C}_F})_{KL}}{\partial(\mathbf{C}_F)_{RT}}\cdot\frac{\partial(\mathbf{C}_F)_{RT}}{(\partial\mathbf{C}_e)_{XY}}\cdot\frac{\partial(\mathbf{C}_e)_{XY}}{(\partial\mathbf{C}_A)_{PQ}}\\ &= J_g(J'_\tau)^{-1}\mathbb{A}^{(6)}\frac{\partial W_1}{\partial(\mathbf{C}_F)_{KL}\partial(\mathbf{C}_F)_{RT}}\mathbb{B}^{(6)},\end{aligned} \tag{6.89}$$

where $\mathbb{B}^{(6)} = \frac{1}{2}\left[(\mathbf{F}'_\tau)_{XR}(\mathbf{F}'_\tau)_{YT} + (\mathbf{F}'_\tau)_{YR}(\mathbf{F}'_\tau)_{XT}\right]\left[(\mathbf{F}_g^{-1})_{PX}(\mathbf{F}_g^{-1})_{QY} + (\mathbf{F}_g^{-1})_{QX}(\mathbf{F}_g^{-1})_{PY}\right]$.

Then, the tangent modulus or *spatial tensor of elasticities* is obtained as

$$\begin{aligned}\mathbf{c}^{(4)} &= J_A^{-1}\mathbf{AAAA}\cdots\mathbb{C}\\ &= J_A^{-1}J_g(J'_\tau)^{-1}\mathbf{A}_{iI}\mathbf{A}_{jJ}\mathbf{A}_{pP}\mathbf{A}_{qQ}\mathbb{A}^{(6)}\frac{\partial W_1}{\partial(\mathbf{C}_F)_{KL}\partial(\mathbf{C}_F)_{RT}}\mathbb{B}^{(6)}\\ &= J_F^{-1}(\mathbf{F}_e)_{iU}(\mathbf{F}_g)_{UI}(\mathbf{F}_e)_{jV}(\mathbf{F}_g)_{VJ}(\mathbf{F}_e)_{pA}(\mathbf{F}_g)_{AP}(\mathbf{F}_e)_{qB}(\mathbf{F}_g)_{BQ}\mathbb{A}^{(6)}\frac{\partial W_1}{\partial(\mathbf{C}_F)_{KL}\partial(\mathbf{C}_F)_{RT}}\mathbb{B}^{(6)}.\end{aligned} \tag{6.90}$$

By arranging last equation, it gives

$$\mathbf{c}^{(4)} = J_F^{-1}(\mathbf{F}_e)_{iU}(\mathbf{F}_e)_{jV}(\mathbf{F}_e)_{pA}(\mathbf{F}_e)_{qB}(\mathbf{F}_g)_{UI}(\mathbf{F}_g)_{VJ}(\mathbf{F}_g)_{AP}(\mathbf{F}_g)_{BQ}\mathbb{G}^{(8)}\mathbb{R}^{(8)}\frac{\partial W_1}{\partial(\mathbf{C}_F)_{KL}\partial(\mathbf{C}_F)_{RT}}, \tag{6.91}$$

where $\mathbb{G}^{(8)} = \frac{1}{2}\left[(\mathbf{F}_g^{-1})_{IM}(\mathbf{F}_g^{-1})_{JN} + (\mathbf{F}_g^{-1})_{JM}(\mathbf{F}_g^{-1})_{IN}\right]\left[(\mathbf{F}_g^{-1})_{PX}(\mathbf{F}_g^{-1})_{QY} + (\mathbf{F}_g^{-1})_{QX}(\mathbf{F}_g^{-1})_{PY}\right]$, and $\mathbb{R}^{(8)} = \frac{1}{2}\left[(\mathbf{F}'_\tau)_{MK}(\mathbf{F}'_\tau)_{NL} + (\mathbf{F}'_\tau)_{NK}(\mathbf{F}'_\tau)_{ML}\right]\left[(\mathbf{F}'_\tau)_{XR}(\mathbf{F}'_\tau)_{YT} + (\mathbf{F}'_\tau)_{YR}(\mathbf{F}'_\tau)_{XT}\right]$.

To the simply last equation, it gives

$$(\mathbf{F}_g)_{UI}(\mathbf{F}_g)_{VJ}(\mathbf{F}_g)_{AP}(\mathbf{F}_g)_{BQ}\mathbb{G}^{(8)} = \frac{1}{2}(\delta_{UM}\delta_{VN} + \delta_{VM}\delta_{UL})(\delta_{AX}\delta_{BY} + \delta_{AY}\delta_{BX}). \tag{6.92}$$

Then, use of eq. (6.92) and $\mathbb{R}^{(8)}$ gives

$$\begin{aligned}(\mathbf{F}_g)_{UI}(\mathbf{F}_g)_{VJ}(\mathbf{F}_g)_{AP}(\mathbf{F}_g)_{BQ}\mathbb{G}^{(8)}\mathbb{R}^{(8)} = &\left[(\mathbf{F}'_\tau)_{UK}(\mathbf{F}'_\tau)_{VL}+(\mathbf{F}'_\tau)_{VK}(\mathbf{F}'_\tau)_{UL}\right]\\ &*\left[(\mathbf{F}'_\tau)_{AR}(\mathbf{F}'_\tau)_{BT}+(\mathbf{F}'_\tau)_{AT}(\mathbf{F}'_\tau)_{BR}\right].\end{aligned} \tag{6.93}$$

Inserting eq. (6.93) into eq. (6.91) yields

$$\begin{aligned}\mathbf{c}^{(4)} =&J_F^{-1}(\mathbf{F}_e)_{iU}(\mathbf{F}_e)_{jV}(\mathbf{F}_e)_{pA}(\mathbf{F}_e)_{qB}\\ &\left[(\mathbf{F}'_\tau)_{UK}(\mathbf{F}'_\tau)_{VL}+(\mathbf{F}'_\tau)_{VK}(\mathbf{F}'_\tau)_{UL}\right]\\ &\left[(\mathbf{F}'_\tau)_{AR}(\mathbf{F}'_\tau)_{BT}+(\mathbf{F}'_\tau)_{AT}(\mathbf{F}'_\tau)_{BR}\right]\frac{\partial W_1}{\partial(\mathbf{C}_F)_{KL}\partial(\mathbf{C}_F)_{RT}}.\end{aligned} \tag{6.94}$$

Since $\mathbf{F}=\mathbf{F}_e\mathbf{F}'_\tau$, eq. (6.94) gives

$$\begin{aligned}\mathbf{c}^{(4)} =&J_F^{-1}\left[(\mathbf{F})_{iK}(\mathbf{F})_{jL}+(\mathbf{F})_{iL}(\mathbf{F})_{jK}\right]\\ &\left[(\mathbf{F})_{pR}(\mathbf{F})_{qT}+(\mathbf{F})_{pT}(\mathbf{F})_{qR}\right]\frac{\partial W_1}{\partial(\mathbf{C}_F)_{KL}\partial(\mathbf{C}_F)_{RT}}.\end{aligned} \tag{6.95}$$

And due to the symmetry in the $4th$ order tensor $\frac{\partial W_1}{\partial(\mathbf{C}_F)_{KL}\partial(\mathbf{C}_F)_{RT}}$, eq. (6.95) yields

$$\mathbf{c}^{(4)} = J_F^{-1}4\mathbf{F}_{iK}\mathbf{F}_{jL}\mathbf{F}_{pR}\mathbf{F}_{qT}\frac{\partial W_1}{\partial(\mathbf{C}_F)_{KL}\partial(\mathbf{C}_F)_{RT}}. \tag{6.96}$$

Actually, referring to $\mathscr{B}_1$ in fig. 6.28, *spatial tensor of elasticities* in $\mathscr{B}_4$ could be also derived as

$$\mathbf{c}^{(4)} = J_F^{-1}4\mathbf{F}_{iK}\mathbf{F}_{jL}\mathbf{F}_{pR}\mathbf{F}_{qT}\frac{\partial W_1}{\partial(\mathbf{C}_F)_{KL}\partial(\mathbf{C}_F)_{RT}}. \tag{6.97}$$

6.12 Summary

In previous researches, to calculate the mechanical behaviours of living organs, it's usually assumed that growth occurs in the natural (reference) configuration. Or it is assumed that the growth could release all the residual stress, and that further growth will start from the updated but stress-free configuration.

In this work, a theoretical framework is developed to calculate the mechanical behaviours of soft tissue after introducing inhomogeneous growth in a residually-stressed current configuration. Under this framework, the growth could be rationally assumed to occur from the residually-stressed configuration, which avoids to assume the growth occurs in a 'virtual' reference configuration in many previous researches. Moreover, growth deformation will be automatically included when computing any further elastic behaviours by the SEF related to growth-updated

configurations. The theoretical framework is introduced to couple the growth and fibre remodelling process to describe the mechanical behaviours of living tissues.

Conclusion and Future Work

6.13 Limitations

The discussions for the calculation results haven been presented in previous chapters. Some limitations will be discussed here.

6.13.1 Multiple Cut Model to Estimate the Residual Stress in LV

In Chapter 5, to develop the heart tube model, all the geometrical information is obtained from the experiments from Omens' work [59], including the geometry of heart tube and opening angles for heart slices after cuts. However, the experimental data are limited, for instance, the geometry of the heart in our model is measured from one photograph of a typical short-axis apical slice of a mouse heart [59]. More experiments are needed to improve the measurement for the geometry of hearts.

Considering the geometric changes after cutting, it is assumed that the heart tube will deform into the new circular cylindrical configuration after multiple cuts. However, due to the impact of shear stress, the heart might not maintain a cylindrical configuration after cutting, which will change the expression of the deformation tensor (like eq. (5.10)) in our work. Besides, the residual stress is induced by the complex growth processes during the life of heart. Previous work shows that the 3d residual stress distribution should be considered [36] to estimate the mechanical behaviour of living tissues, which leads to 3d residual strain. In our work, only circumferential and radial residual strains (2d distribution of residual strain) are considered, which are measurable by radial opening cuts.

A single fibre family is employed to describe the fibre structure of heart. The dispersed fibre families are experimentally observed, which are also used in our later works. The mechanical behaviour of heart tissues will be different with dispersed fibre families, whose effect is not included in this work.

Some revious research suggests that infinite cuts are needed to release all the residual stress in living tissues. In our model, we developed a 4-cut model rather than a model with more cuts, due to lack of sufficient experimental data. Further experimental evidence is needed to demonstrate whether 4-cut is sufficient to release most of the residual stress in the heart.

6.13.2 Coupled Agent-based and FE Model for MI after Infarction

In our work, an idealized half ellipsoid geometry is used to construct FE model for a rat LV. However, in reality, the geometry of LV is much more complex. With the real (and complex) geometry of LV, the mechanical behaviours might be different, which might lead to different mechanical cues and then induce the different migration processes of fibroblast.

The chemokine concentration is assumed to static during the healing process of MI as

$$\frac{\partial C}{\partial t} = 0.$$

In practice, the chemokine concentration responds to the bio-environment of the LV and changes with time; for instance, the nutrition concentration is changed with the healing process. With the time-varied chemokine concentration, the chemokine cue is different from the one in our model, which gives the different patterns of fibroblast migration. It affects the remodelling process of MI in LV.

In our model, the fibroblast is assumed to be a rigid sphere, passively responding to external cues. However, the real fibroblast is deformable, which also contributes to the mechanical behaviours of heart tissues. In our future work, the deformation of fibroblasts will be included, as well as its mechanical contribution for heart functions.

In general, during the heart healing, the remodelling and growth coincidently occur to regulate the heart function. In our coupled model, the (volumetric) growth is ignored, while only the fibre remodelling is investigated. However, the overall mechanical behaviour is affected by the (volumetric) growth of tissues. For instance, the fibre structure is modified by (volumetric) growth (discussed in Chapter 7), which will change the material properties of infarcted tissues. As a result, the mechanical cues will be influenced by growth, which changes the fibre remodelling. For a global view, the interaction between remodelling and growth should be considered to predict the heart function during healing process.

6.14 Conclusion

This thesis focuses on the interactions between mechanical behaviour and G&R processes for living organs. According to nonlinear elastic theories, residual stress, induced by complex G&R processes, is of importance to affect the subsequent mechanical responses of soft tissues to external loading. Here, a multiple cut model is developed to estimate residual stress induced by G&R processes in the heart, which helps to explain recent experiments on residual stress.

To simulate the G&R process during MI, a multiscale algorithm is employed to couple (organ-level) three-dimensional heart models with (cell level) agent-based models. Our models capture interactions and information exchange processes between mechanical behaviour and collagen tissue remodelling guided by bio-environmental cues.

In addition, a volumetric growth approach is developed to simulate the inhomogeneous growth in the residually-stressed current configuration for a living organ, which will be embedded into simulations of the heart G&R process.

In Chaper 5, multiple-cut models are developed to estimate the residual stress distributions in the LVs of mice, inspired by experimental observation by [59]. They show that both radial and circumferential cuts are required to release the residual stresses. Remarkably, the results suggest that using radial cuts alone leads to significantly underestimated residual stress. As mentioned in previous researches, it suggests many cuts are needed to release all residual stress in living organs, since residual stress is induced by the complex (inhomogeneous) growth. Accordingly, our 4-cut model may give better estimations for residual stress than the 2-cut model. This conclusion is also supported by the estimated residual stress distributions. As shown in Chapter 5, stress distributions are smoother when estimated by the 4-cut model, but with a similar magnitude to the 2-cut model. The stress states estimated by the 4-cut model are more reasonable for living organs.

The computational results also explain experimental observation by Fung [3] who concluded that a single cut can release all residual stress in the residually stressed configuration of an artery, since the subsequent radial cuts don't introduce any more elastic deformations. Our models support that the 1-cut configuration is not the stress free configuration for living organs. More cuts are needed to release the residual stress and address the stress-free configuration for the heart during MI healing.

In Chapter 6, a multiscale model is developed by coupling an agent-based model with a three-dimensional left ventricle model. To simulate the appropriate material properties for myocardium, a proper fibre tension-compression 'switch' is developed in constitutive laws of LV tissues. The

time-dependent model captures the interaction and information exchange process between mechanical behaviour and collagen tissue remodelling guided by various external cues. The simulations show shapes and the locations of infarctions could affect the mechanical behaviour of total LV and the local collagen cumulation.

For fibre structure, the mean angle of fibre structure decreases near the endosurface for a circular infarction while it decreases less for the elliptical infarction. At the infarction centre, the anisotropy of the fibre structure for a circular infarction, reflected by kurtosis of the fibre structure, increases more.

For stress states, in the FE model, the overall stress distributions are significantly changed during MI processes for the heart with circular or elliptical infarctions. The stress concentrations are obviously in the infarcted regions. For strain, the evolution of strain fits with the experimental observations for both infarctions. However, strains decrease more for tissues with elliptical infarctions.

A theoretical framework is developed to calculate the mechanical behaviours of soft tissue after introducing inhomogeneous growth in a residually-stressed current configuration. Under this framework, the growth could be rationally assumed to occur from the residually-stressed configuration, which avoids to assume the growth occurs in a 'virtual' reference configuration in many previous researches. Moreover, growth deformation will be automatically included when computing any further elastic behaviours by the SEF related to growth-updated configurations. For this sake, it gives the convenience to avoid remeshing the elastic body under FE computational framework.

6.15 Future Work

For the multiple-cut model in Chapter 4, the tissues are assumed to be composed with matrix material and a single fibre family. However, according to experiments by [70], the fibre orientation is dispersed, while the fibre structure could be considered as dispersed fibre families. Therefore, the constitutive laws for tissues could be modified with a fibre orientation density function for the tissues with dispersed fibre families. For instance, the constitutive law (HO model) in Chapter 3 is employed as

$$\Psi = \Psi_{\mathrm{m}} + \Psi_{\mathrm{f}}, \tag{6.98}$$

where

$$\Psi_{\mathrm{m}} = \frac{a}{2b}\{\exp[b(I_1 - 3)] - 1\}, \quad \Psi_{\mathrm{f}} = \frac{a_{\mathrm{f}}}{2b_{\mathrm{f}}}\{\exp[b_{\mathrm{f}}(I_4 - 1)^2] - 1\}, \tag{6.99}$$

$a, b, a_{\mathrm{f}}, b_{\mathrm{f}}$ are material constants, and

$$I_1 = \mathrm{tr}(\mathbf{C}), \quad I_4 = \mathbf{f}_0 \cdot (\mathbf{C}\mathbf{f}_0), \tag{6.100}$$

I_1 and I_4 being the invariants corresponding to the matrix and fibre structure of the myocardium.

And considering the 2d dispersed fibre families, the SEF for fibre Ψ_{f} is rewritten as

$$\Psi_{\mathrm{f}} = \frac{1}{\pi} \frac{a_{\mathrm{f}}}{2b_{\mathrm{f}}} \int \left[\exp b_{\mathrm{f}}(I_4(\Theta) - 1)^2 - 1\right] \varphi(\Theta)\, \mathrm{d}\Theta, \tag{6.101}$$

where $a_{\mathrm{f}}, b_{\mathrm{f}}$ are the material parameters for fibres, $\varphi(\theta)$ is the fibre orientation density function and Θ is the angle to a specified orientation.

This SEF can give a better estimation for the stress-strain relation for heart tissues. Besides, as mentioned in Chapter 5, the shear stress will be introduced if the SEF is only including a single fibre family. With dispersed (and symmetric) fibre families, the distribution of shear stresses will be symmetry as the fibre structure, while the effects by shear stress will be further reduced due to symmetry of fibre structure (the example can be found at section **5.4.1**).

In Chapter 5, according to experimental observations by Omens, we assumed 2 or 4 cuts can release the residual stress in LV tube. However, if experimental data are available for opening angle measurements with even more cuts, the residual stress can be estimated by multiple-cut models, which can improve the residual stress estimation. Besides, it can prove the validation on questions whether the 4-cut model gives reasonable estimations for the residual stress, even though the 4-cut model has advantages compared with previous single cut models.

The approaches for fibre remodel (Chapter 6) and volumetric growth (Chapter 7) are both presented in our researches. Furthermore, our academic ambition is to develop a framework to investigate the heart remodelling and growth of the heart by coupling the remodelling of fibre structure and volumetric growth through a multiscale model.

As mentioned in Chapters 6 and 7, the volumetric growth and fibre remodelling both occur in the current and loaded configurations. However, the simple combination of the two processes is not a rational way to determine the updated reference configuration and mechanical response of tissues. The different ways of coupling G&R processes will be considered to determine the mechanical behaviour of the fibre-reinforced tissues during G&R processes.

Bibliography

[1] ALASTRUE, V., MARTINEZ, M., AND DOBLARE, M. Modelling adaptative volumetric finite growth in patient-specific residually stressed arteries. *Journal of biomechanics 41*, 8 (2008), 1773–1781.

[2] ALFORD, P. W., HUMPHREY, J. D., AND TABER, L. A. Growth and remodeling in a thick-walled artery model: effects of spatial variations in wall constituents. *Biomechanics and modeling in mechanobiology 7*, 4 (2008), 245–262.

[3] AMAR, M. B., AND GORIELY, A. Growth and instability in elastic tissues. *Journal of the Mechanics and Physics of Solids 53*, 10 (2005), 2284–2319.

[4] BAEK, S., RAJAGOPAL, K., AND HUMPHREY, J. A theoretical model of enlarging intracranial fusiform aneurysms. *Journal of biomechanical engineering 128*, 1 (2006), 142–149.

[5] BERGEL, D. The static elastic properties of the arterial wall. *The Journal of physiology 156*, 3 (1961), 445.

[6] BERGEL, D. The properties of blood vessels. *Biomechanics: Its foundations and objectives* (1972), 105–140.

[7] CHUONG, C., AND FUNG, Y. Three-dimensional stress distribution in arteries. *Journal of biomechanical engineering 105*, 3 (1983), 268–274.

[8] CHUONG, C.-J., AND FUNG, Y.-C. Residual stress in arteries. In *Frontiers in biomechanics*. Springer, 1986, pp. 117–129.

[9] CLARKE, S. A., GOODMAN, N. C., AILAWADI, G., AND HOLMES, J. W. Effect of scar compaction on the therapeutic efficacy of anisotropic reinforcement following myocardial infarction in the dog. *Journal of cardiovascular translational research 8*, 6 (2015), 353–361.

[10] COSTA, K. D., MAY-NEWMAN, K., FARR, D., ODELL, W. G., MCCULLOCH, A. D., AND OMENS, J. H. Three-dimensional residual strain in midanterior canine left ventricle.

American Journal of Physiology-Heart and Circulatory Physiology 273, 4 (1997), H1968–H1976.

[11] DAVIS, E. C. Stability of elastin in the developing mouse aorta: a quantitative radioautographic study. *Histochemistry 100*, 1 (1993), 17–26.

[12] DICKINSON, R. B., GUIDO, S., AND TRANQUILLO, R. T. Biased cell migration of fibroblasts exhibiting contact guidance in oriented collagen gels. *Annals of biomedical engineering 22*, 4 (1994), 342–356.

[13] DRIESSEN, N., PETERS, G., HUYGHE, J., BOUTEN, C., AND BAAIJENS, F. Remodelling of continuously distributed collagen fibres in soft connective tissues. *Journal of biomechanics 36*, 8 (2003), 1151–1158.

[14] DRIESSEN, N., WILSON, W., BOUTEN, C., AND BAAIJENS, F. A computational model for collagen fibre remodelling in the arterial wall. *Journal of theoretical biology 226*, 1 (2004), 53–64.

[15] DRIESSEN, N. J., BOERBOOM, R. A., HUYGHE, J. M., BOUTEN, C. V., AND BAAIJENS, F. P. Computational analyses of mechanically induced collagen fiber remodeling in the aortic heart valve. *Journal of biomechanical engineering 125*, 4 (2003), 549–557.

[16] ERIKSSON, T., WATTON, P., LUO, X., AND VENTIKOS, Y. Modelling volumetric growth in a thick walled fibre reinforced artery. *Journal of the Mechanics and Physics of Solids 73* (2014), 134–150.

[17] FINLAY, H. M., WHITTAKER, P., AND CANHAM, P. B. Collagen organization in the branching region of human brain arteries. *Stroke 29*, 8 (1998), 1595–1601.

[18] FOMOVSKY, G. M., AND HOLMES, J. W. Evolution of scar structure, mechanics, and ventricular function after myocardial infarction in the rat. *American Journal of Physiology-Heart and Circulatory Physiology 298*, 1 (2010), H221–H228.

[19] FOMOVSKY, G. M., MACADANGDANG, J. R., AILAWADI, G., AND HOLMES, J. W. Model-based design of mechanical therapies for myocardial infarction. *Journal of cardiovascular translational research 4*, 1 (2011), 82–91.

[20] FOMOVSKY, G. M., ROUILLARD, A. D., AND HOLMES, J. W. Regional mechanics determine collagen fiber structure in healing myocardial infarcts. *Journal of molecular and cellular cardiology 52*, 5 (2012), 1083–1090.

[21] FUNG, Y., AND CHUONG, C. Three-dimensional stress distribution in arteries. In *ASME* (1983), vol. 105, pp. 268–274.

[22] FUNG, Y., FRONEK, K., AND PATITUCCI, P. Pseudoelasticity of arteries and the choice of its mathematical expression. *American Journal of Physiology-Heart and Circulatory Physiology 237*, 5 (1979), H620–H631.

[23] FUNG, Y., AND LIU, S. Change of residual strains in arteries due to hypertrophy caused by aortic constriction. *Circulation Research 65*, 5 (1989), 1340–1349.

[24] GLEASON, R., TABER, L., AND HUMPHREY, J. A 2-d model of flow-induced alterations in the geometry, structure, and properties of carotid arteries. *Journal of biomechanical engineering 126*, 3 (2004), 371–381.

[25] GÖKTEPE, S., ABILEZ, O. J., AND KUHL, E. A generic approach towards finite growth with examples of athlete's heart, cardiac dilation, and cardiac wall thickening. *Journal of the Mechanics and Physics of Solids 58*, 10 (2010), 1661–1680.

[26] GORIELY, A., AND AMAR, M. B. On the definition and modeling of incremental, cumulative, and continuous growth laws in morphoelasticity. *Biomechanics and Modeling in Mechanobiology 6*, 5 (2007), 289–296.

[27] GUCCIONE, J. M., MOONLY, S. M., WALLACE, A. W., AND RATCLIFFE, M. B. Residual stress produced by ventricular volume reduction surgery has little effect on ventricular function and mechanics: a finite element model study. *The Journal of thoracic and cardiovascular surgery 122*, 3 (2001), 592–599.

[28] HAN, H., AND FUNG, Y. Residual strains in porcine and canine trachea. *Journal of biomechanics 24*, 5 (1991), 307311–309315.

[29] HAN, H.-C., AND FUNG, Y.-C. Longitudinal strain of canine and porcine aortas. *Journal of biomechanics 28*, 5 (1995), 637–641.

[30] HAN, H.-C., ZHAO, L., HUANG, M., HOU, L.-S., HUANG, Y.-T., AND KUANG, Z.-B. Postsurgical changes of the opening angle of canine autogenous vein graft. *Journal of biomechanical engineering 120*, 2 (1998), 211–216.

[31] HARITON, I., GASSER, T., HOLZAPFEL, G., ET AL. Stress-driven collagen fiber remodeling in arterial walls. *Biomechanics and modeling in mechanobiology 6*, 3 (2007), 163–175.

[32] HOLZAPFEL, A. G. Nonlinear solid mechanics ii.

[33] HOLZAPFEL, G. A., AND GASSER, T. C. Computational stress-deformation analysis of arterial walls including high-pressure response. *International journal of cardiology 116*, 1 (2007), 78–85.

[34] HOLZAPFEL, G. A., GASSER, T. C., AND OGDEN, R. W. A new constitutive framework for arterial wall mechanics and a comparative study of material models. *Journal of elasticity and the physical science of solids 61*, 1-3 (2000), 1–48.

[35] HOLZAPFEL, G. A., AND OGDEN, R. W. Constitutive modelling of passive myocardium: a structurally based framework for material characterization. *Philosophical Transactions of the Royal Society of London A: Mathematical, Physical and Engineering Sciences 367*, 1902 (2009), 3445–3475.

[36] HOLZAPFEL, G. A., AND OGDEN, R. W. Modelling the layer-specific three-dimensional residual stresses in arteries, with an application to the human aorta. *Journal of the Royal Society Interface* (2009), rsif20090357.

[37] HOLZAPFEL, G. A., AND OGDEN, R. W. On the tension–compression switch in soft fibrous solids. *European Journal of Mechanics-A/Solids 49* (2015), 561–569.

[38] HOLZAPFEL, G. A., AND OGDEN, R. W. On fiber dispersion models: Exclusion of compressed fibers and spurious model comparisons. *Journal of Elasticity* (2016), 1–20.

[39] HOLZAPFEL, G. A., SOMMER, G., AUER, M., REGITNIG, P., AND OGDEN, R. W. Layer-specific 3d residual deformations of human aortas with non-atherosclerotic intimal thickening. *Annals of biomedical engineering 35*, 4 (2007), 530–545.

[40] HSU, F.-H. The influences of mechanical loads on the form of a growing elastic body. *Journal of biomechanics 1*, 4 (1968), 303–311.

[41] HUISKES, R., RUIMERMAN, R., VAN LENTHE, G. H., AND JANSSEN, J. D. Effects of mechanical forces on maintenance and adaptation of form in trabecular bone. *Nature 405*, 6787 (2000), 704–706.

[42] HUISMAN, R., SIPKEMA, P., WESTERHOF, N., AND ELZINGA, G. Comparison of models used to calculate left ventricular wall force. *Medical and Biological Engineering and Computing 18*, 2 (1980), 133–144.

[43] HUMPHREY, J., AND HOLZAPFEL, G. A. Mechanics, mechanobiology, and modeling of human abdominal aorta and aneurysms. *Journal of biomechanics 45*, 5 (2012), 805–814.

[44] HUMPHREY, J., AND RAJAGOPAL, K. A constrained mixture model for growth and remodeling of soft tissues. *Mathematical models and methods in applied sciences 12*, 03 (2002), 407–430.

[45] KARŠAJ, I., SORIĆ, J., AND HUMPHREY, J. D. A 3-d framework for arterial growth and remodeling in response to altered hemodynamics. *International journal of engineering science 48*, 11 (2010), 1357–1372.

[46] KERCKHOFFS, R. C. Computational modeling of cardiac growth in the post-natal rat with a strain-based growth law. *Journal of biomechanics 45*, 5 (2012), 865–871.

[47] KERCKHOFFS, R. C., OMENS, J. H., AND MCCULLOCH, A. D. A single strain-based growth law predicts concentric and eccentric cardiac growth during pressure and volume overload. *Mechanics research communications 42* (2012), 40–50.

[48] KLEPACH, D., LEE, L. C., WENK, J. F., RATCLIFFE, M. B., ZOHDI, T. I., NAVIA, J. L., KASSAB, G. S., KUHL, E., AND GUCCIONE, J. M. Growth and remodeling of the left ventricle: a case study of myocardial infarction and surgical ventricular restoration. *Mechanics research communications 42* (2012), 134–141.

[49] KROON, M. A continuum mechanics framework and a constitutive model for remodelling of collagen gels and collagenous tissues. *Journal of the Mechanics and Physics of Solids 58*, 6 (2010), 918–933.

[50] KROON, W., DELHAAS, T., ARTS, T., AND BOVENDEERD, P. Computational modeling of volumetric soft tissue growth: application to the cardiac left ventricle. *Biomechanics and modeling in mechanobiology 8*, 4 (2009), 301–309.

[51] LEGRICE, I. J., SMAILL, B., CHAI, L., EDGAR, S., GAVIN, J., AND HUNTER, P. J. Laminar structure of the heart: ventricular myocyte arrangement and connective tissue architecture in the dog. *American Journal of Physiology-Heart and Circulatory Physiology 269*, 2 (1995), H571–H582.

[52] LIU, S., AND FUNG, Y. Zero-stress states of arteries. *Journal of biomechanical engineering 110*, 1 (1988), 82–84.

[53] MCDOUGALL, S., DALLON, J., SHERRATT, J., AND MAINI, P. Fibroblast migration and collagen deposition during dermal wound healing: mathematical modelling and clinical implications. *Philosophical Transactions of the Royal Society of London A: Mathematical, Physical and Engineering Sciences 364*, 1843 (2006), 1385–1405.

[54] MENZEL, A., AND KUHL, E. Frontiers in growth and remodeling. *Mechanics research communications 42* (2012), 1–14.

[55] MERODIO, J., OGDEN, R. W., AND RODRÍGUEZ, J. The influence of residual stress on finite deformation elastic response. *International Journal of Non-Linear Mechanics 56* (2013), 43–49.

[56] NOVAK, V. P., YIN, F., AND HUMPHREY, J. Regional mechanical properties of passive myocardium. *Journal of biomechanics 27*, 4 (1994), 403–412.

[57] OGDEN, R. W. *Non-linear elastic deformations*. Courier Corporation, 1997.

[58] OLSSON, T., AND KLARBRING, A. Residual stresses in soft tissue as a consequence of growth and remodeling: application to an arterial geometry. *European Journal of Mechanics-A/Solids 27*, 6 (2008), 959–974.

[59] OMENS, J., MCCULLOCH, A., AND CRISCIONE, J. Complex distributions of residual stress and strain in the mouse left ventricle: experimental and theoretical models. *Biomechanics and modeling in mechanobiology 1*, 4 (2003), 267–277.

[60] OMENS, J. H., AND FUNG, Y.-C. Residual strain in rat left ventricle. *Circulation Research 66*, 1 (1990), 37–45.

[61] OMENS, J. H., MACKENNA, D. A., AND MCCULLOCH, A. D. Measurement of strain and analysis of stress in resting rat left ventricular myocardium. *Journal of biomechanics 26*, 6 (1993), 665–676.

[62] POOLE, K., KHAIRY, K., FRIEDRICHS, J., FRANZ, C., CISNEROS, D. A., HOWARD, J., AND MUELLER, D. Molecular-scale topographic cues induce the orientation and directional movement of fibroblasts on two-dimensional collagen surfaces. *Journal of molecular biology 349*, 2 (2005), 380–386.

[63] RACHEV, A., KANE, T., AND MEISTER, J. Experimental investigation of the distribution of residual strains in the artery wall.

[64] REN, J.-S. Growth and residual stresses of arterial walls. *Journal of theoretical biology 337* (2013), 80–88.

[65] RODRIGUEZ, E. K., HOGER, A., AND MCCULLOCH, A. D. Stress-dependent finite growth in soft elastic tissues. *Journal of biomechanics 27*, 4 (1994), 455–467.

[66] ROUILLARD, A. D., AND HOLMES, J. W. Mechanical regulation of fibroblast migration and collagen remodelling in healing myocardial infarcts. *The Journal of physiology 590*, 18 (2012), 4585–4602.

[67] ROUILLARD, A. D., AND HOLMES, J. W. Coupled agent-based and finite-element models for predicting scar structure following myocardial infarction. *Progress in biophysics and molecular biology 115*, 2 (2014), 235–243.

[68] SÁEZ, P., PEÑA, E., MARTÍNEZ, M. A., AND KUHL, E. Computational modeling of hypertensive growth in the human carotid artery. *Computational mechanics 53*, 6 (2014), 1183–1196.

[69] SCHMID, H., WATTON, P., MAURER, M., WIMMER, J., WINKLER, P., WANG, Y., RÖHRLE, O., AND ITSKOV, M. Impact of transmural heterogeneities on arterial adaptation. *Biomechanics and modeling in mechanobiology 9*, 3 (2010), 295–315.

[70] SCHRIEFL, A. J., REINISCH, A. J., SANKARAN, S., PIERCE, D. M., AND HOLZAPFEL, G. A. Quantitative assessment of collagen fibre orientations from two-dimensional images of soft biological tissues. *Journal of The Royal Society Interface 9*, 76 (2012), 3081–3093.

[71] SHAMS, M., DESTRADE, M., AND OGDEN, R. W. Initial stresses in elastic solids: constitutive laws and acoustoelasticity. *Wave Motion 48*, 7 (2011), 552–567.

[72] SKALAK, R. Growth as a finite displacement field. In *Proceedings of the IUTAM symposium on finite elasticity* (1981), Springer, pp. 347–355.

[73] TABER, L. A model for aortic growth based on fluid shear and fiber stresses. *TRANSACTIONS-AMERICAN SOCIETY OF MECHANICAL ENGINEERS JOURNAL OF BIOMECHANICAL ENGINEERING 120* (1998), 348–354.

[74] TABER, L., AND CHABERT, S. Theoretical and experimental study of growth and remodeling in the developing heart. *Biomechanics and modeling in mechanobiology 1*, 1 (2002), 29–43.

[75] TABER, L. A. Biomechanics of cardiovascular development. *Annual review of biomedical engineering 3*, 1 (2001), 1–25.

[76] TABER, L. A., AND EGGERS, D. W. Theoretical study of stress-modulated growth in the aorta. *Journal of theoretical biology 180*, 4 (1996), 343–357.

[77] TABER, L. A., HU, N., PEXIEDER, T., CLARK, E. B., AND KELLER, B. B. Residual strain in the ventricle of the stage 16-24 chick embryo. *Circulation research 72*, 2 (1993), 455–462.

[78] TABER, L. A., AND HUMPHREY, J. D. Stress-modulated growth, residual stress, and vascular heterogeneity. *Journal of biomechanical engineering 123*, 6 (2001), 528–535.

[79] TAKAMIZAWA, K., AND HAYASHI, K. Strain energy density function and uniform strain hypothesis for arterial mechanics. *Journal of biomechanics 20*, 1 (1987), 7–17.

[80] TSAMIS, A., CHENG, A., NGUYEN, T. C., LANGER, F., MILLER, D. C., AND KUHL, E. Kinematics of cardiac growth: in vivo characterization of growth tensors and strains. *Journal of the mechanical behavior of biomedical materials 8* (2012), 165–177.

[81] UNTERBERGER, M. J., SCHMOLLER, K. M., BAUSCH, A. R., AND HOLZAPFEL, G. A. A new approach to model cross-linked actin networks: multi-scale continuum formulation and computational analysis. *journal of the mechanical behavior of biomedical materials 22* (2013), 95–114.

[82] VAISHNAV, R. N., YOUNG, J. T., AND PATEL, D. J. Distribution of stresses and of strain-energy density through the wall thickness in a canine aortic segment. *Circulation research 32*, 5 (1973), 577–583.

[83] VALENTIN, A., AND HUMPHREY, J. Evaluation of fundamental hypotheses underlying constrained mixture models of arterial growth and remodelling. *Philosophical Transactions of the Royal Society of London A: Mathematical, Physical and Engineering Sciences 367*, 1902 (2009), 3585–3606.

[84] VALENTÍN, A., HUMPHREY, J., AND HOLZAPFEL, G. A. A finite element-based constrained mixture implementation for arterial growth, remodeling, and adaptation: Theory and numerical verification. *International journal for numerical methods in biomedical engineering 29*, 8 (2013), 822–849.

[85] VANDIVER, R. Effect of residual stress on peak cap stress in arteries. *Mathematical biosciences and engineering: MBE 11*, 5 (2014), 1199–1214.

[86] VOLOKH, K. Stresses in growing soft tissues. *Acta Biomaterialia 2*, 5 (2006), 493–504.

[87] VON MALTZAHN, W. W., WARRIYAR, R. G., AND KEITZER, W. F. Experimental measurements of elastic properties of media and adventitia of bovine carotid arteries. *Journal of biomechanics 17*, 11 (1984), 839–847.

[88] VOSSOUGHI, J., HEDJAZI, Z., AND BORRIS, F. Intimal residual stress and strain in large arteries. *ASME-PUBLICATIONS-BED 24* (1993), 434–434.

[89] WANG, H., GAO, H., LUO, X., BERRY, C., GRIFFITH, B., OGDEN, R., AND WANG, T. Structure-based finite strain modelling of the human left ventricle in diastole. *International journal for numerical methods in biomedical engineering 29*, 1 (2013), 83–103.

[90] WANG, H., LUO, X., GAO, H., OGDEN, R., GRIFFITH, B., BERRY, C., AND WANG, T. A modified holzapfel-ogden law for a residually stressed finite strain model of the human left ventricle in diastole. *Biomechanics and modeling in mechanobiology 13*, 1 (2014), 99–113.

[91] WANG, V. Y., HUSSAN, J. R., YOUSEFI, H., BRADLEY, C. P., HUNTER, P. J., AND NASH, M. P. Modelling cardiac tissue growth and remodelling. *Journal of Elasticity 129*, 1-2 (2017), 283–305.

[92] WATTON, P., AND HILL, N. Evolving mechanical properties of a model of abdominal aortic aneurysm. *Biomechanics and modeling in mechanobiology 8*, 1 (2009), 25–42.

[93] WATTON, P., HILL, N., AND HEIL, M. A mathematical model for the growth of the abdominal aortic aneurysm. *Biomechanics and modeling in mechanobiology 3*, 2 (2004), 98–113.

[94] WATTON, P. N., VENTIKOS, Y., AND HOLZAPFEL, G. A. Modelling the growth and stabilization of cerebral aneurysms. *Mathematical Medicine and Biology 26*, 2 (2009), 133–164.

[95] WONG, J., AND KUHL, E. Generating fibre orientation maps in human heart models using poisson interpolation. *Computer methods in biomechanics and biomedical engineering 17*, 11 (2014), 1217–1226.

[96] YIN, F. C. Ventricular wall stress. *Circulation Research 49*, 4 (1981), 829–842.